Investigating the role of FGF signalling in left-right determination

A thesis present for the degree of Doctor of Philosophy (DPhil)
St Hilda's College, University of Oxford

Rosie Beth Little
Mammalian Genetics Unit, MRC Harwell
Department of Physiology, Anatomy and Genetics, University of Oxford

Supervisors: Dr Dominic Norris (MGU, MRC Harwell)
Prof. Mathilda Mommersteeg (DPAG, Oxford)

Hilary Term 2021

Word count: 42,912

Abstract:

Investigating the role of FGF signalling in left-right determination

Rosie Beth Little, St Hilda's College

Doctor of Philosophy (DPhil)

Hilary Term 2021

Left-right patterning is set up early in development, at embryonic day 8.5 in the mouse. Cilia are present on the cells of a transient structure, termed the node, the location where L/R symmetry is broken. In this pit-like structure, motile cilia generate a leftwards flow of extracellular fluid, which is translated into a left-specific signal by immotile cilia on crown cells at the edge of the node. How exactly this flow is translated remains unknown, with one hypothesis proposing that nodal vesicular parcels (NVPs) within the node transport signalling molecules to the left side. FGF signalling was first implicated in L/R patterning when an *Fgf8* mutant mouse was shown to exhibit situs defects. The precise role of FGFs in L/R patterning is unclear, but they have been proposed to regulate NVP release. Other hypotheses include them functioning in the regulation of node cilia length, and in the formation and maintenance of the node structure. These hypotheses are explored in this thesis, through the re-assessment of the *Fgf8* mouse mutant and through the use of FGF signalling receptor inhibitors in embryo culture. My findings confirm a role for FGF signalling in L/R determination, and support a role for FGF signalling in specifying, maintaining and/or patterning the cells that make up the embryonic node. My data also casts doubt on the evidence previously used to argue for the existence of NVPs. Analysis of the location of FGFRs in the embryo and within cells shows the presence of FGFR2 in the node cilia, but whether ciliary localisation of FGFRs is important in L/R patterning remains unclear. I present evidence that the major mechanism by which FGF signalling affects L/R determination is through the formation/patterning of the node. However, I also present evidence for a lesser role FGFs may play in controlling mammalian cilia length. Intriguingly, my data also indicates a strong influence of genetic background on the *Fgf8* mutants.

Acknowledgements

Firstly, I would like to thank my supervisor, Dr Dominic Norris, for his support throughout my project and in the writing of this thesis. Thank you for correcting my terrible grammar, and for making sense out of my nonsense.

I would also like to thank all past and present members of the lab, and in particular Becca Walker, Dragoș Leordean and Laura Dyer for their support and friendship. I would additionally like to thank the Greenfield lab, with whom we share lab meetings, for their input, advice and discussion relating to this project.

The core services at Harwell have been invaluable and the work described here would not have been possible without their efforts. The staff of the Mary Lyon Centre staff who manage the mice facilities and carry out the day to day care, maintenance and timed breeding that underpinned most of this project. In particular I would like to thank Lucie Visor and her ward team, along with the production ward. Also thanks go to Michelle Stewart, Sara Wells and Anju Paudyal for their support and guidance. I would like to thank the genotyping team for their joint pursuit in my relentless genotyping difficulties of tiny tissue samples: Daniel Coneyworth, Debbie Williams and Rumana Zaman in particular. Thank you also to Rosie Bunton-Stasyshyn and Zsombor-Szoke Kovács for their help in processing and analysing my micro-CT samples and data. Also thanks to Jeremy Sanderson for the microscopy (and general!) advice provided throughout my time at Harwell.

My time spent at Harwell would have been very much less enjoyable and more difficult without the friends I have made here. Special mention to Raissa Kay, Jamie Lee, Lucy Dunbar, Abi Harris, Cathy Livermore and (even more so) Dani Sagar. I could not have done this without you, thank you.

Thank you to my sisters and parents: for their belief that I can do anything I set my mind to, and their support for if and when I fail.

My final and most sincere thanks go to Liam Flanagan, to whom this thesis is dedicated.

For the endless support, patience, words of encouragement and cups of tea: thank you.

I will forever be grateful to have you in my life and by my side.

Abbreviations

A/P	Anterior/posterior
ACH	Achondroplasia
ADPKD	Autosomal dominant polycystic kidney disease
BB	Basal body
BSA	Bovine serum albumin
cDNA	Complementary DNA
CHD	Congenital heart disease
CICR	Calcium-induced Calcium release
CPC	Ciliary pore complex
CSF	Cerebrospinal fluid
CVs	Ciliary vesicles
D/V	Dorsal/ventral
DA	Distal appendage
DAPI	4', 6-diamidino-2-phenylindole
DIG	Digoxigenin
DiI	1,1′-dioctadecyl-3,3,3′,3′-tetramethylindocarbocyanine perchlorate
DMEM	Dulbecco's modified eagle medium
DMSO	Dimethyl sulfoxide
DORV	Double outlet right ventricle
dpc	Days post coitum
dTTP	Deoxythymidine triphosphate
EDTA	Ethylenediaminetetraacetic acid

EGF	Epidermal growth factor
EGFR	Epidermal growth factor receptor
ER	Endoplasmic reticulum
FBS	Fetal bovine serum
FGF	Fibroblast growth factor
FGFR	Fibroblast growth factor receptor
GFP	Green fluorescent protein
GRP	Gastrocoel Roof Plate
Hh	Hedgehog
HISS	Heat-inactivated sheep serum
IAA	Interrupted aortic arch
IDA	Inner dynein arms
IFT	Intraflagellar transport
IGF	Insulin-like growth factor
IgG	Immunoglobulin G
Ihh	Indian hedgehog
IMPC	International mouse phenotyping consortium
IPTG	Isopropyl-β-D-thiogalactoside
IVC	Individually ventilated cages
KV	Kupfer's Vesicle
L/R	Left/right
LB	Luria broth
LPM	Lateral plate mesoderm

LRO	Left-right organiser
MEF	Mouse embryonic fibroblast
MO	Morpholino
mRNA	Messenger RNA
NBT/BCIP	Nitro-blue tetrazolium/5-bromo-4-chloro-3'-indolyphosphate
NP-40	Nonidet P-40
NPC	Nuclear pore complex
NTMT	Alkaline phosphatase buffer (NaCl, Tris-Cl, MgCl2, Tween)
NVPs	Nodal Vesicular parcels
OB	Olfactory bulb
ODA	Outer dynein arms
PBS	Phosphate-buffered saline
PBT	PBS + 0.1% Tween 20
PCP	Planar Cell Polarity
PCVs	Preciliary vesicles
PDGFRα	Platelet-derived growth factor receptor A
PFA	Paraformaldehyde
ppm	Parts per million
qPCR	Quantative polymerase chain reaction
RA	Retanoic acid
RPI	Right pulmonary isomerism
RPM	Revolutions per minute
RT	Room temperature

SA	Situs ambiguus
SAGs	Sulfated Glucoaminoglycans
SDS	Sodium dodecyl sulphate
SELI	Self-enhancement lateral-inhibition
SEM	Scanning electron microscopy
Shh	Sonic hedgehog
SIT	Situs inversus totalis
SPF	Specific pathogen-free
ss	Somite stage
SSC	Saline sodium citrate
TBE	Tris-borate-EDTA
TBST	Tris-buffered saline + 0.1% Tween 20
TD	Thanatophoric dysplasia
TE	Tris-EDTA
TGF	Transforming growth factor
TX-100	Triton-X-100
TZ	Transition zone
µCT	Micro computed tomography
UTR	Untranslated region
WIF	Wholemount immunofluorescence
WISH	Wholemount In Situ Hybridisation
WT	Wild-type
X-gal	5-bromo-4-chloro-3-indolyl-β-D-galactopyranoside

List of Figures

Figure 1.1: Diagrammatic representation of tissues containing/associated with motile cilia in the human body.

Figure 1.2: Diagrammatic comparison of microtubule doublet formation.

Figure 1.3: Diagrammatic representation of situs presentation.

Figure 1.4: The mouse embryo and node.

Figure 1.5: Genetic pathways in the mouse embryonic node and lateral plate mesoderm

Figure 3.1.1: Putative NVPs in mouse embryonic nodes.

Figure 3.2.1 Schematic for embryo culture with DiI.

Figure 3.2.2: Example cultured embryos and scoring system.

Figure 3.2.3: Cell death and node identifiability of cultured embryos.

Figure 3.2.4: *Fgfr1* Wholemount *In Situ* Hybridisation.

Figure 3.2.5: *Fgfr2* Wholemount *In Situ* Hybridisation.

Figure 3.2.6: *Fgfr3* Wholemount *In Situ* Hybridisation.

Figure 3.2.7: *Fgfr4* Wholemount *In Situ* Hybridisation.

Figure 3.2.8: FGFR proteins in the mouse node.

Figure 3.2.9: FGFR protein localisation in ciliated MEF cells.

Figure 3.2.10: FGFR protein localisation in un-ciliated (actively growing) MEF cells.

Figure 3.2.11: FGFR protein localisation in ciliated RPE1 cells.

Figure 3.2.12: FGFR protein localisation in un-ciliated (actively growing) RPE1 cells.

Figure 3.2.13: FGFR protein localisation in ciliated NIH3T3 cells.

Figure 3.2.14: FGFR protein localisation in un-ciliated (actively growing) NIH3T3 cells.

Figure 4.2.1: Gene expression in cultured embryos.

Figure 4.2.2: SEM images of cultured and uncultured nodes.

Figure 4.2.3: SEM images of nodes from embryos cultured with FGF signalling inhibitors.

Figure 4.2.4: Embryo culture score.

Figure 4.2.5: Progression of embryos in culture.

Figure 4.2.6: Number of NVP-like objects within nodes.

Figure 4.2.7: Cilia lengths in cultured embryos.

Figure 4.2.8: Node structure following culture.

Figure 4.2.9: Abnormal node structure following culture.

Figure 4.2.10: Gene expression in cultured embryos.

Figure 5.1.1: Schematic representation of the *Fgf8* alleles produced by Meyers and Martin (1998).

Figure 5.1.2: Brain morphology of *Fgf8* mutants from Meyers and Martin (1998) paper, Figure 2b.

Figure 5.1.3: Nodes of *Fgf8* mutant and wild-type embryos stained with *Nodal*^{LacZ} from Meyers and Martin (1999) paper, Figure 2 (G&H).

Figure 5.2.1: E18.5 brains of *Fgf8* WT, Tm1.1 Hets and Tm1.1 Homs.

Figure 5.2.2: Slices from microCT imaging of E13.5 embryos.

Figure 5.2.3: Analysis of asymmetry in E9.5-10.5 embryos.

Figure 5.2.4: Analysis of phenotypes in E13.5 *Fgf8* mutant embryos.

Figure 5.2.5: Analysis of viability of *Fgf8* mutant embryos at embryonic time-points E8.5, E9.5-10.5 and E13.5.

Figure 5.2.6: Expression of *Pitx2* in the LPM of *Fgf8* mutant mouse embryos.

Figure 5.2.7: Expression of *Cerl2* in the node of *Fgf8* mutant mouse embryos.

Figure 5.2.8: Expression of *Cerl2* in cells posterior to the node of *Fgf8* mutant mouse embryos.

Figure 5.2.9: Analysis of node structure of *Fgf8* mutant embryos.

Figure 5.2.10: Normal morphology of the mouse embryonic node.

Figure 5.2.11: Node morphology phenotypes seen in *Fgf8* mutant embryo nodes.

Figure 5.2.12: Analysis of cilia length in *Fgf8* mutant nodes.

Figure 5.2.13: Analysis of number of NVP-like objects in *Fgf8* mutant nodes.

List of Tables

Table 3.2.1: Node Identifiability

Table 3.2.2: Cell Death

Table 4.2.1: Category definitions for embryo culture progress.

Table 5.1.1: Annotation of *Fgf8* alleles produced by Meyers and Martin (1998).

Table 5.1.2: Annotation of different *Fgf8* genotype mice.

Table 5.2.1: microCT scoring for *Fgf8* WT, Tm1.1 Het and Tm1.1 Hom E13.5 embryos.

Table of Contents

1.0 Introduction 16
1.1 Overview 16
1.2 Cilia 16
1.2.1 Cilia Structure 18
1.2.2 Ciliogenesis 19
1.2.3 Intraflagella Transport 20
1.2.4 The Transition Zone 20
1.2.5 Cilia Function - Immotile cilia 21
1.2.6 Cilia Function - Motile cilia 23
1.3 Laterality – Left-Right patterning 23
1.4 Node formation 25
1.4.1 Emergence of the node 25
1.4.2 Cilia in the node 26
1.4.3 Positioning nodal cilia 28
1.5 Flow and Breaking Symmetry 29
1.5.1 Establishing flow 29
1.5.2 Morphogen Gradient Hypothesis 29
1.5.3 Nodal Vesicular Parcel Hypothesis 30
1.5.4 Mechanosensation Hypothesis 30
1.5.5 Calcium asymmetry 32
1.6 Establishing Asymmetry 32
1.6.1 Genetic asymmetries at the node and LPM 32
1.6.2 Genetic asymmetries at the LPM 33
1.6.3 Transduction of signal from the node to the L-LPM 34
1.7 FGF Signalling 37
1.8 Aims 39
2.0 Materials & Methods 40
2.1 Universal Solutions 40
2.2 Mouse Lines 40
2.2.1 Background Strains 41
2.2.2 WT mice 41
2.2.3 *Fgf8* alleles 41
2.2.4 Relevant developmental stages 42
2.3 Molecular Biology 42
2.3.1 PCR 42

2.3.2 Genotyping 43
2.3.3 Agarose Gel Electrophoresis 43
2.3.4 DNA Sequencing 43
2.3.5 RNA isolation 44
2.3.6 cDNA synthesis 44
2.3.7 Plasmid linearization 44
2.3.8 Probe synthesis 44
2.3.9 TA Cloning for in situ probe plasmid synthesis 45
2.4 Cell Culture & Processing 46
2.4.1 Generating Primary Mouse Embryonic Fibroblasts 46
2.4.2 Thawing Cells 47
2.4.3 Freezing Cells 47
2.4.4 Splitting Cells 47
2.4.5 Fixing Cells 48
2.5 Embryo Dissection & Culture 48
2.5.1 Collection of Embryos 48
2.5.2 Dissection and staging of E8.5 embryos 48
2.5.3 Dissection and Situs Phenotyping of E9.5 embryos 49
2.5.4 Dissection and preparation of E15.5 embryos for µCT 49
2.5.5 Embryo Culture using Static Culture 49
2.5.6 Embryo Culture using Rolling Bottle apparatus 50
2.6 Embryo & Cell/Tissue Analysis 50
2.6.1 Wholemount In Situ Hybridisation 51
2.6.2 Wholemount Immunofluorescence 52
2.6.3 Scanning Electron Microscopy (SEM) 52
2.6.4 Cell Immunofluorescence 53
2.7 Statistical Analysis 53
2.8 Image Processing 54
2.8.1 Cilia length analysis 54
2.8.2 Counting number of vesicles (putative NVPs) in the node 54
2.8.3 Micro-CT analysis 55
3.0 Tanaka (2005) and the NVP hypothesis 56
3.1 Introduction 56
3.2 Results 58
3.2.1 Culture – incubation with DiI – SEM 58
3.2.2 Expression analysis of *Fgfr1-4* and FGFR1-4 63
3.3 Discussion 84

4.0 Investigating the role of FGF signalling in embryonic left-right axis development using embryo culture 90
4.1 Introduction 90
4.2 Results 93
4.2.1 Static culture 93
4.2.2 Rolling Bottle Culture 99
4.3 Discussion 118
4.3.1 FGF signalling and node cilia length 118
4.3.2 FGF Signalling and NVPs 119
4.3.3 The role of FGF signalling in Node morphology and formation 120
4.3.4 Inhibiting FGFR function 122
4.3.5 The impact of developmental timing and delay 123
4.3.6 Fgf8 mutant mouse 126
5.0 Characterisation of *Fgf8* mutant mice 128
5.1 Introduction 128
5.2 Results 132
5.2.1 Genetic background 132
5.2.2 $Fgf8^{Tm1.1}$ line analysis 132
5.2.3 Analysis of $Fgf8^{Tm1.1}$, $Fgf8^{Tm1.2}$, $Fgf8^{Tm1.1/Tm1.2}$ compound heterozygous mutants 139
5.3 Discussion 158
5.3.1 Hypotheses for the role of FGF signalling in L/R patterning 158
5.3.2 Non-situs phenotypes in $Fgf8^{tm1/tm2}$ embryos 160
5.3.3 Dosage sensitivity 161
5.3.4 Differences to Meyers and Martins' phenotypes – likely causes 162
6.0 Discussion 165
6.1 The NVP Hypothesis 165
6.2 A Role for FGF Signalling in Formation of the Node 168
6.3 FGFs in Regulating Cilia Length 169
6.4 Implications for understanding the mechanisms of L/R determination 170
6.5 The Role of Genetic Background in Phenotypes 172
6.6 Future Experiments and Directions 174
6.6.1 Experiments to follow 174
6.6.2 Directions of the field 175
6.6.3 Closing remarks 177
Bibliography 179
Appendix 189

1.0 Introduction

1.1 Overview

The external bilateral symmetry of the vertebrate body conceals a marked asymmetry that lies beneath, in terms of the positioning and patterning of most of the internal organs. This asymmetry is set up early on in embryonic development, at about two weeks post fertilisation in humans. In the mouse, our model organism of study, this occurs at the 8dpc (days post coitum) mark. The embryo at this time exhibits a transient structure (the node) in which L/R symmetry is physically broken. This pit-like structure is comprised of cells each with a single cilium, a subpopulation being immotile and the rest motile (McGrath et al. 2003). These interact through the creation and translation of a leftward flow of extracellular fluid. This flow is set up due to the alignment of the cilia in relation to the dorsal/ventral (D/V) and the anterior/posterior (A/P) axes of the body. As the flow breaks symmetry, downstream signalling cascades are activated, and an initial asymmetry is amplified through feedback loops (Little and Norris 2020). These, along with the cilium itself, will be discussed in the following sections.

1.2 Cilia

The cilium is a cellular organelle which is a hair-like projection from the cell's surface. Throughout the body, many cell types present cilia, which are either motile or immotile, and can be present either singly or in multiples. Arguably the most well-known cilia in the human body are those present in large numbers in a lawn-like fashion on the lining of the respiratory tract. These multiciliated cells exhibit a coordinated beating in order to facilitate mucus clearance of the airways. Other motile cilia are present in a number of organs within the human, namely the brain ventricles and reproductive system: either in the fallopian tubes or the testes (indicated in **Figure 1.1**). Motile cilia are also present during early

embryonic development in the transient structure the node, which acts as a left-right organiser (see section **1.4**).

Cilia are present across the spectrum of life, ranging from in the algae *Chlamydomonas*, which hints to the broad range of important and conserved functions they have. These have been extensively studied to reveal the huge range of vital functions and roles that the cilium has, from in lower organisms like *Chlamydomonas* to vertebrates such as the mouse. Cilia can be categorised in two ways, firstly relating to whether they are motile or immotile, and secondly by the characteristic structural configuration of the axonemal microtubule doublets which comprise the basis of their internal structure. However, not all organisms have cilia of both structural and motility types, with *Chlamydomonas*, for example, only have a motile cilium in the form of the flagella which drives the organism's motion through the environment (Salomé and Merchant 2019). Conversely, *C. elegans*, the nematode, only have immotile primary cilia, used for important cellular signalling functions (Bae and Barr 2008).

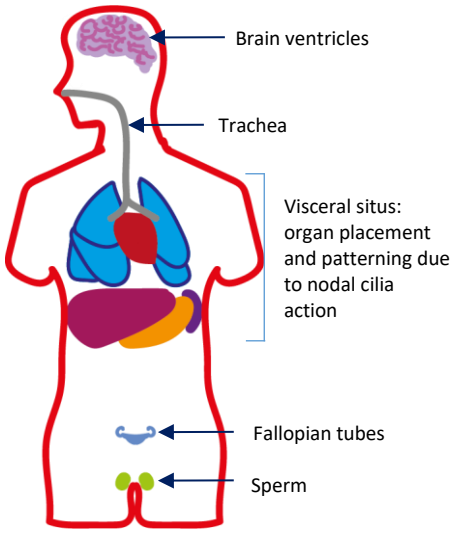


Figure 1.1: Diagrammatic representation of tissues containing/associated with motile cilia in the human body. Each tissue type is labelled.

1.2.1 Cilia Structure

The cilium is templated from the basal body, which is itself a modified centriole (Beisson and Wright 2003). The axonemal core of the basal body is arranged with 9 microtubule triplets arranged with rotational symmetry. Extending from this, two of the three microtubule triplets, the A and B tubules, form the doublets which comprise the basis of the cilia axoneme (Ishikawa and Marshall 2011). The basal body also orients the cilia to give the positive end of the axoneme towards its tip (Linck et al. 2016). The configuration of 9 pairs of microtubule doublets columnarly arranged in a rotationally symmetrical manner forms the axoneme within the cilium. This can be in a 9+0 arrangement, or, conversely, in a 9+2 arrangement, with the 2 relating to the presence of a central pair of microtubules in the centre of the axonemal lumen, or the 0 to the absence of this (**Figure 1.2**).

Motile cilia also show an additional important structure, in the form of dynein arms. These are made up of inner dynein arms (IDA) and outer dynein arms (ODA), which are anchored to the outer A tubule of the microtubule pairs (**Figure 1.2**). These function in a coordinated manner to provide the motion of these cilia; the ODA contract in sequence to produce this force and the IDA are argued to be important for the coordination of their movement (Satir and Christensen 2007).

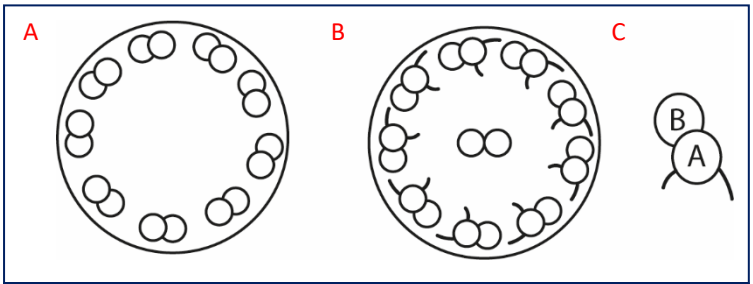


Figure 1.2: Diagrammatic comparison of microtubule doublet formation. A shows a 9+0 arrangement in cross section. **B** shows a 9+2 arrangement in cross section. **C** shows the A and B microtubules, and the outer and inner dynein arms attached to the A tubule.

1.2.2 Ciliogenesis

Ciliogenesis, the process by which a cilium is built, is highly complex and regulated. In most cell types, cilia exist only when the cell is not actively participating in cell replication, due to the crucial role of the centriole in both processes: cilia structure and cell division (Sánchez and Dynlacht 2016). However, there are some cases where cilia are present on cells that are actively growing and dividing, such as in the neural tube (Vogel et al. 2012).

One of the earliest known steps of ciliogenesis is the transport of preciliary vesicles (PCVs) to the mother centriole, where they then dock. These originate from the Golgi as small cytoplasmic vesicles, which are transported to the distal appendages (DAs) of the centriole via dynein, myosin and the actin network (Wu et al. 2018). Small PCVs then fuse to form larger ciliary vesicles (CVs), containing components such as EHD1/SNAP & EHD3, which are membrane pre-modelling proteins, important for remodelling the part of the cellular membrane which is to become the ciliary membrane (Lu et al. 2015).

Also enriched in the CVs are a variety of important components, such as the small GTPase ARL13B, F-BAR domain PACSIN proteins and components of the RAB8/11 GTPase cascade, which are crucial to convert the centriole into the basal body (Insinna et al. 2019; Knödler et al. 2010). RAB11 recruits RAB8, along with ARL13B, which interacts with COP164 to promote growth of the ciliary membrane (Blacque et al. 2018; Mukhopadhyay et al. 2017).

The mother centriole migrates to the membrane of the cell where the cilium will form, and CVs deliver the components necessary to anchor the centriole and convert it to the basal body, via the distal appendages, allowing the initiation of extension of the ciliary axoneme (Tanos et al. 2013). As the centriole matures into the basal body, a number of proteins are recruited to the distal appendages to allow this. Firstly CP110 is localised to this distal end, where is “caps” the growing microtubules, thus regulating ciliogenesis (Yadav et al. 2016).

The removal of CP110 is then driven by CETN2, TTBK2 and CEP164 (Kobayashi and Dynlacht 2011; Tsang and Dynlacht 2013).

As CP110 is removed, the intraflagellar transport (IFT) machinery is recruited to the DAs, and there recruits cytoplasmic dynein 2 and kinesin 2, the motor proteins responsible for driving the IFT machinery (Lu et al. 2015; Ye et al. 2014). CEP164 also functions here, in recruiting INPP5E, which regulates the phosphoinositide (PIP) constitution of the ciliary membrane, important for subsequent ciliary function including trafficking along the length of the cilium (Garcia-Gonzalo and Reiter 2017; Humbert et al. 2012).

1.2.3 Intraflagella Transport

The process of Intraflagella Transport (IFT), first identified in 1993, allows the trafficking of proteins through the cilium, in both anterograde (away from the cell body, towards the ciliary tip) and retrograde (towards the cell body from the cilium) directions (Kozminski et al. 1993). Different proteins are associated with, and drive, these different directions of travel, with plus-end directed KIF3 motors catalysing anterograde, and cytoplasmic dynein 2 retrograde transport (Rosenbaum and Witman 2002). The composition of the KIF3 motor complex consists of KIF3A, KIF3B and KIF-associated protein KAP3 (Cole et al. 1993). In contrast, the composition of cytoplasmic dynein-2 is more complex, with specific heavy, intermediate and light-intermediate chains as well as light chain components that are shared with other dyneins (Asante et al. 2014).

1.2.4 The Transition Zone

After the IFT machinery is recruited to the DAs, the transition zone (TZ) begins to emerge, as Y-units become visible. These characteristic Y-shaped fibres are visible in a cross section of the cilium, and tether the microtubule doublets to the ciliary membrane (Shi et

al. 2017). It has been posited that these form a ciliary pore complex (CPC), analogous to the nuclear pore complex (NPC), which is known to regulate the trafficking of proteins into the nucleus (Kee et al. 2012; Takao et al. 2014). The NPC acts as a size barrier for free diffusion of proteins under 30 kDa, and has an active transport system for those over this, involving recognition of nuclear transport receptors and specific nuclear localisation signals (Stewart 2007). It has been argued that the CPC may have a similar function (Takao et al. 2014), and indeed some specific ciliary localisation sequences, such as those present in PKD2, have been identified (Knobel et al. 2008).

1.2.5 Cilia Function - Immotile cilia

The primary cilium was long thought to be vestigial, remaining after loss of motility (Bloodgood 2009). However, extensive work over the last 20 years has revealed it to have many important functions, particularly in relation to cellular signalling (Anvarian et al. 2019; Pala et al. 2017). This has led some to call it the cell's antenna, as it functions to receive signals from the extracellular environment helping to translate these into cellular responses (Singla and Reiter 2006).

A signalling pathway that is tightly linked with the cilium is the Hedgehog (Hh) signalling pathway. This link was first elucidated when phenotypic similarities seen in the types of defects were reported between embryos with disrupted Hh signalling and those with mutated IFT proteins, such as IFT72&88 (Huangfu et al. 2003; Huangfu and Anderson 2005). The Anderson lab, which found these through large scale genetic screens, also showed that the specific Hh signalling components, *Smo* and *Ptch*, can act genetically upstream of these IFT proteins. Subsequent work has also provided insight into the importance of the role of the cilium tip specifically in regulating the activity of the Hh signalling effectors (Bangs and Anderson 2017).

Other signalling pathways also have important ties to the cilium, with canonical Wnt signalling being implicated through a study showing Wnt dysregulation in a ciliopathy mutant (Wheway et al. 2013). Non-canonical Wnt signalling plays a clear role in Planar Cell Polarity (PCP) (Fanto and McNeill 2004), and through this has a role in basal body positioning (discussed in section **1.4.3**).

Loss of cilia, and knockdown of IFT protein leads to dysregulated Notch signalling, revealing a relationship between cilia and the Notch pathway (Ezratty et al. 2011). Subsequent research in zebrafish and *Xenopus* has also shown a function for Notch signalling in Left-Right Organiser (LRO) specification, with Notch signalling activating the specification of their non-motile LRO cilia; loss of Notch signalling leads to situs defects (Boskovski et al. 2013; Tavares et al. 2017). Hippo also signals through the primary cilium, with one of its core components, MST1/2, localising to the Basal Body and being required for ciliogenesis (Yu and Guan 2013).

A number of receptor tyrosine kinase signalling cascades have also been linked to the primary cilium. Perhaps the best known example is PDGFRα signalling, with the *Pdgfrα* gene being upregulated as primary cilia are formed on Mouse Embryonic Fibroblast (MEF) cells following serum starvation (Schneider et al. 2005). The PDGFRα protein has been shown to localise to the primary cilium in a number of cell types (Awan et al. 2010; Danilov et al. 2009), including MEFs, where activation of the receptor subsequently activates other pathways, including those involved in cell cycle control (Schneider et al. 2010). Insulin-like growth factor (IGF) signalling has also been shown to require the primary cilium, with a specific essential role in preadipocyte differentiation, furthermore its receptors localise to the primary cilium membrane (Zhu et al. 2009). The EGFR signalling pathway has also been linked to the primary cilium, specifically in relation to mechanosensation in the kidneys. In brief, the putative mechanosensitive complex is comprised in part of PKD2, which has been shown in culture to potentially be pre-sensitised to mechanical stimuli by EGF (Ma et al. 2005). This is, in part, based on the similar cystic kidney phenotypes seen

in *Pkd2* and *Egfr* mouse mutants (Gerdes et al. 2009; Threadgill et al. 1995). The function of the primary cilium in order to sense mechanical stimuli using the PKD2/PKD1 complex was posited following the analysis of these PKD2 mutants (and also PKD1 mutants) with cystic kidneys, proposing a role for primary cilia as mechanosensors.

The fibroblast growth factor (FGF) signalling pathway, is also implicated in the primary cilium, and will be discussed in section **1.7**.

1.2.6 Cilia Function - Motile cilia

The role of motile cilia mostly boil down to either moving fluid or mucus over the surface of cells or driving the motion of the cell through a fluid. The most well-known example of the latter in humans is that of the sperm tail, which is essentially a modified motile cilium which allows the movement of the cell through the seminal fluid (Amelar et al. 1980). More abundant throughout different organ systems are those of multiciliated epithelia, which line the trachea and airways in order to provide mucus clearance, function in the brain ependyma to move cerebrospinal fluid, and line the female reproductive tract in order to aid movement of the ovum to the uterus (Roberson et al. 2020). Motile monocilia are present transiently in the developing embryo, within a transient structure termed the node. This is the site of L/R patterning. Here motile cilia rotate to cause a leftwards fluid flow which is translated to produce left specific organogenesis.

1.3 Laterality – Left-Right patterning

External bilateral symmetry is evident for almost all vertebrates, and a number of non-vertebrates with respect to their left and right sides. The exceptions to this are an obvious minority, with specific features showing a specific asymmetry built on top of the more general symmetry. Examples include the narwhal with its single tusk being formed from a

right-sided vestigial tooth, and non-vertebrates such as the snail with its asymmetric shell, and certain crab species with one claw larger than the other (Backwell et al. 2007; Grande and Patel 2009; Nweeia et al. 2012). Internal L/R asymmetry is however apparent in both the positioning and patterning of the internal organs, with the heart and stomach showing a left bias, and the liver showing a right bias. Strikingly, this asymmetry is consistent across all vertebrates (Blum and Ott 2018). The highly conserved prevalence of asymmetry throughout evolutionary lineages implies an early origin of the asymmetry. It must have provided a selective advantage during evolution. It is argued that the selective pressure was the need for increased nutrient absorption, through the increase in gut length, to where the intestines are longer than the body length, and so must be sufficiently organised to fold and coil in the body cavity (Blum and Ott 2018).

The normal L/R positioning of organs in humans (**Figure 1.3 A**) is referred to as *situs solitus*. When abnormalities in left-right patterning occur, a variety of differences in *situs* can arise. *Situs inversus totalis* (SIT) is a complete reversal of the left and right axes (**Figure 1.3 D**), individuals who display this usually do so due a defect in cilia function, and so are correlated with infertility and defective mucus clearance of the airways (Afzelius 1995); SIT occurs in the population at approximately 1:6-8000 (Deng et al. 2015). Other abnormalities in organ positioning can occur and present with a myriad of health implications and variable mortalities: including left and right isomerisms (**Figure 1.3 B** and **C**), and random positioning of organs irrespective of normal left-right axis placement (*situs ambiguous*), which are collectively known as heterotaxies (Splitt et al. 1996). Minor defects in situs determination can also occur, possibly manifesting solely as heart defects, exhibiting varying mortalities/morbidities, and are likely the most abundant defect in patients (Ramsdell 2005).

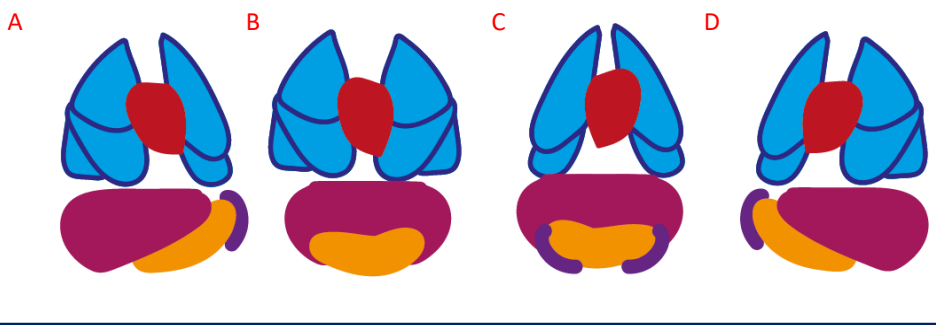


Figure 1.3: Diagrammatic representation of situs presentation. A shows situs solitus. **B** shows right isomerism. **C** shows left isomerism. **D** shows situs inversus totalis (SIT).

1.4 Node formation

1.4.1 Emergence of the node

The developing embryo is initially bilaterally L/R symmetrical, first showing asymmetry during the early somite stages in both mouse and human. The first morphological asymmetries observed are those of the looping of the primitive heart tube, and the direction of embryonic turning in the mouse embryo, at 8.5-9.0dpc. Equivalent processes to turning occur in other organisms, and are generally termed as axial rotations. However, molecular asymmetries predate morphological asymmetry (Beddington and Robertson 1999). The initial event that breaks symmetry occurs in a structure known as the node. The node is a Left-Right Organiser (LRO), which is a generic term that covers similar structures where L/R symmetry is broken in multiple different organisms. This term, coined by Blum, also applies to Kupfer's Vesicle (KV) in the zebrafish, and the Gastrocoel Roof Plate (GRP) in the frog (Blum et al. 2007). There is variation in these structures, however they all function to pattern L/R asymmetry in their respective organisms and have motile cilia, among other similarities.

In the mouse, the fully formed node is a characteristic tear-drop shaped pit, which first forms at the anterior end of the primitive streak at approximately 7.5dpc. The equivalent structure in human embryos forms at approximately 2 weeks post fertilisation (Hirokawa

et al. 2006; Okada et al. 2005). The mouse node first appears as patches of ciliated cells visible through overlying endoderm at the late-streak stage, which then join to form its characteristic shape (**Figure 1.4 A** from (Little and Norris 2020). At its anterior, the node is physically continuous with the notochord, although the cells comprising each are functionally distinct (Blum et al. 2007). Cilia are present on the cells of the node as they first appear. These cilia are around 2 µm in length and grow over the next few hours up to approximately 7 µm (Lee and Anderson 2008).

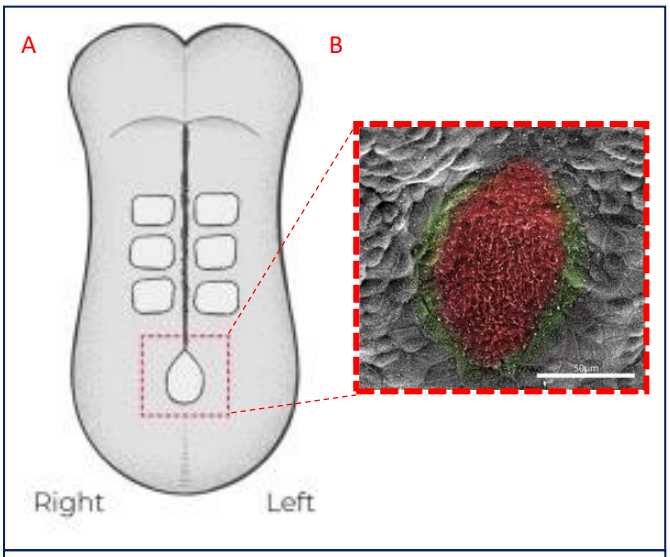


Figure 1.4: The mouse embryo and node. A the mouse embryo at E8.5 (3 somite stage). The red box indicated the node. **B** is a Scanning Electron Microscopy (SEM) image of a mouse embryonic node at E8.5. The red shaded area denotes the pit cells of the node, and the green the crown cells at the edge of the node. Both images taken from Little and Norris, 2020.

1.4.2 Cilia in the node

The fully formed node comprises two cell populations: crown cells and pit cells. Pit cells each have a single motile cilium, whereas crown cells have a single immotile cilium. An image with these subpopulations within the node is shown (**Figure 1.4 B:** red = pit cells, green = crown cells). However, while the cell types are generally categorised by cilia

motility, they are also defined by gene expression in some studies, with certain key genes showing specific crown cell expression, such as *Nodal* and *Cerl2*- these are discussed later. Analysing the ultrastructure of node cilia has proved difficult, due to their size and small number in comparison to other cilia populations. It is however now widely accepted that the motile cilia on the pit cells have 9+0 arrangement as do the immotile cilia on the crown cells (Takeda et al. 1999). One study did report 9+2 arrangement in some cilia in the pit of the node, however while convincing data was shown, it has not been replicated (Caspary et al. 2007).

The first indication that motile cilia are important for L/R patterning came from analysis of human patients with Kartagener's syndrome (now considered to be a sub-set of Primary Ciliary Dyskinesia [PCD] patients). These show infertility, defective airway muco-ciliary clearance, and *situs inversus*, as well as abnormal cilia motility (Afzelius 1976). Yet where the motile cilia required for L/R patterning were expressed remained unclear, until Nonaka and colleagues showed that cilia in the pit of the mouse node were motile (Nonaka et al. 1998). The mouse mutant *inversus viscerum (iv)*, which shows *situs inversus*, were reported to lack motility in the mouse node pit (Okada et al. 1999). Nonaka went on to use the *iv* model in their experiments to show the introduction of a leftward flow in the node of these mutants rescues the *iv* situs phenotype, and that the direction of fluid flow within the mouse node is critical for determining the sidedness of the embryo (Nonaka et al. 1998; Nonaka et al. 2002).

That the node may also contain a second population of cilia, which are immotile, was proposed by McGrath and colleagues. The evidence for this was the specific localisation of *Lrd* (now known to be *Dnah11*), an axonemal dynein required for consistent establishment of sidedness, to cilia in the pit of the node, and its absence on those on the crown cells at the node's edge (McGrath et al. 2003). They posited that these immotile crown cell cilia are necessary for the translation of flow produced by the motile pit cell cilia.

Yet the question remained of how rotating pit cell cilia create the laminar leftwards flow that breaks left-right symmetry in the embryo.

1.4.3 Positioning nodal cilia

The relationship between the motion of nodal cilia and leftward flow was not initially obvious. Rotating cilia that protrude perpendicular to the cell's surface into the node cavity would create localised vortices and not the leftward laminar flow seen. This suggested other factors must be at play. Mathematical modelling revealed that if the node cilia were tilted towards the posterior of the node, their rotation would create a leftwards flow above the cilia, and that an angle of 24° below the vertical would be most efficient (Cartwright et al. 2004). This led groups to more closely analyse nodes, revealing that nodal cilia are indeed polarised towards the posterior of the node and are tilted at an average angle of 26.6° below the vertical (Okada et al. 2005).

The consistent posterior tilt in node pit cell cilia is the result of the Planar Cell Polarity (PCP) pathway. Once it was evident that these cilia had a posterior tilt, it seemed likely that this must rely on PCP, yet the PCP mutants that had been identified and characterised showed normal situs (Marshall and Kintner 2008). This disparity was only resolved when the degeneracy of components of the PCP pathway were uncovered. Embryos double mutant for the PCP genes *Dvl2* and *Dvl3* showed clear situs defects (Hashimoto et al. 2010; Song et al. 2010). This illuminated the functional redundancy of these components, and the degeneracy within the mammalian PCP pathway, and confirmed the involvement and necessity of PCP in situs determination and thus L/R patterning.

The question remained how this PCP was established, and it was discovered that the cilia present on node cells are positioned in response to opposing gradients of WNT5A and its SFRP inhibitors along the AP axis (Minegishi et al. 2017). This leads to polarised localisations of the PCP components, VANGL1&2 and PRICKLE2, within cells, which then

affect the positioning of the cilium, orienting the basal body to the posterior of the cell (Antic et al. 2010; Hashimoto et al. 2010; Song et al. 2010). The dome shape of the cells within the pit of the node along with this polarisation account for the crucial angle as postulated by Cartwright.

1.5 Flow and Breaking Symmetry

1.5.1 Establishing flow

The importance of nodal flow in L/R determination was established over 20 years ago, yet the mechanism by which leftwards fluid flow actually breaks symmetry still remains uncertain. It has been shown that immotile cilia on crown cells at the edge of the node are necessary in order to respond to flow (McGrath et al. 2003). Yet how this occurs is uncertain and a number of hypotheses seek to explain this.

1.5.2 Morphogen Gradient Hypothesis

The first mechanism proposed to explain how nodal flow breaks symmetry in the node was the morphogen gradient hypothesis (Nonaka et al. 1998). This posits the presence of a signalling molecule in the extracellular fluid of the node, which becomes enriched on the left side of the node in response to the flow. This is argued to induce the left-specific signalling cascade in the left crown cells. Biophysical analysis of the node, along with other LROs, showed that such a mechanism could work for molecules between 20-70 kDa in size (Okada et al. 2005). However, there is some scepticism as to the validity of this hypothesis as no such L/R morphogen has been identified in 20 years of study (Cartwright et al. 2020; Little and Norris 2020).

1.5.3 Nodal Vesicular Parcel Hypothesis

The NVP hypothesis is arguably an extension of the morphogen gradient hypothesis; it proposes that signalling molecules wrapped in lipid-membrane-bounded vesicles are transported to the left side of the node by nodal flow (Tanaka et al. 2005). These vesicles are argued to be produced in the pit of the node, travel and eventually release their signalling molecule contents at the crown cells in a cilia-dependent manner. This was initially proposed to be through a smashing of the vesicle into a cilium, mechanically breaking the vesicle and releasing its signalling molecules; mathematical modelling has since shown this is not possible as the energy needed is greater than that carried by the vesicles (Cartwright et al. 2007). Therefore it is now thought to be more likely to occur through an active docking of vesicle to cilium, which has been shown to occur in other contexts (Sreekumar and Norris 2019).

1.5.4 Mechanosensation Hypothesis

The final hypothesis is that of mechanosensation, which proposes that nodal flow is directly detected by the immotile cilia on the crown cells surrounding the node. The work which led to the development of this hypothesis focussed on the polycystin proteins, and their proposed role in the kidney. Loss of PKD2 function was shown to lead to abnormalities in situs determination (Pennekamp et al. 2002). Work by McGrath followed this, and showed the presence of two distinct populations of cilia within the node, one motile and one immotile. They also reported on the presence of a calcium wave which is dependent on PKD2, which can function as a calcium channel (McGrath et al. 2003).

PKD1 and *PKD2* are the genes responsible for causing autosomal dominant polycystic kidney disease (ADPKD) in humans (Happe and Peters 2014). Strikingly the mutations in these genes act dominantly in ADPKD and it is believed that local somatic mutations can

result in cells becoming null for *PKD1* or *PKD2*, and that these cause the characteristic kidney cysts to form (Lu et al. 1997; Wu et al. 2002). Furthermore, the two proteins physically interact (Tsiokas et al. 1997), and it is thought that PKD2 and PKD1 function in tandem in the kidney, acting to mediate the sensation of flow within the kidney tubules (Nauli et al. 2003). As well as its impact on L/R patterning, homozygous loss of *Pkd2* in the mouse leads to kidney cysts (Harris and Torres 2009). Similarly, homozygous loss of *Pkd1* in the mouse leads to kidney cysts, but does not show any situs defects (Lantinga-van Leeuwen et al. 2007; Lu et al. 1997).

It is thought that an alternative polycystin, PKD1L1, acts with PKD2 in the context of the node and L/R patterning. Indeed, when mutated, situs defect phenotypes were seen (Field et al. 2011; P. Vogel et al. 2010). Additionally, the two polycycstins PKD2 and PKD1L1 have been shown to interact in vitro (Grimes et al. 2016).

Experiments in the Hamada lab have supported this model, showing a specific necessity for PKD2 localisation to the crown cell, but not pit cell, cilia (Yoshiba et al. 2012).

Work analysing the *Pkd2*^{lrm4} mutant, showed that PKD2 needs to be able to localise to the cilia of the cells specifically in order for correct L/R asymmetry to be set up. However, some questions remain to be answered if the mechanosensation hypothesis is to be fully accepted. One of these is the question of how PKD2 is upstream of the molecular asymmetries seen within the node. It has been argued that this is due to it having a role as a Ca^{2+} channel, though it is not clear how a change in calcium concentration within the cell or the cilia would be then leading to these molecular asymmetries. A key issue remains relating to the biophysics at play within the node. The extracellular fluid within the node provides a low Reynolds' number environment, whereby inertia is effectively non-existent, meaning the forces pushing the cilia on the left crown cell cilia and those pulling on the right crown cell cilia are equivalent (Ferreira et al. 2019). This means that if the mechanosensation hypothesis works as a model, there needs to be a way for the cilia on

the crown cells of the node to identify the differences between these two equivalent pushing and pulling forces.

1.5.5 Calcium asymmetry

An asymmetric, PKD2-dependent calcium wave in the left margin of the node was reported by McGrath and colleagues (McGrath et al. 2003). This reported Calcium asymmetry at the node has since been shown by Viotti to spread through the endoderm towards the lateral plate mesoderm (LPM) (Viotti et al. 2012). Within the node the calcium signalling appears to be very dynamic but overall shows a left bias (Takao et al. 2013). However other research has failed to replicate this (Yoshiba et al. 2012), and crown cell Calcium asymmetry has not been detected. The putative role for calcium in left right patterning is currently uncertain. Viotti argued that it may function as part of the detection of flow, or additionally have a role in the movement of the signal from the node out to the LPM (Viotti et al. 2012). Alternatively, it may be simply a downstream effect of other signalling pathways following crown cell activation by flow, or possibly a response to signalling molecules transported by NVPs, or even a combination.

1.6 Establishing Asymmetry

1.6.1 Genetic asymmetries at the node and LPM

Downstream of nodal flow we see L/R gene expression asymmetries. The first asymmetric gene expression in the node is thought to be that of *Cerl2* (*Dand5*). This is initially symmetrically expressed in the crown cells surrounding the node's pit, but becomes asymmetric in response to flow (**Figure 1.5 A** and **B**). The flow induces decay of *Cerl2* mRNA at the left edge of the node, mediated by 3' UTR sequences (Nakamura et al. 2012). Due to the existence of a mutually antagonistic feedback loop between WNT3 and CERL2,

downregulation of *Cerl2* leads to upregulation of *Wnt3* expression (Kitajima et al. 2013). This feedback robustly amplifies the small initial change in *Cerl2* mRNA levels between left and right, resulting in a stable asymmetry, whereby *Cerl2* expression is stronger in the right crown cells compared to those on the left. This asymmetry leads to following node asymmetry of *Nodal*, which becomes more strongly expressed in crown cells at the left side of the node in response to *Cerl2* expression (**Figure 1.5 A** and **B**). Through analysis of the relationships between nodal flow, *Pkd1l1* and *Pkd2* have been revealed to have part in a multi-repression mechanism by which flow repressed *Pkd1l1* which then de-represses *Pkd2*, and in turn represses *Cerl2* at the left of the node (**Figure 1.5 A** and **B**) (Grimes et al. 2016).

Additionally, CERL2 protein antagonises the NODAL ligand, preventing interaction of it with its receptors (Marques et al. 2004). Following expression of *Cerl2* on the right of the node, CERL2 protein accumulates on the left side due to translocation via the fluid flow (Inacio et al. 2013). This is likely to prevent NODAL activity in the entire node following the initial suppression of NODAL activity on the right side of the node, thus limiting the time at which NODAL activity is present. Thus, on the left crown cells, lack of *Cerl2* expression and thus CERL2 protein allows the de-repression of NODAL and its induction of its own expression.

1.6.2 Genetic asymmetries at the LPM

Preferential *Nodal* expression on the left side of the node is translated to an activation of *Nodal* expression in the L-LPM. Here NODAL induces the expression of its antagonist LEFTY2, which has a high diffusion velocity, and thus restricts the expression of Nodal specifically to the L-LPM. This, along with the positive feedback loop of NODAL inducing its own expression in the L-LPM, leads to a strong and specific signal within the L-LPM only. The action of NODAL in the L-LPM is also limited by LEFTY1, which is induced by

small amounts of NODAL diffusing from the L-LPM towards the midline, where *Lefty1* expression is induced (Hamada et al. 2002). Here it acts as a midline barrier to prevent movement of the L-LPM signals cross to the right side of the midline (Nakamura et al. 2006).

NODAL action in the L-LPM also induces *Pitx2* expression. PITX2 is the key effector of the Nodal cascade, and acts as a transcription factor to regulate the expression of key genes driving cell proliferation and migration essential to the L/R asymmetric positioning and patterning of the internal organs such as the lungs, liver, stomach etc (Grimes and Burdine 2017).

Nodal expression at the node is also dependent on the Delta/Notch signalling pathway which is activated by WNT3A (Nakaya et al. 2005). The transcription of *Nodal* is controlled by this pathway by DLL1 activating NOTCH receptors, leading to cleavage and nuclear translocation of the NOTCH intracellular domain to the nucleus (Krebs et al. 2003; Raya et al. 2003). Here, this can bind with the DNA binding protein RBP-J to directly regulate the transcription of *Nodal* (Schweisguth 2004).

1.6.3 Transduction of signal from the node to the L-LPM

There is debate in the field as to how the asymmetry at the node crown cells is transported to the LPM to induce left-sided organogenesis, as the physical separation of the two comprises several cell diameters. Exactly how this induction of *Nodal* expression in the cells of the L-LPM occurs molecularly is not clear.

One model for the translation of node signal to the LPM proposes that NODAL protein itself is transported from the left crown cells to the L-LPM via the extracellular matrix (Oki et al. 2007). In the L-LPM it then induces its own expression. It is thought that NODAL is likely functioning as a heterodimer with GDF1, which has been shown to signal more efficiently over a distance than NODAL homodimers (Tanaka et al. 2007). This makes

sense as it provides an extra level of control over long distance NODAL signalling, limiting the timing of *Nodal* expression in the L-LPM, as the homodimers in the L-LPM are not then able to travel to the R-LPM and induce *Nodal* expression there. One study has demonstrated that Sulfated Glucoaminoglycans (sGAGs) are also of importance, as these are localised to the basement-membrane-like structure between node and LPM cells, and have been shown to interact with NODAL *in vitro* (Oki et al. 2007). Therefore it has been suggested that transport of NODAL from the node to the L-LPM may involve interaction with sGAGs.

An alternative model suggests that the signal that transduces asymmetry from the node to the LPM which induces L-LPM *Nodal* expression may be in the form of a calcium wave. Analysis has shown such a Calcium wave to travel through the endodermal cells, from the node to the L-LPM (McGrath et al. 2003; Takao et al. 2013; Viotti et al. 2012). Indeed, gap junctions exist between these cells, and it is proposed that Calcium-induced Calcium release (CICR) allows the propagation of the wave. This is supported by analysis of *Sox17* mutants, in which definitive gut endoderm is not properly established, resulting in the absence of gap junctions, and thereby makes it impossible for CICR-based communication to function in this way to signal to the L-LPM (Viotti et al. 2012).

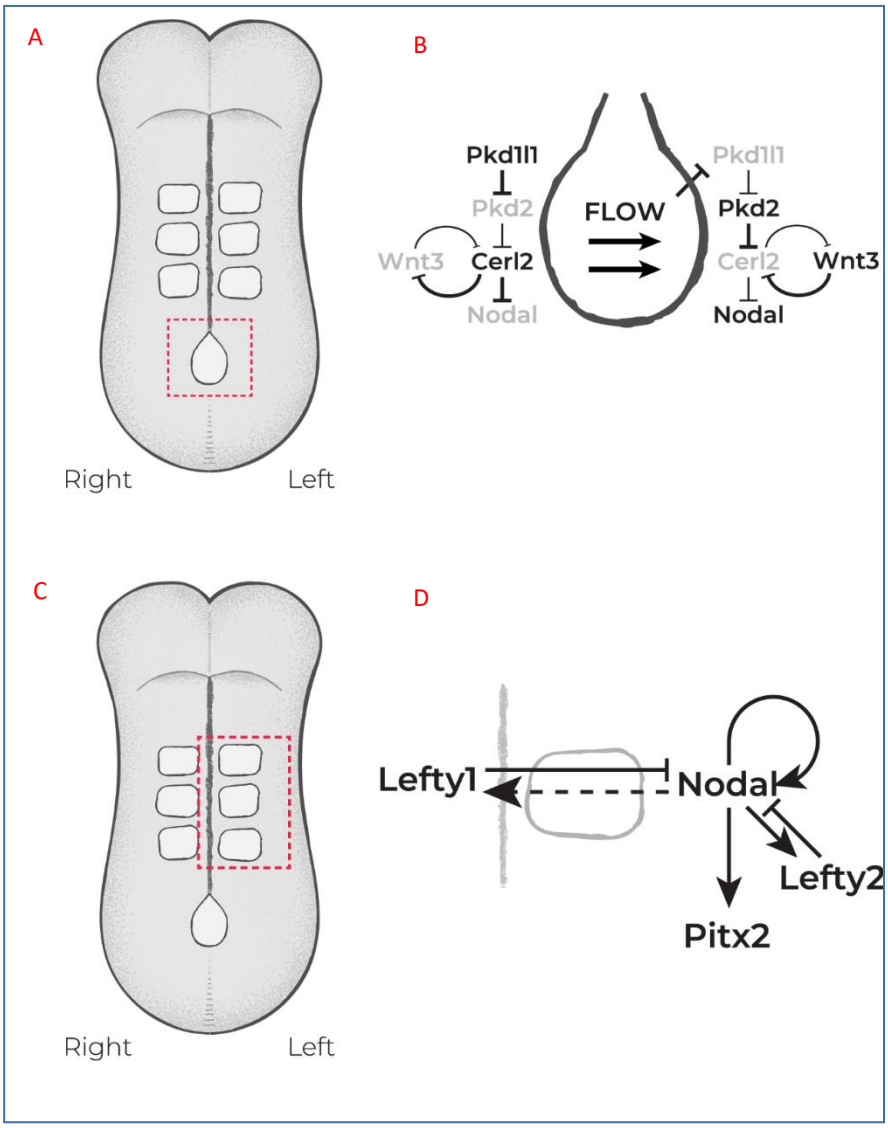


Figure 1.5: Genetic pathways in the mouse embryonic node and lateral plate mesoderm. A the mouse embryo at E8.5 (3 somite stage). The red box indicated the node. **B** indicates a blown-up view of the node area in the red box in **A**. The flow is indicated by arrows, with the genes whose expression is repressed shown in grey, and expressed shown in black, notable *Cerl2* being expressed asymmetrically on the right side of the node, and *Nodal* asymmetrically on the left side of the node. **C** the mouse embryo at E8.5 (3 somite stage) with the red box showing the area from the midline to the left lateral plate. **D** shows the gene expression present relating to left/right asymmetry in these structures. Notably *Nodal* induces itself, *Pitx2* and *Lefty2* in the lateral plate mesoderm. Images taken from Little and Norris, 2020.

1.7 FGF Signalling

As previously described, FGF signalling has been linked to the cilia present in various LROs. Studies in zebrafish and *Xenopus* have shown a direct correlation between the FGF signalling pathway and the regulation of cilia length; analysis of embryos in which FGFR1 was knocked down revealed shortened LRO cilia in both organisms, in addition to situs defects (Neugebauer et al. 2009). However, the role of FGF signalling in the mouse is less clear, even though the link between FGF signalling and L/R patterning in the mouse predates the zebrafish and *Xenopus* work. Analysis of a hypomorphic *Fgf8* mouse mutant showed situs defects as assessed by asymmetric *Nodal* expression and L/R organ patterning, such as defects in lung lobation and other abdominal organ positioning (Meyers and Martin 1999).

However, the underlying mechanism remains unclear. Tanaka and colleagues proposed that FGF8 directly regulates NVP release, as FGFR inhibitors in culture led to a loss of the left-sided calcium signal (Tanaka et al. 2005). A subsequent analysis proposed that *Fgf8* directly activates the Notch signalling components *Tbx6* and *Dll1*, thereby influencing *Nodal* expression, due to disruption of their expression in embryos treated with an FGF inhibitor (Oki et al. 2010). In 2019, the Blum lab proposed another mechanism by which FGF8 signalling may influence L/R patterning in *Xenopus*. They propose that FGF8 signalling converts somatic cells into those that are the *Xenopus* equivalent of crown cells, which are needed to receive flow-specific information; notably these cells exhibit a different lineage to mammalian node crown cells (Schneider et al. 2019).

While multiple mechanisms by which FGF8 may influence L/R patterning have been proposed in different organisms, the role in mammalian L/R determination is not currently understood. Whether the node is even itself permissible to FGF signalling remains unclear, and the precise relationship remains unclear. Indeed, there is information available as to which of the four FGF receptors (FGFRs1-4) that FGF8 can bind, with preferential

specificity, although this does appear to be very context-dependant (Ornitz and Itoh, 2001). Additionally, there are numerous signalling pathways downstream of FGFR activation: RAS/MAPK, JAK/STAT, AKT and PLCɣ, which can in turn regulate pathway-specific target gene expression (Ornitz and Itoh, 2001). Such downstream target genes could include those with specific effects on ciliogenesis, or L/R patterning in other ways (Christensen et al. 2012).

Additionally of consideration, there is evidence for compensatory actions of different FGFs in various contexts (Ornitz and Itoh 2015), and it remains possible that such compensation is occurring in the context of L-R patterning. There are over 20 different FGF signalling ligands, and these can be broadly grouped into paracrine, intracrine and endocrine families, and then further categorised into subfamilies (Ornitz and Itoh 2001). The endocrine FGFs comprise the FGF19 subfamily, which included FGF15/19 (FGF15 is the mouse orthologue of human FGF19), 21 and 23. Intracrine FGFs are also known as fibroblast homologous factors (FHFs) due to their structural and sequence similarities but lack of function and inability to couple with FGFRs, and are made up of FGFs11-14 (Beenken and Mohammadi 2009). The paracrine FGFs comprise four subfamilies: the FGF1 subfamily (FGFs1 and 2), the FGF4 subfamily (FGFs4-6), and the FGF8 subfamily (FGFs8, 17 and 18). All of these are grouped according to both structural and functional considerations, and these groupings are broadly in line with their reactivity with specific FGFR isoforms.

FGF Receptors (FGFRs) 1-4 are the classical receptors, with a fifth, FGFR5 or FGFRL1 (FGFR-like1), having different structure and functionality compared to the others (Zhuang et al. 2010). Depending on context different ligands have differing affinities for each receptors, with most ligands being able to pair with multiple of the four.

1.8 Aims

Due to the complex nature of FGF signalling, and the unknown mechanism behind its role in L/R patterning, this thesis aims to elucidate the role of FGF8 specifically and FGF signalling generally in L/R patterning. A number of different approaches were utilised to address this. This included the use of embryonic culture, and analysis of the specific FGFs present at time points key to L/R patterning (**Chapter 4**), and by analysing the *Fgf8* mutant showing the original situs defects (**Chapter 5**). In addition, I investigated the NVP hypothesis by recapitulation of Tanaka and colleagues methods, in order to look at the validity of their claims (**Chapter 3**).

2.0 Materials & Methods

2.1 Universal Solutions

Reagent	Composition
PBT	PBS + 0.1% Tween-20
TBST	50 mM Tris-HCl pH7.5, 150 nM NaCl, 0.1% Tween-20, made up as 10X, autoclaved, 1X solution made up.
NTMT	100 mM NaCl, 100 mM TrisHCl pH9.5, 50 mM $MgCl_2$, 0.1% Tween-20 in H_2O
WISH Solution I	50% Formamide, 5X SSC pH4.5, 1% SDS in H_2O
WISH Solution III	50% Formamide, 10X SSC pH4.5 in H_2O
WISH Prehybridisation Solution	50% Formamide, 5X SSC pH4.5, 0.1% Tween-20, 50 µg/ml Heparin
WISH Hybridisation Solution	50% Formamide, 5X SSC pH4.5, 0.1% Tween-20, 50 µg/ml Heparin, 100 µg/ml yeast RNA, 100 µg/ml salmon sperm DNA
SSC (20X)	3 mM NaCl, 300mM sodium citrate in H_2O, pH4.5, autoclaved

2.2 Mouse Lines

Mouse work was carried out under the UK Home Office Project License 30/2980 and approved by the Animal Welfare and Ethical Review Body (AWERB) at the MRC Harwell Institute, in accordance with the Animals (Scientific Procedures) Act. 1986, and with the MRCs guidance “Responsibility in the Use of Animal for Medical Research” (1993). Husbandry was carried out by staff of the Mary Lyon Centre (MLC). Mice were housed in

individually ventilated cages (IVCs) in a specified pathogen-free (SPF) environment and maintained in a controlled 12 hour light/dark cycle, with controlled temperature (21°C ±2°C) and humidity (55%±10%). Free access to water with 10-12 ppm chlorine and food (commercial Rat and Mouse Diet No. 3 [RM3]. Special Diet Services, Essex, UK containing 5.3% fat [corn oil], 21.2% protein, 57.4% carbohydrate, 4.6% fibre). Female mice were socially housed at 2-5 individuals per group cage.

Wild-type mice were either C57BL6/6J (B6/J) or C3H strain, and will henceforth be stated as such. Mutant mouse lines were maintained on B6/J genetic background.

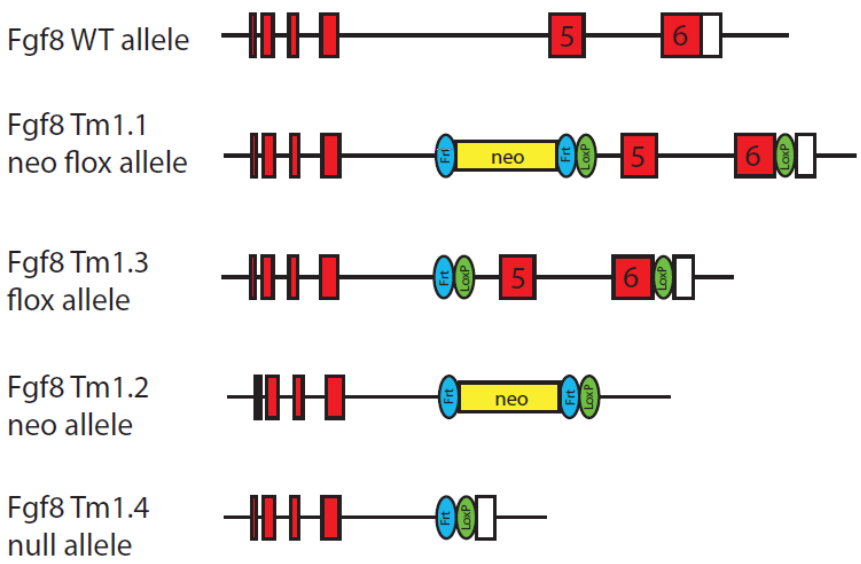
2.2.1 Background Strains

Mutant mouse lines were maintained on a C57BL/6J background with back crossing until congenic.

2.2.2 WT mice

For embryonic culture WT C3H mice were used in order to allow for embryos of the appropriate embryonic stage to be used.

2.2.3 *Fgf8* alleles



The *Fgf8*-tm1.1line was imported from the Jackson laboratories congenic for BL/6J, and it is on this genetic background that I have analysed its phenotype. The *Fgf8*-tm1.2 line was created from the *Fgf8*-tm1.1 line by Cre-mediated recombination.

Mice heterozygous for the *Fgf8*-tm1.1 allele were bred together in order to give heterozygous and homozygous embryos for analysis.

Female mice heterozygous for the Fgf-tm1.1 allele were bred with males heterozygous for the *Fgf8*-tm1.2 allele to give embryos heterozygous for each, or both (*Fgf8*$^{Tm1.1/Tm1.2}$ compound heterozygotes).

2.2.4 Relevant developmental stages

Stage	**Abbreviation**
S	streak stage
B	bud stage
(E/L)HF	(early/late) head-fold stage
0ss	0 somite stage
1ss	1 somite stage
2ss	2 somite stage
3ss	3 somite stage
4ss	4 somite stage
5ss	5 somite stage
6ss	6 somite stage

2.3 Molecular Biology

2.3.1 PCR

Polymerase Chain Reaction (PCR) is performed in order to amplify fragments of DNA for further use or analysis. Reactions were prepared using Qiagen Taq Mastermix (Cat No: 201445) following manufacturer's instructions. A Gstorm thermocycler was used to perform PCRs.

2.3.2 Genotyping

Genotyping was carried out by core services (GEMS) using specific qPCR-based assays for each mouse line. FAM-labelled genotyping assays were run in multiplex with VIC-labelled *Dot1l* internal control. CopyCaller software was used to analyse results, with wild-type assay copy number 1, and mutant assay copy number 2. **Table A1** (appendix), shows the copy numbers for each possible *Fgf8* mutant type.

2.3.3 Agarose Gel Electrophoresis

1-1.5% agarose TBE gels with GelRed (1:40000) were submerged in TBE buffer. Samples were mixed with 20% w/v Ficol Orange G and DNA ladders (1 kb plus/100 bp New England Biolabs) were loaded into wells. A constant voltage of 80-100 V was applied across the gel for 30-90 mins to separate the linear DNA fragments by size. Fluorescence under UV light was visualised through the use of the DNA intercalant GelRed using a GelDoc System (BioRad).

2.3.4 DNA Sequencing

Purified DNA was sequenced by GATC Biotech and subsequently Eurofins Scientific using primers targeted to the region of interest. Samples were prepared following GATC and Eurofins guidelines in relation to concentration and volume of DNA needed.

2.3.5 RNA isolation

Embryos were snap-frozen on dry ice and stored at -70°C until needed. RNA was extracted using the appropriate QIAGEN RNeasy kit (mini [74106], lipid tissue [74804], fibrous tissue 74704]).

2.3.6 cDNA synthesis

cDNA was synthesised from previously isolated RNA using Applied Biosystems High-Capacity cDNA Reverse Transcription Kit (Cat No: 4368814) following manufacturer's instructions.

RT-qPCR for genotyping was set up using TaqMan GTXpress Master Mix (Thermo Fisher Scientific), FAM-labelled genotype-specific assays and VIC-labelled *Dot1l* as a control.

2.3.7 Plasmid linearization

2 µg of plasmid was digested with appropriate enzyme for 1 hr at 37°C, and followed by an enzyme heat-kill step for the necessary time and temperature. Agarose gel electrophoresis was used to demonstrate complete linearization. QIAquick PCR purification kit was used to purify the template (QIAGEN, 28106).

2.3.8 Probe synthesis

Probes were synthesised using a DIG RNA labelling mix (Cat no:11277073910, Roche) with reactions set up with 4 µl DIG labelling mix, 4 µl 10X transcription buffer, 1 µg linearized plasmid, 2 µl appropriate RNA Polymerase (T3/T7, Cat No: EP0101/EP0111, ThermoFisher), 0.25 µl RNase OUT™ (Cat No: 10777019, ThermoFisher). Add RNase-free H_2O to 40 µl. Reaction mixture was incubated in a 37°C water bath for 2+ hours. 100

µl H_2O, 15 µl 3M sodium acetate (pH 5.2), and 300 µl ice-cold 100% ethanol was added, and the mixture incubated overnight at -20°C in order to precipitate RNA. The reaction mixture was then centrifuged at 14000 RPM for 20 mins at 4°C. The resulting pellet was washed twice with 70% ethanol, with 5 mins spins at 14000 RPM 4°C between washes. The pellet was then air-dried and re-suspended in 200 µl TE buffer. Synthesised probes were aliquoted and stored at -70°C.

2.3.9 TA Cloning for in situ probe plasmid synthesis

For most genes whose expression pattern was to be analysed, validated probes had previously been created (https://plasmid.internalproduction.har.mrc.ac.uk/). Where not available, new probe plasmids were synthesised. Firstly, primers were designed against the cDNA sequence of interest (Appendix table A3), and were optimised using Taq polymerase (Cat No: 201445, QIAGEN), and specific mouse tissue previously characterised as showing high expression of the gene of interest (according to Jax expression atlas). Agarose gel electrophoresis was used to confirm size of product and purification of products was carried out using either the QIAquick gel extraction kit (Cat No: 28704) or QIAquick PCR Purification kit (Cat No: 28106) according to manufacturer's protocols.

The T vector was produced by blunt-cutting of 2 µg pBluescript II KS(-) using EcoRV-HF (20U with 2 µg DNA and 2 µl CutSmart® Buffer, with ddH_2O to 40 µl) and incubated at 37°C for 2 hours to digest. A 20 mins heat-kill step was performed at 65°C. Digestion was confirmed using gel electrophoresis. Thymidine bases was added to the cut vector (2 µg DNA, 10 µl 10X PCR Buffer, 5 µl Taq polymerase, 1.5 µl 100 mM dTTP, ddH_2O to 100 µl) during a 2 hour 72°C incubation. Product was purified using QIAGEN PCR purification kit and quantified.

Ligation of insert and vector was carried out with a 4:1 excess of insert:vector. 60 ng vector was used per ligation. A Quick Ligase Kit was used (Cat No: M2200S, NEB) and 10 µl reaction taken forward for use in each transformation.

Blue/white selection was used to confirm for insertion into the pBluescript plasmid. Plates were prepared for this with appropriate antibiotic-containing LB agar and coated in 100 µl 100 mM IPTG and 35 µl 25 mg/ml X-Gal.

Transformants were analysed using PCR by a clean p20 pipette tip being used to pick colonies, smear into a PCR plate well and placed in a culture tube with 3 ml selective LB (stored at 4°C until further use). PCR plate was sealed and spun for 3 mins at 4000 RPM.

2.4 Cell Culture & Processing

Stringent aseptic technique maintained throughout cell and tissue culture work. Commercial NIH3T3 (CRL-1658™) and RPE1 (CRL-4000™) cells were obtained from ATCC. Primary MEFs were generated as outlined below.

2.4.1 Generating Primary Mouse Embryonic Fibroblasts

Wilf-type mouse embryos were harvested from pregnant females at 13.5-14.5dpc. Head, limbs and organs were removed and each carcass washed thoroughly with sterile PBS to remove blood cells. For each carcass, 200µl 25% Trypsin was added and the sample minced finely, and then pipetted up and down with 5ml medium (DMEM + Glutamax-1, 4.5g/L D-Glucose, 10% FBS and 1% Penstrep) using a 5ml stripette. This was then added to a 10cm dish of medium, and volume increased to 10ml with complete medium. Cells were allowed t settle and incubated at 37°C 5% CO_2. Medium was changed regularly.

2.4.2 Thawing Cells

Vials to be thawed were removed from storage in liquid nitrogen and maintained as frozen on dry ice prior to thawing. Each vial was swirled in a 37°C water bath and removed with a small amount remaining frozen within the vial. Cells were then added dropwise to a 10 cm dish with 14 ml pre-warmed appropriate cell culture medium. Culture medium was exchanged within 18 hours.

2.4.3 Freezing Cells

Cells were expanded by seeding a number of plates (as many as possible) from a founder plate. When confluent, cells were washed with warm, sterile PBS. After removal of PBS, 1.5 ml 5% Trypsin was added and cells incubated until detached from the dish. Trypsin was then neutralised using medium, and cells pelleted by centrifugation at 800 rpm for 5 mins. Supernatant was aspirated off and the resulting pellet re-suspended in 1 ml Freezing medium (40% FBS, 50% DMEM, 10% DMSO). Cells were placed in cryotubes and stored at -70°C for 1 week in a freeze down box (Mr Frosty) before being transferred to storage in liquid nitrogen.

2.4.4 Splitting Cells

Cells were washed with pre-warmed sterile PBS and 1.5 ml 5% Trypsin added. Once the cells detached, the Trypsin was neutralised using 9 ml medium. Cells were then split into two plates at least, dilution depending on cell line growth rate. Cells were incubated at 37°C 4% CO_2 until confluency reached.

2.4.5 Fixing Cells

Medium was aspirated off cells that were previously seeded on cover slips in a 12-well plate. Cells were washed twice using PBS and aspirating off. 100% ice-cold methanol was added to cells and these placed at -20°C for 3-4 mins in order to fix. The Methanol was aspirated off, and the cells washed with fresh PBS twice before addition of fresh PBS and plates sealed using parafilm and stored at 4°C prior to use.

2.5 Embryo Dissection & Culture

2.5.1 Collection of Embryos

In order to collect embryos at specific ages, timed mates were set up and females were changed for vaginal plugs (indicating occurrence of mating) the following morning. Noon was designated the value of 0.5dpc (days post coitum) with the assumption of conception occurring at 12 midnight the day of male introduction to the female cage. Mouse in reverse light dark (rev L/D) conditions had matings set up following a 2 week introductory period in order to acclimatise to new conditions, with 0dpc designated at midday after introduction. Use of rev L/D allowed embryos of differing stages of development to be collected in order to procure embryonic time points that would otherwise occur at unsociable times. Plugged females were culled by cervical dislocation (under Schedule One Home Office regulations) and uteri removed following confirmation of death.

2.5.2 Dissection and staging of E8.5 embryos

For analysis by whole-mount *in situ* hybridisation (WISH), whole-mount immunofluorescence (WIF) and scanning electron microscopy (SEM), embryos were dissected out of the uterine horn and then the decidua in ice cold PBS under a Nikon

SMZ800 microscope. Reichart's membrane was removed, and the yolk sac or partial embryonic tissue taken and stored at -20°C for later genotyping if required.

Embryos for qPCR were dissected in 37°C 10% FBS in DMEM in order to maintain viability. After removal from the deciduae, Reichart's membrane was removed, and individual embryos were staged, snap-frozen on dry ice, and stored at -70°C.

Staging of embryos was noted where appropriate in relation to streak, bud, head-fold of somite stage.

2.5.3 Dissection and Situs Phenotyping of E9.5 embryos

Decidua were dissected out of the uterine horn with care in PBS, and cut open to allow maintenance of embryo within yolk sac. This allowed for direction of embryonic turning to be scored. Heart looping analysis was carried out under appropriate magnification to observe left and right ventricular structures.

2.5.4 Dissection and preparation of E15.5 embryos for µCT

For µCT analysis, E15.5 embryos were dissected and yolk sac / tail tip were taken for genotyping. Exsanguination was performed by severing of the umbilical artery and removal of blood clot every 5 mins for 20 mins total in order to remove as much blood as possible. Following this, embryos were fixed overnight in 4% PFA in 6-well plates on a rocker at 4°C. Samples were further processed and scanned by core services (Transgenics).

2.5.5 Embryo Culture using Static Culture

Embryos for culture were kept at 37°C after decidua were dissected out of the uterine horn. Individual embryos were then dissected out of decidua, with Reichart's membrane being removed but the ectoplacental cone remaining attached. The dissections were carried out

in pre-warmed PB1/FBS. Static culture of embryos in an 8-well chambered slide was carried out for incubation of embryos with the lipophilic dye, DiI (Molecular Probes) at 4 µM in PB1/FBS for 30 mins at room temperature. Embryos were then transferred into a culture medium containing 75% rat-serum replacement (Gibco-10828), 25% DMEM, 1 mM glutamine (GlutaMAX – Gibco: 3505006), 100 µM Na-pyruvate, 1 mM Hepes (pH 7.0).

2.5.6 Embryo Culture using Rolling Bottle apparatus

Embryos for culture were kept at 37°C after decidua were dissected out of the uterine horn. Individual embryos were then dissected out of decidua, with Reichart's membrane being removed but the ectoplacental cone remaining attached. The dissections were carried out in pre-warmed M2 medium (Sigma: M7167). Following dissection, individual embryos were washed into medium containing 50% KO serum 50% DMEM/F12 (1:1 – Gibco: 11320074) with GlutaMAX containing inhibitor or vehicle DMSO (1.6 µl of 50 µM stock in 8 ml total volume medium). Embryos were placed into glass bottles for rolling culture apparatus, with rubber lids that allow insertion into middle rotating chamber with continuous gas flow (5% CO_2), which is set-up in a 37°C pre-warmed incubator. Embryos were cultured for appropriate indicated times (varying from 5-24 hrs), with a media change at the 12 hr mark. Embryos were then placed into PBS, ectoplacental cone removed by dissection, and processed for further analysis (put into appropriate fixative for SEM or WISH processing). The concentration of FGFR inhibitors utilised in embryonic culture (Appendix Table A2) were selected due to their previous published usage (Oki et al. 2010; Tanaka et al. 2005).

2.6 Embryo & Cell/Tissue Analysis

All steps were carried out at room temperature (15-25°C) unless otherwise stated.

2.6.1 Wholemount In Situ Hybridisation

Following dissection embryos were fixed in 4% PFA in PBS overnight at 4°C. Following fixation embryos were then dehydrated using a methanol (MeOH) series: 1x 25% MeOH/PBS, 1x 50% MeOH/PBS, 1x 75% MeOH/PBS, 2x 100% MeOH. Dehydrated embryos were then stored in fresh 100% MeOH at -20°C.

Fixed embryos were rehydrated through a methanol series (MeOH) in PBS: 75% 5 min, 50% 5 min, 25% 5 min. Samples were then washed in PBT for 5 min x3. Samples were bleached with 6% H_2O_2 in PBT for 1 hr, before being washed in PBT (3x 5 min). Permeabilisation of embryos was carried out with 10 µg/ml Proteinase K in PBT for 5 min. Proteinase K was inactivated by a 20 mg/ml glycine in PBT wash for 5 min. Embryos were washed (2x 5 min PBT) and post-fixed in 0.2% glutaraldehyde in 4% PFA in PBS for 20 min. Embryos were washed (2x 5 min PBT) and blocked for 1 hr at 70°C in pre-warmed pre-hybridisation solution. Probes to be used were inactivated by heating to 70°C for 30 mins. Probes were then diluted to 1:500 in hybridisation solution and incubated with embryos overnight (approx. 18 hrs) at 70°C. Embryos were washed for 3x 30 min in Solution I (2x at 70°C, followed by 1x 65°C) followed by 3x 30 min Solution III washes (all at 65°C). Embryos were washed in TBST 3x 5 min, then preblocked in 10% HISS (heat inactivated sheep serum) in TBST for 2.5 hours. Antibody (Anti-DIG-AP Fab Fragments [Roche]) was blocked in 1% HISS in TBST with heat-inactivated embryo powder for 1hr at 4°C with mild agitation by rotator. Antibody and probe hybridisation occurred overnight in 1% HISS in TBST at 4°C. Sequential washing with TBST then occurred (3x 5 min, 5x 1 hr, overnight). Embryos were then washed with NTMT (1x 5 min, 2x 15 min), before stain solution added and allowed to develop in dark. Stain solution contains 5 µl NBT/BCIP per ml NTMT and stains areas of probe hybridisation, indication gene expression. Following stain development, embryos were washed in NTMT (2x 5 min) and post-fixed in 4% PFA in PBS for 30 min. Embryos were stored in PBT at 4°C prior to imaging, with yolk sac or whole embryo being collected at imaging for genotyping if necessary.

2.6.2 Wholemount Immunofluorescence

Following dissection embryos were fixed in 4% PFA in PBS overnight at 4°C. Following fixation embryos were then dehydrated using a methanol (MeOH) series: 1x 25% MeOH/PBS, 1x 50% MeOH/PBS, 1x 75% MeOH/PBS, 2x 100% MeOH. Dehydrated embryos were then stored in fresh 100% MeOH at -20°C.

Fixed embryos were rehydrated through a methanol series (MeOH) in PBS: 75% 5 min, 50% 5 min, 25% 5 min. Alternatively, fresh embryos were dissected, washed with PBS and fixed in 4% PFA for 15 min.

Embryos were then washed with PBS (2x 5 min) before being permeabilised in a series of TX-100 washes diluted in PBS (3x 5 min 0.1% TX-100 PBS; 2x 10 min TX-100 PBS; 2x 5 min TX-100 PBS). Embryos were blocked in block solution (2.5% horse serum, 3% bovine serum albumin in 0.1% Tween in PBS) for 1 hr. Primary antibodies were diluted at recommended concentrations (Appendix Table A3) in 1:1:2 block solution:0.1% TX-100 PBS:PBS. These were incubated with embryos for approximately 18 hrs at 4°C. Embryos were then washed (3x 30 min 0.04% TX-100 PBS). Secondary antibodies were diluted at recommended concentrations in 1:1:2 block solution: 0.1% TX-100 PBS: PBS. Incubation was carried out in dark conditions (darkened box) for 1 hr. Embryos were washed (4x 30 min 0.04% TX-100 PBS) before being stored in PBS at 4°C prior to mounting for imaging.

2.6.3 Scanning Electron Microscopy (SEM)

Embryos were fixed overnight in 0.1 M sodium cacodylate, 2.5% glutaraldehyde in ddH_2O. Following this embryos were washed with 0.1M sodium cacodylate (2x 10 minute), then post-fixed in 1% osmium tetroxide in 0.1M sodium cacodylate for 1hr. Embryos were then washed 6x 3 min ddH_2O, before dehydrated into ethanol: 1x 50%, 1x 75%, 2x 100% (10

min each). Embryos were then washed into 100% acetone 2x for 10 min each, before being stored in fresh acetone at 4°C.

Embryos were placed into fresh acetone and processed using a critical point dryer. Embryos were then mounted on stubs and sputter coated with platinum before imaging. Imaging was carried out using a Jeol SEM 6010LV.

2.6.4 Cell Immunofluorescence

Fixed cells were washed twice in PBS and then blocked for 30 mins with 4% BSA in PBS. Primary antibodies were diluted to the appropriate concentration in 4% BSA in PBS up to 100 µl per coverslip. Dots of diluted antibody were pipetted onto parafilm in a humidified chamber. Excess solution was carefully removed from each coverslip using tissue and then placed onto antibody droplets cells down. They were incubated at room temperature for 1 hr. Cells were washed 3x in PBS for 5 mins each time, on a rocker. Secondary antibodies were then diluted in 4% BSA in PBS and dotted on parafilm. 1 hr incubation at room temperature in the dark was carried out. Cells were again washed 3x 5 mins in PBS on rocker, before mounting on slides. Antibodies and concentrations listed in Table A3 (Appendix).

2.7 Statistical Analysis

Statistical tests were chosen based on whether data was paired or unpaired, and depended upon how many data sets were being analysed. In most cases, One-Way ANOVA was the appropriate statistical test, due to more than 3 groups or unpaired data being compared. In other circumstances, the Wilcoxon Rank Sum Test was utilised. This was appropriate in the analysis of non-parametric data sets where it was necessary to compare two data sets directly to each other. For the control data in the case of this, a

multiple testing correction was applied (Benjamini and Hochberg False Discovery Rate) in order to limit the occurrence of false positive results.

2.8 Image Processing

2.8.1 Cilia length analysis

The average length of cilia in the node of an individual embryo were measured (blind to genotype/experimental condition) using the JEOL InTouch Scope software “measure” function. Multiple cilia (13) were measured wherever possible for each embryo node, with random cilia chosen across the entirety of the structure (some cilia measurements were taken each from the left, right, anterior, posterior and middle of the node), however, to limit error an attempt was made to generally chose cilia to measure when both the tip and the base of the cilium was clearly visible, meaning the more straight cilia were on average more readily measureable.

2.8.2 Counting number of vesicles (putative NVPs) in the node

The number of vesicles within the node of an embryo were assessed using a high magnification SEM image (produced by the Jeol SEM 6010LV, 1500X-2000X) and the “multiple point” function on ImageJ software (FUJI). This function allows individual “NVPs” to be counted and marked to eliminate repeat counting of the same object. In order for vesicles to be counted, they must both be present in the node (within the tear-drop structure, no further outside than where cilia are no longer present), and at least 0.1 µm but no larger than 4 µm in diameter. It was not often that nodal vesicles were seen approaching the upper limit of this range, with almost all being < 3 µm.

2.8.3 Micro-CT analysis

Images produced by micro computed tomography (μCT) were assessed by both input through a computed analysis pipeline and manually scored by core services (Transgenics). Data analysis and segmentations were carried out using Fiji (Schindelin et al. 2012), 3D Slicer (Fedorov et al. 2012) and ITK-SNAP (Yushkevich et al. 2006) platforms.

3.0 Tanaka (2005) and the NVP hypothesis

3.1 Introduction

As discussed (**Introduction 1.5**), the mechanism by which leftward flow produced by cilia in the embryonic node is translated into a left/right gene asymmetry and subsequent cascades has been the subject of debate for many years. Proposed by Tanaka and colleagues in 2005, the NVP hypothesis posited that small lipid-membrane-bounded vesicles are the vehicle by which signalling molecules are transported to the left of the node by this fluid flow (Tanaka et al. 2005). The spherical objects which they argued were NVPs were not newly discovered in this paper, having been visualised by scanning electron microscopy (SEM) many years previously (Sulik et al. 1994). Although not commented on by Sulik when they visualised the developing node, particles similar to those argued to be the NVPs by Tanaka are clearly visible (**Figure 3.1.1** (Sulik et al. 1994; Tanaka et al. 2005)). Indeed these structures are consistently visible in SEM images throughout the literature, but were not discussed as a potential mechanism translating flow into asymmetry until Tanaka's seminal paper. Analysis of the distribution of these NVPs by SEM has shown that they are not asymmetrically distributed throughout the node (Norris lab, unpublished data). This is at odds with biophysical modelling carried out by Cartwright, which suggests that such particles should become asymmetrically distributed within the node (Cartwright et al. 2007). However, one key point to note is that *in vivo* the node cavity is a closed system; the membrane that covers the node must be removed in order to image it, including for SEM. This may impact the presence of signalling particles or NVPs free within the node at this time.

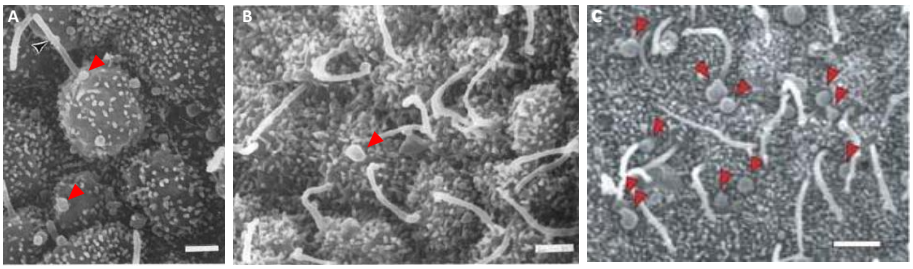


Figure 3.1.1: Putative NVPs in mouse embryonic nodes. A and **B** are both from Sulik et al, 1994. Red arrows show putative NVPs, scale bar = 1 µm. **C** shows image from Tanaka et al, 2005. Red arrows show putative NVPs, scale bar = 1 µm.

It is unknown exactly where NVPs originate in the pit of the node: the initial Tanaka paper suggests they are being produced by microvilli, and alternatively it has been suggested they may be produced by the cilium, as can occur with other vesicle types from cilia (Wood et al. 2013). It is unclear if they are produced in the pit of the node only, at the edges or across the node. Tanaka's live imaging analysis suggests that up to 5 vesicles are being produced every minute, and move across the node to the left side one or two at a time (Tanaka et al. 2005). There is some conflict of this with the SEM data, which shows a number of putative NVPs being visualised in the node at a snap shot in time.

The NVP theory proposes that NVPs "smash" when they hit cilia on the crown cells at the edge of the node, based on live imaging, however biophysical analysis (Cartwright et al. 2007) reveals this to be unlikely, as the energy carried by the vesicles is not great enough for such a breakage to occur. Indeed, it seems more likely that, if NVPs are a vehicle for signalling molecule transport, they would actively dock to initiate signalling molecule release. Imaging using SEM has not shown such a process occurring.

Finally, the method of embryo culture used by Tanaka prior to live imaging raises concerns. Their protocol incubates embryos with DiI for 30 minutes at room temperature prior to imaging. This is in contrast to published mouse embryo culture protocols that all indicate an optimal incubation temperature of 37°C; this replicates *in utero* temperatures (Piliszek et al. 2011). Additionally, anecdotal evidence suggests the possible cytotoxicity of DiI.

These together piqued my interest to investigate whether temperature or DiI cytotoxicity may be a significant factor in Tanaka's study. I was intrigued by the possibility that the NVPs they imaged may be artefactual, perhaps the result of cytotoxic effects of DiI. The size of NVPs they reported in live imaging ranged from 0.3-5 µm in diameter, which represents an order of magnitude variation in size. It is difficult to imagine a 5µm diameter vesicle originating from a cilium or microvillus, whereas this size for a piece of cellular debris is far more conceivable. Additional to this, Tanaka did not show anything of this size by SEM. Together this suggests that the particles that they image by SEM may not be the same as those imaged by live fluorescence microscopy.

3.2 Results

3.2.1 Culture – incubation with DiI – SEM

A striking omission in Tanaka's paper was their failure to show images of nodes post-incubation with the lipophilic dye DiI, leaving the possibility open that their *in vivo* imaged NVPs were artefacts created by their incubation protocol. I, therefore, replicated their protocols for culture as detailed in **Figure 3.2.1** (detailed description in **Methods 2.5**). In brief, I dissected E8.5 embryos with intact ectoplacental cones were from the uterine horn, the enclosing decidua and Reichert's membrane. I then washed embryos with the appropriate medium before being transferred to individual wells in an 8-well chambered slide and incubated in either the DiI-containing, or vehicle containing (hereby referred to as Mock) medium for 30mins at RT; these were then transferred into the secondary medium and incubated in this for 1hr at 37°C 5% CO_2. Finally, I fixed embryos for SEM imaging. A secondary control group of embryos were dissected and transferred directly into the secondary medium in order to control for the culture at 37°C. Following fixation, I critical point dried, mounted and sputter coated the embryos, as described (**Methods 2.6.3**).

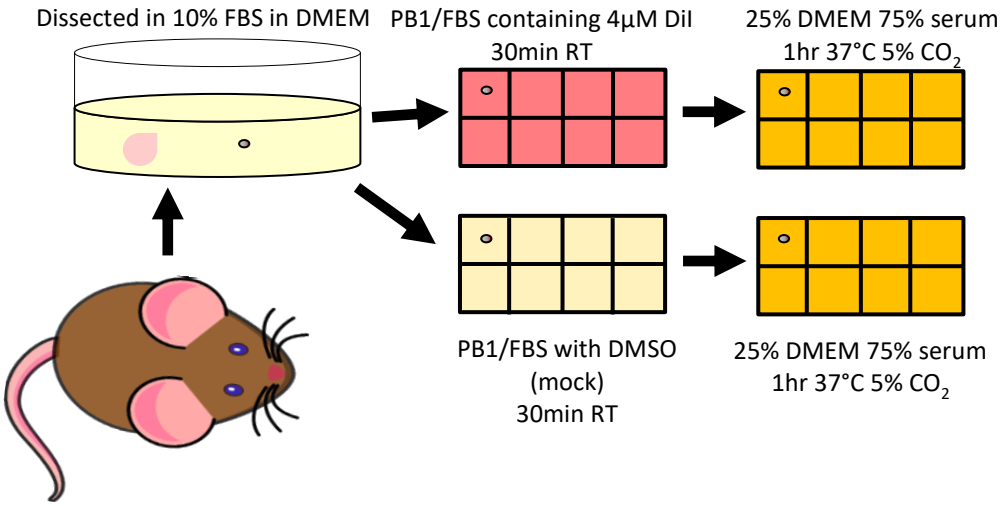


Figure 3.2.1: Schematic for embryo culture with DiI. Methodology of embryo culture with either DiI or Mock culture parameters, as indicated. Dissection of embryo out of mouse uterus and enclosed decidua indicated as first step, in 10% FBS in DMEM, with ectoplacental cone retained with embryo to maintain viability. Second step shows transfer of embryo into a medium with 1:1 ratio of PB1:FBS, containing either DiI or DMSO vehicle. Embryos were incubated at room temperature for 30 minutes. Third step shows washing and moving of embryos into a 25% DMEM, 75% serum medium, and incubated at 37°C 5% CO_2 for 1hr. Full methods in section **2.**

I then visualised the embryos by SEM and categorised (blind to previous culture conditions) in two ways: one relating to the structure of the node (**Table 3.2.1**), the other the level of cellular death, analysed indirectly through SEM visulisation (**Table 3.2.2**). These categories relate to the appearance of the imaged embryos: large amounts of cellular death were seen in a number of embryos, and also defects in the node structure. The categories which refer to the amount of cellular death are as follows: A - no cellular death seen, B - very small to negligible amount of cell death seen, C - small amount of cell death seen, D – some cell death seen, E - large amount of cell death seen, and F - widespread, abundant cell death seen. The categories relating to the structure of the node are: 5 - clear, characteristic node, 4 - small anomaly in visible node, 3 - multiple small anomalies in visible node, 2 - large anomalies in the shape/structure of the node, 1 - node outline barely visible, and 0 - no identifiable node. Example images and their respective category annotations are shown (**Figure 3.2.2**). As embryos are undergoing a violent

process of removal from uterus, dissection and addition to media, variations in the condition of control embryos is seen following culture, as multiple insults have been made to the embryo.

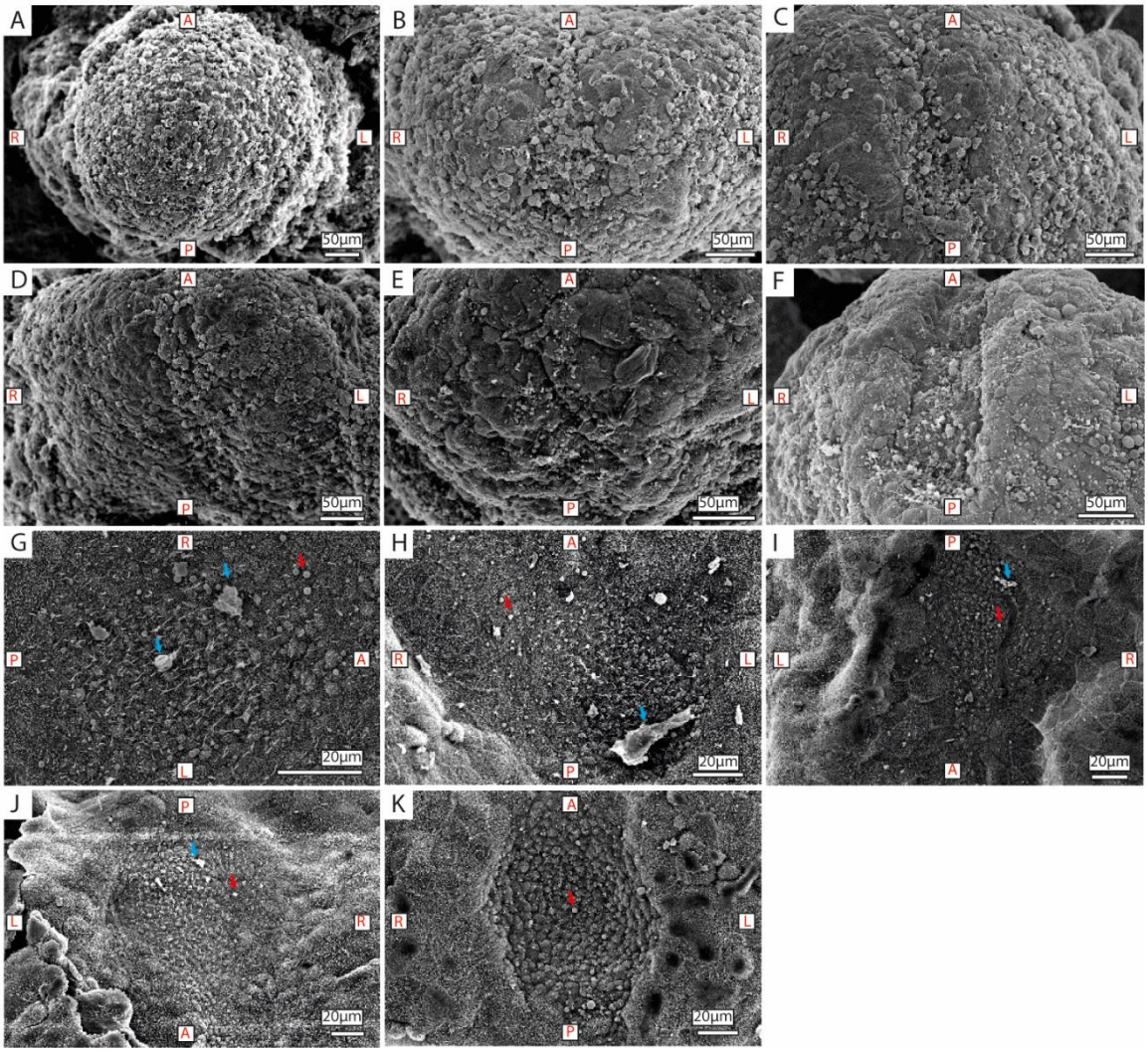
Table 3.2.1: Node Identifiability. Categories for how identifiable the node is in embryos following culture, 0-5, to allow scoring.

Category	Definition
0	Node unidentifiable
1	Node outline barely visible
2	Large anomaly in node shape/structure
3	Multiple anomalies in visible node
4	Small anomaly in visible node
5	Clear, characteristic node

Table 3.2.2: Cell Death Visualised. Categories for amount of cell death seen by SEM in embryos post-culture, to allow scoring F-A.

Category	Definition
F	Widespread, abundant cell death
E	Large amount of cell death
D	Some cell death
C	Small amount of cell death
B	Very small, negligible cell death
A	No cell death

Figure 3.2.2: Example cultured embryos and scoring system. Embryos are categorised relating to Node identifiability (**Table 3.2.1**) abd amount of cell death (**Table 3.2.2**). **A** shows an embryo of categories 0 and F. **B** shows an embryo of categories 1 and F. **C** shows an embryo of categories 1 and E. **D** shows an embryo of categories 1 and D. **E** shows an embryo of categories 1 and C. **F** shows an embryo of categories 2 and D. **G** shows an embryo of categories 2 and A. **H** shows an embryo of categories 3 and B. **I** shows an embryo of categories 3 and A. **J** shows an embryo of categories B and B. **K** shows an embryo of categories 5 and A. Anterior (red A in white box), posterior (red P in white box), left (red L in white box) and right (red R in white box) orientations are annotated in each image. Scale bars for **A-F** =50µm. Scale bars for **G-K** =20µm. For images **G-I**, blue arrows indicate anomalies in the node (refer to table **3.2.1)**. For images **G**-**K**, red arrows indicate putative vesicles or "NVPs".



Embryos were cultured as outlined (**Figure 3.2.1**), either in DiI or mock DMSO cultures, and scored for node identifiability and cell death. Additionally, uncultured wild-type control embryos were scored, along with 1-2 hr cultured controls (which were placed into the final

medium outlined in **Figure 3.2.1** following dissection, and incubated for 1-2 hrs at 37°C 5% CO_2). The results of these scores plotted against each other are shown (**Figure 3.2.3**). When plotted together, two clusters are evident. One contains the control embryos, both cultured and uncultured. The other is comprised of the Mock and the DiI cultured embryos: this second cluster shows low quality node structure, and high cellular death when compared to those embryos in the uncultured and control secondary medium cultured embryos (first cluster). Strikingly, control cultured and Mock cultured embryos are distinct. The overlap of the Mock and DiI cultured embryos is telling, as both result in low quality node patterning and high cellular death. From this it is clear that DiI is not the cause. Instead the culture method employed, most likely the 30 min incubation at room temperature appears to be responsible. This raises major concerns that Tanaka and colleagues may have imaged the movement of cellular debris rather than NVPs.

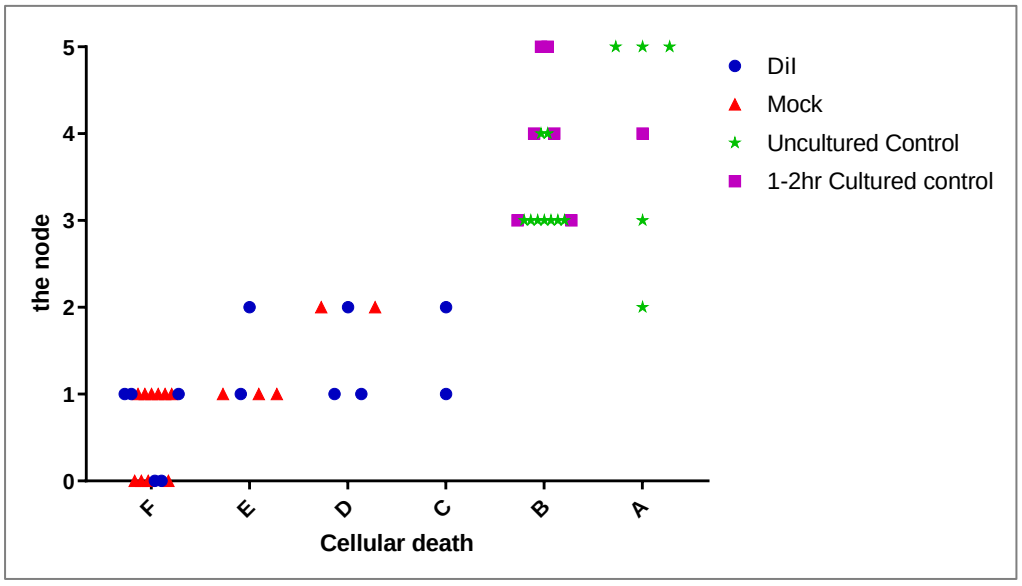


Figure 3.2.3: Cell death and node identifiability of cultured embryos. Embryos cultured with DiI (blue circle), Mock DMSO vehicle (red triangle), cultured for 1-2hrs in final medium as per **Figure 3.2.1** (purple square), and uncultured control embryos (green star) are plotted according to their scorings outlined in **Tables 3.2.1** and **3.2.2**. X-axis shows the score in terms of cellular death, maxing from maximum (F) to minimum (A) amounts. Similarly the y-axis shows the score in terms of how easily identifiable the node is, ranging from not able to identify (0), to a fully clear and characteristic node (5). Each data point on the graph corresponds to an individual embryo.

3.2.2 Expression analysis of *Fgfr1-4* and FGFR1-4

Tanaka and colleagues proposed that FGF8 signalling regulates NVP release in the pit of the node. Using immunofluorescent antibody staining they localised protein expression of FGFR1-3 to nodal cilia. However, as the identities of the antibodies used for this study are not specified it is not possible to determine whether they truly detected FGF receptor proteins. As such, I repeated this analysis, using validated antibodies to investigate protein localisation in the node (Appendix Table A3). As this is the primary source of evidence for FGFR expression in cilia I also examined expression in cell lines. I further assessed embryonic FGFR gene expression by WISH. The WISH probes were validated through comparison of expression patterns with those published and viewed on the Jax expression atlas (data not shown – www.informatics.jax.org/expression). I carried out a more exhaustive time series than was available on the atlas, looking from the EHF to 9 somite stages for each of the *Fgfrs*, during the period when L/R patterning is being established. This allowed me to investigate localisation of expression, and to assess any overt L/R asymmetry in expression. Preliminary experimental results showed low level staining, and as such I chose to carry out two separate "batches" of staining, the first being a low level stain, the second a high stain level. The high level staining was designed to reveal low level expression in the embryos.

Fgfr1 shows low level node expression

Expression of *Fgfr1* is shown in embryos ranging from the EHF stage to the 8 somite stage (ss) (**Figure 3.2.4**). Expression is uniform throughout the embryo at the EHF stage (panel **A**). At later stages, stronger expression is evident in the developing pre-somitic mesoderm, anterior to the node (**Figure 3.2.4** panels and inserts **D**-**F** and **H**-**J**). Strikingly the node shows lower levels of staining than the surrounding tissues; however the crown cells around the edge of the node show higher expression (**Figure 3.2.4** panels **D**-**F**, **H**-**I**).When high magnification images of the node itself are viewed (insert panels), we can see that

the expression within the node is comparatively higher at the 5 and 6 somites stages (**Figure 3.2.4 I** and **F** respectively).

Fgfr2 expression is very low or absent from the node

Expression data for *Fgfr2* between EHF and 9 somite stage embryos is shown in **Figure 3.2.5**. Expression is evident in the developing somites (**Figure 3.2.5** panels **B**-**F** and **H**-**J**) as well as lower level expression in the developing headfolds (**Figure 3.2.5 A**-**J**) from the earliest to the latest stages we looked at. The insert panels show the node when embryos were lightly stained (**Figure 3.2.5 D** and **E**), showing a lack of node expression. Very low level node expression of *Fgfr2* towards the anterior of the node is visible with heavier staining (**Figure 3.2.5 H** and **I**).

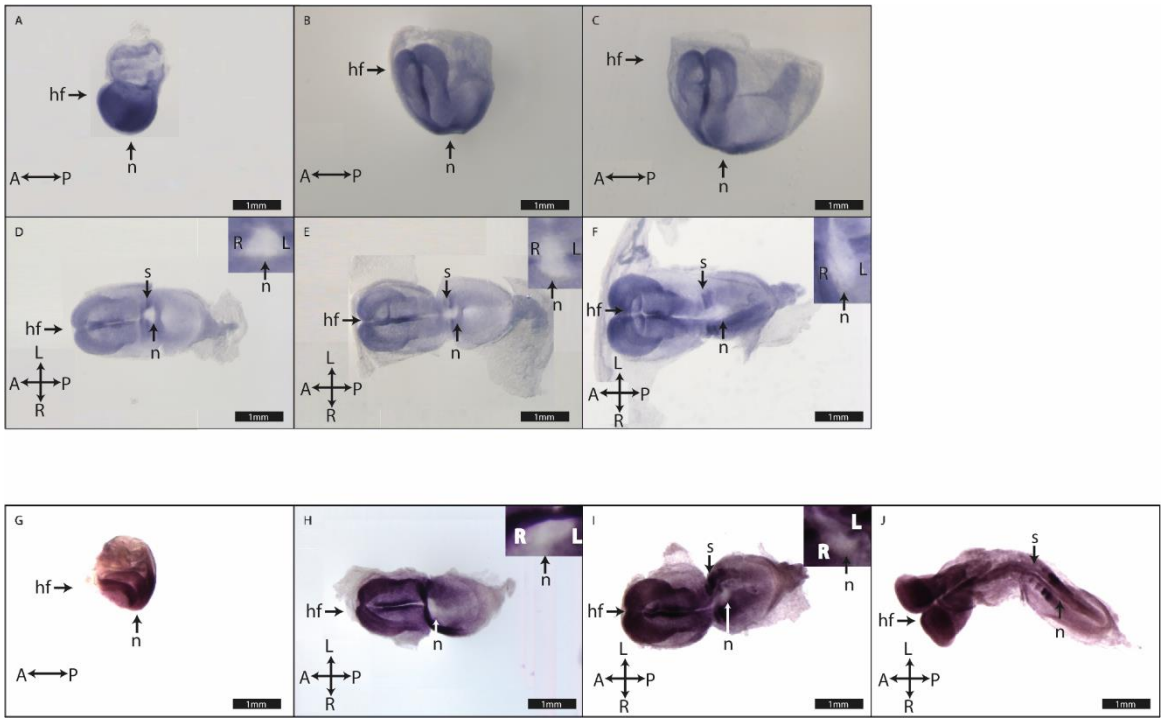


Figure 3.2.4: *Fgfr1* Wholemount *In Situ* Hybridisation. Embryos between Early Head-Fold (EHF) and 8 somite stage (8ss) stained following incubation with a riboprobe for *Fgfr1*. Staining indicated expression of *Fgfr1* in the embryo. Images **A-F** show one batch of embryos left until stain developed. Batch 2, images **G-J** show embryos left in stain to allow strong over-development of the stain, in order to visualise cells and tissues containing low levels of *Fgfr1* expression. Developmental stages of embryos: **A -** EHF, **B -** 3ss, **C -** 4ss, **D -** 3ss, **E -** 4ss, **F -** 6ss, **G -** LHF, **H -** 3ss, **I -** 5ss, **J -** 8ss. Insert panels in images show the embryonic node. Head-folds (hf), node (n) and somites (s) are indicated with arrows. Anterior (A), posterior (P), left (L) and right (R) are as indicated in each panel and inset images. Scale bar=1mm.

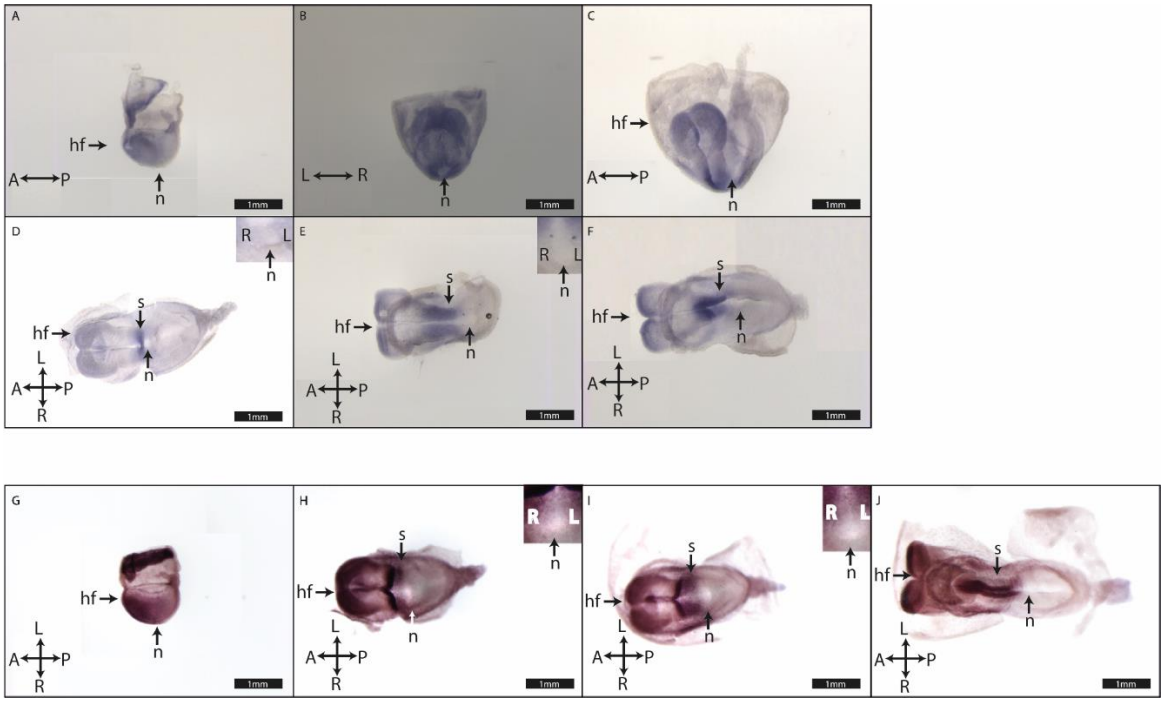


Figure 3.2.5: *Fgfr2* Wholemount *In Situ* Hybridisation. Embryos between Early Head-Fold (EHF) and 9 somite stage (9ss) stained following incubation with a riboprobe for *Fgfr2*. Staining indicated expression of *Fgfr2* in the embryo. Images **A-F** show one batch of embryos left until stain developed. Batch 2, images **G-J** show embryos left in stain to allow strong over-development of the stain, in order to visualise cells and tissues containing low levels of *Fgfr2* expression. Developmental stages of embryos: **A –** EHF, **B -** 3ss, **C -** 5ss, **D -** 4ss, **E -** 5ss, **F -** 7ss, **G –** EHF, **H -** 3ss, **I -** 4ss, **J -** 9ss. Insert panels in images show the embryonic node. Head-folds (hf), node (n) and somites (s) are indicated with arrows. Anterior (A), posterior (P), left (L) and right (R) are as indicated in each panel and inset images. Scale bar=1mm.

Fgfr3 shows low level node expression

Expression of *Fgfr3* is shown in EHF to 6 somite embryos (**Figure 3.2.6**). Ubiquitous expression is present throughout the embryo over the stages looked at. Lack of expression was seen in the node in lightly stained samples (**Figure 3.2.6** insert images **C** and **D**), however low level expression was seen in the node in highly stained samples (**Figure 3.2.6** insert images **H**-**J**).

Fgfr4 shows low level node expression

In **Figure 3.2.7** *Fgfr4* expression is shown in EHF to 6 somite stage embryos. Again, both low (**Figure 3.2.7 A-C**) and high (**Figure 3.2.7 D-G**) stained embryos are shown. The

developing embryo shows generally low expression, with some stronger expression present in the head folds and developing somites (particularly visible in **Figure 3.2.7 B** and **G**). Expression in the node was visible at the LHF in low staining (**Figure 3.2.7 A**-insert-arrow), and at the 4ss with heavy staining (**Figure 3.2.7 F**-insert, arrow).

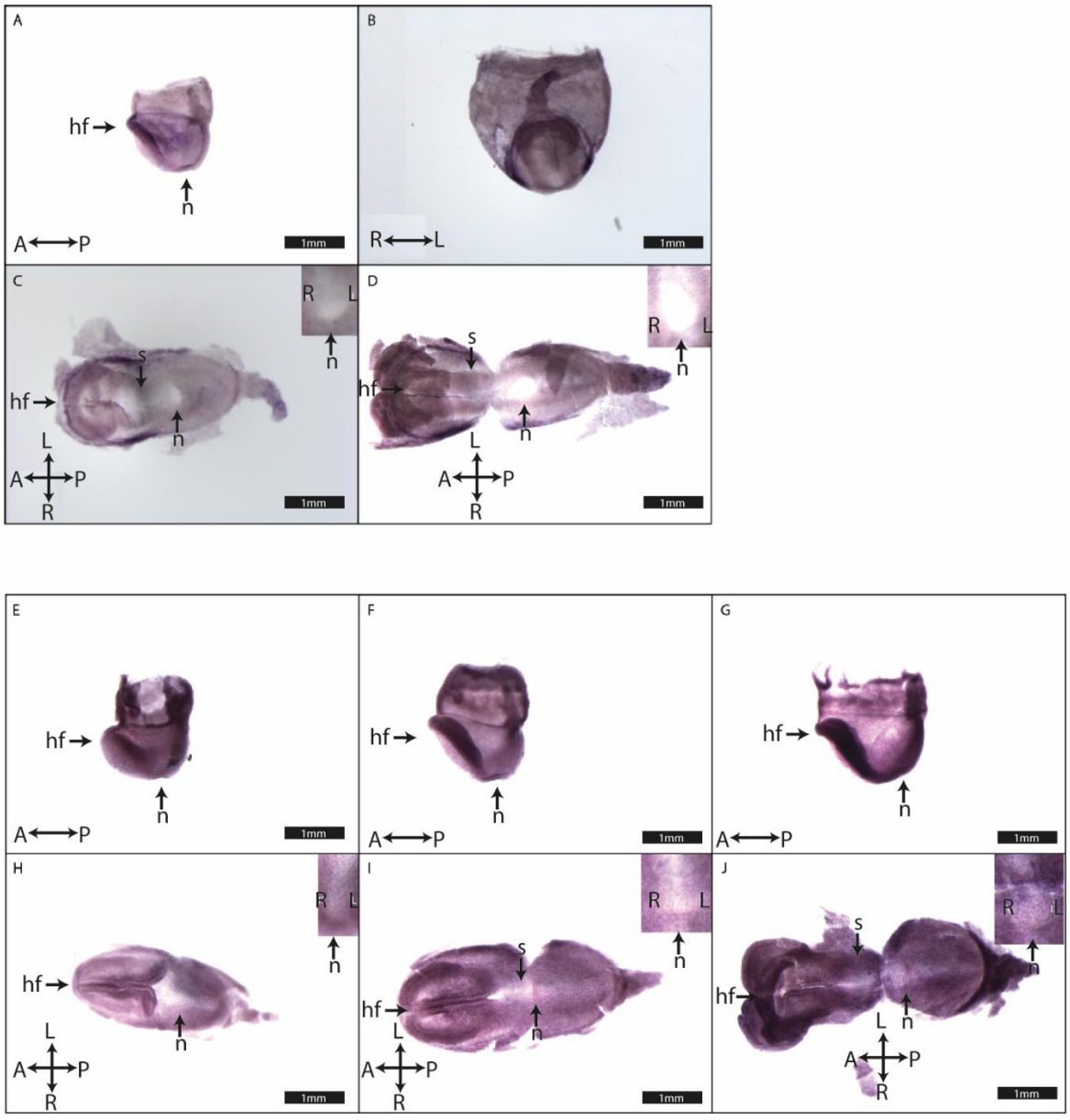


Figure 3.2.6: *Fgfr3* Wholemount *In Situ* Hybridisation. Embryos between Early Head-Fold (EHF) and 6 somite stage (6ss) stained following incubation with a riboprobe for *Fgfr3*. Staining indicated expression of *Fgfr3* in the embryo. Images **A-D** show one batch of embryos left until stain developed. Batch 2, images **E-J** show embryos left in stain to allow strong over-development of the stain, in order to visualise cells and tissues containing low levels of *Fgfr3* expression. Developmental stages of embryos: **A –** EHF, **B -** 4ss, **C -** 4ss, **D -** 6ss, **E –** LHF, **F -** 1ss, **G -** 3ss, **H -** 1ss, **I -** 3ss, **J -** 6ss. Insert panels in images show the embryonic node. Head-folds (hf), node (n) and somites (s) are indicated with arrows. Anterior (A), posterior (P), left (L) and right (R) are as indicated in each panel and inset images. Scale bar=1mm.

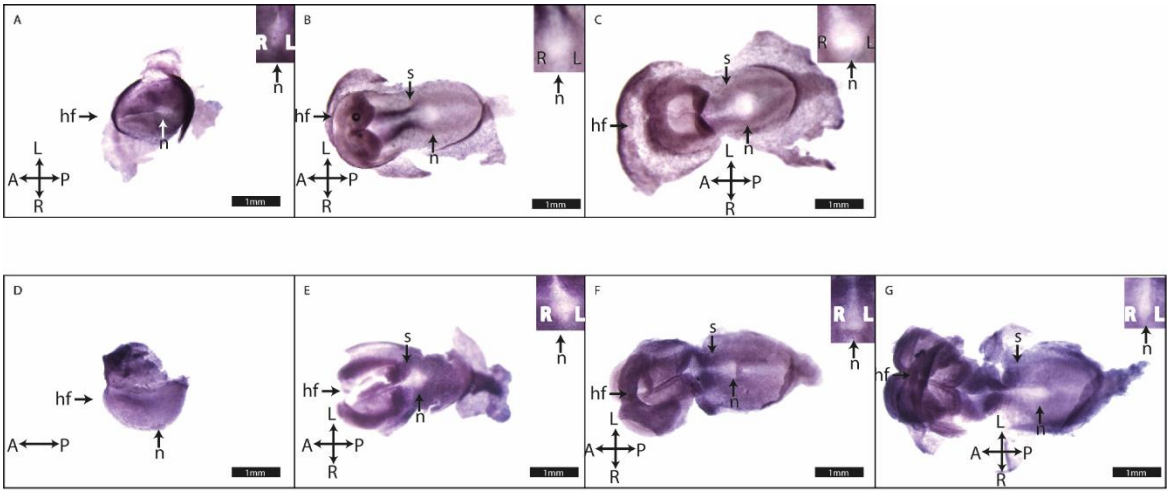


Figure 3.2.7: *Fgfr4* Wholemount *In Situ* Hybridisation. Embryos between Early Head-Fold (EHF) and 6 somite stage (6ss) stained following incubation with a riboprobe for *Fgfr4*. Staining indicated expression of *Fgfr4* in the embryo. Images **A-C** show one batch of embryos left until stain developed. Batch 2, images **D-G** show embryos left in stain to allow strong over-development of the stain, in order to visualise cells and tissues containing low levels of *Fgfr4* expression. Developmental stages of embryos: **A –** LHF, **B -** 3ss, **C -** 4ss, **D –** EHF, **E -** 2ss, **F -** 4ss, **G -** 6ss. Insert panels in images show the embryonic node. Head-folds (hf), node (n) and somites (s) are indicated with arrows. Anterior (A), posterior (P), left (L) and right (R) are as indicated in each panel and inset images. Scale bar=1mm.

Overall, analyses of *Fgfr1-4* expression by WISH revealed relatively low, but clear, mRNA expression of *Fgfr1, 3* and *4* in the node, when compared to the rest of the embryo; there was negligible expression of *Fgfr2* detected in these experiments. Although this node expression was much less than seen in other regions of the embryo, with high *Fgfr1* and *2* expression in the developing somites, and of *Fgfr1, 2, 3* and *4* in the head, WISH is not quantitative, and so further analysis would be necessary in order to better quantify this. As the timepoints investigated span the critical times for the breaking of L/R symmetry, I specifically looked to see if I could detect any L/R asymmetry in their expression: none was evident at any of the stages analysed. The *Fgfr* expression in the node, albeit low level, does appear to be more pronounced at certain developmental stages. *Fgfr1* shows its highest expression at 5ss, the latest stage looked at which heavy staining in which the node is still visible. *Fgfr2* node expression levels appear broadly consistent across the stages examined (EHF to 9ss). *Fgfr4* node expression is also fairly consistent, though

appears highest at the LHF stage and then more strongly at the 4ss exhibiting heavy staining in comparison to the lighter stained 3 and 4ss embryos, and the heavily stained 2 and 6ss embryos. Interestingly, *Fgfr3* node expression was highest at the 1 and 6ss, but not at 3ss.

Although none of the *Fgfrs* show a node-specific or asymmetric expression pattern, all the *Fgfrs* are expressed either in or near the node, even though only at low levels in some cases. With *Fgfr1* and *Fgfr2*, we see strong expression in the developing pair of somites which are physically close to the node. To follow on from this I looked in detail at the protein localisation, as it is possible for gene products to be present following earlier or low level mRNA expression. Additionally, it cannot be absolutely ruled out that gene products may be translocated from elsewhere in the embryo to the node, in order to function in the setup of L/R asymmetry.

Protein expression of FGFR1-4 in embryos

To assess the localisation of the FGFR1-4 proteins in embryos I performed whole-mount immunofluorescence (WIF) (**Methods 2.6.2**). To do this I utilised antibodies against the FGFRs1-4, and co-stained for ARL13B to mark the cilia; representative images showing embryos at the 4ss are shown (**Figure 3.2.8**). Note that although stage was assessed, it appears the cilia in panel **A** (FGFR1) are considerably shorter than those in the other panels.

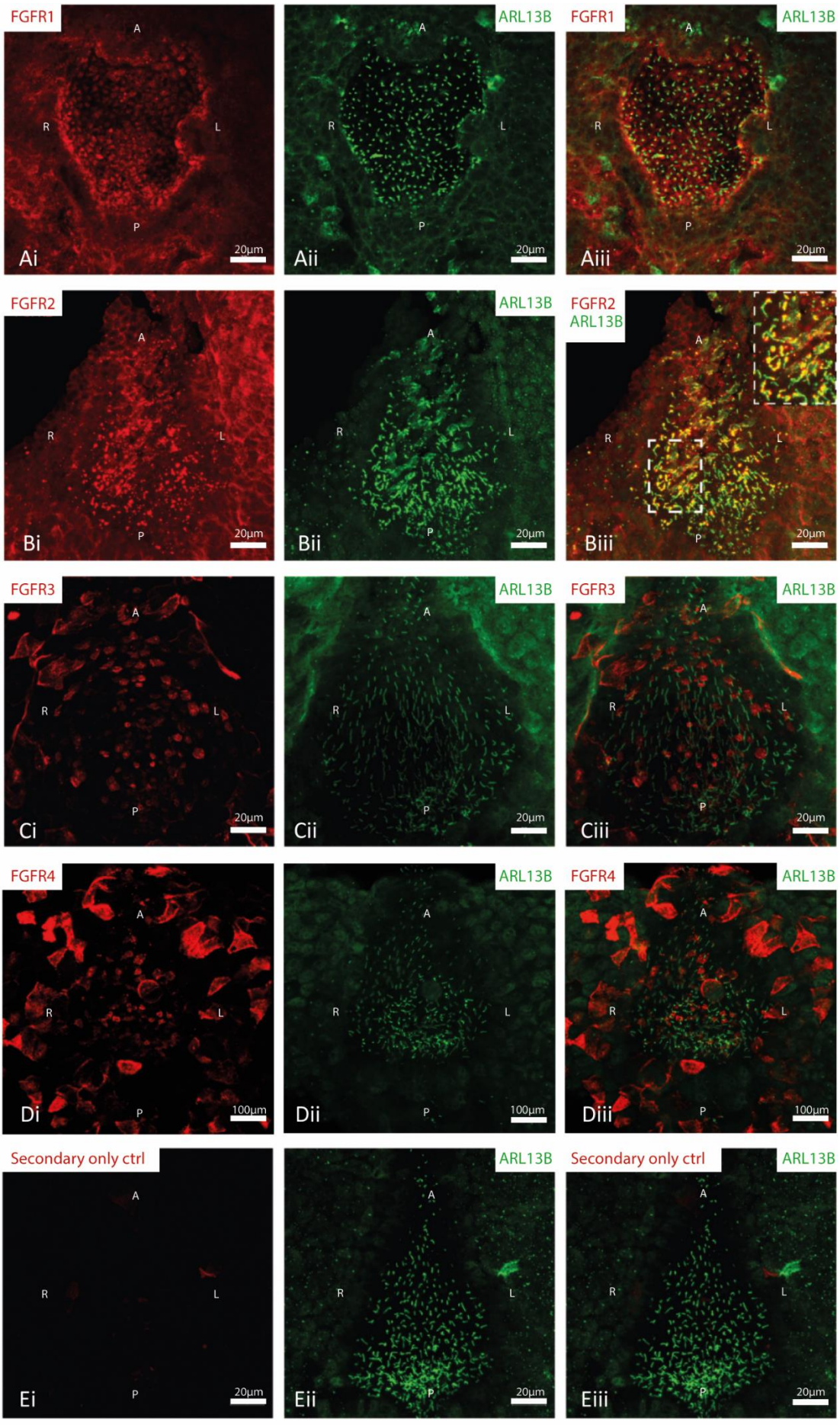
FGFR1 shows general localisation to all embryonic cells at 8.5 dpc, having no specific node ciliary expression (**Figure 3.2.8 A**). In contrast, FGFR2 shows strong cilia-specific expression in both pit and crown cells of the node, I did not detect any L/R asymmetry in this expression (**Figure 3.2.8 B**). At higher magnification (insert in **Aiii**) it is apparent that the localisation of FGFR2 is not consistent along the length of the cilium, showing instead a punctate expression pattern as is reported for many ciliary proteins. Nor is FGFR2 expression of the same level in all cilia; some have protein appearing to be present more

highly at the tip or base of the cilium, and some have consistent high expression along their whole length, while others have no detectable FGFR2 protein.

Anti-FGFR3 antibody staining revealed a salt and pepper expression pattern of protein in cells both within and outside of the node, though appearing to be somewhat more concentrated within the node itself (**Figure 3.2.8 C**).

FGFR4 shows expression similar to FGFR3: there was general patchy expression, with only some cells being positive (**Figure 3.2.8 D**). However there is no difference in expression levels overall in node cells compared to the other cells which comprise the embryo.

Figure 3.2.8: FGFR proteins in the mouse node. A-D show the protein localisations of FGFRs1-4 respectively (in red), along with the cilia marker ARL13B (green). For each, individual channel images are in **i** (red – FGFR), **ii** (green – ARL13B) and combined in **iii**. In **E**, the secondary only control is shown (red channel- **i**), to prove specificity of the FGFR antibodies. In **Biii**, a higher magnification inset is shown (white dashed-line box). Scale bars for **A**, **B**, **C** and **E** =20μm. Scale bar for **D**=100μm.


FGFR1
ARL13B
FGFR1
ARL13B
A
R
L
P
Ai
Aii
Aiii
20μm
FGFR2
ARL13B
FGFR2
ARL13B
Bi
Bii
Biii
FGFR3
ARL13B
FGFR3
ARL13B
Ci
Cii
Ciii
FGFR4
ARL13B
FGFR4
ARL13B
Di
Dii
Diii
100μm
Secondary only ctrl
ARL13B
Secondary only ctrl
ARL13B
Ei
Eii
Eiii

Protein expression of FGFR1-4 in cultured cells

For each of the FGFRs, I analysed the expression pattern of their protein in a panel of well characterised cell lines. In order to look specifically in the cilia, cells were serum starved to pause cell cycle growth and allow the growth of the primary cilium. This was carried out to assess in FGFRs are generally and/or specifically localised to the primary cilium. For each of the cell lines, I analysed the FGFR protein localisation in serum starved, ciliated cells, and also in actively growing cells, where cilia are only present in very small number and are of short length (G1/2 cilia). In all of these cell types and growth states, ARL13B marks the cilia, and DAPI marks the nucleus (**Figures 3.2.9 – 3.2.14**).

FGFR1 localisation in characterised cell lines

In ciliated Mouse Embryonic Fibroblasts (MEFs), FGFR1 shows localisation to discrete areas in the nucleus, and also to the ER (**Figure 3.2.9 A**), whereas in actively growing MEFs it appears to show a much more ER-specific localisation, although there is still some nuclear protein (**Figure 3.2.10 A**). In RPE1 cells both with and without induced cilia, FGFR1 shows nuclear localisation (**Figure 3.2.11 A** and **Figure 3.2.12 A** respectively). In both NIH3T3 ciliated and unciliated cells, FGFR1 shows strong nuclear and ER localisation (**Figure 3.2.13 A** and **Figure 3.2.14 A** respectively), as it did in the MEFs. No cilia localisation was seen for FGFR1 in any of the cell types looked at.

FGFR2 localisation in characterised cell lines

For ciliated MEFs (**Figure 3.2.9 B**), there are discrete strong points of expression within the nucleus, whereas in actively growing MEFs (**Figure 3.2.10 B**), nuclear localisation appears to be more constant throughout the entire nucleus. A similar pattern of general nuclear expression is seen in ciliated RPE1 cells (**Figure 3.2.11 B**), in un-ciliated RPE1s the discrete points of FGFR2 localisation within the nucleus are again present (**Figure 3.2.12 B**). Also similarly to RPE1 ciliated cells, ciliated NIH3T3 cells show general FGFR2 nuclear localisation (**Figure 3.2.13 B**). However, in unciliated NIH3T3 cells, no FGFR2

protein was detected (**Figure 3.2.14 B**). No expression of FGFR2 protein was detected in the cilia in any of the cell types investigated.

FGFR3 localisation in characterised cell lines

FGFR3 lacks specific expression in MEFs and NHI3T3 cell lines (**Figures 3.2.9 C, 3.2.10C, 3.2.11 C. 3.2.12 C**). However, it does show specific localisation in RPE1 ciliated cells, with low level nuclear localisation, and ciliary localisation (**Figure 3.2.13 C**). In RPE1s that have not been serum starved, and thus are actively growing, no FGFR3 is detected (**Figure 3.2.14 C**).

FGFR4 localisation in characterised cell lines

FGFR4 has very low level plasma membrane expression in actively growing MEFs (**Figure 3.2.10 D**). In ciliated MEFs, there is no FGFR4 detectable (**Figure 3.2.9 D**). In ciliated RPE1 cells, FGFR4 shows low level plasma membrane localisation, and cilia specific localisation (**Figure 3.2.11 D**). In un-ciliated RPE1s, the general plasma membrane localisation is also present (**Figure 3.2.12 D**). In ciliated NIH3T3 cells, FGFR4 also shows low level plasma membrane and cilia localisation (**Figure 3.2.13 D**). In contrast, in unciliated NIH3T3 cells, only plasma membrane expression of FGFR4 is present (**Figure 3.2.14 D**).

Figure 3.2.9: FGFR protein localisation in ciliated MEF cells. A shows the localisation of FGFR1 protein (**i**)**,** with ARL12B cilia marker (**ii**) and DAPI nuclear marker (**iii**). These are combined in **Aiv** – FGFR1 in red, ARL13B in green and DAPI in blue. **B** shows the localisation of FGFR2 protein (**i**)**,** with ARL12B cilia marker (**ii**) and DAPI nuclear marker (**iii**). These are combined in **Biv** – FGFR2 in red, ARL13B in green and DAPI in blue. **C** shows the localisation of FGFR3 protein (**i**)**,** with ARL12B cilia marker (**ii**) and DAPI nuclear marker (**iii**). These are combined in **Civ** – FGFR3 in red, ARL13B in green and DAPI in blue. **D** shows the localisation of FGFR4 protein (**i**)**,** with ARL12B cilia marker (**ii**) and DAPI nuclear marker (**iii**). These are combined in **Div** – FGFR4 in red, ARL13B in green and DAPI in blue. **E** shows the secondary only control used for FGFR1 protein (**i**)**,** with ARL12B cilia marker (**ii**) and DAPI nuclear marker (**iii**). These are combined in **Eiv** – secondary only control for FGFR1 in red, ARL13B in green and DAPI in blue. **F** shows the secondary only control used for FGFR2-4 proteins (**i**)**,** with ARL12B cilia marker (**ii**) and DAPI nuclear marker (**iii**). These are combined in **Fiv** – secondary only control for FGFR2-4 in red, ARL13B in green and DAPI in blue. In **iv** panels, scale bars=20µm and inset panels show higher magnification of a single cell (white and white dashed-line boxes).

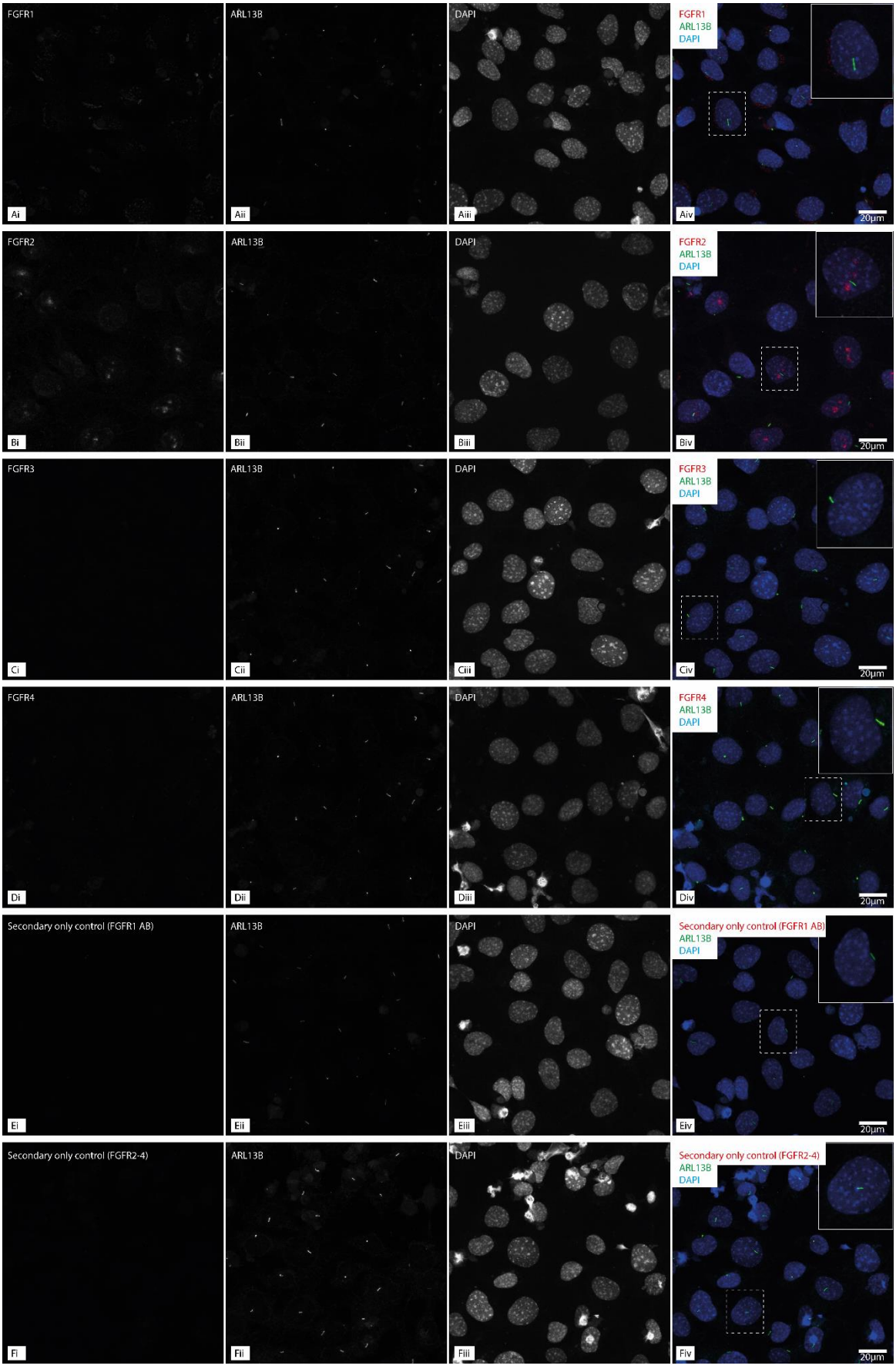

FGFR1
ARL13B
DAPI
FGFR1
ARL13B
DAPI
Ai
Aii
Aiii
Aiv
20μm
FGFR2
ARL13B
DAPI
FGFR2
ARL13B
DAPI
Bi
Bii
Biii
Biv
20μm
FGFR3
ARL13B
DAPI
FGFR3
ARL13B
DAPI
Ci
Cii
Ciii
Civ
20μm
FGFR4
ARL13B
DAPI
FGFR4
ARL13B
DAPI
Di
Dii
Diii
Div
20μm
Secondary only control (FGFR1 AB)
ARL13B
DAPI
Secondary only control (FGFR1 AB)
ARL13B
DAPI
Ei
Eii
Eiii
Eiv
20μm
Secondary only control (FGFR2-4)
ARL13B
DAPI
Secondary only control (FGFR2-4)
ARL13B
DAPI
Fi
Fii
Fiii
Fiv
20μm

Figure 3.2.10: FGFR protein localisation in un-ciliated (actively growing) MEF cells. A shows the localisation of FGFR1 protein (**i**)**,** with ARL12B cilia marker (**ii**) and DAPI nuclear marker (**iii**). These are combined in **Aiv** – FGFR1 in red, ARL13B in green and DAPI in blue. **B** shows the localisation of FGFR2 protein (**i**)**,** with ARL12B cilia marker (**ii**) and DAPI nuclear marker (**iii**). These are combined in **Biv** – FGFR2 in red, ARL13B in green and DAPI in blue. **C** shows the localisation of FGFR3 protein (**i**)**,** with ARL12B cilia marker (**ii**) and DAPI nuclear marker (**iii**). These are combined in **Civ** – FGFR3 in red, ARL13B in green and DAPI in blue. **D** shows the localisation of FGFR4 protein (**i**)**,** with ARL12B cilia marker (**ii**) and DAPI nuclear marker (**iii**). These are combined in **Div** – FGFR4 in red, ARL13B in green and DAPI in blue. **E** shows the secondary only control used for FGFR1 protein (**i**)**,** with ARL12B cilia marker (**ii**) and DAPI nuclear marker (**iii**). These are combined in **Eiv** – secondary only control for FGFR1 in red, ARL13B in green and DAPI in blue. **F** shows the secondary only control used for FGFR2-4 proteins (**i**)**,** with ARL12B cilia marker (**ii**) and DAPI nuclear marker (**iii**). These are combined in **Fiv** – secondary only control for FGFR2-4 in red, ARL13B in green and DAPI in blue. In **iv** panels, scale bars=20μm and inset panels show higher magnification of a single cell (white and white dashed-line boxes).

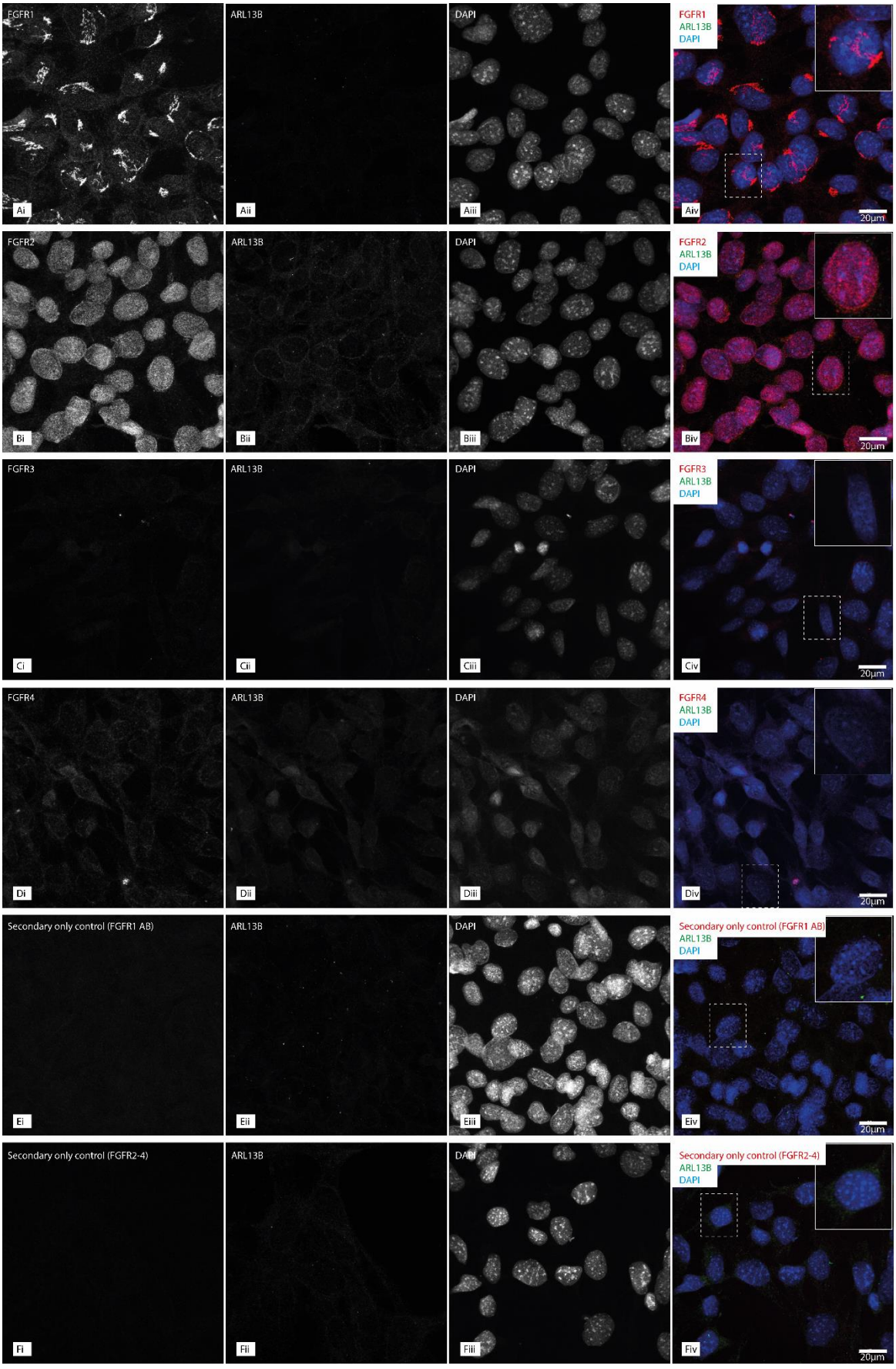

FGFR1
ARL13B
DAPI
Ai
Aii
Aiii
FGFR1
ARL13B
DAPI
Aiv
20µm
FGFR2
ARL13B
DAPI
Bi
Bii
Biii
FGFR2
ARL13B
DAPI
Biv
20µm
FGFR3
ARL13B
DAPI
Ci
Cii
Ciii
FGFR3
ARL13B
DAPI
Civ
20µm
FGFR4
ARL13B
DAPI
Di
Dii
Diii
FGFR4
ARL13B
DAPI
Div
20µm
Secondary only control (FGFR1 AB)
ARL13B
DAPI
Ei
Eii
Eiii
Secondary only control (FGFR1 AB)
ARL13B
DAPI
Eiv
20µm
Secondary only control (FGFR2-4)
ARL13B
DAPI
Fi
Fii
Fiii
Secondary only control (FGFR2-4)
ARL13B
DAPI
Fiv
20µm

Figure 3.2.11: FGFR protein localisation in ciliated RPE1 cells. A shows the localisation of FGFR1 protein (**i**)**,** with ARL12B cilia marker (**ii**) and DAPI nuclear marker (**iii**). These are combined in **Aiv** – FGFR1 in red, ARL13B in green and DAPI in blue. **B** shows the localisation of FGFR2 protein (**i**)**,** with ARL12B cilia marker (**ii**) and DAPI nuclear marker (**iii**). These are combined in **Biv** – FGFR2 in red, ARL13B in green and DAPI in blue. **C** shows the localisation of FGFR3 protein (**i**)**,** with ARL12B cilia marker (**ii**) and DAPI nuclear marker (**iii**). These are combined in **Civ** – FGFR3 in red, ARL13B in green and DAPI in blue. **D** shows the localisation of FGFR4 protein (**i**)**,** with ARL12B cilia marker (**ii**) and DAPI nuclear marker (**iii**). These are combined in **Div** – FGFR4 in red, ARL13B in green and DAPI in blue. **E** shows the secondary only control used for FGFR1 protein (**i**)**,** with ARL12B cilia marker (**ii**) and DAPI nuclear marker (**iii**). These are combined in **Eiv** – secondary only control for FGFR1 in red, ARL13B in green and DAPI in blue. **F** shows the secondary only control used for FGFR2-4 proteins (**i**)**,** with ARL12B cilia marker (**ii**) and DAPI nuclear marker (**iii**). These are combined in **Fiv** – secondary only control for FGFR2-4 in red, ARL13B in green and DAPI in blue. In **iv** panels, scale bars=20μm and inset panels show higher magnification of a single cell (white and white dashed-line boxes).

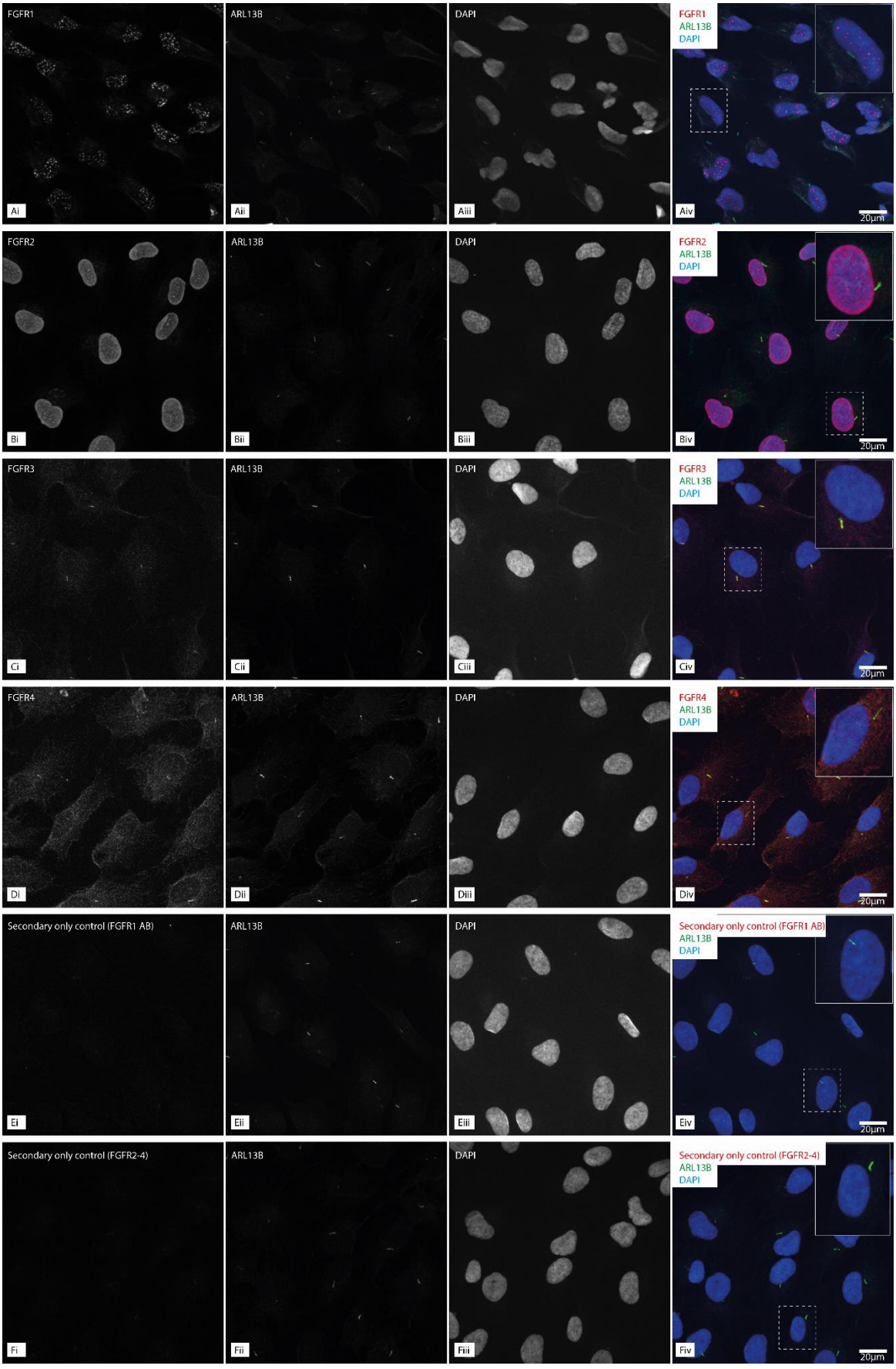

FGFR1
ARL13B
DAPI
Ai
Aii
Aiii
FGFR1
ARL13B
DAPI
Aiv
20µm
FGFR2
ARL13B
DAPI
Bi
Bii
Biii
FGFR2
ARL13B
DAPI
Biv
20µm
FGFR3
ARL13B
DAPI
Ci
Cii
Ciii
FGFR3
ARL13B
DAPI
Civ
20µm
FGFR4
ARL13B
DAPI
Di
Dii
Diii
FGFR4
ARL13B
DAPI
Div
20µm
Secondary only control (FGFR1 AB)
ARL13B
DAPI
Ei
Eii
Eiii
Secondary only control (FGFR1 AB)
ARL13B
DAPI
Eiv
20µm
Secondary only control (FGFR2-4)
ARL13B
DAPI
Fi
Fii
Fiii
Secondary only control (FGFR2-4)
ARL13B
DAPI
Fiv
20µm

Figure 3.2.12: FGFR protein localisation in un-ciliated (actively growing) RPE1 cells. A shows the localisation of FGFR1 protein (**i**)**,** with ARL12B cilia marker (**ii**) and DAPI nuclear marker (**iii**). These are combined in **Aiv** – FGFR1 in red, ARL13B in green and DAPI in blue. **B** shows the localisation of FGFR2 protein (**i**)**,** with ARL12B cilia marker (**ii**) and DAPI nuclear marker (**iii**). These are combined in **Biv** – FGFR2 in red, ARL13B in green and DAPI in blue. **C** shows the localisation of FGFR3 protein (**i**)**,** with ARL12B cilia marker (**ii**) and DAPI nuclear marker (**iii**). These are combined in **Civ** – FGFR3 in red, ARL13B in green and DAPI in blue. **D** shows the localisation of FGFR4 protein (**i**)**,** with ARL12B cilia marker (**ii**) and DAPI nuclear marker (**iii**). These are combined in **Div** – FGFR4 in red, ARL13B in green and DAPI in blue. **E** shows the secondary only control used for FGFR1 protein (**i**)**,** with ARL12B cilia marker (**ii**) and DAPI nuclear marker (**iii**). These are combined in **Eiv** – secondary only control for FGFR1 in red, ARL13B in green and DAPI in blue. **F** shows the secondary only control used for FGFR2-4 proteins (**i**)**,** with ARL12B cilia marker (**ii**) and DAPI nuclear marker (**iii**). These are combined in **Fiv** – secondary only control for FGFR2-4 in red, ARL13B in green and DAPI in blue. In **iv** panels, scale bars=20µm and inset panels show higher magnification of a single cell (white and white dashed-line boxes).

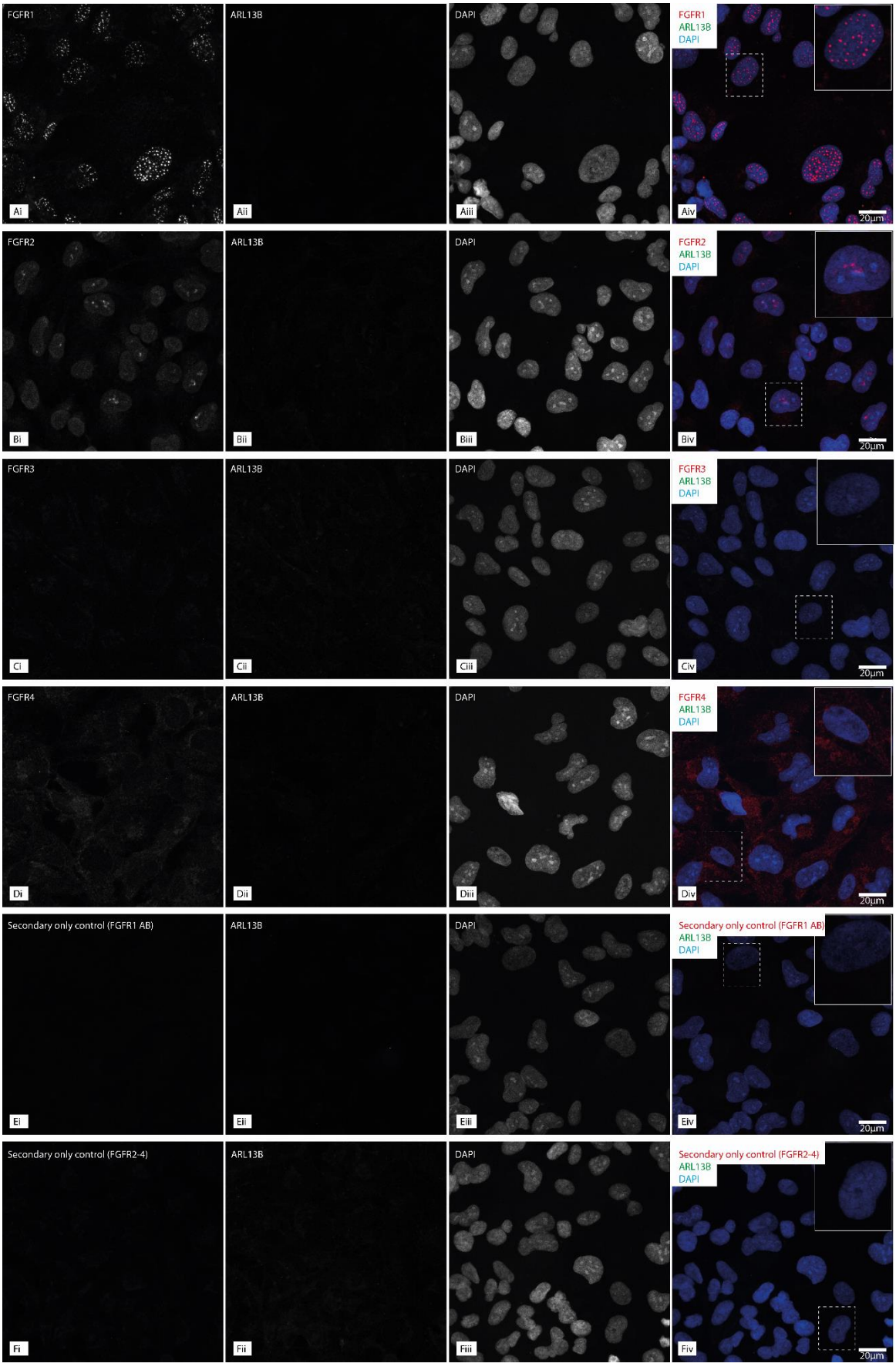

FGFR1
ARL13B
DAPI
FGFR1
ARL13B
DAPI
Ai
Aii
Aiii
Aiv
20μm
FGFR2
ARL13B
DAPI
FGFR2
ARL13B
DAPI
Bi
Bii
Biii
Biv
20μm
FGFR3
ARL13B
DAPI
FGFR3
ARL13B
DAPI
Ci
Cii
Ciii
Civ
20μm
FGFR4
ARL13B
DAPI
FGFR4
ARL13B
DAPI
Di
Dii
Diii
Div
20μm
Secondary only control (FGFR1 AB)
ARL13B
DAPI
Secondary only control (FGFR1 AB)
ARL13B
DAPI
Ei
Eii
Eiii
Eiv
20μm
Secondary only control (FGFR2-4)
ARL13B
DAPI
Secondary only control (FGFR2-4)
ARL13B
DAPI
Fi
Fii
Fiii
Fiv
20μm

Figure 3.2.13: FGFR protein localisation in ciliated NIH3T3 cells. A shows the localisation of FGFR1 protein (**i**)**,** with ARL12B cilia marker (**ii**) and DAPI nuclear marker (**iii**). These are combined in **Aiv** – FGFR1 in red, ARL13B in green and DAPI in blue. **B** shows the localisation of FGFR2 protein (**i**)**,** with ARL12B cilia marker (**ii**) and DAPI nuclear marker (**iii**). These are combined in **Biv** – FGFR2 in red, ARL13B in green and DAPI in blue. **C** shows the localisation of FGFR3 protein (**i**)**,** with ARL12B cilia marker (**ii**) and DAPI nuclear marker (**iii**). These are combined in **Civ** – FGFR3 in red, ARL13B in green and DAPI in blue. **D** shows the localisation of FGFR4 protein (**i**)**,** with ARL12B cilia marker (**ii**) and DAPI nuclear marker (**iii**). These are combined in **Div** – FGFR4 in red, ARL13B in green and DAPI in blue. **E** shows the secondary only control used for FGFR1 protein (**i**)**,** with ARL12B cilia marker (**ii**) and DAPI nuclear marker (**iii**). These are combined in **Eiv** – secondary only control for FGFR1 in red, ARL13B in green and DAPI in blue. **F** shows the secondary only control used for FGFR2-4 proteinS (**i**)**,** with ARL12B cilia marker (**ii**) and DAPI nuclear marker (**iii**). These are combined in **Fiv** – secondary only control for FGFR2-4 in red, ARL13B in green and DAPI in blue. In **iv** panels, scale bars=20µm and inset panels show higher magnification of a single cell (white and white dashed-line boxes).

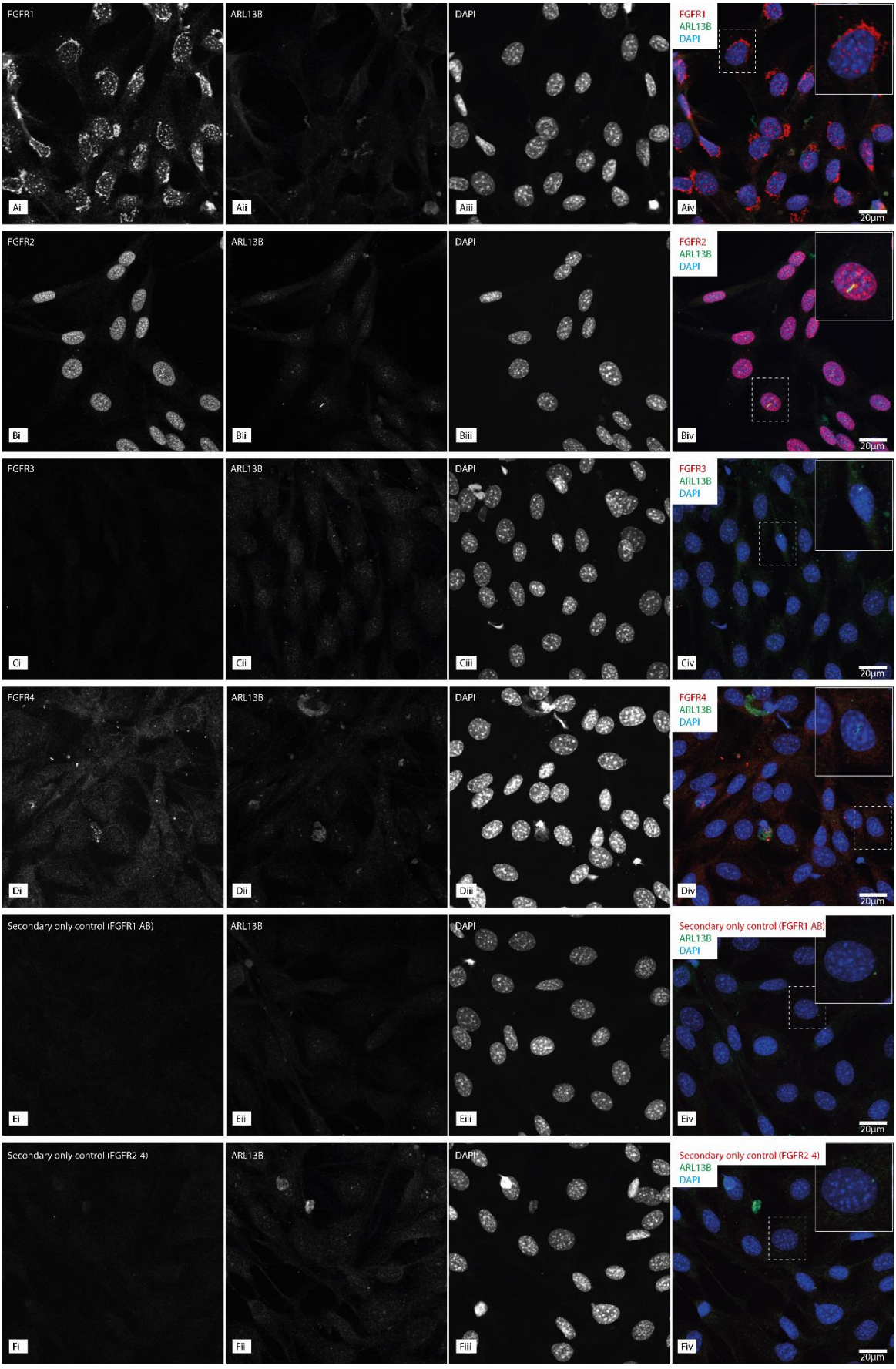
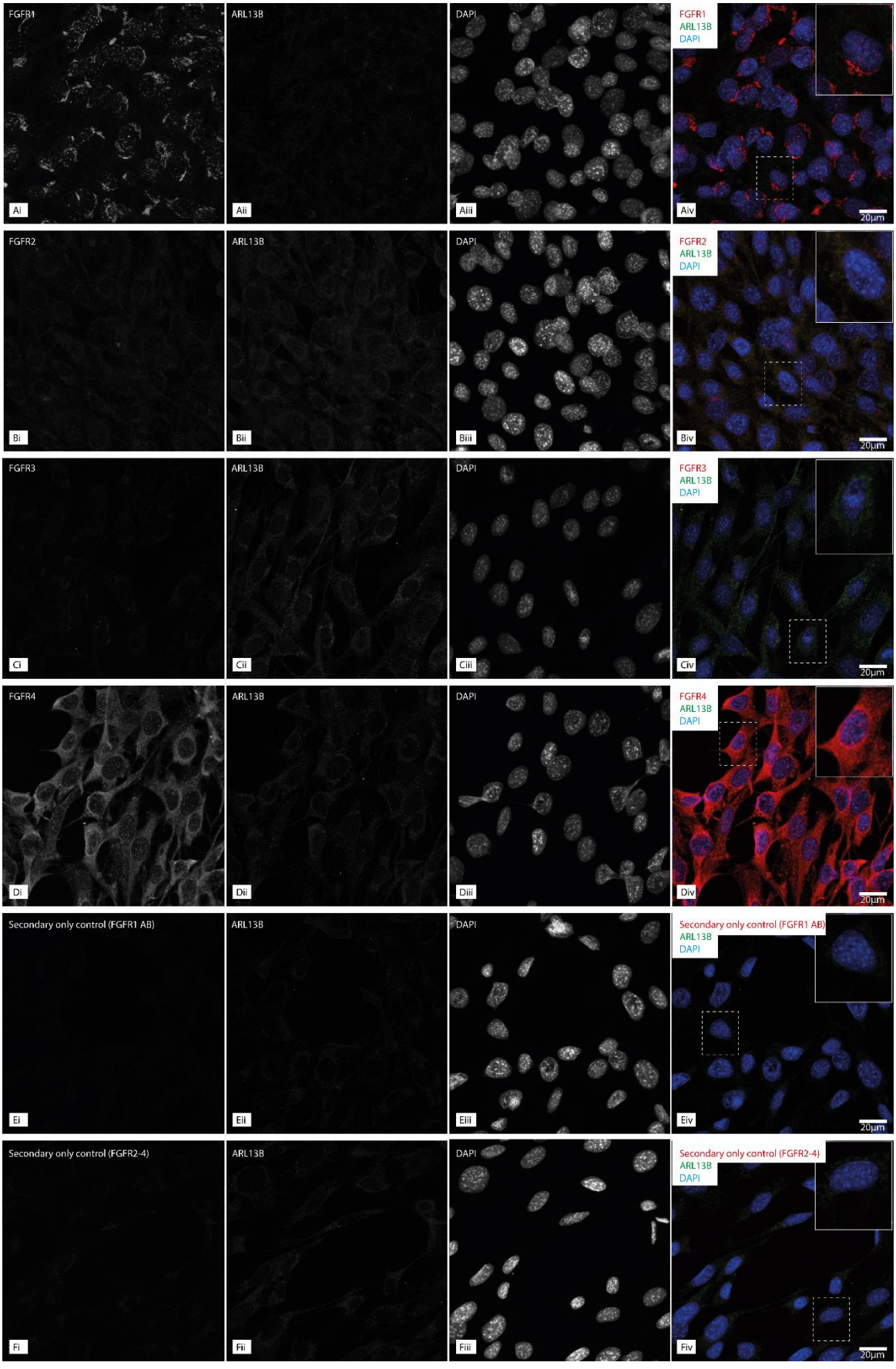

FGFR1
ARL13B
DAPI
Ai
Aii
Aiii
Aiv
20μm
FGFR2
Bi
Bii
Biii
Biv
FGFR3
Ci
Cii
Ciii
Civ
FGFR4
Di
Dii
Diii
Div
Secondary only control (FGFR1 AB)
Ei
Eii
Eiii
Eiv
Secondary only control (FGFR2-4)
Fi
Fii
Fiii
Fiv

Figure 3.2.14: FGFR protein localisation in un-ciliated (actively growing) NIH3T3 cells. A shows the localisation of FGFR1 protein (**i**)**,** with ARL12B cilia marker (**ii**) and DAPI nuclear marker (**iii**). These are combined in **Aiv** – FGFR1 in red, ARL13B in green and DAPI in blue. **B** shows the localisation of FGFR2 protein (**i**)**,** with ARL12B cilia marker (**ii**) and DAPI nuclear marker (**iii**). These are combined in **Biv** – FGFR2 in red, ARL13B in green and DAPI in blue. **C** shows the localisation of FGFR3 protein (**i**)**,** with ARL12B cilia marker (**ii**) and DAPI nuclear marker (**iii**). These are combined in **Civ** – FGFR3 in red, ARL13B in green and DAPI in blue. **D** shows the localisation of FGFR4 protein (**i**)**,** with ARL12B cilia marker (**ii**) and DAPI nuclear marker (**iii**). These are combined in **Div** – FGFR4 in red, ARL13B in green and DAPI in blue. **E** shows the secondary only control used for FGFR1 protein (**i**)**,** with ARL12B cilia marker (**ii**) and DAPI nuclear marker (**iii**). These are combined in **Eiv** – secondary only control for FGFR1 in red, ARL13B in green and DAPI in blue. **F** shows the secondary only control used for FGFR2-4 proteins (**i**)**,** with ARL12B cilia marker (**ii**) and DAPI nuclear marker (**iii**). These are combined in **Fiv** – secondary only control for FGFR2-4 in red, ARL13B in green and DAPI in blue. In **iv** panels, scale bars=20µm and inset panels show higher magnification of a single cell (white and white dashed-line boxes).


FGFR1
ARL13B
DAPI
Ai
Aii
Aiii
FGFR1
ARL13B
DAPI
Aiv
20µm
FGFR2
ARL13B
DAPI
Bi
Bii
Biii
FGFR2
ARL13B
DAPI
Biv
20µm
FGFR3
ARL13B
DAPI
Ci
Cii
Ciii
FGFR3
ARL13B
DAPI
Civ
20µm
FGFR4
ARL13B
DAPI
Di
Dii
Diii
FGFR4
ARL13B
DAPI
Div
20µm
Secondary only control (FGFR1 AB)
ARL13B
DAPI
Ei
Eii
Eiii
Secondary only control (FGFR1 AB)
ARL13B
DAPI
Eiv
20µm
Secondary only control (FGFR2-4)
ARL13B
DAPI
Fi
Fii
Fiii
Secondary only control (FGFR2-4)
ARL13B
DAPI
Fiv
20µm

3.3 Discussion

Tanaka and colleagues proposed the existence of Nodal Vesicular Parcels (or NVPs) as a vehicle for the enrichment of signalling molecules to the left of the mouse embryonic node, and therefore the method by which L/R asymmetry is first established (Tanaka et al. 2005). A key piece of experimental evidence for this was obtained through their use of the lipophilic dye, DiI to label the lipid-membrane bounded NVPs, and visualise their transport from right to left in the node. However, there are wide anecdotal reports of DiI cytotoxicity, which led me to further scrutinise their methods and conclusions. Through replicating their DiI culture methods, and subsequently analysing the nodes of embryos using SEM, I provide evidence that the results of their DiI experiments may in fact be artificial. I detected gross cellular death, and abnormal node structure both in embryos cultured with DiI, and strikingly in mock treated controls. I propose the objects seen to be moving across the node, labelled by DiI are in fact pieces of cellular debris, that have blebbed off as cells of the embryo are dying. This would additionally explain the large variation in reported size (0.3-5.0 µm) of objects seen by Tanaka (Tanaka et al. 2005).

The presence of low quality node structure and the extensive cellular death in both DiI and mock-treated embryos supports that these phenotypes are most likely a result of the method of culture, and not the direct result of DiI treatment. As incubation of the embryos with DiI or vehicle control was carried out for 30 minutes at room temperature, temperature itself seems most likely to be the cause of the phenotype. Indeed, 1-2 hrs of embryo culture without this 30 minutes RT incubation resulted in very little cell death and a much more normal node structures. When plotted, the results for these embryos cluster with wild-type uncultured embryo scores, which supports my assertions. As normal *in utero* environmental temperature is 37°C, in seems most likely that these embryos are simply not equipped to survive at room temperature for this length of time. In order to definitively prove this, however, further experimentation where the 30 minutes incubation with DiI is

carried out at 37°C is necessary. While my data shows that the NVPs detected by Tanaka were almost certainly artefactual, it does not prove that NVPs do not exist. Indeed, there is evidence for cilia derived particles in different contexts, including in the kidney (Hogan et al. 2009).

Tanaka's analysis argues that FGF signalling functions to regulate NVP release. They showed a lack of normal L/R calcium asymmetry around the node in embryos following use of an FGF signalling inhibitor (SU5402). However, this calcium asymmetry has failed to be shown as an accurate, replicable indicator of a left-specific signal (Yoshiba et al. 2012). Additionally of note is the important relationship between calcium and cell death, with reported environmental damage leading to pathological calcium signals and apoptotic cellular death (Verkhratsky 2007).

Strikingly, when Tanaka analysed protein localisation of FGFR1-3 in the embryo, they showed ciliary localisation of all three FGFRs. However, they fail to give details of the antibodies used, and do not validate them in the manuscript, making it impossible to rule out cross-reactivity of the antibodies with other proteins. In order to analyse FGFR localisation in the mouse node I carefully chose antibodies which have been widely used and published with a good degree of specificity. In this analysis I detected ciliary localisation of FGFR2 protein in node cilia, and FGFR1, 3 and 4 in the cells of the node, although not the cilia. In contrast, WISH analysis of *Fgfr* gene expression revealed only very low level node specific expression. The underlying disconnect between these two data sets suggests that only a small amount of mRNA produced in the node leads to the protein production, or that the protein may be produced elsewhere. As high levels of *Fgfr1, 2* and *4* mRNA are present in the developing somites, it remains a formal possibility that this is the source of the protein production, which is subsequently translocated to the node. Another possibility is that the protein may have been produced in cells earlier during node formation, thus explaining why low gene expression is seen. Of note is that the antibodies used to show the presence of FGFR proteins, do not confirm the functional state of the

protein, and do not report on whether it has actively been signalled to by any of its corresponding ligands. Further analysis of all isoforms of all FGF receptors at the mRNA and protein levels may lead to a better understanding of FGF signalling in the context of L/R patterning.

As my analysis shows the presence of FGFR2 in cilia within the node, it might suggest that this is the most likely receptor to be involved in FGF signalling that affects L/R determination. However, the presence itself does not prove this functional capability, or the specific mechanism of function. In our analysis, we also find that there is not a clear, defined, expression pattern: instead, FGFR2 is present on some node cilia, but not all, and on some it appears to be punctate in its localisation, but uniform in others. If it is functioning as a receptor involved in L/R determination in the node, we also do not know if it is actively being signalled to.

Another consideration when examining the node cilia FGFR2 expression, is the possibility that this protein localisation may be an inherent characteristic of all cilia. The presence/absence of FGF receptors on cilia has not been widely reported, although such analysis would need to include the presence of cilia markers, and examination of cells under high magnification, which is not commonly the case unless the cilium is being specifically investigated. The presence of FGFR1 has been reported in the kinocilium in the developing inner ear (Honda et al. 2018), but otherwise is not widely reported or commented on. Due to this, we analysed expression of all the FGFRs in a number of cell lines that can produce cilia. In order for the widest data set, we did this in both ciliated (serum starved cells) and actively growing cell lines. My analysis showed that FGFR2 does not innately localise to cilia, and does not show cilia localisation in ciliated MEFs, NIH3T3 or RPE1 cell lines. FGFR2's localisation does however, vary between cell types and between growth states, but not in a consistent manner. Low levels of nuclear FGFR2 in ciliated MEFs are accompanied by higher levels in actively growing MEFs. Conversely, the opposite is true for RPE1 cells, and no FGFR2 is present in actively growing NIH3T3

cells, but is consistently strong in the nuclei of this cell type when serum-starved. As the amount of nuclear FGFR2 appears to change with the growth/starvation of these different cell types, it suggests that its status may be tied into the cell growth cycle. Alternatively, it could be that higher nuclear FGFR2 in ciliated RPE1 and NIH3T3 cell lines indicates a relationship with cilia growth, as nuclear FGFR localisation has been reported following receptor activation, to allow the protein to directly affect transcription (Yu et al. 2004). Of note is that the presence of extra-cellular FGFs varies between these data, as the serum present with the actively growing cells likely contains FGFs. However, as my data do not show a directionality in the changing nuclear FGFR2 levels in relations to the growth state of the cells, the effect of this may be negligible. Additionally of interest would be a correlation of species origin of the cells lines with the direction of changing protein levels, with RPE1 cells of human origin and MEFs and NIH3T3s both from mouse; there appears to be no such species specific link in FGFR2 levels in my data.

The localisation of FGFR1, similarly to FGFR2, revealed varying nuclear and endoplasmic reticulum (ER) levels across cell types and growth states. Again this variation showed no specific correlation coupled with the growth of the cells. Intriguingly, ER expression was evident in both mouse cell types (MEFs and NIH3T3s) and not in the human-derived RPE1 cells. This ER localisation could be due to recent production of the protein and preparation for transport, although the functional relevance of this, or its link to the cilium is not currently clear.

FGFR3 protein interestingly shows localisation to the cilia of RPE1 cells, but is not present at any discernible level in these cells when actively growing; nor is it present in NIH3T3 or MEFs. This could suggest a function as a receptor in cilia in human cells under some circumstances/in some environments. Indeed, FGFR3 mutations in humans cause specific dwarfisms achondroplasia (ACH) and thanatophoric dysplasia (TD) (Ornitz and Legeai-Mallet 2017; Rousseau et al. 1994; Shiang et al. 1994). The mechanism of function for the causation of these dwarfisms has been shown to be disrupted primary cilia function, with

consistently active FGFR3 leading to a shortening in the length of primary cilia in the cartilage growth plate, and FGFR inhibition rescuing the cilia length phenotype (Martin et al. 2018).

FGFR4 also shows localisation to the cilia of RPE1 cells, along with varying level plasma membrane localisation in all other cell types and growth states, except for serum starved MEFs. In *Xenopus*, FGFR4 has been suggested to have a role in L/R axis formation through specification of the amphibian LRO (Sempou et al. 2018). However, as the cell lineage differs between the mouse and the frog, there are likely to be many differences in terms of function. The low level *Fgfr4* mRNA in the mouse node, along with the FGFR4 protein presence, may indicate a role for FGFR4 in mouse L/R axis formation. Additionally, a possible role for FGFR4 in mammalian L/R patterning has been implied by analysis which found the presence of damaging *FGFR4* mutations in 3 human congenital heart disease (CHD) patients (Jin et al. 2017; Zaidi et al. 2013).

The presence or absence of the varying FGF receptor proteins in the cell lines however must be critically assessed as there are many fundamental differences between the primary cilia of cultured cell lines and the cilia of the mouse node. As the primary cilium in cells in used principally for signalling, my finding of cell signalling receptors FGFR3 and FGFR4 in the cilia is not altogether surprising. The lack of FGFR2 in the cilia of the cell types analysed provides important information, and suggests that FGFR2 is not inherently characteristic present in all cilia. Indeed, this may suggest the presence of FGFR2 in mouse node cilia has a functional importance, which might tie it to a role in L/R patterning. However, analysis of *Fgfr2* null mice does not show L/R patterning defects, which might suggest that this receptor is not involved in L/R determination, or that it can be compensated for by other FGFR action, as is indicated by functional redundancy in FGFRs (Poladia et al. 2006; Zhao et al. 2004). The presence of FGFR2 on cilia could be argued to be consistent with the cells being competent to respond to an active FGF ligand signalling. However, even though *Fgf8* has been implicated in L/R patterning and is

therefore the most likely ligand candidate in this context, it remains possible that another ligand or ligands are functionally important in terms of asymmetric signalling for L/R determination.

4.0 Investigating the role of FGF signalling in embryonic left-right axis development using embryo culture

4.1 Introduction

Analysis by Meyers and Martin shows that FGF signalling is required for L/R patterning (Meyers and Martin 1999), however the underlying mechanism remains uncertain. A number of hypotheses to explain this exist. *Fgf8* may regulate the length of the cilia within the node. Indeed, work in both zebrafish and *Xenopus* has shown a link between FGF receptor 1 (encoded by *fgfr1*), and cilia length: MO knockdowns of *fgfr1* in zebrafish, and dominant negative Fgfr1 expression in *Xenopus* lead to shortened cilia (Neugebauer et al. 2009). This decreased cilia length perturbs leftward fluid flow in the LRO, and thus affects L/R patterning. Knockdown of both *fgf8* and its functionally redundant counterpart *fgf24* in the zebrafish lead to similar reduced cilia lengths in the KV, and the authors propose that in the LRO these two ligands act through Fgfr1.

An alternate hypothesis, proposed by Oki, is that FGF signalling influences expression of genes upstream of *Nodal* thereby affecting L/R patterning (Oki et al. 2010). They provide evidence for disturbed *Tbx6* expression in embryos treated with a RAS/MAPK pathway inhibitor; RAS/MAPK is one of multiple pathways that act downstream of FGF signalling. *Tbx6* in turn is argued to enhance *Dll1* expression, which allows activation of *Nodal* expression by the NOTCH signalling cascade. This activates the *Nodal* node specific enhancer NDE, which is the element responsible for inducing *Nodal* in the node, and, when lost, leads to L/R patterning defects (Adachi et al. 1999; Norris and Robertson 1999). This model therefore proposes a signalling cascade downstream of FGF8 signalling, and the role for this in L/R determination being through FGF8-induced activation of the NDE *Nodal* enhancer. However, this explanation fails to elucidate the asymmetric expression of *Nodal* around the node, which is controlled by a different enhancer, the ASE, and thus cannot be explained by the *Tbx6-Dll1* cascade (Adachi et al. 1999; Norris and Robertson 1999; Oki

et al. 2010). Therefore, the question remains as to how *Fgf8* affects asymmetric *Nodal* expression at the node and thus impacts L/R determination.

Another hypothesis for the role of *Fgf8* in L/R patterning, suggested by Tanaka, is that it regulates the release of NVPs containing sonic hedgehog (SHH) and retinoic acid (RA) (Tanaka et al. 2005). This work showed that incubating embryos with the FGF signalling inhibitor SU5402 led to perturbation of both NVP release and asymmetric Ca^{2+} signalling at the node. They were able to rescue this by ectopic Indian hedgehog IHH, SHH and RA addition. Since publication of this paper the role of these 3 molecules in establishing L/R asymmetry in mouse has been reassessed, and their roles have been explained in other ways. IHH is highly expressed in the extraembryonic ectoderm of the yolk sac, which sits lateral to the LPM, but loss of IHH is not sufficient to influence L/R asymmetry, as the *Ihh* null mutant show no L/R defects (Tsiairis and McMahon 2009). Similarly, SHH's role in L/R axis formation is less direct than that proposed by Tanaka. Instead of being the L/R morphogen, it influences the L/R axis formation through a role in specifying the midline, which establishes an important barrier between left and right-sided signalling (Tsiairis and McMahon 2009). By limiting Hh signalling Tsiairis and McMahon showed it to only be required in the LPM, where it provides a permissive signal which is crucial to prepare the cells for the initiation of NODAL signalling. Similarly, the likelihood of RA being a L/R morphogen has been questioned following analysis showing a lack of asymmetry, or indeed presence, at the embryonic node (Sirbu and Duester 2006). Further investigation has established that RA influences L/R patterning by antagonising FGF8, rather than acting downstream to FGF8 as Tanaka suggests (Diez del Corral et al. 2003; Moreno and Kintner 2004; Tanaka et al. 2005). However, it is important to remember that while the signalling molecules Tanaka proposes do not lie downstream of NVP release as suggested, this does not in itself preclude FGF8 playing a role in regulating the release of NVPs. Indeed, failure to correctly release NVPs could explain the aberrant *Nodal* signalling and L/R defects that Meyers and Martin describe in their *Fgf8* mutants (Meyers and Martin

1999). Similarly, so could the failure of correct cilia length regulation, which could affect the ability of motile nodal cilia to create leftward flow, or of the immotile crown cilia's ability to respond to flow.

Another possibility that must be considered is FGF signalling having a role of the formation of the node itself. Close examination of Meyers and Martins' published data reveals the possibility of an incorrectly formed node. In their mutant it is possible that the pattern of *Nodal* expression is incorrect, or alternatively that the crown cells which usually express *Nodal* have not been formed correctly. In this study the pattern of *Nodal* expression is visualised using the $Nodal^{LacZ}$ allele, and as such these embryos carry only one functional copy of *Nodal*; *Nodal* itself is required to produce a correctly patterned node (Norris et al. 2002) and a number of loci have been revealed to exhibit synthetic phenotypes when doubly heterozygous with *Nodal* (Collignon et al. 1996; Constam et al. 1996; Mavrakis et al. 2007). In addition to these observations, recent research provides evidence for *Fgf8* playing a role in the formation of the *Xenopus* LRO (Schneider et al. 2019). This paper showed FGF signalling to be required to induce somitic cells to become LRO crown cells. However, differences in cell lineage and fate between frog and mouse mean that mouse LRO crown cells originate from a different lineage. This suggests that there may be a difference in genetic control between these two, and therefore a different mechanism at play.

To assess these potential mechanisms by which *Fgf8* signalling may be influencing L/R axis formation I have utilised FGF signalling inhibitors to influence development in an embryonic culture system. The SU5402 inhibitor has been used extensively by others, including by Tanaka (Oki et al. 2010; Tanaka et al. 2005). However, a perpetual worry with the use of pharmacological inhibitors is their specificity. While SU5402 is stated to be specific for FGFR1, analysis reveals it does in fact have activity against the other FGF receptors also, along with VEGFR-2 and PDGFRβ (Sun et al. 1999a). It is however reported to show strong preferential inhibition of FGFR1 compared to the other FGFRs.

Due to its historical use in many studies I included this in my analysis. To provide a more complete picture I also used AZD4547 (a strong inhibitor of FGFRs1-3), and the pan-FGFR inhibitor BGJ398, which exhibits high inhibition of FGFRs1-3, and lower inhibition for FGFR4. Importantly BGJ398 has no reported off-target effects. While ideally, I would use inhibitors specific to each individual FGFR, no such compounds have been characterised, perhaps due to similarities between the FGFRs. The use of embryo culture with inhibitors allows me to assess the role of FGF signalling during specific time windows in the establishment of the L/R axis. Furthermore, this allows investigation of the different hypotheses of how FGF8 functions in L/R determination: influencing cilia length, node formation or NVP release.

4.2 Results

A note about staging

FGF signalling is known to be important in the process of somitogenesis, and counting of somite pairs is one of the most common ways in which the developmental stage of an embryo is assessed. As the use of inhibitors of FGF signalling could perturb somite development, the somite count may be an unreliable method of staging. Therefore, to limit inaccuracy due to this affect, I staged embryos according to general morphology including the shape of the developing headfolds, rather than relying solely on somite number. Notation throughout will refer to somite stage (ss) for ease of use, although this is in fact somite stage as perceived by assessment of size, shape and headfold shape.

4.2.1 Static culture

Embryonic culture can be carried out using a number of approaches. The simplest method is “static culture” in which embryos are placed in a static lidded receptacle that is not

airtight, in an incubator at 37°C, 5% CO_2. This method does not need any specialised equipment, and therefore I first focussed on using static culture (**Methods 2.5.5**). I harvested embryos aged between 7.5-8.5dpc (days *post coitum*) from the maternal uterus in pre-warmed (37°C) medium, to limit shock. I placed individual embryos into a single well in an 8-well chambered slide. Embryos were cultured either with DMSO (vehicle control), SU5402, AZD5402 or BGJ398 compounds (dissolved in DMSO) for a period of 6-8 hrs.

Asymmetric gene expression

In order to assess the impact of FGF inhibition on L/R patterning I analysed the expression pattern of key asymmetric markers using WISH (**Figure 4.2.1**).

Nodal is usually asymmetrically expressed around the node from the 1 somite stage (1ss), with stronger expression on the left edge of the node (R<L). Embryos cultured with control, AZD4547 and SU5402 that were between this stage and the 3ss were analysed for gene expression (**Figure 4.2.1 C**). Approximately half of embryos cultured with either of these compounds, or with the control medium showed the expected asymmetric, R<L expression of *Nodal*, as shown (**Figure 4.2.1 C**) (5/10 control, 4/7 SU5402, 2/5 AZD4547). The remaining embryos (5/10 control, 3/7 SU5402, 3/5 AZD4547) showed symmetric R=L *Nodal* expression (**Figure 4.2.1 C**).

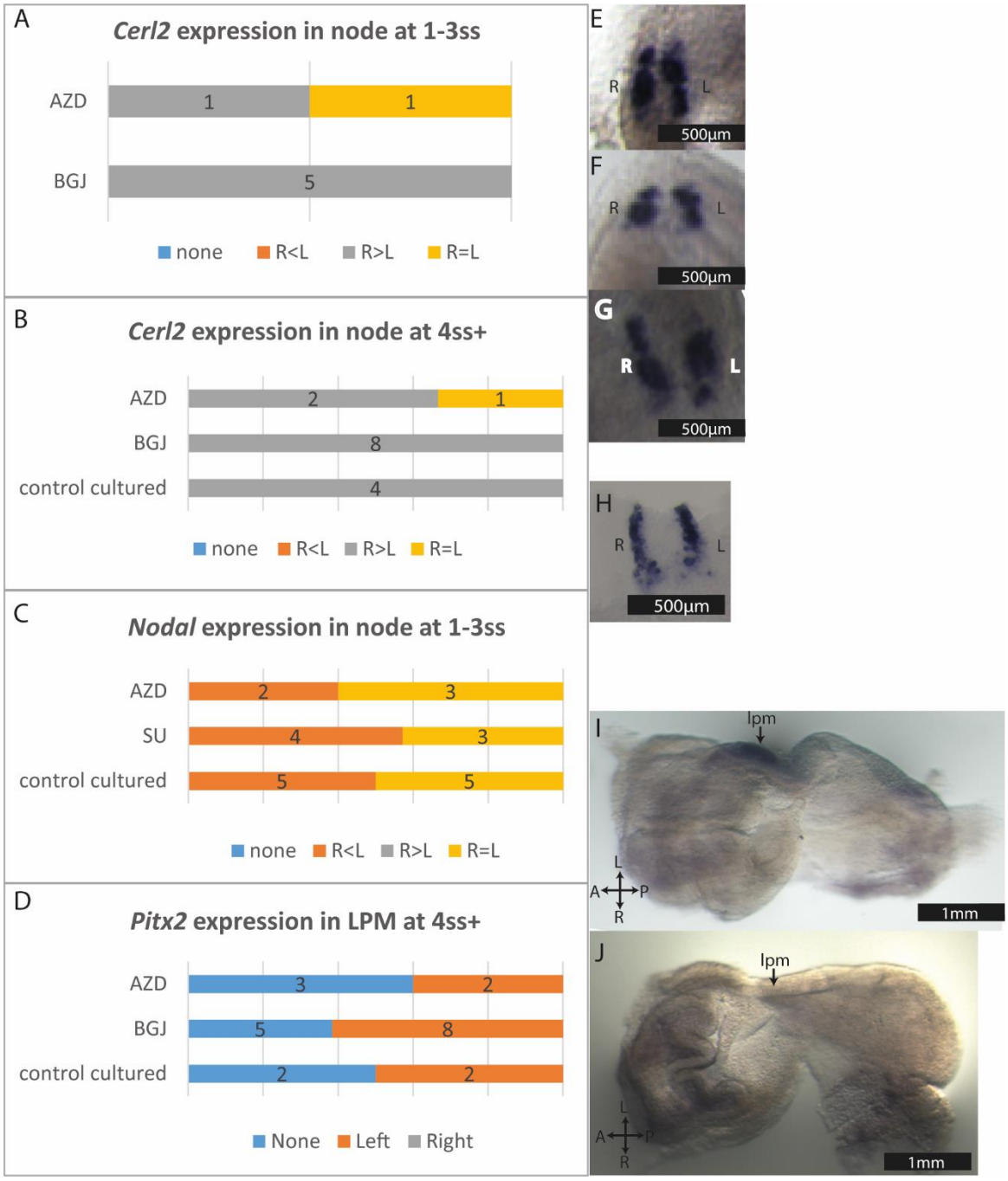
Cerl2 is the first gene to show asymmetry at the node, showing R>L asymmetry around the node from the late-headfold (LHF) stage onwards . Embryos were cultured with control, BGJ and AZD containing medium as indicated (**Figure 4.2.1 A** and **B**). Embryos were split by development stage following culture (1-3ss in **Figure 4.2.1 A** and 4ss+ in **B**). Analysis shows that the 4 control cultured embryos (all in the 4ss grouping – **Figure 4.2.1 B**) showed the expected R>L expression. Similarly, in BGJ-containing medium, 5 embryos at the 1-3ss and 8 at the 4ss+ (**Figure 4.2.1 A** and **B** respectively) showed expected R>L *Cerl2* asymmetry. For AZD cultured embryos between 1-3ss following culture, 1 embryo showed the expected *Cerl2* R>L asymmetry, while 1 other showed R=L symmetry (**Figure**

4.2.1 A). In the 4ss+ group, 2 AZD cultured embryos showed R>L asymmetry, and 1 R=L *Cerl2* expression (**Figure 4.2.1 B**).

Following *Nodal* asymmetry, *Pitx2* is induced in the left lateral plate mesoderm (LPM) from the 4ss. I assessed the sidedness of LPM *Pitx2* expression (**Figure 4.2.1 D**). In control cultured embryos, 2 embryos at the 4ss+ failed to show LPM expression of *Pitx2*, and 2 showed the expected left-LPM (L-LPM) expression (**Figure 4.2.1 D**). In BGJ cultured embryos, 5 showed no LPM *Pitx2* and 8 showed L-LPM *Pitx2*. For AZD cultured embryos, 3/5 showed no LPM *Pitx2*, and the remaining 2/5 showed the L-LPM expression (**Figure 4.2.1 D**).

It appears overall that there is some delay of L/R patterning, as roughly half the embryos cultured in all media showed a lack of asymmetric *Nodal* node expression and a failure of timely *Pitx2* L-LPM expression. As there were no differences between the vehicle control and experimental samples, it seems unlikely that this delay is due to the effect of any of the inhibitors, and is more likely a general result of this culture.

Figure 4.2.1: Gene expression in cultured embryos. Embryos were cultured with indicated inhibitors or control cultured with vehicle (DMSO). **A** shows *Cerl2* expression in the node of embryos cultured to between the 1-3 somite stages, indicated as symmetric R=L expression (yellow), or expected asymmetric pattern of R>L expression (grey), no embryos showed a lack of *Cerl2* expression (blue) or R<L asymmetric expression (orange). For AZD cultured embryos within this group, 1 each showed R=L (yellow) and R>L (grey) (**E**)**.** For BGJ cultured embryos within this group, all 5 showed R>L asymmetric *Cerl2* expression (grey). **B** shows *Cerl2* expression in the node of embryos cultured to the 4 somite stage onwards, indicated as symmetric R=L expression (yellow) (**F**)**,** or expected asymmetric pattern of R>L expression (grey) (**G**)**.** Of the AZD cultured embryos in this group, 1 showed R=L *Cerl2* node expression (yellow), and 2 showed R>L asymmetric *Cerl2* node expression (grey). All 8 BGJ cultured embryos showed R>L asymmetry (grey), as did all 4 control cultured embryos. No embryos showed no *Cerl2* node expression (blue) or R<L asymmetric expression (orange). **C** shows *Nodal* expression in the node of embryos cultured to between the 1-3 somite stages. AZD cultured embryos showed R<L asymmetry in 2/5 embryos (orange) (**H**), and R=L symmetry in 3/5 (yellow). SU cultured embryos showed R<L asymmetry in 4/7 embryos (orange), and R=L symmetry in 3/7 (yellow). Control cultured embryos showed R<L asymmetry in 5/10 embryos (orange), and R=L symmetry in 5/10 (yellow). No embryos showed no expression of *Nodal* in the node (blue), or R>L asymmetric expression (grey). **D** shows *Pitx2* expression in the Lateral Plate Mesoderm (LPM) of embryos cultured to the 4 somite stage onwards, indicated as present in neither LPMs (blue), or present in the left (orange) or right (grey) only. AZD cultured embryos showed no *Pitx2* LPM expression in 3/5 samples, and left-LPM (LLPM) expression in 2/5. BGJ cultured embryos showed no expression of *Pitx2* in 5/13 embryos, and LLPM expression in 8/13 (**I**). Control cultured embryos had no LPM *Pitx2* in 2/4 embryos (**J**), and left only expression in the remaining 2. In images **E-J,** scale bars are indicated (500µm in **E-H** and 1mm in **I-J**) along with right (R) and left (L) axes for all, and additionally anterior (A) and posterior (P) axes for **I-J**. Lateral plate mesoderm (lpm) is indicated in **I** and **J** also (note *Pitx2* expression in **I** lpm, absence in **J** lpm).


A
Cerl2 expression in node at 1-3ss
AZD
BGJ
1
1
5
none
R<L
R>L
R=L
B
Cerl2 expression in node at 4ss+
AZD
BGJ
control cultured
2
1
8
4
none
R<L
R>L
R=L
C
Nodal expression in node at 1-3ss
AZD
SU
control cultured
2
3
4
3
5
5
none
R<L
R>L
R=L
D
Pitx2 expression in LPM at 4ss+
AZD
BGJ
control cultured
3
2
5
8
2
2
None
Left
Right
E
R
L
500µm
F
R
L
500µm
G
R
L
500µm
H
R
L
500µm
I
lpm
L
A
P
R
1mm
J
lpm
L
A
P
R
1mm

Assessing embryo morphology

Using SEM I also looked at the embryo morphology, particularly in order to assess the development of the node. The wildtype node shows a characteristic teardrop shaped pit surrounded by crown cells (as shown in **Figure 1.4**) and this was evident in uncultured embryos (**Figure 4.2.2 A-C**).

In embryos cultured for 8 hrs in vehicle control (DMSO-containing) medium, we saw maintenance of the characteristic node shape and structure (**Figure 4.2.2 D**). When culture time was increased up to 24 hrs, instead of the normal node structure we saw a more “closed” node with a reduced node size and abnormal crown cell appearance (**Figure 4.2.2 E** and **F**), though not in all cases (**Figure 4.2.2 G**). When looking at embryos cultured for 8 hrs with inhibitors of FGF signalling (**Figure 4.2.3**), I saw similar (**Figure 4.2.3 A, C, F**), and more severe (**Figure 4.2.3 B, D, E**), “closed” nodes.

The presence of these abnormal “closed” nodes in control cultured embryos, when using the static culture method raised concerns about the impact of culture itself on embryonic development, and I therefore chose to change approach to the use of specialised rolling-bottle culture apparatus (**Methods 2.5.6**). This provides a continuous gas flow of 5% CO_2 and increased movement of embryos within the culture medium, providing improved delivery of nutrients.

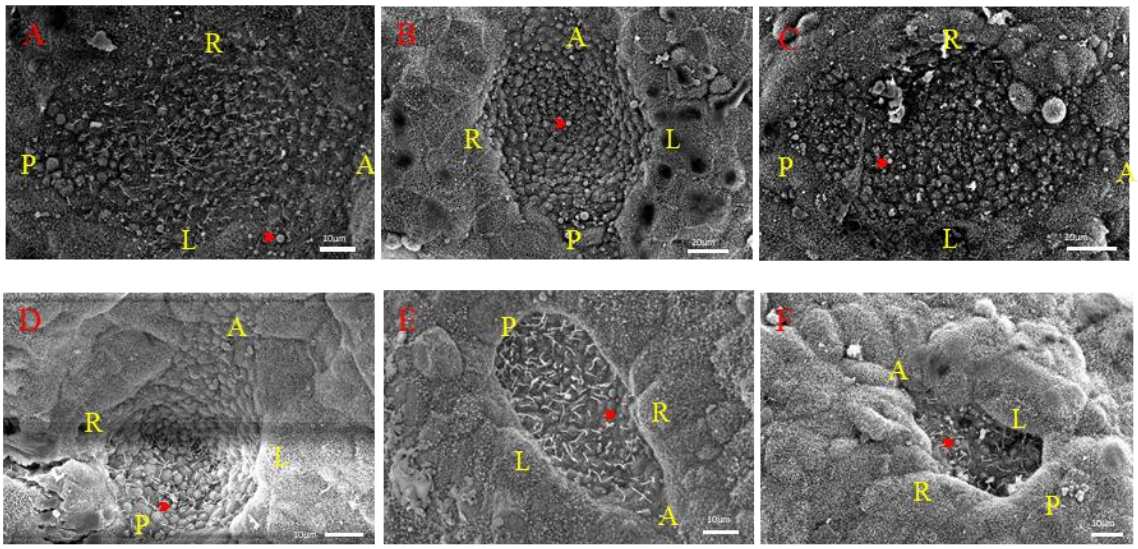


Figure 4.2.2: SEM images of cultured and uncultured nodes. A, **B** and **C** all show the nodes of uncultured mouse embryos. **D**, **E**, **F** and **G** shows the nodes of embryos cultured in control medium. **D** was cultured for 8hrs from LHF-1s. **E** was cultured for 26hrs from pHF-2/3s. **F** was cultured from 1s-5/6s for 24hrs. **G** was cultured from LB-1/2s for 24hrs. Indication of anterior (A), posterior (P), left (L) and right (R) orientation of the node in respect to the whole embryo is given. Scale bars in **A**, **D**-**G** = 10 µm. Scale bars in **B** & **C** = 20 µm. In all, red arrows indicate putative nodal vesicles.

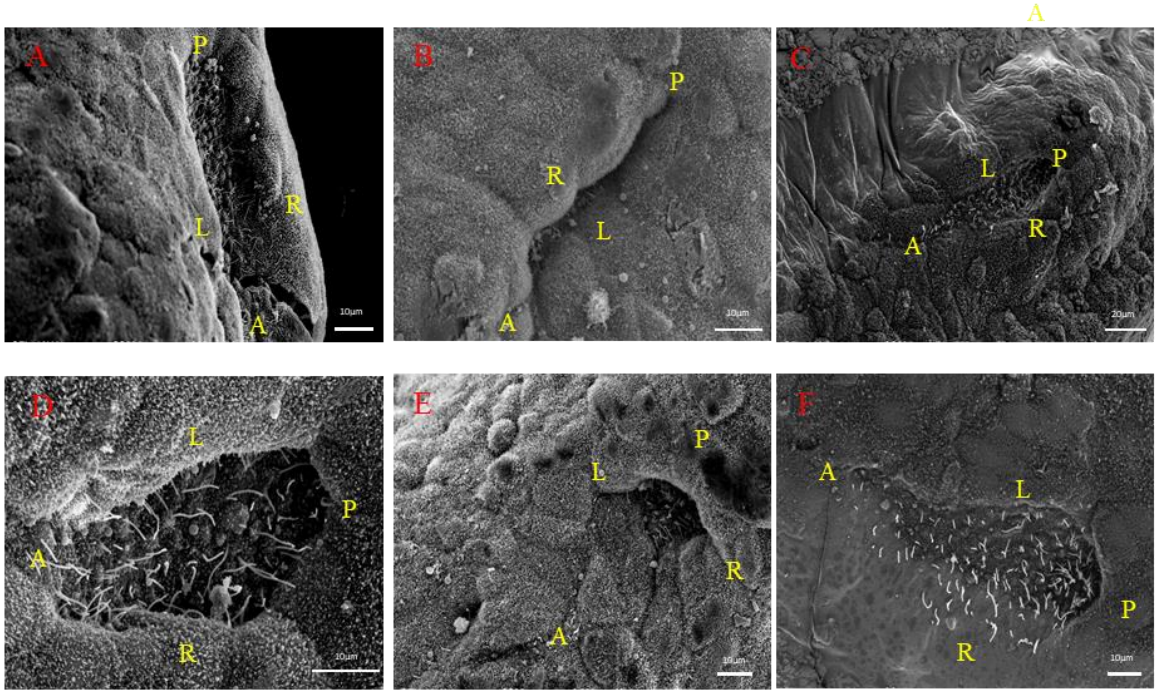
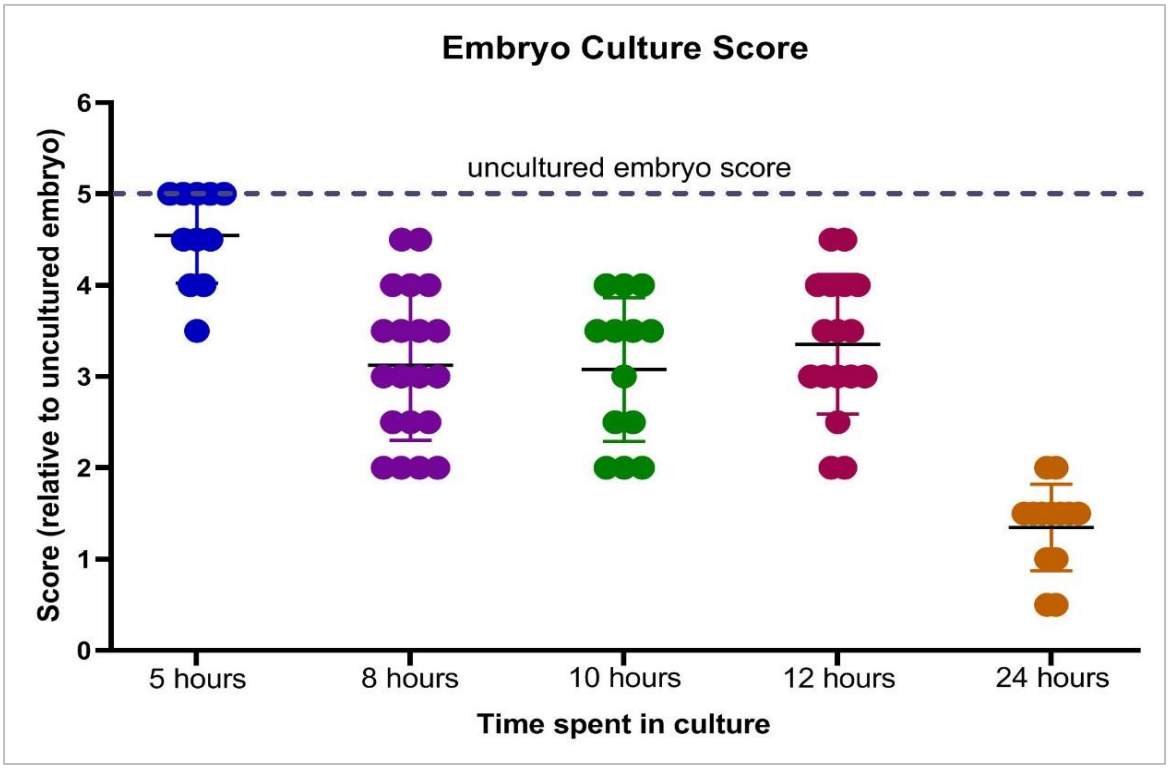


Figure 4.2.3: SEM images of nodes from embryos cultured with SU5402. A shows the node of an embryo cultured from 3s–4s for 24hrs. Scale bar = 10µm. **B** shows the node of an embryo cultured from LB–3s over 24hrs. Scale bar = 10µm. **C** shows the node of an embryo cultured from EHF–2s for 26hrs. Scale bar = 20µm. **D** shows the node of an embryo cultured from EHF–4s for 24hrs. Scale bar = 10µm. **E** shows the node of an embryo cultured from 1s–4s for 24hrs. Scale bar = 10µm. **F** shows the node of an embryo cultured from EB–2s for 24hrs. Scale bar = 10µm.

4.2.2 Rolling Bottle Culture

In order to test the process of rolling bottle embryo culture, I collected WT embryos aged between 7.5-8.5dpc and cultured them for periods of 5 to 24 hours. I then scored embryos relative to uncultured control embryos, assessing their embryology and morphology with respect to the appropriate stage of development (**Figure 4.2.4**).

Embryos cultured for up to 12 hrs were seen to have an appropriate score following culture (average 3.0 and higher deemed appropriate for culture (**Figure 4.2.4**)). Embryos cultured for 24 hrs, however, showed unacceptable scores following culture (average less than 3.0 (**Figure 4.2.4**), and statistical analysis (Wilcoxon Rank Sum test, $P<.001$ when compared with all other groups). This led me to decide to examine embryos cultured for up to 12 hours. Most embryo culture experiments were carried out for the full 12 hrs, in order to maximise embryo development. This is specifically important as an original delay of normal development when embryos are placed into culture is generally seen. In addition, maximising culture time also allowed for earlier stage embryos to progress from prior to the formation of the node to a stage where node gene asymmetries are expected to be seen, and node morphology can be assessed.



Score	Definition
5.0	Indistinguishable from uncultured embryos
4.5	Small delay in development
4.0	Slight delay in development
3.5	Delayed development
3.0	Pronounced delay in development
2.5	Very delayed/possibly atypical development
2.0	Atypical development
1.5	Embryo is abnormal
1.0	Embryo looks very abnormal
0.5	Embryo is close to death

Figure 4.2.4: Embryo culture score. Embryos were scored for morphology post-culture over the time periods indicated. The scoring system is defined in the table. For a 5 hour culture time embryos scored between 3.5 (1 embryo) to 5.0. For an 8 hour culture period embryos scored between 2.0 and 4.5. Embryos cultured for 10 hours scored between 2.0 and 4.0. Embryos cultured for 12 hours scored between 2.0 and 4.5. Embryos cultured for 24hrs scored between 0.5 and 2.0. Statistical analysis (Wilcoxon Rank Sum Test) showed significant differences between the following groups: 5 hours and 8 hours (*P<.001*), 5 hours and 10 hours (*P<.001*), 5 hours and 12 hours (*P<.001*), 5 hours and 24 hours (*P<.001*), 8 hours and 24 hours (*P<.001*), 10 hours and 24 hours (*P<.001*), 12 hours and 24 hours (*P<.001*).
As the embryos were cultured in batches, and embryos were scored individually, there were concerns about the time it would take to image individual embryos (including transport from dissection microscope to imaging microscope), and the possible deterioration of the condition of embryos yet to be scored. Due to this, there are no corresponding images for this data set.

Assessing development

Rolling bottle cultured embryos were assessed for developmental stage prior to and following culture, to address the impact of FGF inhibitors on embryonic development (**Figure 4.2.5**). 69 control (DMSO vehicle) cultured embryos which entered culture at streak-bud stage were assessed (**Figure 4.2.5 A**), 22 embryos failed to develop past the bud stage (blue- S/B-S/B). 23 developed to the head-fold stages (orange- S/B-HFs), 8 to the 0-1ss (grey- S/B-0/1SS) and 16 to the 2/3ss (yellow- S/B-2/3SS). Of 44 streak/bud stage embryos cultured with SU5402, 19 progressed no further than the bud stage (blue- S/B-S/B), 13 developed to the head-fold stages (orange- S/B-HFs), 3 to the 0/1ss (grey- S/B-0/1SS) and 9 at the 2/3ss (yellow- S/B-2/3SS) (**Figure 4.2.5 A**). 17/42 bud/streak embryos cultured with BGJ398 failed to progress past the bud stage (blue- S/B-S/B), whereas 6 developed to the head-fold stages (orange- S/B-HFs), 9 to the 0/1ss (grey- S/B-0/1SS) and 10 to 2/3ss (yellow- S/B-2/3SS) (**Figure 4.2.5 A**). 48 bud/steak embryos were cultured with AZD4547, 9 of which failed to progress past bud stage (blue- S/B-S/B); 18 progressed to the head-fold stages (orange- S/B-HFs), 14 to 0/1ss (grey- S/B-0/1SS) and 7 to 2/3ss (yellow- S/B-2/3SS) (**Figure 4.2.5 A**). Generally, for embryos entering culture at the streak-bud stages, similar proportions were seen to develop to each stage, although AZD shows a lower proportion (~20%) of embryos that failed to progress (blue) than both the other inhibitors (both ~40%) and control medium (~30%). Conversely, proportionally fewer embryos have progressed to the HF stages (orange) in BGJ containing medium (~15%) than for the other inhibitor and control cultured embryos (~30-40%). Less than 10% of embryos progressed to the 0/1ss (grey) for both control and SU cultured streak/bud embryos, but ~20% in AZD and BGJ containing medium. Similar proportions (~20%) of embryos for all culture conditions progressed to the 2-3ss (yellow).

Of 20 embryos which entered the control culture medium at the head-folds stages, 15 progressed to the 2/3ss (blue- HFs-2/3SS) and 5 to the 4/5ss (orange- HFs- 4/5SS)

(**Figure 4.2.5 B**). SU5402 cultured head-fold stage embryos all developed to the 2/3ss (8/8) (blue- HFs-2/3SS) (**Figure 4.2.5 B**). Of 11 head-fold stage embryos cultured in BGJ398, 10 progressed to the 2/3ss (blue- HFs-2/3SS) and 1 to the 4/5ss (orange- HFs-4/5SS) (**Figure 4.2.5 B**). For head-fold stage embryos cultured in AZD4547 8/10 progressed to 2/3ss (blue- HFs-2/3SS) and the remaining 2 to the 4/5ss (orange- HFs-4/5SS) (**Figure 4.2.5 B**). There appears to be marginally greater progression of headfold stage embryos in the control medium (orange >25%) in comparison to the inhibitor cultured embryos of the same stages (20% for AZD, <10% for BGJ and 0 for SU).

Similar effects were evident for embryos that were 1ss prior to culture and progressed to the 3ss were as follows for each of the mediums (**Figure 4.2.5 C**): 3 control, 12 SU, 2 BGJ and 7 AZD (blue).

For embryos between 1-3ss prior to culture, for control medium 22/29 developed to the 4/5ss (orange), and the remaining 7 to the 6+ss (grey) (**Figure 4.2.5 C**). For the SU5402 cultured embryos, 11 progressed to the 4/5ss (orange) and 2 to the 6+ss (grey); for BGJ cultured embryos 12 progressed from 1-3ss to 4/5ss (orange), and 1 to 6+ss (grey); and for AZD4547 there were 4 which developed from 1-3ss to 4/5ss (orange), and 2 to 6+ss (grey) (**Figure 4.2.5 C**). For these embryos at the 1-3ss prior to culture, a higher proportion developing to the 6ss and beyond in control medium (grey) compared to those which developed to the 4/5ss (orange).

Overall, a general trend for slightly delayed development in embryos cultured with inhibitors in comparison to vehicle control cultured is evident (**Figure 4.2.5**), however this is not statistically significant (Wilcoxon Rank Sum Test), except in the case of embryos put into culture at S/B stage with the SU5402 inhibitor when compared to those in control medium. An effect of culture on delaying development is not surprising due to the wide role FGF signalling has in development.

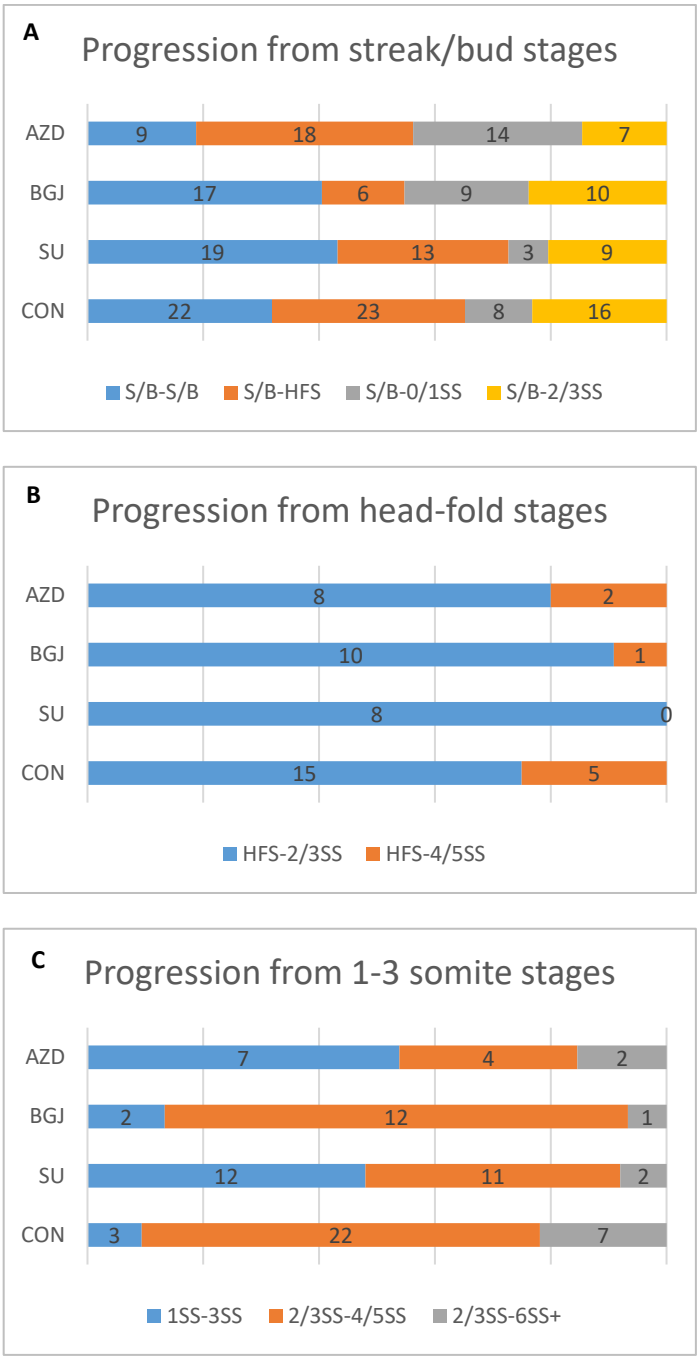


Figure 4.2.5: Progression of embryos in culture. Embryos were scored before and after culture with inhibitor compounds (AZD, BGJ, SU) or control DMSO vehicle (CON). Scale increments along x-axis=20% total. **A** embryos at the streak-bud stages prior to introduction to culture, scored as S/B (streak/bud) either to streak/bud stages (S/B-S/B [yellow]), headfold stages (S/B-HFs [orange]), 0-1 somite stages (S/B-0/1SS [grey]), or 2/3 somite stages (S/B-2/3SS [yellow])**. B** embryos at the headfold stages prior to introduction to culture, scored as HFs either to 2-3 somite stages (HFs-2/3SS [blue]), or 4/5 somite stages (HFs-4/5SS [orange]).
C embryos at the 1-3 somite stages prior to introduction to culture, scored as 1 somite stage to the 3 somite stage (1SS-3SS [blue]) or from the 2/3 somite stage to the 4-5 somite stages (2/3SS-4/5SS [orange]) or to the 6 somite stage onwards (2/3SS-6SS+ [grey]).
Numbers over each colour section show the numbers of embryos in the corresponding category. Statistical analysis (Wilcoxon Rank Sum Test) showed no significant difference for all treated vs control groups at each set of developmental stages, except for one incidence where the development of SU treated and control cultured embryos when put into culture at the S/B stage were significantly different to each other (*P=.003*). Embryos included here went on for analysis by Scanning Electron Microscopy or Wholemount In Situ Hybridisation (see Appendix Table A5).

Category	Definition	Abbreviation
A	streak/bud stage - streak/bud stage	S/B-S/B
B	streak/bud stage - head-folds stage	S/B-HFS
C	streak/bud stage - 0/1 somite stage	S/B-0/1SS
D	streak/bud stage - 2/3 somite stage	S/B-2/3SS
E	head-folds stage - 2/3 somite stage	HFS-2/3SS
F	head-folds stage - 4/5 somite stage	HFS-4/5SS
G	1 somite stage - 3 somite stage	1SS-3SS
H	2/3 somite stage - 4/5 somite stage	2/3SS-4/5SS
I	2/3 somite stage - 6+ somite stage	2/3SS-6SS+
J	4/5 somite stage - 6+ somite stage	4/5SS-6SS+

Table 4.2.1: Category definitions for embryo culture progress. Category is indicated by a letter A-J, which is defined by the stage of the embryo prior to and following culture. Corresponding abbreviations are noted.

Assessing NVPs and cilia length

Next I investigated the numbers of spherical vesicular objects in the nodes of cultured embryos, annotated as NVPs by Tanaka, using Scanning Electron Microscopy (SEM). This allowed me to assess if there was an effect of FGF inhibition on the numbers of putative NVPs produced, as Tanaka proposed that FGF8 regulates NVP release in the node.

WT uncultured control nodes were assessed (**Figure 4.2.6 A**), along with those of control and inhibitor cultured embryos (**Figure 4.2.6 A** and **B**). Strikingly, a large reduction in number of NVPs was evident in cultured embryo nodes in comparison to uncultured (**Figure 4.2.6 A**). When looking at total NVP counts for just cultured embryos (**Figure 4.2.6 B**), we see a wide variation in the numbers for each culture condition, although it appears there are generally less NVPs in embryos cultured with AZD4547. The data was then further split according to the developmental progression categories outlined in **Table 4.2.1**. This allowed data to be compared by the developmental stage prior and post-culture (**Figure 4.2.6 C**). However, accounting for the staging of embryos did not provide

additional clarity, as it appears that NVP number is variable across culture conditions and developmental stages, with no overt trends (**Figure 4.2.6 C**).

Similarly, I assessed the length of cilia within the node for embryos in the different culture conditions (**Figure 4.2.7**). When looking at these values for all developmental stages, it appears that the cilia are slightly shorter in SU, BGJ and AZD cultured embryos compared to control cultured ones (**Figure 4.2.7 A**), consistent with FGF signalling influencing cilia length. By splitting the embryos by stage (according to **Table 4.2.1** categories), there is not any clear correlation between developmental stage and the presence of inhibitor in culture (**Figure 4.2.7 C**). I further split the measurements by the categories outlined in **Table 4.2.1**, and plotted individual cilia length measurements (**Figure 4.2.7 D-H**). When looked at in this way, statistical analysis is also possible, though this revealed only one statistical difference, between group G SU and AZD cultured embryos (indicated by *** P value <.001). As only 1 embryo for the appropriate control-cultured category exists, this analysis cannot include the corresponding control-cultured measurements (**Figure 4.2.7 E**). It is possible that grouping the data of NVP numbers and cilia length measurements purely by stage the embryo was at pre- or post-culture, that different statistical analyses and conclusions may be drawn, however.

Figure 4.2.6: Number of NVP-like objects within nodes. A shows the numbers of spherical objects (designated NVPs) between 0.3-4.0µm in diameter that present in nodes for uncultured control embryos (black outlined circles), cultured control (green circles), and inhibitor-cultured SU (orange squares), BGJ (blue triangles) and AZD (purple diamonds) embryos. **B** shows the same data points as **A**, but with the uncultured control embryo data removed, to allow easier visualisation of data for cultured embryos, and increased scale of y axis. Statistical analysis (one-way ANOVA test) was carried out, and is indicated (*, **) where difference is significant (between cultured control and SU * *P*=.01; between cultured control and AZD ** *P*=.003). **C** shows the numbers of NVPs counted in the different culture mediums and the corresponding group categories of these embryos, respective to the stage prior and post-culture, as designated in **Table 4.2.1**. **D-G** show example images where NVPs were counted from. Each putative vesicle is marked by an orange dot and number. Scale bars = 10µm. anterior (A), posterior (P), left (L) and right (R) axes are indicated. **D** = 29 vesicles, embryo cultured with BGJ medium, group H. **E** = 38 vesicles, embryo cultured with control medium, group H. **F** = 79 vesicles, embryo cultured with AZD medium, group H. **G** = 125 vesicles, embryo cultured with SU medium, group H.

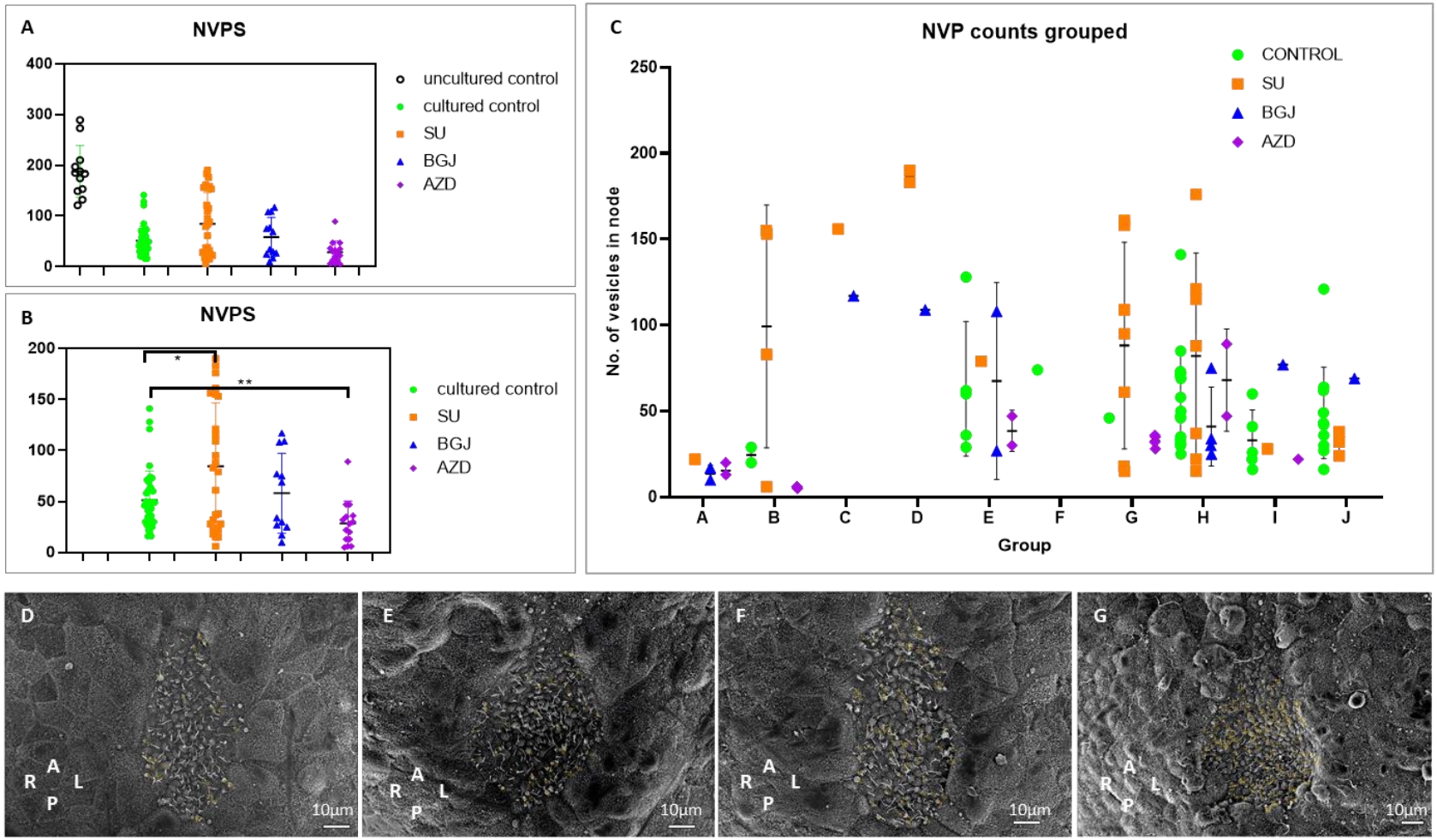
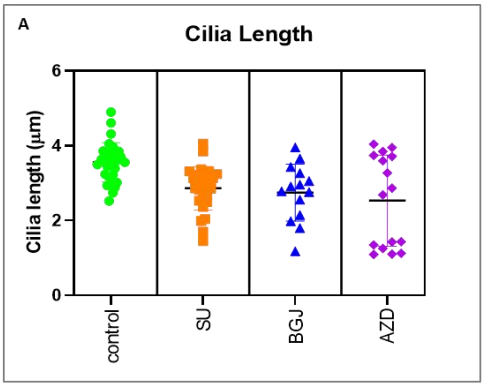
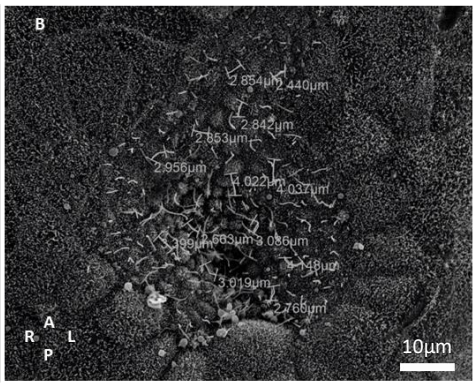
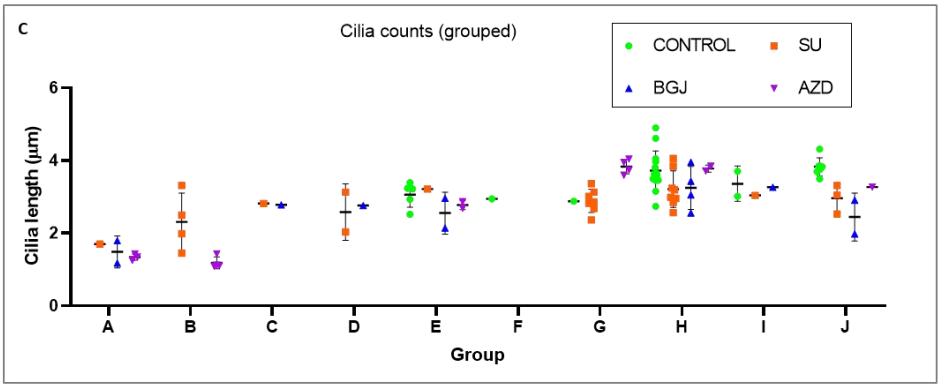
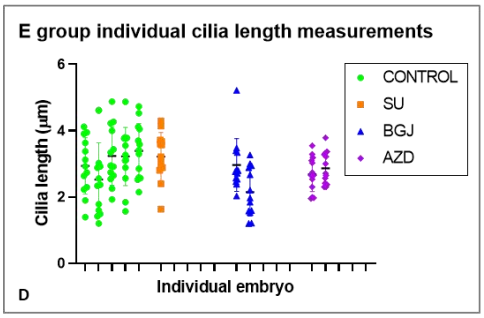

A
NVPS
400
300
200
100
0
uncultured control
cultured control
SU
BGJ
AZD
B
NVPS
200
150
100
50
0
*
**
cultured control
SU
BGJ
AZD
C
NVP counts grouped
CONTROL
SU
BGJ
AZD
No. of vesicles in node
250
200
150
100
50
0
A
B
C
D
E
F
G
H
I
J
Group
D
E
F
G
R
A
L
P
10µm

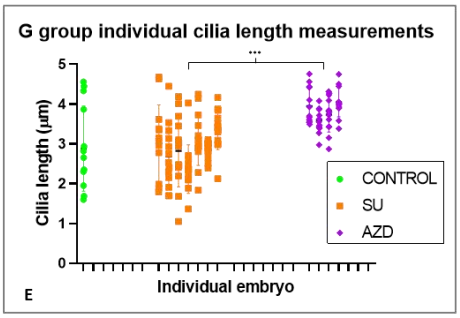
Figure 4.2.7: Cilia lengths in cultured embryos. A-B points indicating cilia length are averaged from 13 cilia within the node of each embryo. **A** shows these collectively for each of the categories of control (green circles), SU (orange squares), BGJ (blue triangles) and AZD (purple diamonds) cultured embryos. **B** shows an example image indicating cilia length measurements super-imposed onto SEM image of a node. Scale bar = 10μm, anterior (A), posterior (P), left (L) and right (R) axes are indicated. **C** shows the same values as in **A** but plotted corresponding to categories outlined in **Table 4.2.1** respective to culture stage before and after culture period. **D-H** shows grouped values from **C** split into the groups (where appropriate controls are present). Individual embryos have 13 cilia measured, and plotted. **D** shows group E embryos, with 5 control-cultured, 1 SU cultured, 2 BGJ cultured and 2 AZD cultured embryos. **E** shows group G embryos, with 1 control-cultured, 7 SU cultured and 4 AZD cultured embryos (one-way ANOVA test shows significant difference between these two groups *** $P<.001$). **F** shows group H embryos, with 14 control-cultured, 8 SU cultured, 5 BGJ cultured and 2 AZD cultured embryos. **G** shows group I embryos, with 2 control-cultured, 1 SU cultured and 1 BGJ cultured embryo. **H** shows group J embryos, with 5 control-cultured, 3 SU cultured, 2 BGJ cultured and 1 AZD cultured embryo.

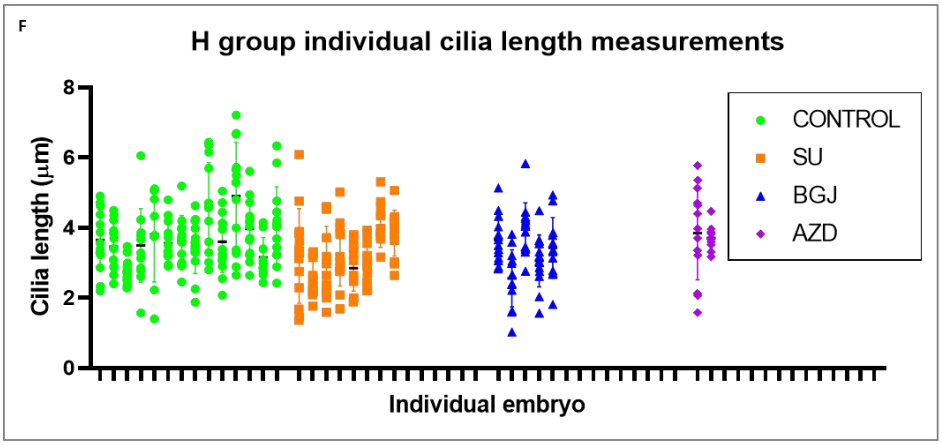

A
Cilia Length
Cilia length (µm)
0
2
4
6
control
SU
BGJ
AZD

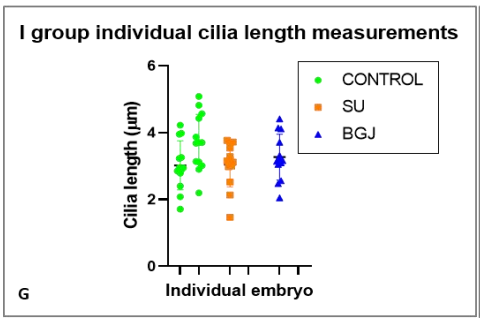

B
2.854µm
2.440µm
2.842µm
2.853µm
2.956µm
3.022µm
3.037µm
2.603µm
3.086µm
3.019µm
2.766µm
A
R
L
P
10µm

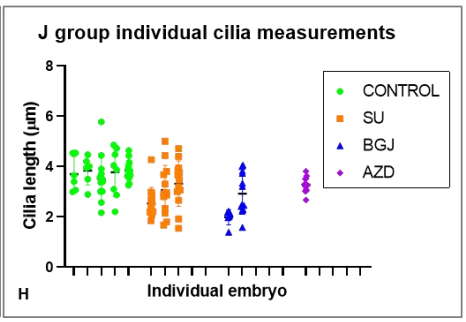

C
Cilia counts (grouped)
CONTROL
SU
BGJ
AZD
Cilia length (µm)
0
2
4
6
A
B
C
D
E
F
G
H
I
J
Group


E group individual cilia length measurements
Cilia length (µm)
0
2
4
6
CONTROL
SU
BGJ
AZD
Individual embryo
D


G group individual cilia length measurements
Cilia length (µm)
0
1
2
3
4
5
CONTROL
SU
AZD
Individual embryo
E


F
H group individual cilia length measurements
Cilia length (µm)
0
2
4
6
8
CONTROL
SU
BGJ
AZD
Individual embryo


I group individual cilia length measurements
Cilia length (µm)
0
2
4
6
CONTROL
SU
BGJ
Individual embryo
G


J group individual cilia measurements
Cilia length (µm)
0
2
4
6
8
CONTROL
SU
BGJ
AZD
Individual embryo
H

Examining node structure

I also looked at the structure of the nodes analysed by SEM, and assessed whether their appearance was normal or abnormal for the stage in development the embryo has reached (**Figure 4.2.8**). 27/28 control cultured embryos had normal nodes, 25/30 SU5402 cultured embryos displayed normal nodes, 8/14 normal in AZD4547 cultured, and 13/14 BGJ398 cultured embryos had normal nodes (**Figure 4.2.8 A**). A number of cultured embryo nodes are shown at different developmental stages (**Figure 4.2.8 B-H**), as indicated. The abnormal/atypical nodes were sub-categorised by morphology (**Figure 4.2.9**). In a proportion, there was a failure of the node structure to fully emerge, as evidenced by overlying endodermal cells; this was evident in the abnormal node of one control cultured embryo (**Figure 4.2.9 B**), and for 4/5 SU5402, and 4/6 AZD4547 abnormal nodes (**Figure 4.2.9 A, C, E** and **F**). These embryos were those which has been cultured from the streak/bud stages up to the head-fold stages (category B embryos in **Table 4.2.1**), suggesting that this spans a time point at which FGF signalling is of importance. Additionally, some embryos (categories E, G, J) showed a “deep” pit structure of the node not normally seen (**Figure 4.2.9 D, G** and **H**), for 1 each SU5402 and BGJ398, and 2 of AZD4547 cultured embryos. Category B embryos have been placed in culture prior to the formation of the node, and so it appears that there has been a failure of the node to emerge in some of these. The embryos in categories E, G and J had developed nodes prior to the introduction of the embryo into culture and FGF inhibition. This may explain the difference in phenotypes seen, with embryos placed into culture earlier in development showing nodes which fail to correctly emerge, and those introduced into culture after the node has formed showing “deep” node structures. These embryos with “deep” nodes could suggest a mechanism by which the structure of the node is being failed to be maintained, and thus that FGF signalling has a role in the maintenance of node structure.

Figure 4.2.8: Node structure following culture. A shows the proportion of embryos with normal (blue) and abnormal/atypical (orange) nodes when cultured in medium indicated – control vehicle, su, azd and bgj. Normal nodes at various stages are shown in **B-H,** with anterior (A), posterior (P), left (L) and right (R) axes indicated. **B** shows a streak stage embryo with developing node, following culture with AZD (category A relating to **Table 4.2.1**). Scale bar = 50µm. **C** shows a 2 somite stage embryo with developing node, following culture with SU (category D relating to **Table 4.2.1**). Scale bar = 20µm. **D** shows a 4ss embryo following culture with control medium (category H relating to **Table 4.2.1**). Scale bar = 10µm. **E** shows a 5ss embryo following culture with control medium (category H relating to **Table 4.2.1**). Scale bar = 20µm. **F** shows a 6ss embryo after culture with AZD category J relating to **Table 4.2.1**). Scale bar = 100µm. **G** shows a streak stage embryo with developing node, following culture with AZD (category A relating to **Table 4.2.1**). **H** shows an 8ss embryo following culture with SU (category J relating to **Table 4.2.1**). Scale bar = 50µm.

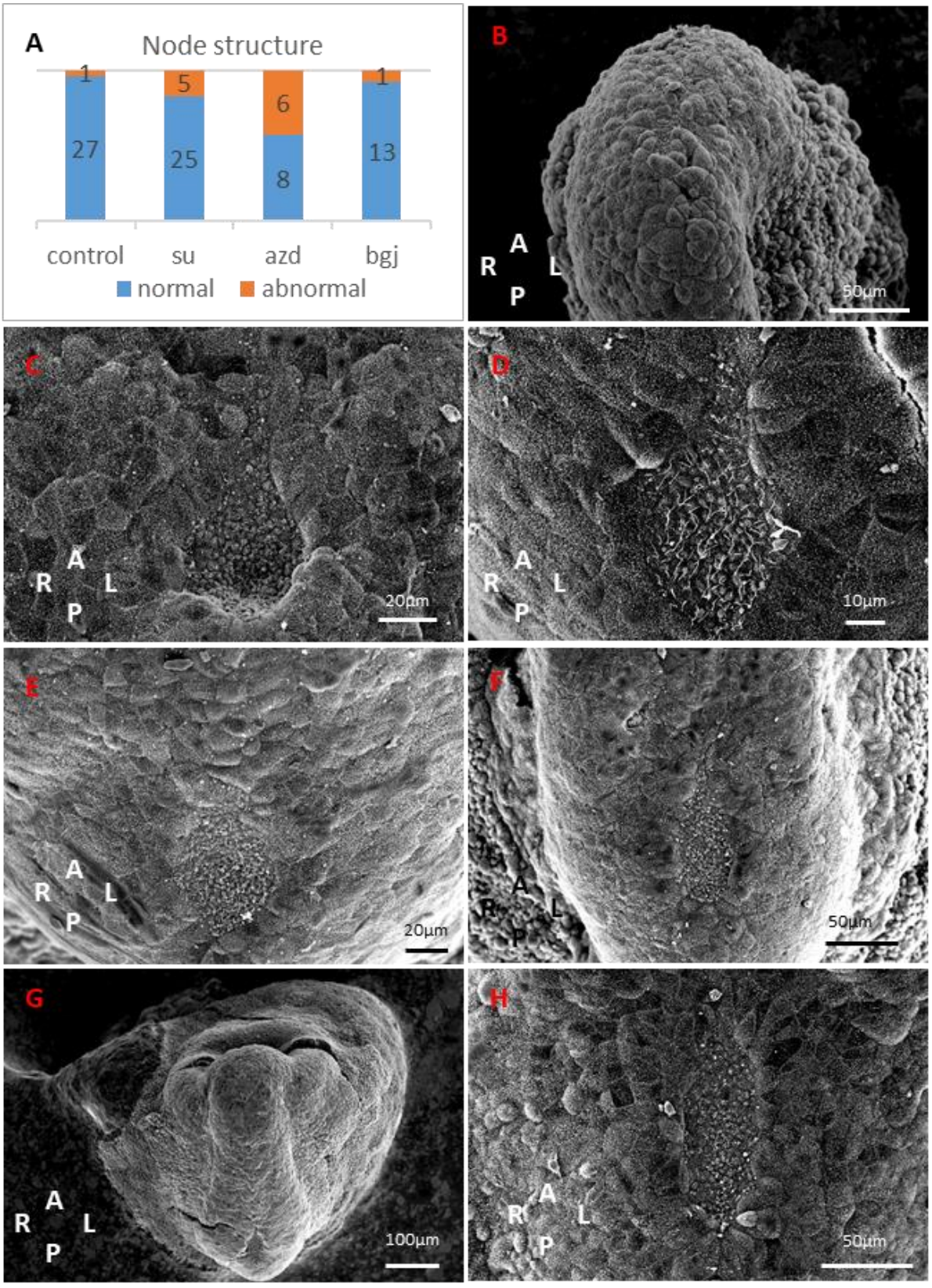
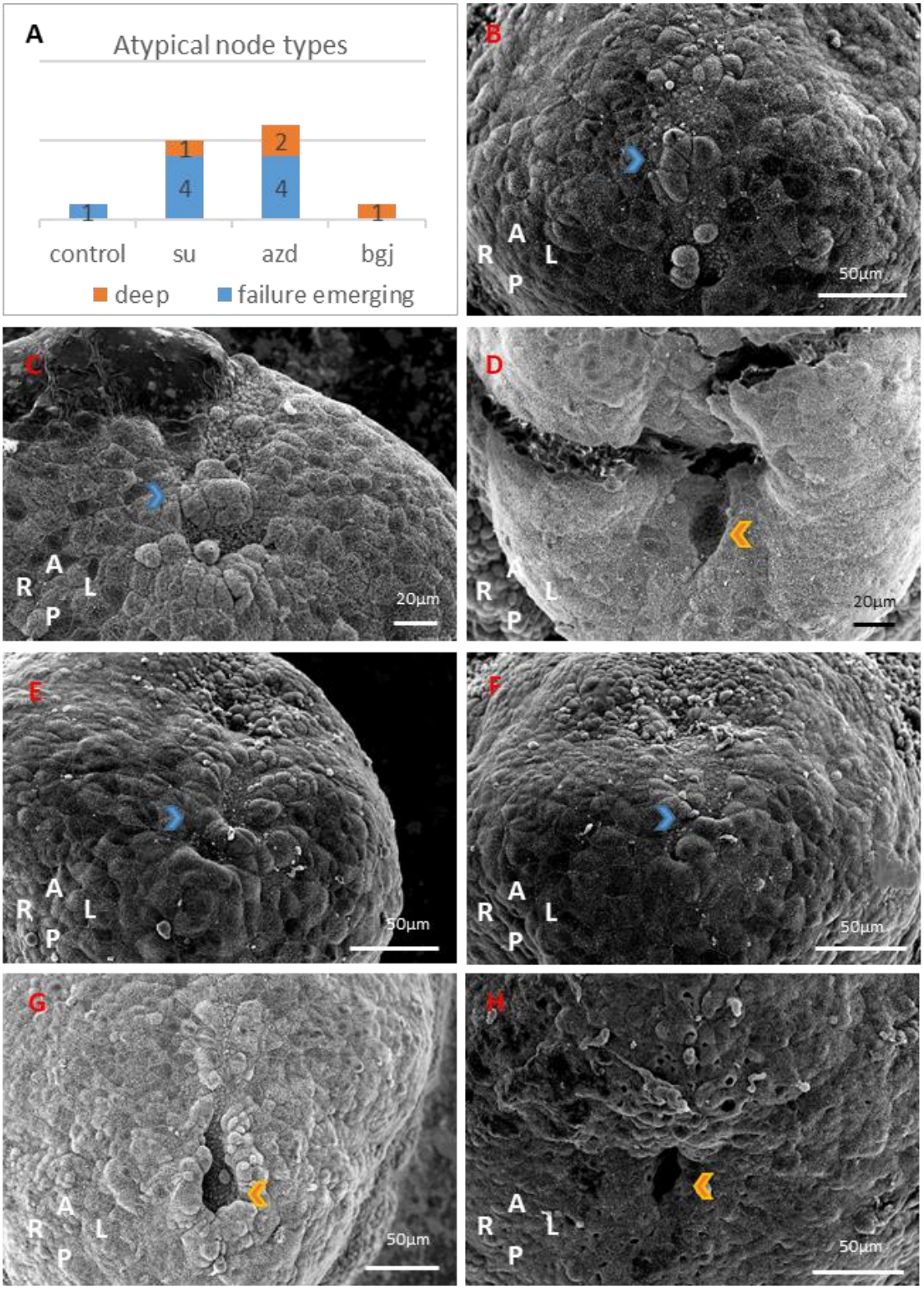

A
Node structure
1
27
5
25
6
8
1
13
control
su
azd
bgj
normal
abnormal
B
A
R
L
P
50µm
C
A
R
L
P
20µm
D
A
R
L
P
10µm
E
A
R
L
P
20µm
F
A
R
L
P
50µm
G
A
R
L
P
100µm
H
A
R
L
P
50µm

Figure 4.2.9: Abnormal node structure following culture.
A shows abnormal nodes following culture categorised into types of structure seen: either a "deep" hole-like structure (orange) or a failure of the node to emerge (blue). Culture medium is indicated. Example nodes are shown in the SEM images **B-H**, with anterior (A), posterior (P), left (L) and right (R) axes indicated. Blue arrows indicate where overlying cells are present. Orange arrows indicate deep node structures. **B** shows a control cultured embryo (category B relating to **Table 4.2.1**) where the node has failed to emerge. Scale bar = 50µm. **C** shows a su-cultured embryo (category D relating to **Table 4.2.1**) where the node has failed to emerge. Scale bar = 20µm. **D** shows a su-cultured embryo (category G relating to **Table 4.2.1**) where the node exhibits an atypical "deep" pit structure. Scale bar = 20µm. **E** shows an azd-cultured embryo (category B relating to **Table 4.2.1**) where the node has failed to emerge. Scale bar = 50µm. **F** shows an azd-cultured embryo (category B relating to **Table 4.2.1**) where the node has failed to emerge. Scale bar = 50µm. **G** shows an azd-cultured embryo (category E relating to **Table 4.2.1**) where the node exhibits an atypical "deep" pit structure. Scale bar = 50µm. **H** shows an azd-cultured embryo (category H relating to **Table 4.2.1**) where the node exhibits an atypical "deep" pit structure. Scale bar = 50µm.


A
Atypical node types
1
1
4
2
4
1
control
su
azd
bgj
deep
failure emerging
B
A
R
L
P
50µm
C
A
R
L
P
20µm
D
A
R
L
P
20µm
E
A
R
L
P
50µm
F
A
R
L
P
50µm
G
A
R
L
P
50µm
H
A
R
L
P
50µm

Assessing asymmetric gene expression

Cultured embryos were also assessed for expression of the L/R asymmetric gene markers *Cerl2, Nodal,* and *Pitx2* (**Figure 4.2.10**). *Cerl2* is the earliest known marker of asymmetry, exhibiting R>L asymmetry surrounding the node from the LHF stage. Of 31 control cultured embryos, 26 in categories C-H (as outlined in **Table 4.2.1**) showed the R>L node *Cerl2* asymmetry (image **Bi**), whilst 4 showed R=L and 1 showed R<L (**Figure 4.2.10 A,** example images **Bii** [R=L] and **Biii** [R<L]). The embryos that showed the atypical expression (4 R=L and 1 R<L) all belong to category B and potentially are too early to express nodal *Cerl2* asymmetrically, as they are a category which includes both early and late HFs embryos (the former are not likely to have established asymmetry). For SU5402 cultured embryos that were in categories B and C, I saw R>L asymmetry for 5 embryos, and R=L symmetry for 7 (**Figure 4.2.10 A** and **B**). 8 embryos of categories C-J cultured with AZD4547 showed the expected R<L *Cerl2* asymmetry, and 3 in category B showed R=L symmetry (**Figure 4.2.10 A**). A further 5 in category B and C showed R<L asymmetry, and 5 more showed unclear/odd expression (**Figure 4.2.10 Biv-vi**). 13 BGJ398 cultured embryos in groups E-J showed the expected R>L *Cerl2* asymmetry, whilst 1 (G) showed R=L symmetric expression (**Figure 4.2.10 Bii**). 2 embryos in categories B and C showed R<L *Cerl2* node asymmetry (**Figure 4.2.10 Biii**) and 2 also in category C showed unclear/odd expression of *Cerl2* and extra non-node cells exhibiting expression of *Cerl2* (**Figure 4.2.10 Biv-vi**). Overall, *Cerl2* expression in control-cultured embryos showed R>L asymmetry, and inhibitor cultured embryos showed more variability, with over half the embryos cultured with AZD and SU each showing atypical expression.

The expression of *Nodal* in the node was also assessed, with 14 control cultured embryos in culture categories C-E (**Table 4.2.1**) showing the expected R<L asymmetry, while 6 embryos (category C and D) showed symmetric *Nodal* at the node (**Figure 4.2.10 C**). For SU5402 cultured embryos, 10 samples in categories G and H showed R<L asymmetry of *Nodal* at the node, 7 samples (G and H category) showed equal expression on the left and

right sides of the node, and 1 sample, category D, showed right biased node *Nodal* asymmetry (**Figure 4.2.10 C**). For both BGJ398 and AZD4547 cultured embryos, 4 embryos in categories C and D showed unclear/odd expression of *Nodal*. Here again extra non-node cells expressing *Nodal* were evident in some samples, showing this rather than the normal horseshoe shaped pattern of expression we expect to see. For AZD4547 cultured embryos 7 further samples, all in category G, showed R<L asymmetry of *Nodal* at the node, whilst 6 ranging from category E-G showed R=L symmetry of *Nodal* at the node, and 1 sample, category C, showed R>L *Nodal* node asymmetry (**Figure 4.2.10 C**). For BGJ398 cultured embryos, a further 4 in categories G-J showed stronger left-sided *Nodal* expression at the node, whilst 3 in group C showed R=L *Nodal* symmetry, and 2, 1 each in groups C and D, showed R>L asymmetry (**Figure 4.2.10 C**).

Next, expression of *Nodal* in the LPM in embryos that had developed to the 4ss or further was assessed (categories H to J); this is a stage by which we expect to see L-LPM *Nodal* expression established under normal conditions. Embryos cultured with all inhibitor-cultured embryos failing to show expression of *Nodal* in the L-LPM (3 each for SU and AZD, 2 for BGJ), and most (3/5) control-cultured embryos also failing to show this *Nodal* LPM expression at the 4+ss (**Figure 4.2.10 D**). 2 of the 5 control-cultured showed L-LPM *Nodal* expression, and these were at later developmental stages than those that did not exhibit L-LPM *Nodal* expression (5 and 6ss vs 4, 4 and 5ss). The inhibitor cultured embryos were in categories H and I for SU; H and J for BGJ and for AZD. This suggests that there is a delay of the induction of *Nodal* in the L-LPM for all our cultured embryos.

I also used *Pitx2* to assess LPM asymmetry, and saw expression in the left (but not right) LPM for 6/8 control-cultured embryos and no LPM expression in 2 embryos; all embryos analysed were category J (**Figure 4.2.10 E** and **F**). Embryos cultured with SU5402 were in categories H-J, and all 3 analysed showed L-LPM expression (**Figure 4.2.10 Fi** and **iv**). For AZD4547 cultured embryos, 6/9 showed L-LPM *Pitx2* (stages J-H); 1 embryo showed partial L-LPM expression (**Figure 4.2.10 Fii** and **v**, category J), and 2 showed no *Pitx2*

expression, although these embryos were in category G, so we would only just be expecting the beginning of *Pitx2* L-LPM expression. Similarly, for BGJ398, most (10/14) embryos showed L-LPM *Pitx2* expression, from embryos ranging from category G-J. A single category H embryo showed only partial L-LPM *Pitx2* expression (**Figure 4.2.10 Fii** and **Fv**), and one showed partial left and right LPM expression (**Figure 4.2.10 Fiii** and **Fvi**); two further embryos (category G and H) failed to exhibit any LPM *Pitx2* expression. *Pitx2* LPM expression overall seems as though it may be delayed, with some embryos failing to show L-LPM even though they are 4ss+. Partial L-LPM expression is apparent for two embryos, one cultured with BGJ and the other with AZD, which also is consistent with a delay in L-LPM *Pitx2* induction.

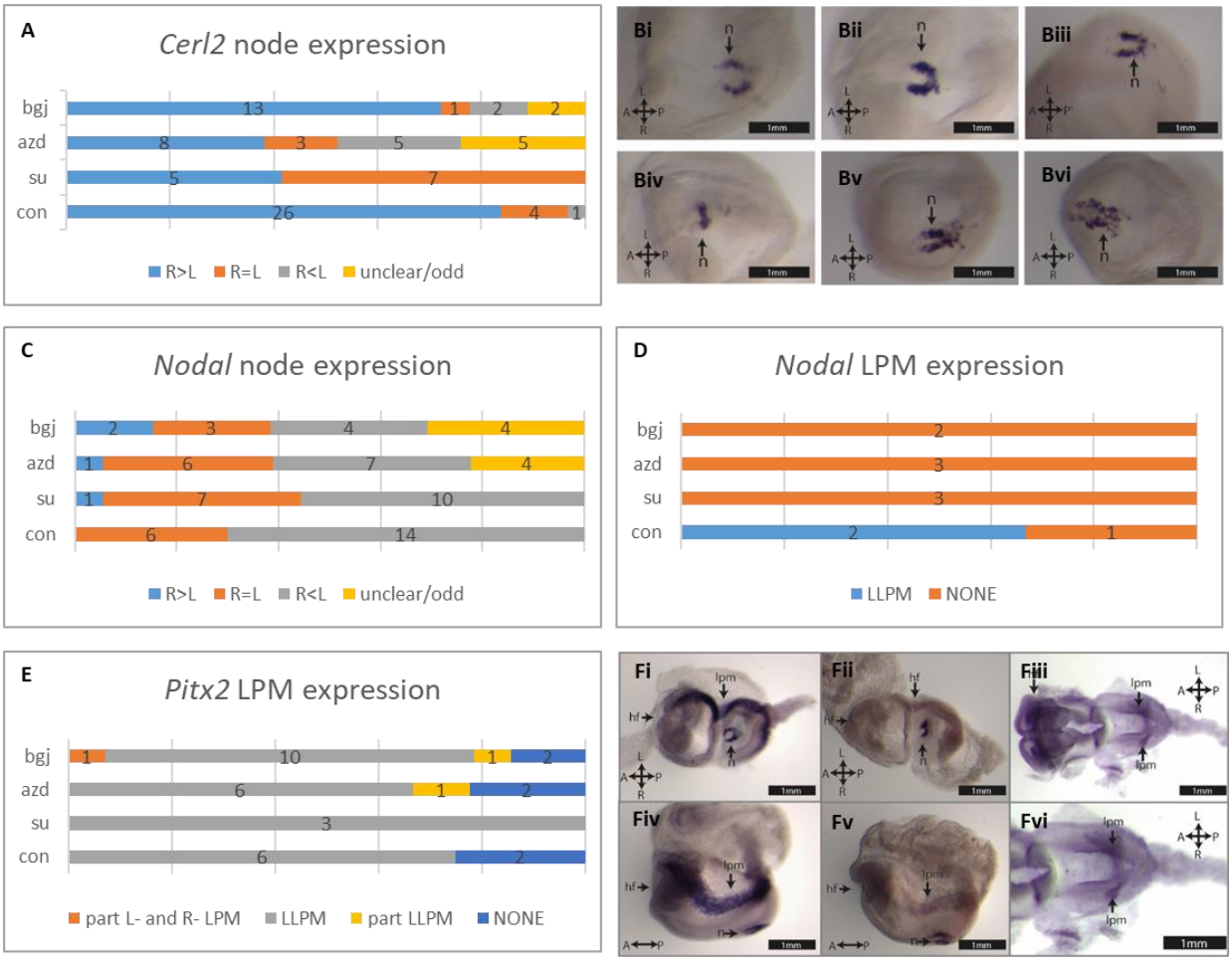


Figure 4.2.10: Gene expression in cultured embryos. Embryos were cultured with indicated inhibitors (BGJ398, AZD4547 or SU5402 – shortened to bgj, azd and su respectively) or control cultured with vehicle (DMSO). Numbers over bars indicate numbers of embryos. **A** and **B** show *Cerl2* expression in the node of cultured embryos, indicated as expected (wt) asymmetric expression R>L (blue- **Bi**), symmetric R=L (orange- **Bii**), asymmetric R<L (grey- **Biii**) or unclear/odd expression (yellow- **Biv,v,vi**). Scale bar = 1mm, anterior (A), posterior (P), left (L), right (R) axes and node (n) are indicated. **C** shows *Nodal* expression in cultured embryos, with expression patterns indicated as R>L asymmetric expression (blue), R=L symmetric expression (orange), expected/wt R<L asymmetric expression (grey) or unclear/odd expression (yellow). **D** shows *Nodal* expression in the lateral plate mesoderm (LPM) in embryos cultured to the 4ss+ (when we expect to see *Nodal* expression in the left-LPM), LLPM asymmetric expression (blue) and no LPM expression of *Nodal* (orange) are shown. **E** and **F** show LPM expression pattern of *Pitx2* in embryos 4ss+, which we expect to show LLPM expression (grey- **Fi** and **Fiv**). Embryos also exhibited some part LLPM *Pitx2* only (yellow- **Fii** and **Fv**), partial left and right LPM *Pitx2* (orange- **Fiii** and **Fvi**), or no LPM expression (dark blue). Scale bar = 1mm, anterior (A), posterior (P), left (L), right (R) axes, node (n), head folds (hf) and lateral plate mesoderm (lpm) are indicated.

4.3 Discussion

Through the experiments outlined above, I looked to assess 3 possible hypotheses for how FGF signalling is functioning in the establishment of L/R asymmetry. The first of these is that FGF signalling is regulating or influencing the cilia length in the node; the second that FGF signalling is controlling the release of NVPs within the node; and the third that FGF signalling is influencing the formation and/or patterning of the node. I discuss my data in relation to these three hypotheses below.

4.3.1 FGF signalling and node cilia length

Previous studies in zebrafish and *Xenopus* revealed a role for FGF signalling in regulating the length of cilia in the LROs of these organisms (Neugebauer et al. 2009). When assessing differences in node cilia length it is important to remember that cilia length increases in the node over developmental time (Lee and Anderson 2008; Little and Norris 2020). When looking at the nodes of my cultured embryos I saw some differences in cilia length in the nodes of control cultured, vs inhibitor cultured embryos, with the cilia in cultured embryo nodes appearing shorter. However, when I analysed these with respect to developmental stage (prior and post-culture), it became evident that these differences can most likely be attributed to the difference in stage of the embryos, due to cilia length increasing over developmental time following the emergence of the node. Indeed, the only statistically significant difference between different cultured embryos when analysed by group is between group G embryos in the SU and AZD cultured groups. In group G, only 1 control cultured embryo is present, however, which makes statistical comparison between wild-type and experimental data impossible. The control most closely clusters with the SU-cultured embryo cilia lengths, and not the AZD-cultured embryo data that express longer cilia lengths. This would support the idea that inhibiting FGFRs (and by extension FGF signalling) leads to dysregulation of cilia length within the node. It is of note

that, in other species (namely the frog and zebrafish), FGFR1 was seen to have a role in this, which does not seem likely to be the case if we are to believe the increased cilia length in AZD, but not SU-cultured embryonic nodes, as SU inhibits FGFR1, and AZD does FGFR1-3. Also, as no comparative BGJ cultured embryos are present in this group (group G), along with a lack of appropriate controls, meaning that any conclusions can only be very loosely drawn. Furthermore, in the frog and the fish, lack of normal FGFR1 led to a decrease in cilia length, whereas my data could be argued to be consistent with an increase in cilia length, when FGFR1-3 are inhibited over the 1-3 somite stages. Additionally, the importance of the specific stages pre- and post-culture of the inhibitor cultured embryos should not be minimised, as between these 1-3 somite stages the strong laminar leftward flow of extracellular fluid within the node is being established. Therefore, any defects/differences in cilia length at this time could potentially have the greatest impact on L/R patterning establishment.

4.3.2 FGF Signalling and NVPs

Tanaka and colleagues proposed FGF8 regulates the release of NVPs (Tanaka et al. 2005). I directly analysed the number of NVP-like spherical vesicles (referred to simply as NVPs in this discussion) in the nodes of embryos cultured with inhibitors of FGF signalling When I compared NVP numbers in uncultured vs cultured embryos I detected much larger NVP numbers in the uncultured nodes. In hindsight this may not be altogether surprising, as embryos for SEM analysis were placed into fixative as quickly as possible, following dissection. Unlike control embryos, cultured embryos are agitated in culture medium for a number of hours. As Reichert's membrane is removed for culture the node is uncovered, making it plausible that signalling molecules and/or NVPs may be washed out of the node during culture. This could account for the large difference in NVP number between uncultured and cultured embryos. However the possibility that something in the culture is causing a reduction in the numbers of NVPs cannot be excluded. Particularly of

consideration is the possibility that the culture medium may contain FGFs, as it is comprised of commercially available compounds which do not all define their complete ingredients.

The exact positioning of individual NVPs within each node with respect to the different axes was not recorded, but general distribution was examined when counting NVP numbers, and appeared uniform in all samples assessed. When the NVP numbers in cultured embryos are analysed, there is some noticeable variation between the control and SU cultured embryos. Also, the number of NVPs in AZD cultured embryos are clearly lower than those of control cultured embryos. The difference between these may suggest a dysregulation of NVP release. However, as BGJ inhibits all FGFRs1-4, that there was no difference seen in embryos cultured with this inhibitor contradicts this.

Of additional note is that the difference between the control and the SU-cultured embryos is in an increased and greater variation in the number of NVPs, whereas, compared to the control, AZD cultured embryos show a lower NVP number on average than in control cultured embryos. This could support the idea that FGF signalling has a role in the regulation of NVP release, but that this role is complex, with compensatory FGFRs acting in multiple ways.

4.3.3 The role of FGF signalling in Node morphology and formation

Arguments for a role for FGF signalling in node formation stem from data in Meyer's 1999 paper, where they showed their *Fgf8* mutant to have abnormal *Nodal* expression at the node. Although they did not formally state this putative role, their data implies this, as *Nodal* expression did not show the normal horseshoe shaped pattern of crown cells at the edge of the node, but instead exhibited scattered *Nodal*-expressing cells in the vicinity of the node (Meyers and Martin 1999). The culture experimentation discussed in this chapter

indicates a role for FGF signalling in the formation of the node, affecting L/R patterning through node morphology. Gene expression analysis provides some support for the proposed mechanism of FGF signalling acting in the formation of the node. Certain odd expression patterns were seen when looking at *Cerl2* and *Nodal*, with extra non-node cells expressing these genes, which we expect to see either just in the node crown cells, or in the crown cells and in the L-LPM in the case of *Nodal*. The expression in these additional cells could be said to line up well with the data shown by Meyers and Martin: their aberrant *Nodal* node expression in their mutant does appear to show a similar pattern of expression.

It is not known what exactly is occurring with the extra cells that are expressing *Nodal/Cerl2* at the posterior of the node. It is possible that this is due to these cells exhibiting crown cell identity while not normally being destined to become crown cells, or that they are misplaced crown cells. If the node has not formed correctly, and has failed to fully emerge from overlying endoderm, it may be that there are crown and pit cells which have only partially erupted, or failed to erupt. Alternatively, it may be that some aberrant signalling has induced cells which were not destined to become crown cells under normal circumstances, to now crown this cell identity.

Analysis by SEM imaging revealed atypical node structure in embryos cultured with FGF inhibitors. These embryos were in the minority in each cohort, but exhibit a high degree of gross structural anomaly. Some showed a lack of a fully or correctly emerging node, and others had a defect in the node structure exhibiting a phenotype of a “deep” node pit. The failure of the node to correctly emerge in some inhibitor-cultured embryos and the presence of “deep” nodes in others both may be due to a lack of functional FGF signalling resulting in anomalous/incorrect cell movement or incorrect crown cell formation or maintenance.

What exactly could be the cause of this, however, is unclear. FGFs function at the cellular level in many ways, and have roles in the regulation of cell proliferation, survival, migration and differentiation (Ornitz and Itoh 2015). Potentially the overlying endodermal cells which

migrate to reveal the underling node pit cells could have failed to correctly move, due to a lack of FGF signalling. Alternatively, it may be that the cells which make up the node have not properly formed, and therefore cannot emerge as they do normally. As the embryos which exhibited a “deep” node phenotype were put into culture at later stages of development, while those with nodes failing to emerge were placed into culture earlier, this illuminates why we see two disparate phenotypes. Indeed, it suggests that FGF signalling may have two distinct roles in the node at two different times: first in the emergence of the node structure and then in the maintenance of crown cells.

4.3.4 Inhibiting FGFR function

As discussed in the introduction to this chapter, SU5402 is a strong inhibitor of FGFR1, and AZD and BGJ both inhibit FGFRs1-3, and BGJ also inhibits FGFR4 (although at a lower specificity).

When looking at the NVP numbers in the cultured embryos, significant differences were evident between both the control and SU cultured and the control and AZD cultured embryos. However no difference was seen between the numbers of NVPs in control and BGJ cultured embryos. This variation could be due to a lack of FGF signalling leading to a dysregulation of NVP release, though as BGJ inhibits all the FGFRs AZD does, and the one SU does, if a specific receptor is involved it is unclear. However, of additional note is that the difference between the SU-cultured embryos is in an increased and greater spread of NVP number, and the difference in AZD cultured compared to control cultured, is in a lesser NVP number. The different directions of these is somewhat puzzling, but could suggest to compensatory action of FGFR2 or FGFR3 in SU-inhibited embryos, and therefore, a more pronounced dysregulation in AZD-inhibited embryos, which lack action of FGFR1-3. My gene expression data conversely suggests that FGFR2 and FGFR3 maybe having a more important role in node formation than FGFR1, and potentially

FGFR4 also, as my data showed anomalous *Nodal* and *Cerl2* expression only in the cohort of AZD and BGJ cultured embryos.Additional to this, no embryos in the SU-cultured group showed anything abnormal for *Pitx2* expression, and all showed the expected L-LPM expression, further supporting that FGFR1 may not be the main FGFR of importance in L/R patterning. However, for the *Pitx2* analysed embryos, only a small number were within this group, and in addition to this we saw some embryos in the control-cultured group to be lacking any LPM *Pitx2*, which clouds the picture further.

The commercially available FGFR inhibitors also have inherent problems as their advertised specificity is not always proven. SU5402, for one, is advertised as specific to FGFR1, but in some cases it appears that other FGFRs have not actually been assessed for reactivity with this compound (Sun et al, 1999). Elsewhere it has been reported to have inhibition of FGFR3 *in vitro* (Grand et al, 2004). For the other two inhibitors I used (AZD4547 and BGJ398) their reactivity with has been characterised with all FGFRs1-4 (Gavine et al. 2012; Guagnano et al. 2011; Konecny et al. 2013), though there are differing reports on whether FGFR4 is inhibited by AZD4547, depending on the supplier. FGF8 has activity with all of the FGFRs, but specifically interacts with the IIIc isoforms of FGFR1-3, and non-spliced FGFR4 (Estienne and Price 2018; Hao et al. 2019).

4.3.5 The impact of developmental timing and delay

Through my analysis of the markers of molecular asymmetry (*Nodal, Cerl2* and *Pitx2*), I could not directly assess the mechanisms of FGF signalling involved in L/R patterning, but I did confirm an effect of a loss of FGF signalling in disrupting L/R asymmetric gene expression. However, there was not always a clear distinction as to whether unexpected gene expression data produced was an effect of the specific inhibitor action, or a result of the culture methods generally. Our analysis of *Pitx2* expression showed a general lack of L-LPM *Pitx2* in similar proportions for the control and inhibitor-cultured embryos. However,

partial LPM *Pitx2* was seen in some I inhibitor cultured embryos, but not in any cultured in the control medium. This partial LPM *Pitx2* suggests that its expression has been induced, but delayed in these embryos (Norris et al. 2002). This supports there being a more pronounced delay in inhibitor-cultured embryos and therefore that inhibition of FGF signalling is causative. How FGF signalling is acting in this context, and which ligands and receptor combinations are involved is not clear. As FGF signalling is important for many developmental processes, such as somitogenesis and gastrulation (Guzzetta et al. 2020; Niwa et al. 2011; Sun and Stathopoulos 2018), it may be that there is a cumulative effect of a loss of FGF signalling leading to a general developmental delay. Indeed, *Fgf8* has a role in cell migration in the primitive streak of the gastrulating embryo, where embryonic epiblast cells transform into mesoderm and definitive endoderm: without *Fgf8,* the mesoderm cells cannot move away from the streak (Sun et al. 1999b). It may be that a general inhibition of FGF signalling can cause a general delay in the development of the embryos, which could lead to a delay in the timing at which key asymmetric gene expression patterns become established. This may also be influenced by the stages which are encompassed by the culture time, as we know that there are specific times of importance in establishing L/R asymmetry. The first genetic asymmetries are seen in *Cerl2* R>L expression at the node at the LHF stage, but the strong laminar leftward flow is not fully established until the 1-2ss stage, when we see *Nodal* R<L node expression. Therefore, if an embryo is in culture during the establishment of the initial weak flow, which then leads to *Cerl2* asymmetry, but is out of culture by the 2ss where strong flow is activated, this may lead to difference when compared to an embryo which goes into culture after the initial asymmetry is already set up. Those embryos which go into culture at later stages (up to the 3ss), may have established asymmetry normally, but the act of culture itself might lead to a lack of induction of asymmetric expression of genes in the LPM.

Additional to this, the effect FGF inhibition could be having in embryos which have already established asymmetry is unknown. For one line of argument, if FGF signalling is usually

influencing cilia length as the cilia grow, it may also cause a regression or lengthening of cilia at embryos introduced to culture after the cilia have grown, though this would be too late to impact the setting up of asymmetry, as flow has already led to the genetic asymmetries. Similarly, if NVP release is regulated by FGF signalling, the timing at which the signalling pathway is inhibited may influence the production of NVPs in different manners. If FGF signalling is inhibited when asymmetry is already established, it may be a different effect is produced than it would be prior to the establishment of asymmetry. As the evidence currently points to FGF signalling having a role in the regulation of the formation of the node, developmental stage is also of importance in this potential mechanism. If the node is not yet formed when the embryo is placed into culture, and FGF signalling is inhibited, the node may be unable to be correctly formed. This result this would give, in terms of node morphology, along with gene expression, may be very different than we would see in an embryo which has already formed a node prior to introduction into culture containing FGF inhibitors. If this is the case, the manner in which FGF signalling inhibition acts would vary over time, as cell identities and locations within the node alter and become established. The lack of FGF signalling could potentially have an impact on the ability of cells to migrate, as is seen with disruption of *Fgf8* and *Fgf4* in the primitive streak (Sun et al. 1999b). This could present as the overlying endodermal cells which move to reveal the node, failing to migrate and uncover the node structure. Similarly, the node crown cells may need some form of FGF signal in order to be primed to express genes required for the establishment of asymmetry.

4.3.6 Fgf8 mutant mouse

Analysis of an *Fgf8* mutant allelic series by the Martin lab first established that FGF signalling is required for normal L/R patterning (Meyers et al. 1998; Meyers and Martin 1999). There are some obvious discrepancies between the phenotypes seen in my FGF inhibitor-cultured embryos and those exhibited by the *Fgf8* mutant. The most striking of these is the expression of asymmetric genes in the L-LPM. I did not see a stark difference in L-LPM *Nodal* expression between my inhibitor culture vs control cultured embryos, and saw partial L-LPM *Pitx2* in some. Meyers, on the other hand, presented data showing a very clear lack of L-LPM *Nodal* and *Pitx2* expression in their *Fgf8* mutants. Although this could be due to their mutants only lacking *Fgf8*, and our cultured embryos having broad inhibition of FGFRs, it seems most likely that it is the result of culture itself. In addition, the differences in developmental stages of embryos introduced to culture is likely to be causing some of the discrepancies seen in the phenotype of inhibitor-cultured embryos. Strikingly, the presence of *Pitx2* in part, but not all, of the L-LPM in some of our inhibitor-cultured embryos, may in part correspond to phenotypes seen in the Meyers cohort. They reported a 49% incidence of right pulmonary isomerism (RPI) in their mutants, similar to the phenotypes of mice lacking asymmetric *Pitx2*, which showed RPI but normal stomach and spleen situs (Shiratori et al. 2006). As *Pitx2* expression is lacking in the whole of the L-LPM, with the expression missing in the anterior L-LPM, this expression pattern would correspond with a lung mispatterning due to lack of *Pitx2*. The gene expression patterns exhibited in our inhibitor-cultured mutants, however, would not be likely to give rise to phenotypes such as SIT, which were seen sporadically by Meyers in their *Fgf8* mutant cohort.

Where my results from embryo culture experiments do line up with the data from the *Fgf8* L/R mutant, however, is in the presence of sporadic cells expressing *Cerl2* and *Nodal,* posterior to the node. This corresponds with the data published by Meyers and Martin

which showed similar sporadic *Nodal*^{LacZ} expressing cells in the region of the node, and does appear to show a potentially similar pattern of expression (Meyers and Martin 1999). However, it is important to note here that their analysis used a *Nodal*^{LacZ} reporter allele, meaning that *Nodal* is expressed from only one copy. This in effect means that embryos expressing this only have half the normal amount of *Nodal* usually expressed. *Nodal* has been previously shown to exhibit synthetic phenotypes when doubly heterozygous with other developmental genes (Collignon et al. 1996; Constam et al. 1996; Mavrakis et al. 2007). This, along with the fact that no data on the physical structure of the node was presented in their analysis, piqued my interest. As the nodes in my embryo culture show a similar expression pattern of *Nodal* in the vicinity of the node, and also show abnormal node structure, I decided to further investigate Meyers *Fgf8* mutant.

5.0 Characterisation of *Fgf8* mutant mice

5.1 Introduction

In the late 1990s Meyers and Martin published the first paper to show an effect of *Fgf8* in mouse L/R axis development. In 1998 they published a paper describing an allelic series produced in the generation of a conditional *Fgf8* allele, which included production of a hypomorphic allele (Meyers et al. 1998). The targeting construct used a PGK-driven neomycin resistance cassette, flanked by Frt sites, to give an allele with a flanked Neo^R cassette and LoxP sites before exon 5 and after exon 6 (Tm1.1 allele – **Figure 5.1.1**). Deletion of the Neo^R by Flp-Frt recombination results in the Tm1.3 allele. Two alternative null alleles can be generated, one with (Tm1.2) and one without (Tm1.4) the neomycin cassette due to the recombinase reactions (**Figure 5.1.1**). The hypomorphic allele created (Tm1.1 neo allele) contains a cryptic splice site along with the PGK promoter, which is implicated in interference with the expression of a gene near to it (Meier et al. 2010; Pham et al. 1996). Meyers and Martin's analysis showed a reduction in the amount of functional gene product, in this case FGF8, in mice carrying this Tm1.1 allele.

Their paper additionally reported on the phenotypes of homozygous Tm1.1 embryos, which revealed specific brain abnormalities, notably absence of the olfactory bulbs, and a deletion of posterior midbrain and cerebellum (**Figure 5.1.2** (Meyers et al. 1998)). Following this, they published their 1999 paper, which reported that embryos homozygous for this allele also had an incidence of 8% right pulmonary isomerism (RPI) (Meyers and Martin 1999). Normal lung patterning in the mouse leads to 4 lobes in the right lung (cranial, middle, caudal and accessory), and 1 left lung lobe. Meyers and Martin reported their embryos as presenting RPI when they showed 3-4 lobes present on each the right and the left lung. In this paper they mainly focus on the phenotype of embryos heterozygous for both the Tm1.1 and Tm1.2 alleles, which showed an increase in L/R patterning defects, including a 49% incidence of right pulmonary isomerism. They argue

that the increased prevalence of this phenotype in their *Fgf8*$^{Tm1.1/Tm1.2}$ compound heterozygotes, vs their Tm1.1 homozygotes, comes from the 50% loss of functional *Fgf8* RNA. These *Fgf8*$^{Tm1.1/Tm1.2}$ compound heterozygotes were also examined at earlier stages (E9.5-11.5), where the direction of heart looping was assessed, and shown to be abnormal in 49% of their mutants. They also looked at E8.0-8.5 embryos, and analysed expression of key markers of asymmetry. This included *Pitx2*, which is usually expressed in the L-LPM from the 3/4ss onwards, and is known to affect non-cardiac situs. In *Fgf8*$^{Tm1.1/Tm1.2}$ compound heterozygotes, they failed to detect *Pitx2* expression in the LPM for 41% of their samples. They also analysed asymmetry using the *Nodal*^{LacZ} allele, to analyse expression of *Nodal* in the node and the LPM and found that 63% did not show LPM expression. As L-LPM *Nodal* expression induces *Pitx2* expression in the L-LPM, there is a clear discrepancy here, with a number of mutants, lacking *Nodal* expression in the L-LPM, but not *Pitx2*. This may be in part due to their use of the *LacZ* allele to follow *Nodal* expression, as embryos carrying this only have one wild-type functional copy of *Nodal*, and so less NODAL protein is likely to be produced in these, which could have an impact on the expression of *Pitx2*. Their use of the *Nodal*^{LacZ} also allowed them to assess expression at the node, where L>R *Nodal* is normally seen from the 2ss-6ss. In 4/10 mutants, they report normal the *Nodal* expression pattern at the node. However, in the remaining 6 only a scattering of *Nodal* expressing cells were seen, all in the vicinity of where the node is expected to be (**Figure 5.1.3**). This raised questions about the formation of the node, and the possibility that the structure may not be as it is in wild-type embryos. Direct analysis of the node was not carried out at the time, leaving open questions of the mechanism by which *Fgf8* affects L/R axis development. By re-examining this mutant in the light of our current more extensive understanding of L/R determination, including direct analysis of node structure by SEM, I am able to build upon my inhibitor culture work to assess the in vivo role of *Fgf8* in L/R patterning. This will allow me to further assess the hypotheses I have set out, namely that FGF8 is involved in regulation of cilia length, NVP formation/release, and/or in the formation of the node.

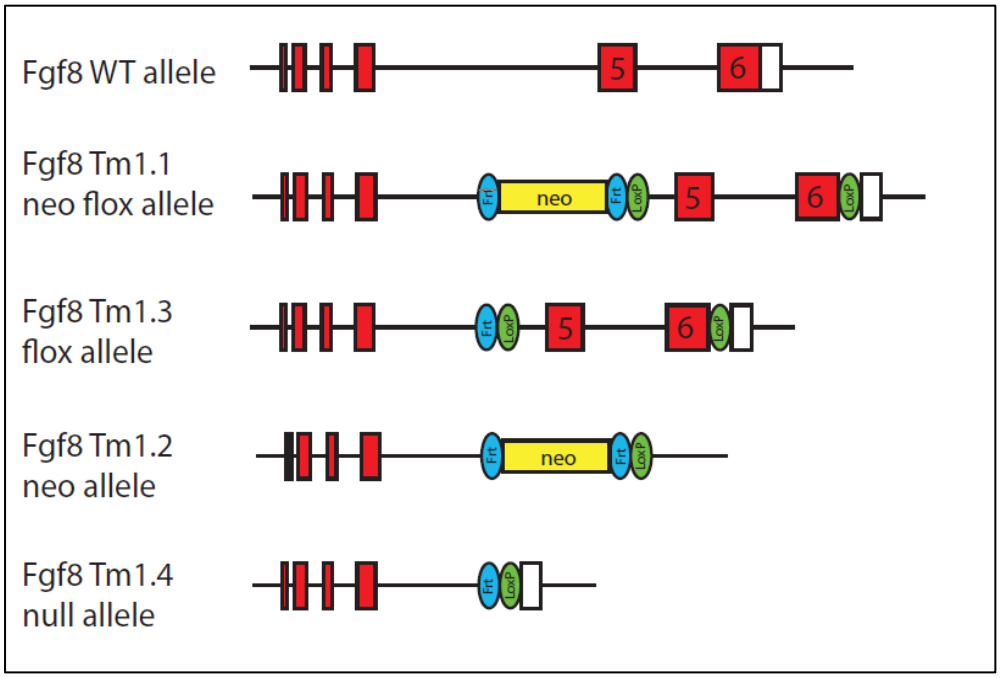


Figure 5.1.1: Schematic representation of the *Fgf8* alleles produced by Meyers and Martin (1998). As labelled, the *Fgf8* alleles, with each red box indicating an exon and the white the 3' UTR. Yellow neo box indicates *Neo*^{R} driven by a *Pgk* promoter. Blue oval indicates Frt sites and green ovals indicate LoxP sites. Alleles as labelled are explained with references to Meyers' paper in **Table 5.1.1**.

Annotation as in Figure 5.1.1	Meyers and Martin annotation 1998
Fgf8 WT allele	*Fgf8* Wild-type allele
Fgf8 Tm1.1 neo flox allele	*Fgf8*^{neo} allele
Fgf8 Tm1.3 flox allele	*Fgf8*^{flox} allele
Fgf8 Tm1.2 neo allele	*Fgf8*$^{\Delta 2,3n}$ allele
Fgf8 Tm1.4 null allele	*Fgf8*$^{\Delta 2,3}$ allele

Table 5.1.1: Annotation of *Fgf8* alleles produced by Meyers and Martin (1998).Table shows annotation relating to **Figure 5.1.1**

My annotation	Meyers and Martin 1998 paper	Meyers and Martin 1999 paper
Fgf8$^{Tm1.1}$ heterozygotes	*Fgf8*^{neo} heterozygotes	*Fgf8*$^{neo/+}$
Fgf8$^{Tm1.1}$ homozygotes	*Fgf8*^{neo} homozygotes	n/a (*Fgf8*$^{neo/neo}$)
Fgf8$^{Tm1.2}$ heterozygotes	*Fgf8*$^{\Delta 2,3n}$ heterozygotes	*Fgf8*$^{+/-}$
Fgf8$^{Tm1.1/Tm1.2}$ compound heterozygotes	*Fgf8*$^{\Delta 2,3n}$ / *Fgf8*^{neo} compound heterozygotes	*Fgf8*$^{neo/-}$ compound heterozygotes / *Fgf8* mutant

Table 5.1.2: Annotation of different *Fgf8* genotype mice. Annotation according to possible *Fgf8* genotypes (alleles as in **Figure 5.1.1** and **Table 5.1.1**) by my notation, Meyers and Martins' 1998 paper and 1999 paper notations.

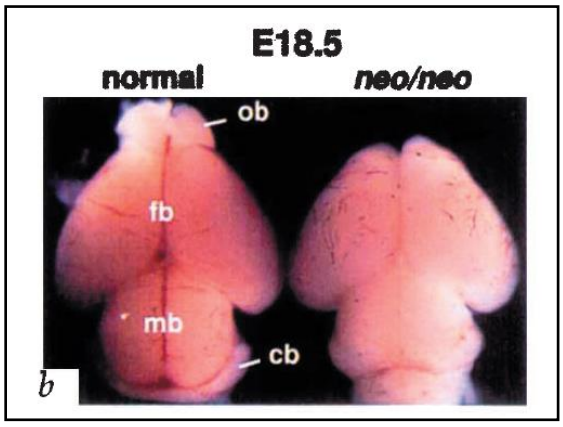


Figure 5.1.2: Brain morphology of *Fgf8* mutants from Meyers and Martin (1998) paper, Figure 2b. E18.5 brains of wild-type littermate (left) and *Fgf8*$^{Tm1.1}$ homozygous (right) embryos. Wild-type (normal) brain is labelled with olfactory bulb (ob), forebrain (fb), midbrain (mb) and cerebellum). Note *Fgf8*$^{Tm1.1}$ homozygous *(neo/neo)* brain has no olfactory bulb.

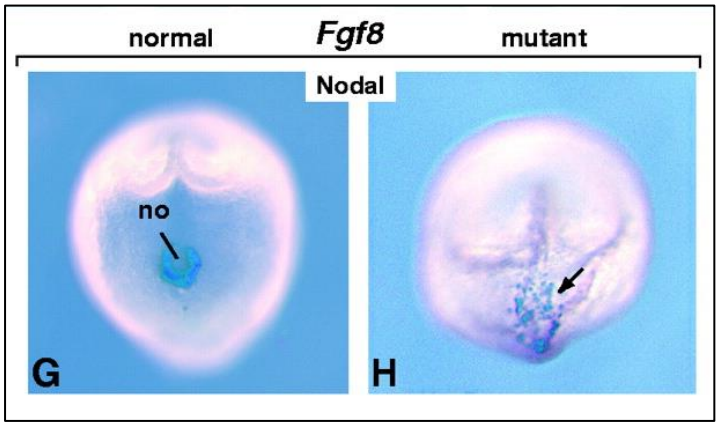


Figure 5.1.3: Nodes of *Fgf8* mutant and wild-type embryos stained with *Nodal*^{LacZ} from Meyers and Martin (1999) paper, Figure 2 (G&H). Wild-type (normal) and mutant *Fgf8* (*Fgf8*$^{Tm1.1/Tm1.2}$ compound heterozygous) embryos at E8.0 (0-1ss) with *Nodal* expression indicated by *Nodal*^{LacZ} mutant. Arrows point to node, and anterior is to the top and posterior to the bottom of the image.

5.2 Results

5.2.1 Genetic background

The Tm1.1 line was imported from the Jackson laboratories congenic for BL/6J, and it is on this genetic background that I have analysed its phenotype. The Tm1.2 line was created from the Tm1.1 line by Cre-mediated recombination. The genotypic identities of the lines were confirmed by high quality PCR analysis. The genetic background of the embryos analysed by Meyers and Martin is unknown, although they state HM1 embryonic stem cells (129 strain) were targeted and then combined with single 8-16-cell CD1 embryos (Meyers et al. 1998). It is likely that these were then crossed to outbred strains to provide large litters for analysis, as was common for the time (Nagy and Rossant 1993). We established our line at Harwell on B6J as the line was on this genetic background prior to our importing it, and this line is commonly used in our groups' studies of L/R patterning in the embryo, allowing meaningful comparison with our other analyses.

5.2.2 *Fgf8*$^{Tm1.1}$ line analysis

Firstly, we generated *Fgf8*$^{Tm1.1}$ homozygotes in order to confirm we recapitulated the phenotypes reported by Meyers and Martin (Meyers et al. 1998). We analysed a small number of embryos at E18.5, and saw either a lack of or very small olfactory bulbs in 4/4 homozygotes, with the heterozygous and wild-type littermates showing normal olfactory bulb morphology (4/4 and 5/5 each respectively) (**Figure 5.2.1**). We extended our analysis to look at embryos at an earlier stage of development, utilising micro-CT imaging. Here, we found that both homozygotes and heterozygotes showed variable phenotypes at E13.5 (**Table 5.2.1** and **Figure 5.2.2**). We found that 1 out of 6 *Fgf8*$^{Tm1.1}$ heterozygotes analysed at this stage had no olfactory bulb, and 1 had a small OB. In our homozygous embryos, 2 out of 7 analysed had a missing or underdeveloped OB (**Figure 5.2.2 Ci-iv**). The

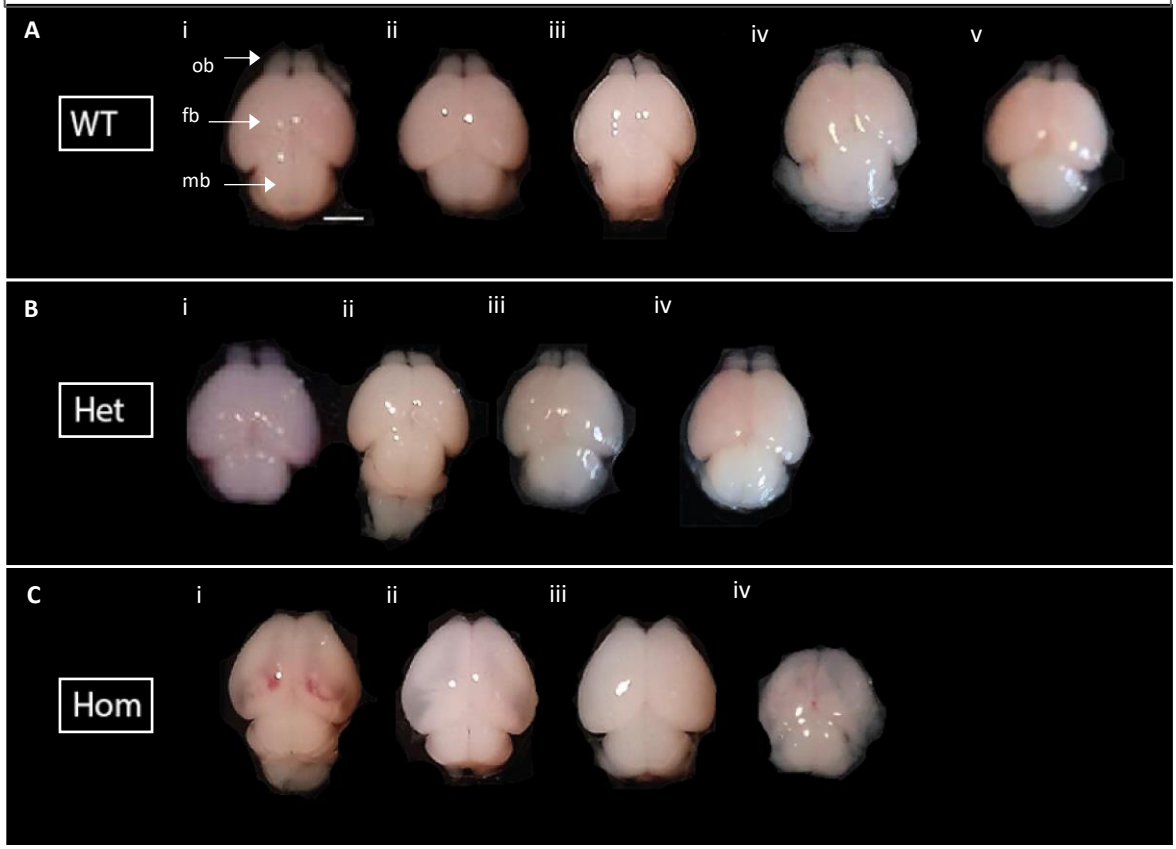
cerebellum was absent in 2/6 of our heterozygotes (**Figure 5.2.2 Bii** and **Biii**; blue arrow identifies the cerebellum and yellow arrow missing cerebellum). In homozygous embryos, 3/7 had absent cerebellum (**Figure 5.2.2 Biv** – yellow arrow). In contrast, when Meyers and Martin analysed the Tm1.1 line, they reported no phenotype in the heterozygotes, while 8/8 homozygotes that they analysed at E18.5 showed absent olfactory bulbs, along with loss of cerebellar and posterior midbrain tissue. Strikingly, high throughput scoring of the micro-CT data reported abnormal craniofacial morphology in 3/6 *Fgf8*$^{Tm1.1}$ heterozygotes and 4/7 homozygotes (**Figure 5.2.2 A**), combined with incomplete closure of the soft palate in the homozygotes (**Table 5.2.1**).

No gross situs defects were observed in our micro-CT analysis of the *Fgf8*$^{Tm1.1}$ heterozygote and homozygote embryos, with thoracic organ positioning being normal in all heterozygote and homozygote embryos assessed. However, when the lung morphology was closely analysed (**Figure 5.2.2 E-F**), in one heterozygote the cranial, middle, and caudal right lung lobes were abnormal in terms of shape. In one homozygous embryo, the middle and caudal right lung lobes were abnormal (**Figure 5.2.2 Ev** and **Fv**, red arrows). No such phenotypes were reported in the Meyers and Martin analysis, although they did in their 1999 paper report an 8% incidence of right pulmonary isomerism in mutants homozygous for *Fgf8*$^{Tm1.1}$ (Meyers and Martin 1999). However their method of analysis may be the reason for this, as they assessed lung lobes by eye, so only very obvious abnormalities in lung morphology would be likely to be noticed and reported on.

There are clear disparities between the phenotypes we observed and those reported by Meyers and Martin. The hypomorphic nature of the *Fgf8*$^{Tm1.1}$ allele means that some variability in phenotypes between embryos is not unexpected, as variable expressivity in tissues is likely to be a cause of this. It is of note that we observed novel phenotypes in the embryos heterozygous for the *Fgf8*$^{Tm1.1}$ allele. However, as our analysis was at an earlier developmental stage than that carried out by Meyers, this may be the cause of this difference. Other possible causes include differences in genetic background, and the

method of analysis used: Meyers and Martin analysed lung lobes by eye, whereas my analysis used micro-CT, which can arguably visualise anatomical detail more closely.

Figure 5.2.1: E18.5 brains of Fgf8 WT, Tm1.1 Hets and Tm1.1 Homs. Brains were dissected and the presence of olfactory bulbs noted in the WTs (**A**) and hets (**B**), and absence of/ reduction of size in homs noted (**C**). For each genotype, individual brains are shown and labelled i-v or i-iv. Scale bar = 5mm. Olfactory bulb (ob), fore-brain (fb) and midbrain (mb) are indicated in **Ai**.



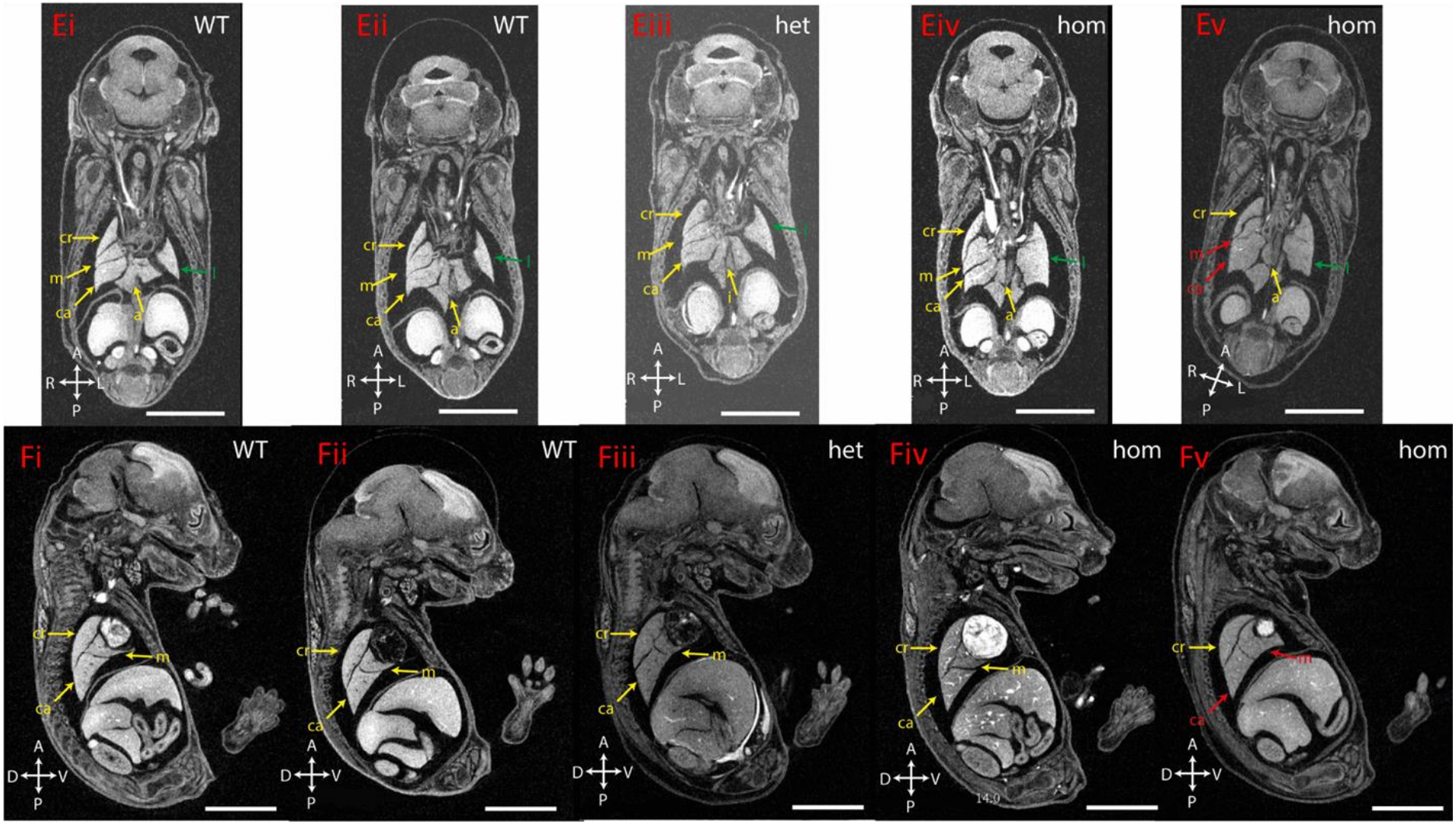
	WT	HET	HOM
FACE			
Soft palate		1/6 incomplete closure	4/7 incomplete
craniofacial morphology		3/6 abnormal	4/7 abnormal
Nasal cavity		2/6 abnormal	3/7 deformed asymmetry
vomeronasal organ		2/6 unobservable	3/7 missing/unobservable
LUNGS			
Right lung: cranial lobe		1/6 abnormal	
Right lung: Middle lobes		1/6 abnormal	1/7 abnormal
Right lung: Caudal lobes		1/6 abnormal	1/7 abnormal
HEART			
Vena cava (R/L)			1/7 small
Atrium (heart) (R/L)			4/7 small
Heart ventricle (R/L)		1/6 thick ventricular wall	2/7 abnormal/poss abnormal
BRAIN -CNS			
Midbrain roof plate			1/7 abnormal
Cerebellum		2/6 missing cerebellum	3/7 absent
cerebral aqueduct		1/6 wide cerebral aqueduct	1/7 enlarged
cerebral cortex		1/6 domed cortex	4/7 abnormal
lateral ventricles	1/4 small	1/6 compressed lateral ventricle	5/7 abnormal
mesencephalic vesicle			3/7 abnormal
3rd Ventricle		2/6 abnormal	4/7 abnormal
Olfactory lobe		2/6 small/missing olfactory bulb	3/7 abnormal/missing

Table 5.2.1: microCT scoring for *Fgf8* WT, Tm1.1 Het and Tm1.1 Hom E13.5 embryos. Abnormalities in a number of categories were noted and are shown in the table, where 4 WT embryos, 6 heterozygote and 7 homozygote embryos for the *Fgf8* Tm1.1 allele were assessed.

Figure 5.2.2: MicroCT images of E13.5 embryos. A shows the external view of embryos, with anterior (A), posterior (P), dorsal (D), ventral (V), left (L), right (R) axes as indicated. **Ai** shows a wild-type (WT) embryo, with normal facial morphology and snout indicated by purple arrow. **Aii** shows an *Fgf8* Tm1.1 heterozygote (het) embryo, with normal facial morphology and snout indicated by purple arrow. **Aiii** shows an *Fgf8* Tm1.1 homozygote (hom) embryo, with abnormal facial morphology and snout indicated by red arrow. **Aiv** shows an *Fgf8* Tm1.1 homozygote (hom) embryo, with abnormal facial morphology and snout indicated by red arrow. **B** shows a lateral view of embryos of indicated genotypes, with axes as indicated. **Bi** shows a WT embryo, with the blue arrow indicating presence of cerebellum. **Bii** shows a heterozygote embryo, with the blue arrow indicating presence of cerebellum. **Biii** shows a heterozygote embryo, with the yellow arrow indicating absent cerebellum. **Biv** shows a homozygote embryo, with the red arrow indicating absence of cerebellum. **C** shows a transverse section through the heads of embryos of indicated genotypes. **Ci** shows a WT embryo, with normal nasal cavities (green arrows) and olfactory bulbs (yellow arrows). **Cii** shows a homozygote embryo, with normal nasal cavities (green arrows) and olfactory bulbs (yellow arrows). **Ciii** shows a homozygote embryo, with abnormal nasal cavities (orange arrows) and olfactory bulbs (pink arrows). **Civ** shows a homozygote embryo, with abnormal nasal cavities (orange arrows) and olfactory bulbs (pink arrows). **D** shows a section through the coronal plane of the head of embryos of indicated genotypes. **Di** shows a heterozygote embryo with normal 3rd ventricle, indicated by blue arrow. **Dii** shows a heterozygote embryo with 3rd ventricle of a normal size, indicated by blue arrow, but with the presence of an abnormal growth in the cavity (orange arrow). **Diii** shows a heterozygote embryo with narrow 3rd ventricle, indicated by a yellow arrow. **Div** shows a homozygote embryo with narrow 3rd ventricle, indicated by a yellow arrow. **Dv** shows a homozygote embryo with absent 3rd ventricle, indicated by a red arrow. **E-F** show two views for each embryo depicted (**i-v**), given to show the lobes of the right lung for each embryo. Right lung lobes are labelled as cr-cranial lobe, m-middle lobe, ca-caudal lobe and a-accessory lobe. Left lung lobe is labelled (l-green arrow). **Ei-ii** and **Fi-ii** show two WT embryos with normal lungs (normal right lung lobes in yellow, left in green). **Eiii** and **Fiii** show a *Fgf8* Tm1.1 heterozygote embryo with normal lungs (normal right lung lobes in yellow, left in green). **Eiv** and **Fiv** shows a *Fgf8* Tm1.1 homozygote embryo with normal lungs (normal right lung lobes in yellow, left in green). **Ev** and **Fv** show a *Fgf8* Tm1.1 homozygote embryo with abnormal shaped middle and caudal right lung lobes (red arrows and labels). In all images, scale bars = 2mm and genotypes of embryos indicated in the top right of each image.

Ai
WT
Aii
het
Aiii
hom
Aiv
hom
Bi
WT
Bii
het
Biii
het
Biv
hom

Ci
WT
Cii
hom
Ciii
hom
Civ
hom
Di
het
Dii
het
Diii
het
Diii
hom
Div
hom


Ei
WT
Eii
WT
Eiii
het
Eiv
hom
Ev
hom
cr
m
ca
a
l
i
A
R
L
P
Fi
WT
Fii
WT
Fiii
het
Fiv
hom
Fv
hom
D
V
14.0

5.2.3 Analysis of *Fgf8*$^{Tm1.1}$, *Fgf8*$^{Tm1.2}$, *Fgf8*$^{Tm1.1/Tm1.2}$ compound heterozygous mutants

Assessing situs

The *Fgf8*$^{Tm1.1/Tm1.2}$ compound heterozygous embryos assessed by Meyers and Martin at E9.5-11.5, showed a failure to correctly loop the heart in 49% of 144 mutants analysed. The looping of the heart is the first morphological marker of L/R asymmetry in the embryo, and can be assessed along with the direction of embryonic turning in E9.5 embryos. The direction of embryonic turning is evident from the positioning of the caudal end of the embryo to the right side of its head at this stage. However, the embryo must be carefully dissected from the uterus and deciduum to prevent damage to the yolk sac that can otherwise make it unreliable to score - as such some embryos have been scored for heart looping, but not for embryonic turning. My first analysis of the *Fgf8*$^{Tm1.1/Tm1.2}$ compound heterozygotes was carried out at the E9.5-10.5, and I found the direction of embryonic turning to be normal in all embryos that could be reliably assessed: 11 wild-types, 14 *Fgf8*$^{Tm1.1}$ heterozygotes, 7 *Fgf8*$^{Tm1.2}$ heterozygotes and 9 *Fgf8*$^{Tm1.1/Tm1.2}$ compound heterozygotes (**Figure 5.2.3 A**). The heart looping was also examined in this same cohort, and a normal right-sided looping (D-loop) was evident in 12/12 wild-type embryos, 15/15 *Fgf8*$^{Tm1.1}$ heterozygotes and 9/9 *Fgf8*$^{Tm1.2}$ heterozygotes (**Figure 5.2.3 B, E-F**). The *Fgf8*$^{Tm1.1/Tm1.2}$ compound heterozygotes showed normal looping of the heart in 9/10 embryos, however 1 embryo showed abnormal looping, with a central-protruding loop (A-loop - **Figure 5.2.3 B-D**). This suggests that a less penetrant L/R patterning phenotype is present in the *Fgf8*$^{Tm1.1/Tm1.2}$ compound heterozygote embryos I am analysing, and it seems possible that this relates to differences in their genetic background.

As the information that can be gathered in regards to morphological L/R patterning at E9.5 is limited to gross cardiac situs and embryonic turning, I next assessed situs in E13.5 embryos. At this stage the positioning of all the thoracic organs can be examined, along

with left and right lung lobation and the patterning of the great vessels of the heart. I therefore examined heart, lung and stomach positioning in E13.5 embryos. The positioning of the stomach was scored and found to be normal in all embryos examined: 29 wild-type, 12 *Fgf8*$^{Tm1.1}$ heterozygote, 35 *Fgf8*$^{Tm1.2}$ heterozygote and 29 *Fgf8*$^{Tm1.1/Tm1.2}$ compound heterozygote embryos (**Figure 5.2.4 C**). I assessed lung situs by examining of the number of lobes in the left and right lungs; all genotypes showed normal lung morphology (29 WT, 12 *Fgf8*$^{Tm1.1}$heterozygotes, 35 *Fgf8*$^{Tm1.2}$ heterozygotes and 29 *Fgf8*$^{Tm1.1/Tm1.2}$ compound heterozygotes (**Figure 5.2.4 D, Appendix Figure 2 F**).

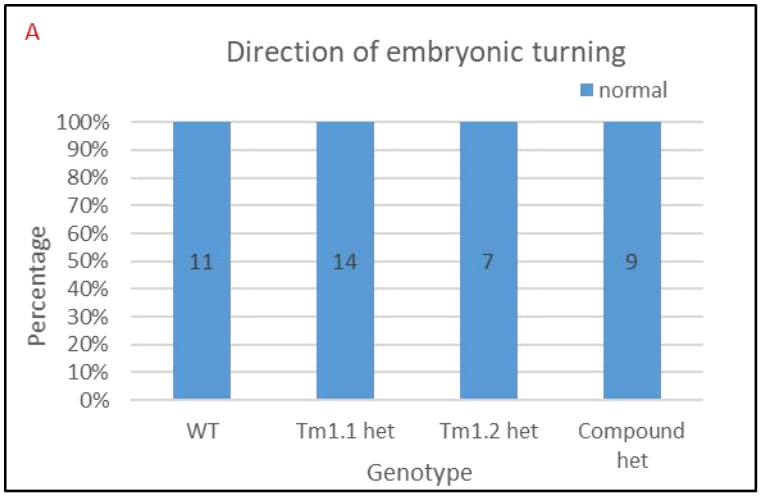
The direction of the heart apex was also scored, with this pointing to the left in normal wild-type embryos. We observed the normal left bias in all the wild-type (29) and *Fgf8*$^{Tm1.1}$ heterozygous (12) embryos. In *Fgf8*$^{Tm1.2}$ heterozygotes, 1/35 embryos showed a central pointing heart, with the remaining 34 having a left pointing heart (**Figure 5.2.4 E**). 6/30 *Fgf8*$^{Tm1.1/Tm1.2}$ compound heterozygous embryos showed central pointing heart apexes, with the rest (24) showing apparently wild-type, leftward pointing heart apexes. The patterning of the great vessels of the heart was similarly assessed, and a number of defects seen in *Fgf8*$^{Tm1.1/Tm1.2}$ compound heterozygote mutants (**Figure 5.2.4 F, Appendix Figure 2 G-I**). Most common (16/35) was the presence of an interrupted aortic arch (IAA), whilst a double-outlet right ventricle defect (DORV) was present in 7/35. Only 12 of 35 *Fgf8*$^{Tm1.1/Tm1.2}$ compound heterozygous mutants appeared to have normal great vessels. Additionally, 1 *Fgf8*$^{Tm1.2}$ heterozygote embryo (1/34) showed an IAA. All of the *Fgf8*$^{Tm1.1}$ heterozygotes (12/12) and wild-type embryos (27/27) assessed showed normal great vessel positioning.

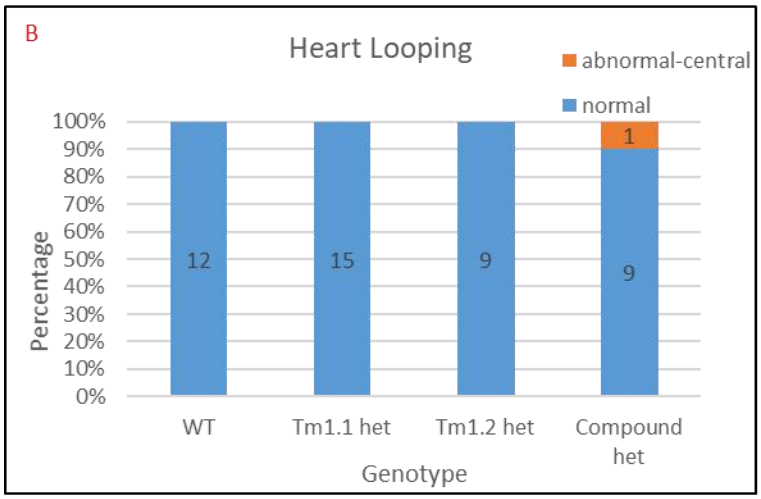
An elongated and pointed head shape was seen in the majority (23/29) of the *Fgf8*$^{Tm1.1/Tm1.2}$ compound heterozygote mutants at E13.5 (**Figure 5.2.4 B, Appendix Figure 2 B-E**). This seems likely to be coupled with the brain abnormalities reported in these mutants by Meyers and Martin, however, we did not analyse the brains directly. We also saw 1 *Fgf8*$^{Tm1.2}$ heterozygote with the same elongated and pointed head phenotype, and 1 with

a malformed snout (**Figure 5.2.4 B, Appendix Figure 2 A**). This again may well be coupled with brain abnormalities, with the malformed snout most likely reflecting the olfactory bulb deformity. No such phenotypes were reported in *Fgf8*$^{Tm1.2}$ heterozygotes by Meyers and Martin. However it is not clear if this was assessed in their analysis.

Embryonic viability was assessed, with numbers of embryos for each genotype noted (**Figure 5.2.5**). For E8.5 embryos the ratios of each genotype showed the expected Mendelian frequencies (**Figure 5.2.5 A**). At the E9.5-10.5 group, the *Fgf8*$^{Tm1.1}$ heterozygote embryos seem to comprise a higher proportion than expected, though this could be due to the overall small size of this group (**Figure 5.2.5 B**). Notably, at the E13.5 stage, a number of dead *Fgf8*$^{Tm1.1}$ heterozygote embryos were found (**Figure 5.2.4 A**). When this was assessed statistically, this was found to be significantly lower than the number predicted by Mendelian ratios (Chi squared test, P= 0.0415) (**Figure 5.2.5 C**). However it is not clear as to the mechanism of this. As we previously investigated the Tm1.1 line and saw heterozygotes and homozygotes at the E18.5, this data is suggestive of a variable viability, perhaps depending on the amount of functional FGF8 protein varying between tissues in individual *Fgf8*$^{Tm1.1}$ heterozygotes.

Overall, at E13.5 our analysis shows the presence of L/R defects in a number of *Fgf8*$^{Tm1.1/Tm1.2}$ compound heterozygous embryos. The presence of central pointing heart apexes at this stage, combined with one A-loop found at E9.5-10.5, suggest a failure in correct heart positioning. Additionally, the presence of heart great vessel defects in embryos of this genotype also points towards a L/R patterning defect. Therefore, these morphological defects must result from incorrect molecular asymmetry. As such, we assessed E8.5 embryos with markers of L/R asymmetry, at stages around the initial event of breaking of L/R symmetry.





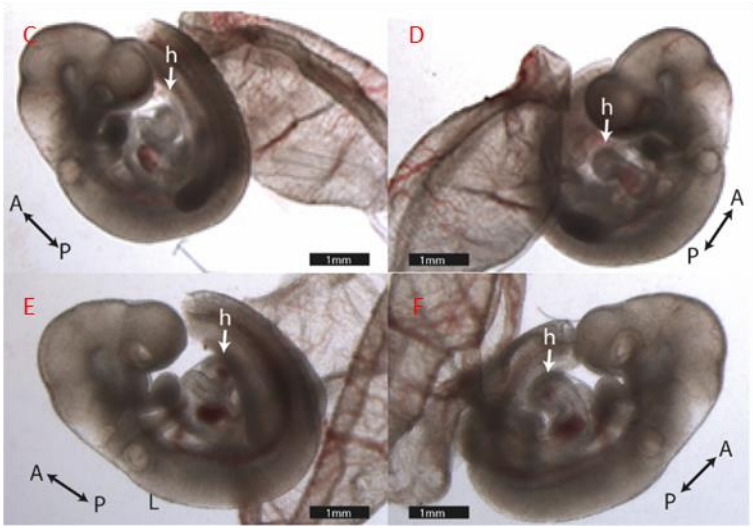


Figure 5.2.3: Analysis of asymmetry in E9.5-10.5 embryos. **A** shows the direction of turning for Fgf8 WT, Tm1.1 heterozygote, Tm1.2 heterozygote and Compound (Tm1.1 and Tm1.2) heterozygote embryos. **B** shows the direction of heart looping for Fgf8 WT, Tm1.1 heterozygote, Tm1.2 heterozygote and Compound (Tm1.1 and Tm1.2) heterozygote embryos. **C-F** show example E9.5 embryos, with anterior (A) and posterior (P) axes and heart (h) indicated. Scale bar = 1mm. **C** shows a compound heterozygote embryo with a central projected heart from the left view. **D** shows the same embryo from the right side. **E** shows a compound heterozygote embryo with a normal heart from the left view. **F** shows the same embryo from the right side.

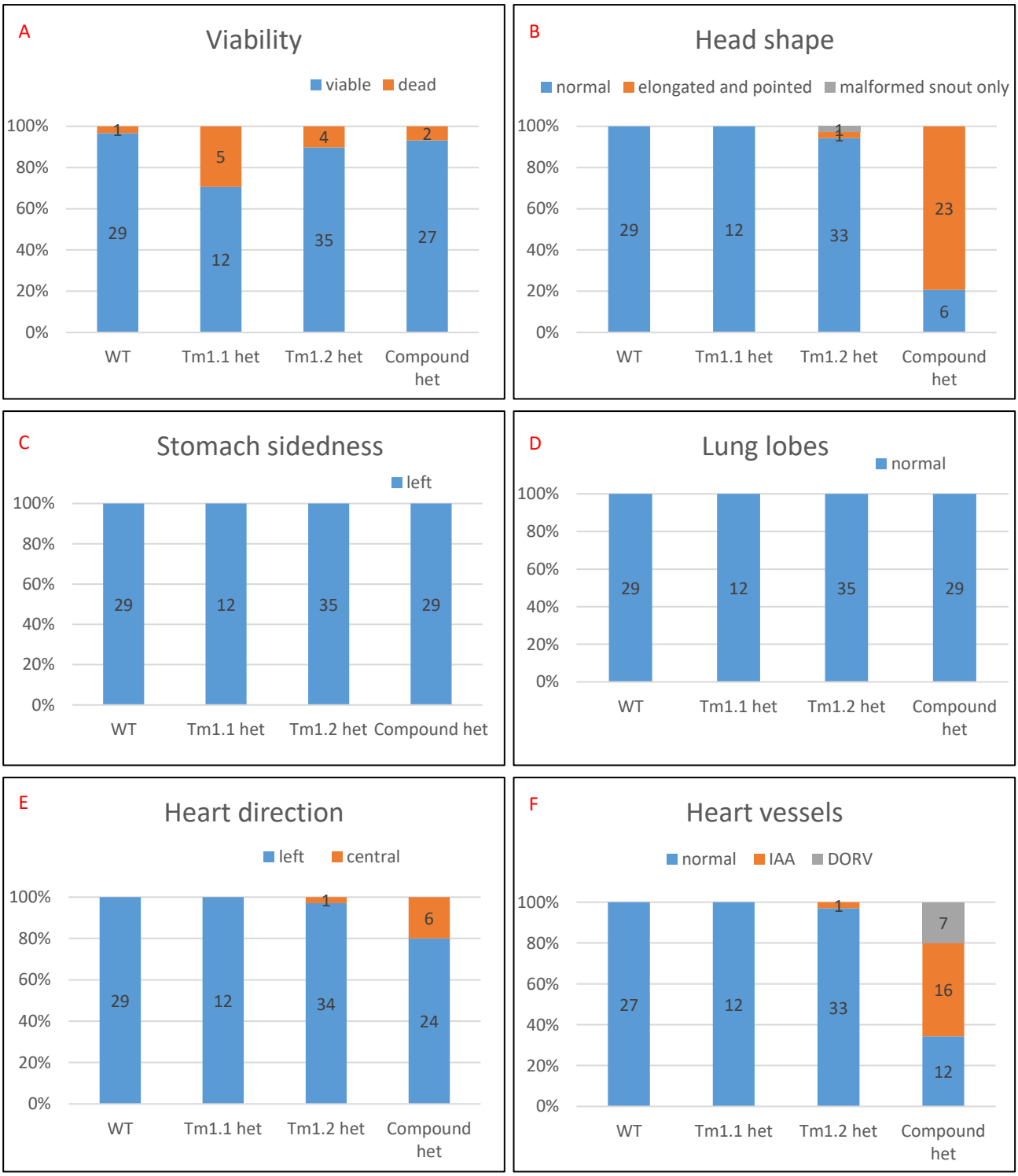


Figure 5.2.4: Analysis of phenotypes in E13.5 *Fgf8* mutant embryos. A shows the number of viable (living) and dead embryos for each of the labelled *Fgf8* genotypes (*Fgf8* WT, Tm1.1 heterozygote, Tm1.2 heterozygote and Compound (Tm1.1 and Tm1.2) heterozygotes). **B** shows the head shape for *Fgf8* WT, Tm1.1 heterozygote, Tm1.2 heterozygote and Compound (Tm1.1 and Tm1.2) heterozygote embryos. **C** shows the positioning of the stomach for *Fgf8* WT, Tm1.1 heterozygote, Tm1.2 heterozygote and Compound (Tm1.1 and Tm1.2) heterozygote embryos. **D** shows the number of lung lobes for *Fgf8* WT, Tm1.1 heterozygote, Tm1.2 heterozygote and Compound (Tm1.1 and Tm1.2) heterozygote embryos, normal refers to characteristic 4 right lobes and 1 left lobe in mouse. **E** shows the direction of the heart apex for *Fgf8* WT, Tm1.1 heterozygote, Tm1.2 heterozygote and Compound (Tm1.1 and Tm1.2) heterozygote embryos. **F** shows the phenotypes of the great vessels of the heart for *Fgf8* WT, Tm1.1 heterozygote, Tm1.2 heterozygote and Compound (Tm1.1 and Tm1.2) heterozygote embryos. IAA= interrupted aortic arch. DORV= double outlet right ventricle. See **Appendix Figure 2** for corresponding example images.

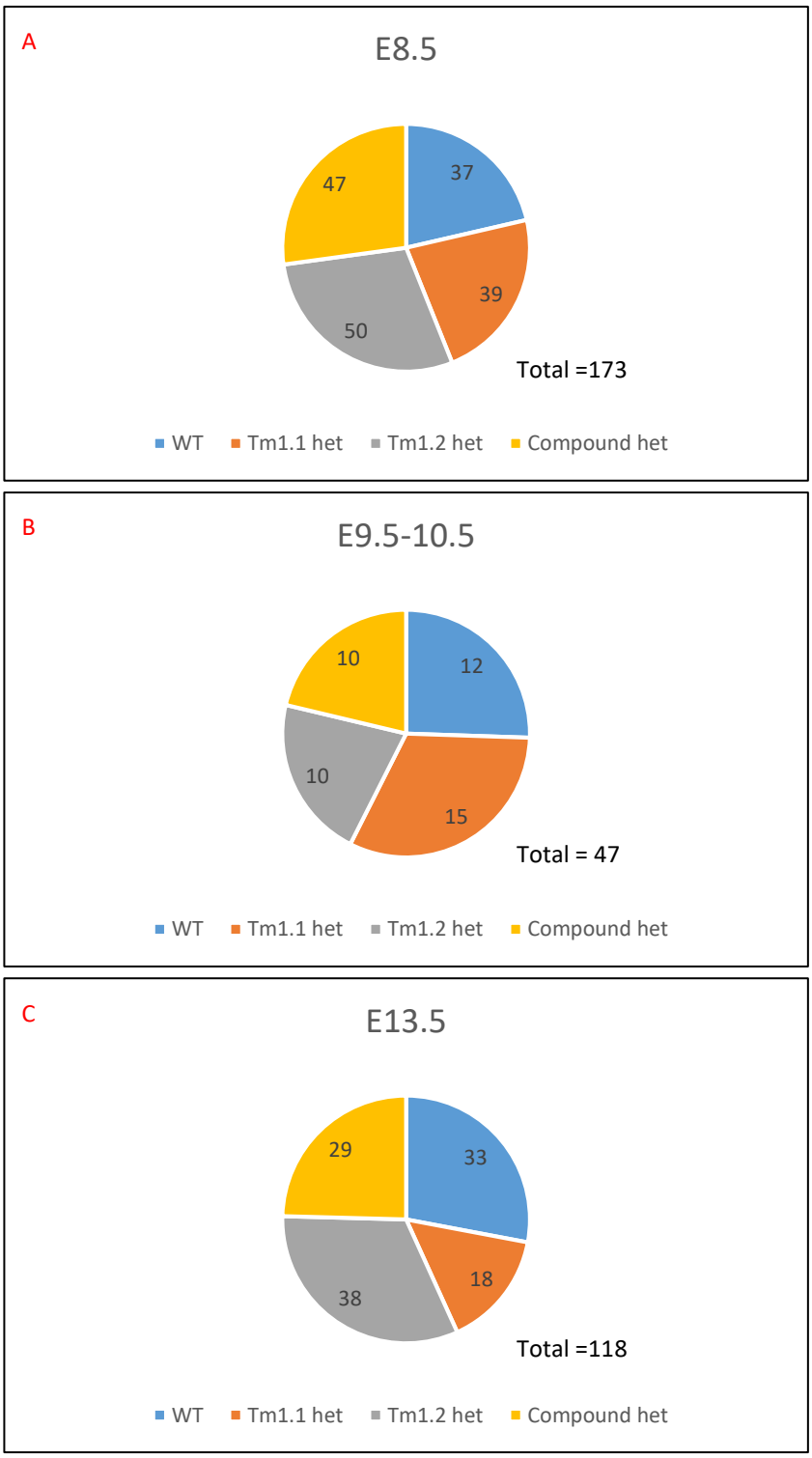


Figure 5.2.5: Analysis of viability of *Fgf8* mutant embryos at embryonic time-points E8.5, E9.5-10.5 and E13.5. **A** shows the number of viable (living) embryos for each of the labelled *Fgf8* genotypes (*Fgf8* WT, Tm1.1 heterozygote, Tm1.2 heterozygote and Compound (Tm1.1 and Tm1.2) heterozygotes) at E8.5. **B** shows the number of viable (living) embryos for each of the labelled *Fgf8* genotypes (*Fgf8* WT, Tm1.1 heterozygote, Tm1.2 heterozygote and Compound (Tm1.1 and Tm1.2) heterozygotes) at E9.5-10.5. **C** shows the number of viable (living) embryos for each of the labelled *Fgf8* genotypes (*Fgf8* WT, Tm1.1 heterozygote, Tm1.2 heterozygote and Compound (Tm1.1 and Tm1.2) heterozygotes) at E13.5.

Analysis of gene expression in E8.5 mutant embryos

To assess the genetic asymmetries which underlie L/R patterning defects, I simultaneously assessed expression of two genes in E8.5 embryos: *Cerl2* and *Pitx2*. The expression patterns of these two genes are distinct, with *Cerl2* being the first gene known to show asymmetry at the node, with R>L expression from the LHF stage. In contrast, *Pitx2* is expressed symmetrically in the developing head-folds and asymmetrically in the L-LPM but not R-LPM from 3/4ss. This is induced by asymmetric R<L *Nodal* node and L-LPM expression (Little and Norris 2020). My simultaneous analysis of *Cerl2* and *Pitx2* expression was preceded by experimentation to determine the relative levels required for each probe (data not shown).

Pitx2 expression was detected in the L-LPM of 8/9 wild-type 4ss+ embryos (**Figure 5.2.6**). In one embryo no *Pitx2* expression was seen, consistent with failure of WISH in that sample. However, the expression in other genotypes proved more variable. Three of five $Fgf8^{Tm1.1}$ heterozygotes, 7/10 $Fgf8^{Tm1.2}$ heterozygotes and 3/6 $Fgf8^{Tm1.1/Tm1.2}$ compound heterozygotes showed L-LPM *Pitx2* expression. Strikingly, the 2/5 $Fgf8^{Tm1.1}$ heterozygotes, 3/10 $Fgf8^{Tm1.2}$ heterozygotes and 3/6 $Fgf8^{Tm1.1/Tm1.2}$ compound heterozygotes not showing LPM *Pitx2* were all 4ss embryos. This is the stage when we expect to see *Pitx2* expression in the L-LPM first begin to become apparent, consistent with delayed in induction of L-LPM *Pitx2*. The presence of *Pitx2* expression in the developing head-folds of these embryos provides an internal control, establishing that WISH has worked and that the lack of L-LPM *Pitx2* in not artefactual. Amongst the $Fgf8^{Tm1.1}$ heterozygote, $Fgf8^{Tm1.2}$ and $Fgf8^{Tm1.1/Tm1.2}$ compound heterozygote genotypes, the embryos which showed L-LPM *Pitx2* expression were all at the 5ss or later. This would support the hypothesis that *Pitx2* L-LPM expression is only delayed, rather than absent.

LPM asymmetry is normally controlled by earlier molecular asymmetry at the node. In order to assess this I analysed *Cerl2* expression by WISH. Consistent with published data *Cerl2* showed R>L asymmetry in 20/22 wild-type embryos (**Figure 5.2.7**). The remaining

2 embryos (both 0ss) were scored as R=L *Cerl2* expression at the node. This is almost certainly due to high levels of staining making *Cerl2* asymmetry challenging to score. Of the 21 *Fgf8*$^{Tm1.1}$ heterozygote embryo analysed, 14 expected R>L *Cerl2*, whilst 5 showed R=L symmetry. All of these 5 embryos were at the LHF stage, the stage when we first expect to see *Cerl2* asymmetry. A further 2 embryos showed unclear or odd expression, as shown in **Figure 5.2.7 E**, with a single line of expression at the node, which is arguably a very strong asymmetry or indicative of major node mispatterning. Similar to the wild-type embryos, the *Fgf8*$^{Tm1.2}$ heterozygotes showed R>L asymmetry in 21/23 embryos, and R=L symmetry in the remaining 2. The *Fgf8*$^{Tm1.1/Tm1.2}$ compound heterozygotes had a distinctly more variable *Cerl2* expression pattern, with only 9/29 showing the expected R>L asymmetry, 13/29 having R=L expression, 4 R<L asymmetric expression and 3 embryos showing unclear node expression, as in **Figure 5.2.7,** with only 1 line of *Cerl2* expression at the node. The presence of embryos with the abnormal (unclear/odd categorised) *Cerl2* node expression pattern in both *Fgf8*$^{Tm1.1}$ heterozygotes and the *Fgf8*$^{Tm1.1/Tm1.2}$ compound heterozygotes is intriguing, especially when considering the presence of cardiac and great vessel defects seen in the *Fgf8*$^{Tm1.1/Tm1.2}$ compound heterozygotes, but no situs defects/phenotypes in the *Fgf8*$^{Tm1.1}$ heterozygotes, or even the homozygotes.

While assessing the asymmetry of the expression of perinodal *Cerl2*, I also noticed a number of embryos exhibiting some “extra-nodal” *Cerl2* or *Pitx2* expressing cells. These cells were present across a variety of embryonic stages, including prior to the 3ss when LPM *Pitx2* is first seen. In combination with their localisation close to the node it seems most likely that this expression is of *Cerl2* rather than *Pitx2*. These cells were generally positioned posterior to the node, and were present in varying numbers. I characterised these by number seen (**Figure 5.2.8**), with no cells expressing *Cerl2* except at the node categorised as “none” (**Figure 5.2.8** E), with “few” being 1 or 2 extra-nodal cells (**Figure 5.2.8 D**), “some” being 3 cells or more (**Figure 5.2.8 C**), and “many” being a number of extra-nodal *Cerl2* expressing cells that are not possible to distinctly count (such as in

Figure 5.2.8 B, where the cells are densely clustered), or greater than 10 individual cells. When this data is displayed according to genotype (**Figure 5.2.8 A**), it is apparent that the presence of a few of such cells occurs in wild-type embryos (5/14 assessed), with the same proportion also being present in *Fgf8*$^{Tm1.2}$ heterozygote embryos (5/9). 1 of the 6 *Fgf8*$^{Tm1.1}$ heterozygote embryos analysed showed 3-10 cells expressing *Cerl2* near to the node. The presence of extra-nodal *Cerl2* expressing cells is however much more apparent in *Fgf8*$^{Tm1.1/Tm1.2}$ compound heterozygous embryos, with only 2/17 embryos having none of these cells, 10/17 showing a few, 2 showing some and a further 3 showing many extra-nodal *Cerl2* expressing cells. These data suggest that there may be some defect in cell identity, with cells predominantly posterior to the node exhibiting gene expression consistent with them being node crown cells. Other possibilities include that these cells may have migrated away from the node, or be endodermal cells produced by the node. It is also possible, though unlikely, that the expression seen in these cells posterior to the node is actually *Pitx2*, in which case these could prove to be ectopic head-fold of L-LPM cells.

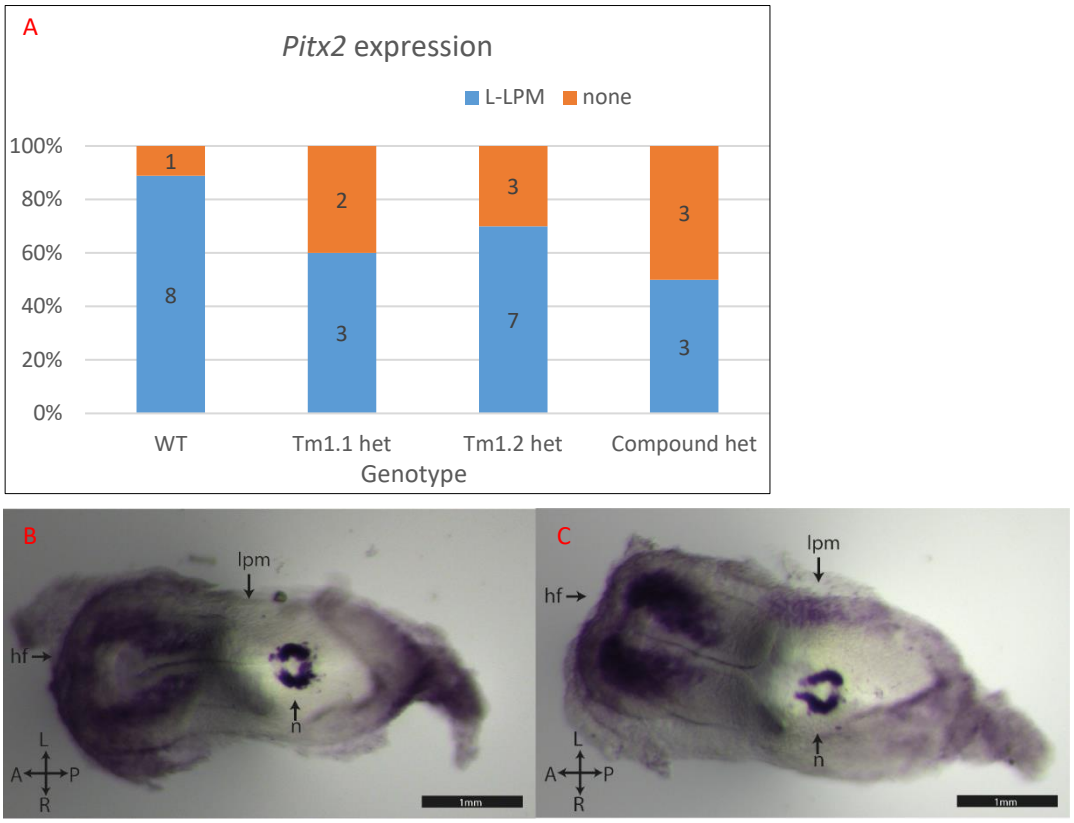


Figure 5.2.6: Expression of *Pitx2* in the LPM of Fgf8 mutant mouse embryos. A shows the numbers of each of the labelled genotype embryos with L-LPM *Pitx2* expression (blue) and with no LPM *Pitx2* expression (orange). **B-C** are example images for each of these categories, both at the 4ss. Head-folds (hf), node (n) and lateral plate mesoderm (lpm). Anterior (A), posterior (P), left (L) and right (R) axes are indicated. Scale bar = 1mm. **B** shows a compound heterozygote embryo with no *Pitx2* LPM expression. **C** shows a wild-type embryo with L-LPM *Pitx2* expression. The stain at the node (n) for both embryos shows *Cerl2* expression.

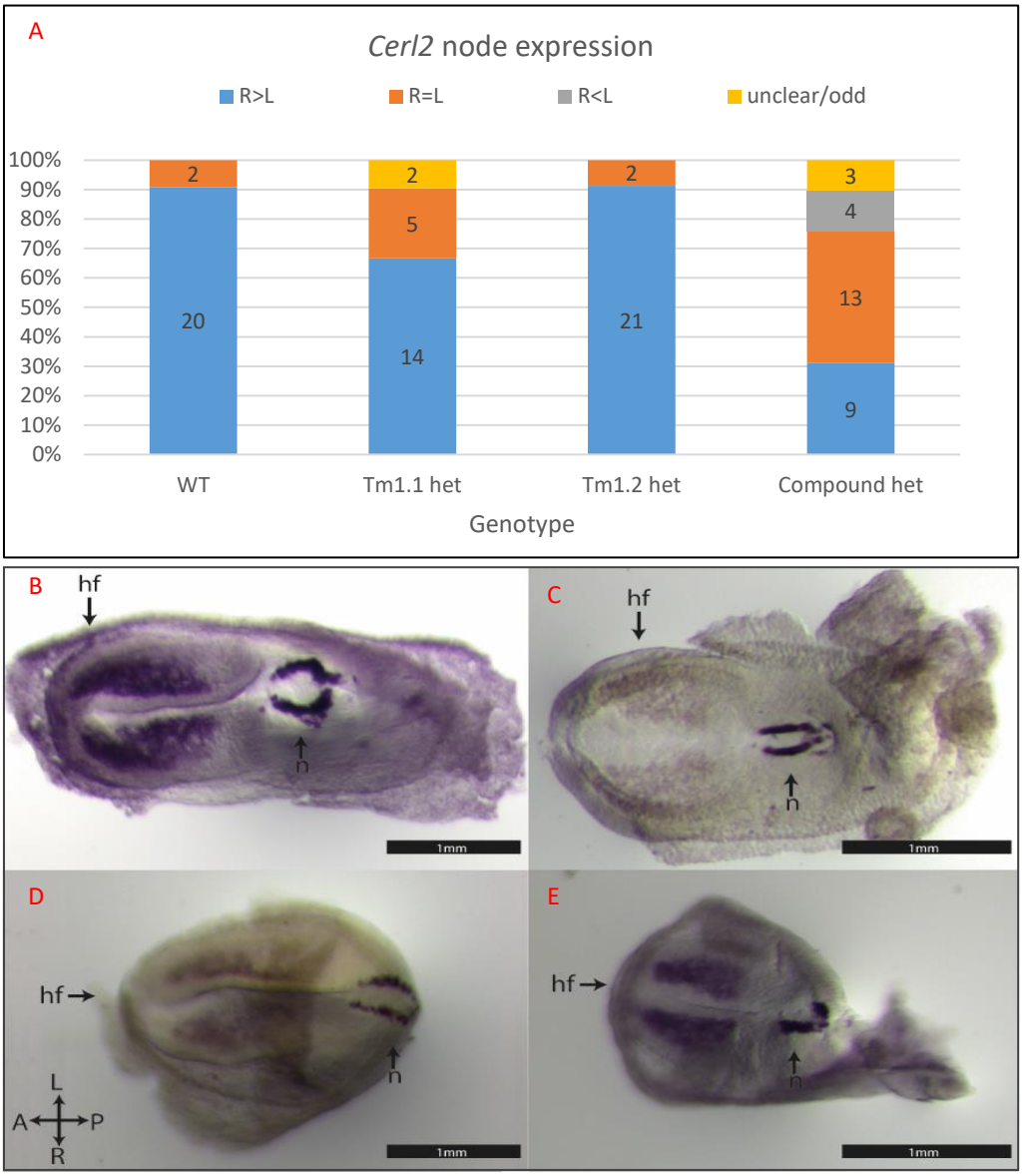


Figure 5.2.7: Expression of *Cerl2* in the node of Fgf8 mutant mouse embryos. A shows the numbers of each of the labelled genotype embryos with R>L (blue), R=L (orange). R<L (grey) and unclear/odd (yellow) *Cerl2* node expression. **B-E** are example images for each of these categories, various genotypes and developmental stages, with anterior (A), posterior (P), left (L) and right (R) axes, node (n) and head-folds (hf) indicated. Scale bars = 1mm. **B** shows R>L *Cerl2* node expression in a 2ss compound heterozygote embryo. **C** shows R=L *Cerl2* node expression in a 2ss compound heterozygote embryo. **D** shows R<L *Cerl2* node expression in a 1ss compound heterozygote embryo. **E** shows unclear *Cerl2* node expression in a 2ss Tm1.1 heterozygote embryo. In **B-E**, *Pitx2* expression is visible in the developing head.

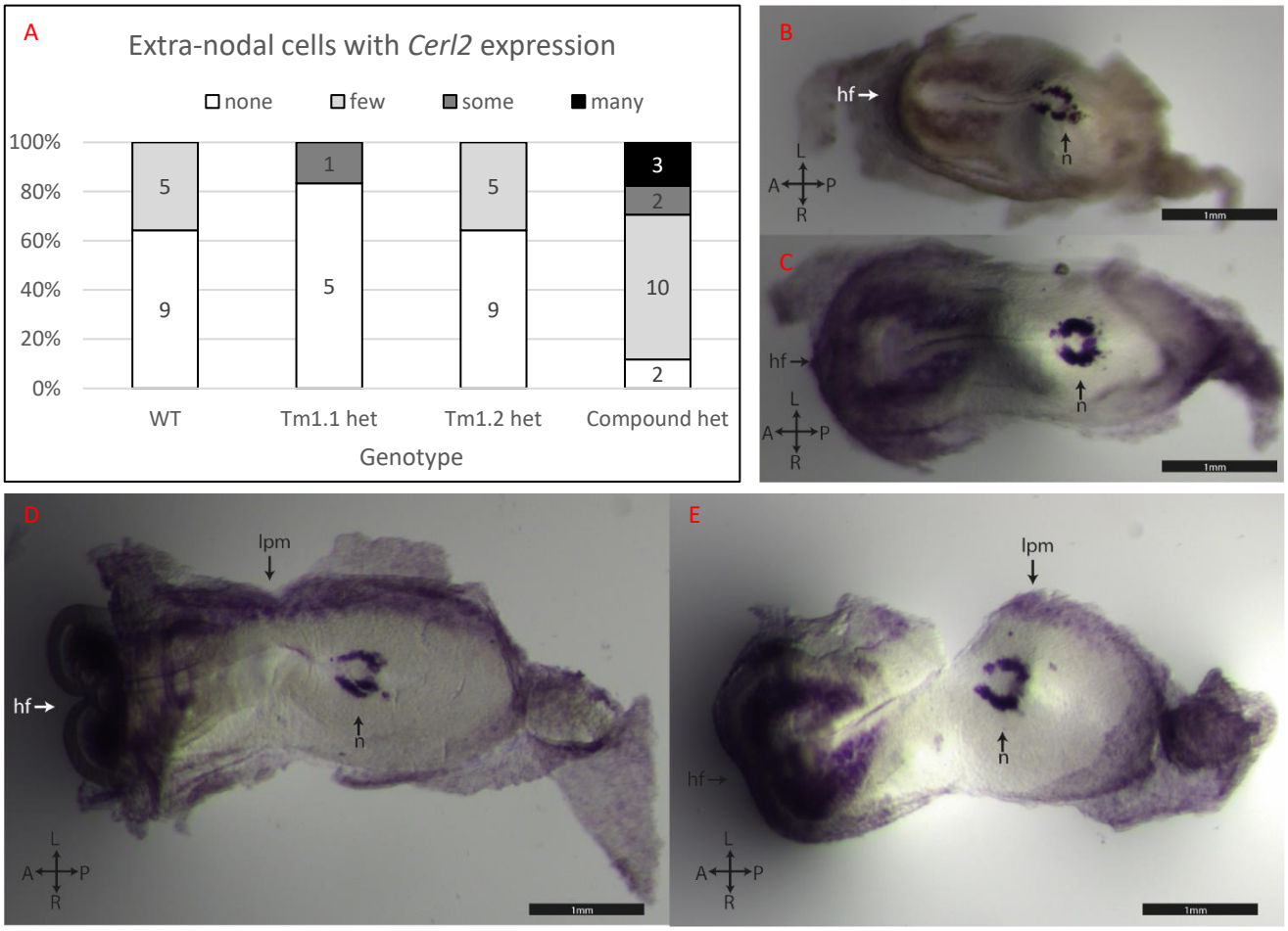


Figure 5.2.8: Expression of *Cerl2* in cells posterior to the node of Fgf8 mutant mouse embryos. A shows the numbers of each of the labelled genotype embryos with no extra cells (white), few extra cells (light grey). Some extra cells (dark grey) and many extra cells (black) with *Cerl2* expression. **B-E** are example images for each of these categories, with various genotypes and developmental stages. Anterior (A), posterior (P), left (L) and right (R) axes, node (n), head-folds (hf) and lateral plate mesoderm (lpm) are indicated. Scale bars = 1mm. **B** shows a 2ss compound heterozygote embryo with many extra-nodal *Cerl2* expressing cells. **C** shows a 5ss compound heterozygote embryo with some extra-nodal *Cerl2* expressing cells. **D** shows a 7ss Tm1.2 heterozygote embryo with few extra-nodal *Cerl2* expressing cells. **E** shows a 6ss wild-type embryo with no extra-nodal *Cerl2* expressing cells. In **B-E**, *Pitx2* expression is visible in the developing head, and also present in the L-LPM in **D-E**.

Analysis of E8.5 mutants- SEM

My FGF inhibitor culture experimentation suggested a potential defect in the formation of the node when FGF signalling is perturbed. This was combined with gene expression analysis which suggests the possibility of aberrant cell identity in the region of the node of the *Fgf8* mutants. It therefore seemed logical to directly examine the physical morphology of the node in $Fgf8^{Tm1.1/Tm1.2}$ compound heterozygous embryos. Analysing this by SEM allows not only node structure to be assessed, but also of cilia length and the presence of putative NVPs, both of which have been implicated to be regulated in some manner by FGF signalling.

When examining E8.5 embryos by SEM the stage of development must be taken into consideration, as this stage spans the maturation of the node. During this time it fully emerges from overlying endoderm, becomes tear-drop shaped and elongates as the embryo grows, before beginning to close as the closing hindgut covers it. I observed a variety of differences in the shape and structure of the node, leading me to categorise the shape of these nodes into 5 discrete categories. Example images for each category are shown: normal (**Figure 5.2.9 B-D**), normal-but-broken (**Figure 5.2.9 E-F**), elongated (**Figure 5.2.9 G-H**), overlying cells (**Figure 5.2.9 I-J**) and incomplete node with overlying cells (**Figure 5.2.9 K-L**). The normal category includes embryos which have characteristic node shape and structure for the developmental stage which they are at. The normal-but-broken group indicates that embryos are as expected for developmental stage, but some damage (due to processing) at or near the node means a complete view of structure/shape is not possible. Elongated nodes were so categorised due to a long, rather than characteristic tear-drop shape. Nodes with overlying cells have some overlying endodermal cells present that have failed to migrate to reveal the underlying node. Similarly, incomplete nodes with overlying cells could be said to be a more severe version of the previous category, and encompass node structures which are incomplete, and in some cases present as multiple mini nodes, which have not resolved to form one

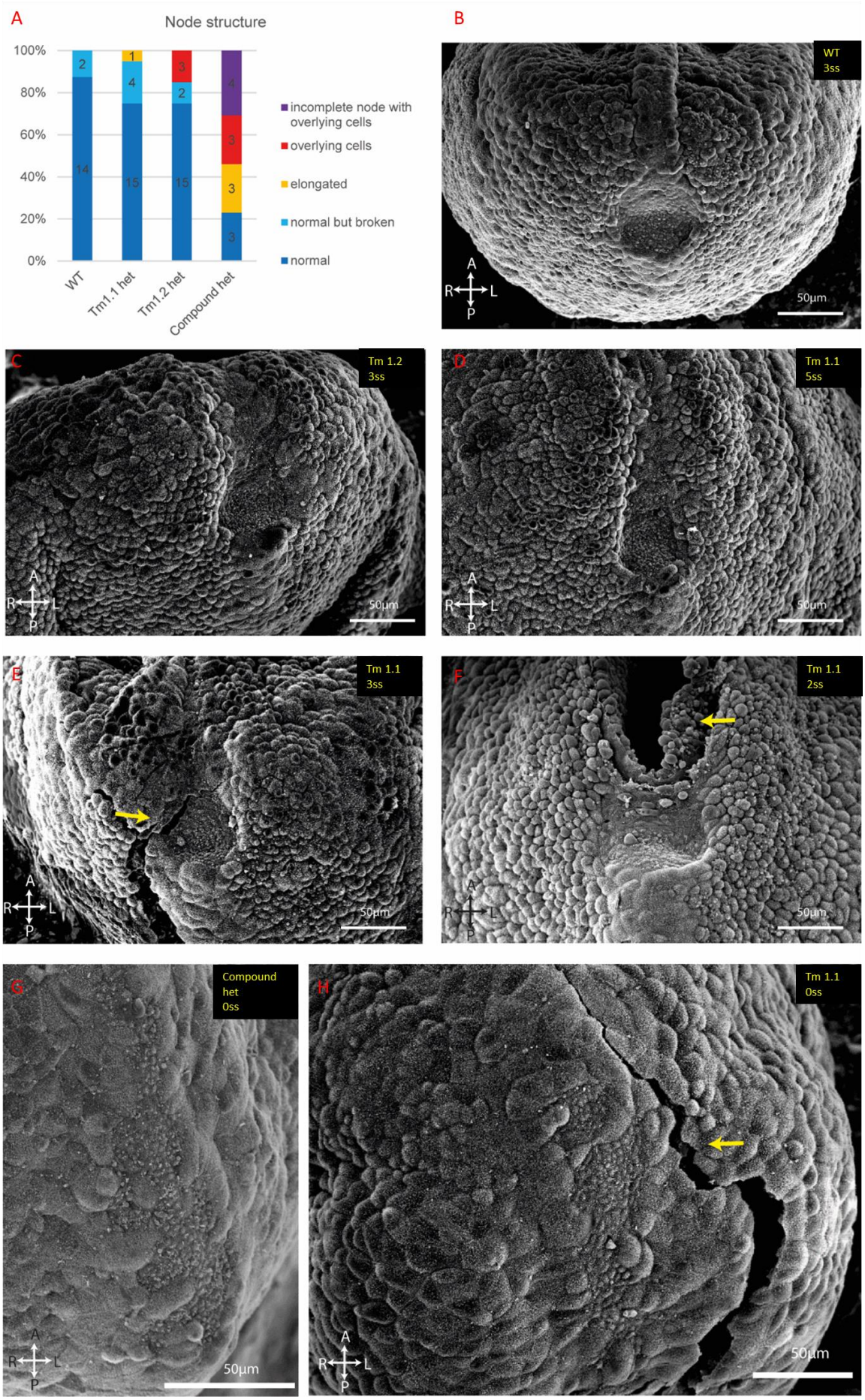
continuous tear-drop shape. All wild-type embryos showed normal node structure/morphology, with 2/16 categorised as normal-but-broken, and the rest as normal (**Figure 5.2.9 A**). *Fgf8*$^{Tm1.1}$heterozygous embryos showed normal structure in 15/20 that were examined, with 4 more that were normal-but-broken, and one additional embryo which showed an elongated node (**Figure 5.2.9**). Similarly, the majority of *Fgf8*$^{Tm1.2}$ heterozygous embryo nodes showed normal structure (15 normal and 2 normal-but-broken out of 20 total), although 3 embryos had overlying cells present partially occluding the node structure (**Figure 5.2.9**). When examining the structure of *Fgf8*$^{Tm1.1/Tm1.2}$ compound heterozygote embryos nodes, I found that only a small proportion showed normal node structure (3/13), with 3 embryos each in the categories of elongated node shape and presence of overlying endodermal cells. A further 4 embryos showed incomplete node structure, with a large number of cells from the overlying endoderm that appear to have failed to move away to reveal the underlying node (**Figure 5.2.9**).

These results show that the node has failed to form correctly in the majority of *Fgf8*$^{Tm1.1/Tm1.2}$ compound heterozygotes. This may be coupled with the high proportion of *Fgf8*$^{Tm1.1/Tm1.2}$ compound heterozygous embryos which showed abnormal *Cerl2* expression at the node, and ultimately translate into L/R defects evident in the formation and patterning of cardiac great vessel deformities at the E13.5.

From these same SEM images I analysed the average length of the cilia within each node (**Figure 5.2.10**). To do this 13 cilia in each embryo were measured (Joel software), and an average cilia length calculated for that embryo (**Figure 5.2.10**). When examined by genotype, there are significant (p=0.011, two-tailed t-test) differences in average cilia length between wild-type (mean = approximately 2.5 µm) and *Fgf8*$^{Tm1.2}$ heterozygotes (mean = approx. 2.1 µm), and also between wild-type and *Fgf8*$^{Tm1.1/Tm1.2}$ compound heterozygotes (mean cilia length 1.95 µm) (p=0.007, two-tailed t-test) (**Figure 5.2.10 A**). Due to the expected increase in cilia length over developmental time (Lee and Anderson 2008), I re-plotted my data by developmental stage (**Figure 5.2.10 B**). A clear trend is

evident when examining the length of the cilia in the *Fgf8*$^{Tm1.1/Tm1.2}$ compound heterozygotes compared to the wild-types, with a shorter cilia length in the *Fgf8*$^{Tm1.1/Tm1.2}$ compound heterozygotes than wild-types at all stages except for the LHF. For both the *Fgf8*$^{Tm1.1}$ and *Fgf8*$^{Tm1.2}$ individual heterozygote genotypes, there appears to be a slight decrease in the cilia length also, though less pronounced/obvious than with the *Fgf8*$^{Tm1.1/Tm1.2}$ compound heterozygotes. Unfortunately, statistical analysis was not possible when the data was separated in this manner, due to low numbers of some genotypes at each developmental stage examined.

Finally, as Tanaka and colleagues had posited a role for FGF8 in the regulation of NVP release, I assessed the number of spherical vesicular (NVP-like) objects within the nodes of these embryos (henceforth referred to as NVPs for convenience). There were no significant differences between the number of these by genotype (unpaired Welch's t-test), though some outliers were present with much higher values for one *Fgf8*$^{Tm1.1}$ heterozygous embryo, and 2 *Fgf8*$^{Tm1.1/Tm1.2}$ compound heterozygous embryos (**Figure 5.2.11 A**). When separated by developmental stage (**Figure 5.2.11 C**), statistical analysis cannot be carried out due to the low number of samples at each stage. In order to achieve enough experimental power a very large cohort would be required to allow for the genotypes and stages required, which is beyond the scope of analysis I could complete. However, there is a general trend of increased number of NVPs in the *Fgf8*$^{Tm1.1/Tm1.2}$ compound heterozygotes at most developmental stages. This suggests there may be some correlation between FGF signalling and NVP release.


A
Node structure
100%
80%
60%
40%
20%
0%
WT
Tm1.1 het
Tm1.2 het
Compound het
incomplete node with overlying cells
overlying cells
elongated
normal but broken
normal
B
WT
3ss
C
Tm 1.2
3ss
D
Tm 1.1
5ss
E
Tm 1.1
3ss
F
Tm 1.1
2ss
G
Compound
het
0ss
H
Tm 1.1
0ss
50µm

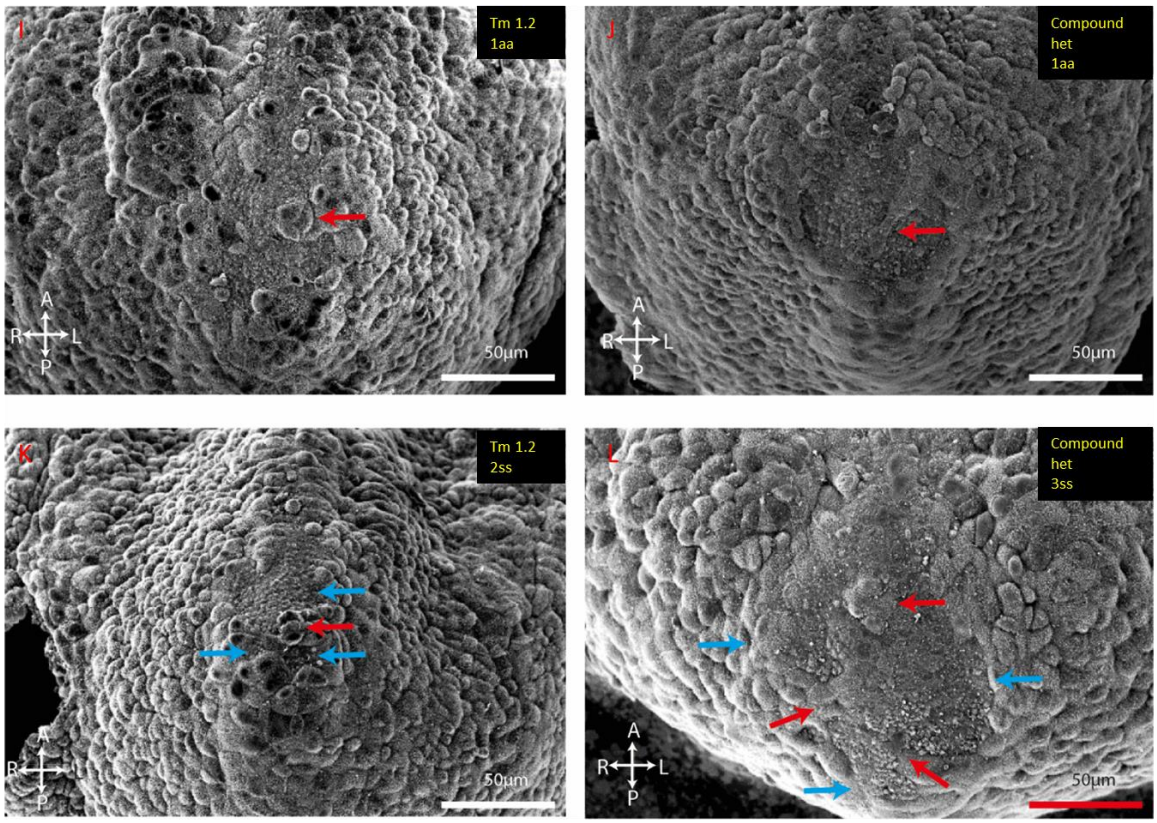
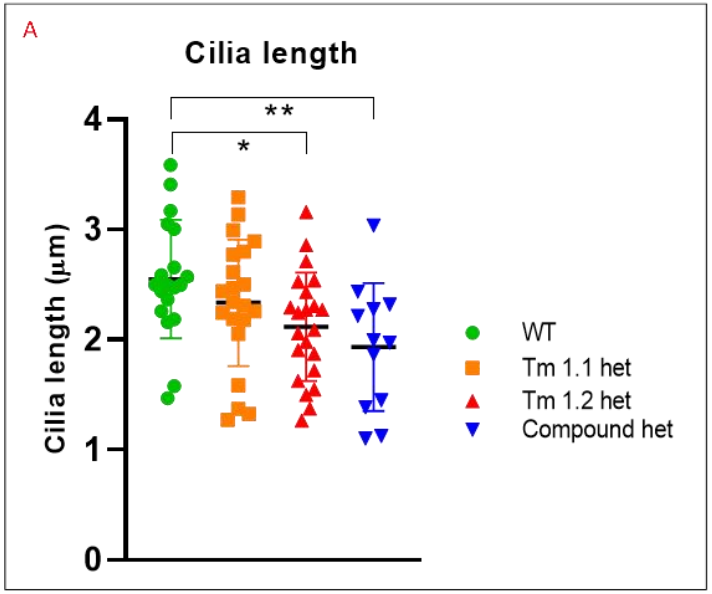
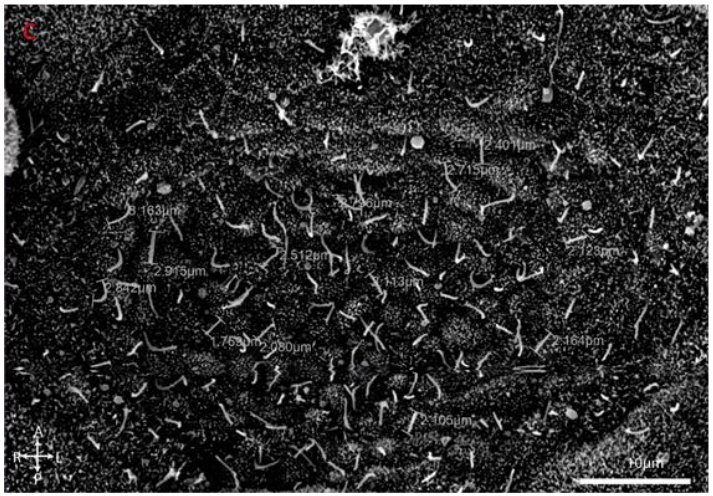


Figure 5.2.9: Node structure of *Fgf8* mutant embryos. **A** the nodes of embryos belonging to the labelled genotypes were categorised compared to normal morphology for developmental stage. Images in **B-L** are examples from each of the categories in **A**. For each, the anterior (A), posterior (P), left (L) and right (R) axes are indicated, and scale bar = 50µm. **B**-**D** show example nodes categorised as normal (dark blue in **A**). **E**-**F** shows example embryos with nodes categorised as normal but broken (light blue in **A**). Here, the node as can be seen in normal, but cracks (indicated by yellow arrows) are visible. **G**-**H** show abnormal nodes scored as elongated (yellow in **A**). **I**-**J** show nodes with overlying cells present (indicated by red arrows), which are not usually seen in WT embryos (these embryos are represented in red in **A**). **K**-**L** show embryos with incomplete nodes with overlying cells. Overlying cells are indicated (red arrows), along with patches of ciliated node cells indicated by blue arrows; these embryos are represented in purple in **A**. Genotypes and stages of each embryo are indicated in yellow text, black box, top right of each SEM image.





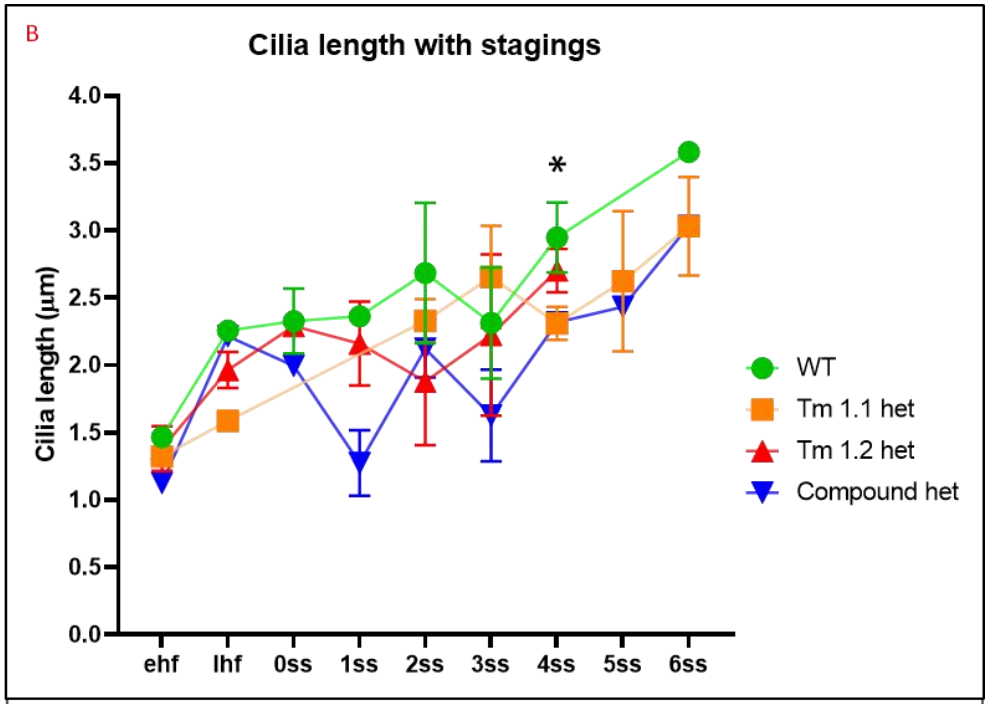


Figure 5.2.10: Analysis of cilia length in Fgf8 mutant nodes.. **A** shows the length of cilia in WT, Tm1.1 heterozygous, Tm1.2 heterozygous and compound (Tm1.1 and Tm1.2) heterozygous mouse nodes. * shows a significant difference in the length of wild-type embryo (green circle) cilia and Tm1.2 heterozygous embryo (red triangle) cilia (p=0.011, two-tailed t-test). ** shows a significant difference in the length of wild-type embryo (green circle) cilia and compound heterozygous embryos (blue triangle) cilia (p=0.007, two-tailed t-test). **B** shows the length of cilia in WT, Tm1.1 heterozygous, Tm1.2 heterozygous and compound (Tm1.1 and Tm1.2) heterozygous mouse nodes, along with developmental stage of the embryos from which the average cilia length measurements were taken. Where no error bars are present only 1 embryo was present for this particular genotype and developmental stage. * denotes a significant difference between the WT (green circle) and Tm1.1 het (orange square) values at the 4ss (p=0.0191 student's t-test). **C** shows an example of cilia measurements taken. Individual cilia lengths are measured and indicated, scale bar = 10µm.

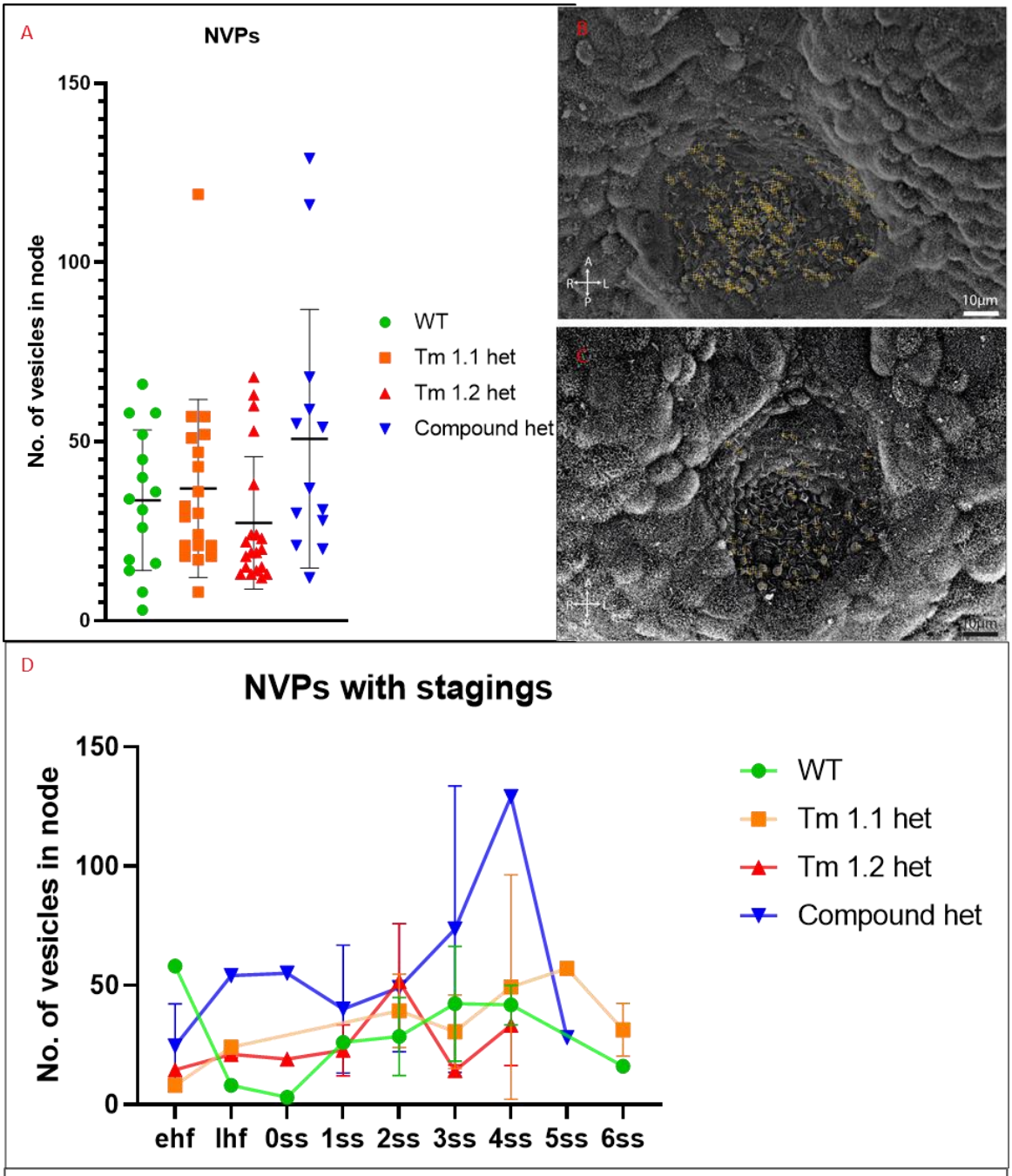


Figure 5.2.11: Analysis of number of NVP-like objects in Fgf8 mutant nodes. A shows the number of spherical vesicles (NVPs) in the nodes of Fgf8 WT, Tm1.1 heterozygotes, Tm1.2 heterozygotes and compound (Tm1.1 and Tm1.2) heterozygote embryos. **B** and **C** show images of vesicle counts in compound heterozygote (**B**) and wild-type (**C**) examples. In both, anterior (A), posterior (P), left (L) and right (R) axes are indicated. Scale bars = 10µm. **D** shows the number of spherical vesicles (NVPs) in the nodes of Fgf8 WT, Tm1.1 heterozygotes, Tm1.2 heterozygotes and compound (Tm1.1 and Tm1.2) heterozygote embryos with the developmental stage of the embryo. Where no error bars are present only 1 embryo was present for this particular genotype and developmental stage.

5.3 Discussion

5.3.1 Hypotheses for the role of FGF signalling in L/R patterning

The presence of heart situs and great vessel defects in the *Fgf8*$^{Tm1.1/Tm1.2}$ compound heterozygote embryos, combined with the aberrant *Cerl2* expression, indicate that L/R patterning is perturbed in a proportion of these mutants. An independent role for *Fgf8* in the formation of the heart has previously been described (Abu-Issa et al. 2002), with *Fgf8* expression in the pharyngeal endoderm being required for normal cardiovascular morphology (Brown et al. 2004). However, it is difficult to unravel the disparate roles of *Fgf8* in the heart and L/R patterning, as L/R asymmetry and *Nodal* expression directly influences heart patterning (Desgrange et al. 2020). The presence of extra-nodal cells expressing node crown cell markers seems to indicate that the node has not correctly formed. Indeed, SEM analysis clearly shows the presence of malformed nodes in the majority of *Fgf8*$^{Tm1.1/Tm1.2}$ compound heterozygotes. As the node structure is abnormal in a large proportion of these mutants, it may be that there is still enough normal nodal flow created and crown cells correctly patterned present to interpret the flow. Therefore, even though the node is not correctly formed in a number of these embryos, a reduced proportion actually show aberrant *Pitx2* expression and heart situs defects.

The presence of a similar node structure defect in a single *Fgf8*$^{Tm1.1}$ heterozygote, and in a few *Fgf8*$^{Tm1.2}$ heterozygotes suggests that there is both dosage sensitivity and variable expressivity for *Fgf8*. However, the number of extra-nodal *Cerl2* expressing cells posterior to the node for both of these genotypes were not dissimilar to that of the wild-types, although the *Cerl2* node expression in the *Fgf8*$^{Tm1.1}$ heterozygotes was more variable than for the *Fgf8*$^{Tm1.2}$ in phenotypic presentation across the genotypes for the different *Fgf8* alleles.

Alternatively, or even additionally to a role in node patterning, the data examining the length of cilia in the nodes of the *Fgf8* mutant embryos supports the hypothesis that *Fgf8*

functions to regulate the length of nodal cilia. The general trend of a decreased cilia length in *Fgf8*$^{Tm1.1/Tm1.2}$ compound heterozygous embryo nodes, when compared to those of wild-types at the same developmental stage, suggests that there is a role for FGF signalling in the regulation of cilia length. My data showing decreased cilia length in the mouse node, where FGF8 function is perturbed, concurs with analysis of FGFR1 knock-downs in the frog and fish (Neugebauer et al. 2009). Their data also shows a decrease in the length of cilia in the equivalent LROs when FGFR1 function is limited, by either dominant-negative protein expression, or morpholino knock-down of intrinsic *fgfr1*. This suggests a role for FGF signalling in cilia growth, though the precise mechanism by which this would be functioning is unclear. Any effect on cilia length could plausibly impact flow, and might lead to a delay in the production of the leftward laminar flow needed to break symmetry.

A role for *Fgf8* in the regulation of the release of NVPs in the node, is neither supported nor disproven by my analysis presented in this chapter. Generally, when matched by developmental stage, the numbers of vesicles in wild-type embryo nodes was lower than in those of *Fgf8*$^{Tm1.1/Tm1.2}$ compound heterozygotes. However, there is no statistical support for the results when split by developmental stage, due to the numbers analysed. A number of further embryos for a variety of stages would need to be analysed in order to give a better understanding of how FGF signalling and nodal vesicles may be related, and as this analysis would need to include both comparative developmental stages and genotypes, is beyond the scope of analysis possible during my thesis. If FGF8 does function in regulating the release of NVPs in the node, we would expect there to be an obvious difference in the number of these in *Fgf8*$^{Tm1.1/Tm1.2}$ compound heterozygotes when compared to the wild-type littermates' nodes. However, it may be that this is dependent on the amount of functional FGF8 present specifically in each node, and that there is variable expressivity of this between different embryos of the same *Fgf8*$^{Tm1.1/Tm1.2}$ genotype, and as such any difference is masked by unaffected samples.

Overall, my data does not discount any of the three hypotheses proposed here for a putative role for *Fgf8* and its product. However, the evidence presented here does strongly support a role in the formation of the node, along with the suggestion of a potential of a role for *Fgf8* in the regulation of the length of nodal cilia. It may be that *Fgf8* has a role in both of these, which together provide the mechanism for the basis of perturbed L/R asymmetry, as seen in some *Fgf8*$^{Tm1.1/Tm1.2}$ embryos. Alternatively, the role of one may have more functional importance than the other. Additionally it remains formally possible that there is a role in regulation of NVP release.

5.3.2 Non-situs phenotypes in *Fgf8*$^{tm1/tm2}$ embryos

The presence of brain defects in our analysis of embryos carrying the *Fgf8*$^{Tm1.1}$ allele was expected from the analysis of Meyers and Martin (1998), which had previously characterised phenotypes affecting the cerebellum and olfactory bulb. Meyers and Martin explain the underlying pathology of these phenotypes in terms of *Fgf8* expression, which was known to be present in the developing midbrain/hindbrain junction; a role in the formation of the cerebellum was therefore implied. Similarly, *Fgf8* is present in the olfactory placode, which develops into the olfactory bulbs (Menini 2010; Visel et al. 2004). Since their analysis, more has been discovered about the role of FGF8 in these contexts. Signalling through FGFR1, FGF8 has been shown to function in the A-P patterning of the telencephalon, which is the embryonic structure which forms distinct brain regions including the olfactory bulb (Hébert et al. 2003; Sato et al. 2017). FGF8 also functions to organise the midbrain/hindbrain junction by induction of *En1* and *Pax2* expression, which act to specify the midbrain; FGF8 also activates the Ras-ERK pathway to specify the hindbrain (Harada et al. 2016). Therefore, the phenotypes of olfactory bulb and cerebellum defects fit with what is known about FGF8 signalling function. The presence of these phenotypes in heterozygous *Fgf8*$^{Tm1.1}$ embryos at E13.5, however, was unexpected, as no

phenotype was reported for this genotype in the 1998-9 analyses (Meyers et al. 1998; Meyers and Martin 1999). It is, perhaps, due to the difference in genetic background between our analysis and that analysed by Meyers, leading to variability in the expressivity of *Fgf8*.

The abnormalities in the lobe morphology of the right lung, seen in one each of the *Fgf8*$^{Tm1.1}$ heterozygous and homozygous E13.5 embryos analysed by micro-CT was not something that Meyers and Martin had reported. They did report an 8% incidence of RPI in their *Fgf8*$^{Tm1.1}$ homozygous embryos, but no other lung abnormalities were mentioned. It is possible that, as these defects in shape of the right lung lobes are more subtle than a RPI phenotype, leading them to be missed by their analyses. However, as they reported no phenotypes in heterozygotes, it is perhaps more likely that no such phenotypic abnormalities of lung lobe shape were present. The underlying mechanism controlling the precise size and shape of individual lung lobes is not well understood (Warburton et al. 2005), and how this may be related to L/R patterning remains uncertain. The branching programme of the lungs as they are formed is better characterised, and interestingly requires FGF10 for correct branching morphogenesis, although the mechanism is not fully understood (Jones et al. 2020). FGF8 and FGF10 have been proposed to have overlapping roles in the context of the formation of the secondary heart field (Watanabe et al. 2010), and so a similar functional redundancy or compensatory in this context is plausible.

5.3.3 Dosage sensitivity

The differences in phenotype seen between individual embryos of the same genotype is most likely due to the nature of the alleles and the quantity of functional mRNA produced, with the amount of active, functional FGF8 protein varying between individual embryos. This leads to variable expressivity and ultimately a stochastic outcome whereby some

embryos exhibit a phenotype and others do not. This was reported and discussed by Meyers and Martin in their 1998 paper following their examination of the *Fgf8*$^{Tm1.1}$ homozygotes. They reported on the presence of cryptic splice donor and acceptor sites in the neomycin resistance cassette, which leads to the production of what they term *Fgf8-neo* hybrid mRNA, which is expressed along with normal *Fgf8* mRNA. The hybrid mRNA contains a premature stop codon which leads to no exons after (3' to) the *Neo*^{R} cassette being transcribed, and thus any protein produced by this transcript lacks exons 5 and 6, making it equivalent to the null *Fgf8*$^{Tm1.2}$ allele. They additionally show q-PCR data which quantifies a 45% reduction in the level of the wild-type *Fgf8* mRNA transcript in their *Fgf8*$^{Tm1.1}$ homozygotes. As discussed by Meyers and Martin, it is not possible to detect if this reduction in wild-type *Fgf8* mRNA is due to aberrant splicing due to the cryptic splice sites in the *Neo*^{R} cassette, or if this is due to the *Pgk* promoter used to drive the cassette interfering more directly with the *Fgf8* expression, as reported in other contexts (Olson et al. 1996). As we have the same allele, our embryos should exhibit the same hypomorphic characteristics, and this is consistent with the varying phenotypes seen in our lines, both the Tm1.1 line and our analysis of the homozygotes showing variability, and in our *Fgf8*$^{Tm1.1/Tm1.2}$ compound heterozygote embryos with variable node morphology and incidence of heart great vessel phenotypes. Of note is that we were unable to carry out quantitative analysis of levels of *Fgf8* expression, which would have been informative and provided greater understanding as to why our line showed differences to that of the 1999 line.

5.3.4 Differences to Meyers and Martins' phenotypes – likely causes

There are clear disparities between the phenotypes seen in my analysis compared to that of Meyers and Martin. The cause of these differences is most likely due to differences in genetic background between the two analyses. There is limited information on the genetic background of the mutant in the original analysis. It is stated that the ES cells used for

production of the targeting vector were from 129 mice, which were then introduced to 8-16 cells embryos from CD1 mice. It is not clear if this line was kept on a CD1 background, or made congenic on any other background. When frozen down for storage by the Jackson laboratory, the line was first made congenic on B6J, and this is the genetic background of the mutants in my analyses. It seems likely that this background is not the same as that utilised by Meyers. The presence of brain abnormalities in *Fgf8*$^{Tm1.1}$ heterozygous embryos by micro-CT suggests an increase in phenotypic severity, as no phenotypes were reported by Meyers and Martin. Similarly, our early embryonic L/R asymmetric gene expression and node analysis showed abnormalities in the *Fgf8*$^{Tm1.2}$ and *Fgf8*$^{Tm1.1}$ heterozygotes that were not reported by Meyers and Martin. However, the incidence of gross L/R situs defects reported by Meyers and Martin in *Fgf8*$^{Tm1.1/Tm1.2}$ compound heterozygote mutants was very high, with over half showing abnormal lung morphology, including a 4% incidence of situs inversus totalis, and 49% right pulmonary isomerism. Our line on a B6J background showed no such phenotypes, with all lungs analysed at the E13.5 stage showing classic 4:1 R:L lung lobation. This suggests a decreased phenotypic severity compared to Meyers and Martin. It is possible that the phenotypic differences seen not only between individual embryos, but also between different genetic backgrounds, may be due to differing amounts of functional FGF8 protein in different parts of the developing embryo. It may be in some mutants that the ratio of normal *Fgf8* to hybrid mRNA may not be consistent, and lead to more severe or obvious phenotypes in the brain. Indeed, the ratio may be different in the early embryo as the node is being formed and the nodal cilia grow. It may be that in B6J the threshold of functional gene product varies from that of other genetic backgrounds, such that differences in the effect of a gene perturbation may have a strain-specific impact. Such effects have previously been studied, and interestingly, genetic background has been shown to have an impact on the phenotypes present in an *Fgf-16* null mouse (Lu et al. 2010). These authors showed a difference in craniofacial and heart phenotypes and an altered embryonic lethality of their *Fgf16* null mouse on different genetic backgrounds. Their C57BL/6 background embryos showed a degree of rescue of these phenotypes,

combined with a significant difference in RNA levels of *Fgf8* (S. Y. Lu et al. 2010). This supports the potential for the genetic background of my mice having an impact on the amount of *Fgf8* RNA present, along with the differences in phenotypes seen in our mutant embryos.

6.0 Discussion

The work in this thesis primarily relates to three hypotheses for the mechanism underlying the role of FGF signalling in L/R determination. I address these below.

6.1 The NVP Hypothesis

To critically assess the validity of the NVP hypothesis as a mechanism for the breaking of L/R symmetry, we should first consider the methods Tanaka and colleagues used to visualise NVPs in motion. My replication of their protocols strongly suggests that the objects labelled by DiI and viewed through live fluorescent imaging are artefactual. I propose that their incubation of embryos at room temperature has caused extensive cellular death. This may explain the large variation in the reported size of NVPs, which strangely ranges from 0.3-5.0 μm in diameter. Tanaka also proposes that these NVPs emerge from the microvilli present on the cells of the node. These are much smaller than the proposed NVPs, having an average diameter between 100-700 nm (Lange 2011). Together these suggest that the emergence of such large vesicles from small microvilli seems unlikely. I argue that the objects Tanaka and colleagues imaged by fluorescent labelling are pieces of cellular debris, formed as parts of the cell membrane bleb off from dying cells.

Tanaka proposed that FGF signalling, and specifically FGF8, regulated the release of NVPs in the node (Tanaka et al. 2005). My analysis of embryos cultured with inhibitors of FGF signalling does not support or discount a role for NVPs in breaking L/R symmetry, or how FGFs may be implicated in regulating this process, but it does raise important questions. Indeed, my culture experiments revealed a difference in number of vesicular objects (assumed to be analogous to the NVPs posited by Tanaka and Hirokawa) in the nodes of uncultured vs cultured embryos. As discussed earlier, the node is naturally an

enclosed system, with Reichert's membrane acting to complete and cover the top of the node, and as such is a barrier between the node and the external environment. However, as this is removed before embryo culture, signalling molecules contained in the node could potentially be released into the culture medium, meaning a lower concentration in the node. As embryos that have undergone culture can reliably establish normal L/R asymmetry (Glanville-Jones et al. 2013; Harris 2012), this suggests that any release of signalling molecules or vesicles is not detrimental to normal establishment of asymmetry.

Another interpretation, as we did see a general developmental delay, is that there is a pleitropic effect of culture on a number of different things; which could lead to a reduction in NVP numbers as a symptom of this general delay. Alternatively, it may be that the NVPs we detect in SEM images have no functional consequence at all, and are merely a reproducible, consistent artefact associated with the process of embryo preparation for SEM imaging. Indeed, in a paper from Sulik (Sulik et al. 1994), although NVP-like objects are visible (**Figure 1.1**), they appear much less numerous than in Tanaka's and my own images.

The inhibitor culture itself did not support a role for FGF signalling in the regulation of NVP release. The different inhibitors I used have different FGFR specificity. While there were differences in the numbers of NVPs in the nodes of embryos cultured with the different inhibitors, it was not possible to conclude anything from these results. As such this did not give us an increased understanding of which particular FGFR(s) may be involved.

Culture of embryos with the FGFR1 inhibitor (SU5402) showed both higher NVP numbers, and greater variability in the number of NVPs seen, whereas embryos cultured with the FGFR1-3 inhibitor (AZD4547) showed reduced NVP numbers. Intriguingly, culture of embryos with the FGFR1-4 inhibitor (BGJ398) showed no difference in NVP number when compared to uncultured, which further confuses the situation. As such, we cannot deduce if a specific FGFR is involved in the regulation of NVP release, although the data from embryonic culture experiments suggest a potential link between the two. Although this

does not say anything about whether the NVP hypothesis is viable, it does suggest that FGF signalling is not functioning in the way proposed by Tanaka. When this is combined with my data, showing that what Tanaka and colleagues imaged is likely to be cellular debris, this raises questions about the NVP paper that proposes NVPs as the mechanism of breaking L/R symmetry, and the proposed role for FGF signalling in this process.

My analysis of the *Fgf8*$^{Tm1.1/Tm1.2}$ compound heterozygote embryo nodes did not further elucidate a role for FGF signalling in the regulation of NVP release. A slight elevation in the number of NVPs in the *Fgf8*$^{Tm1.1/Tm1.2}$ compound heterozygote nodes when the data was split by developmental stage was evident. If FGF8 is functionally important in regulating the release of NVPs in the node, it is possible that reduced FGF8 could lead to increased NVP numbers if we assume that those we are seeing are the ones which have yet to be released. However, this difference is not statistically significant, and a further analysis of an increased scope would be necessary to determine this relationship. It may be the case that, if FGF8 does have a role in regulating NVP release, that it works in tandem with other FGF ligands, and so a depleted level of functional FGF8 may be being compensated for by other factors. Also, were the levels of FGF8 to naturally vary between individual embryos, it may be that such variation directly relates to the differences in phenotypes exhibited.

My work casts doubt on the NVP hypothesis as proposed by Tanaka. However, this is not proof that NVPs do not exist. A wider analysis of the NVP hypothesis is needed in order to fully understand the feasibility of the hypothesis as a method of breaking of symmetry in the node. Although NVP number does appear to have a least some link to FGF signalling, whether this is functionally important is not clear, and what they might contain is a question that remains to be answered.

6.2 A Role for FGF Signalling in Formation of the Node

Analysis of the nodes of embryos cultured with FGF signalling inhibitors and embryos mutant for *Fgf8* together point to a role for FGF signalling in the formation and/or maintenance of the node. This suggests that the mechanism by which FGF signalling influences L/R determination is through a role in forming the node. This hypothesis is strongly supported by direct SEM analysis of the physical shape and structure of the nodes of the following experimental groups. The *Fgf8*$^{Tm1.1/Tm1.2}$ compound heterozygous embryos showed a high proportion of abnormal node structures. Similarly, examination of nodes of embryos cultured with inhibitors of FGFR1 and FGFR1-3 showed abnormal node structure. In both, two disparate categories of atypical node structure were found. In inhibitor cultured embryos some nodes failed to properly emerge from the overlying endoderm and others showed a “deep” node phenotype. In the *Fgf8*$^{Tm1.1/Tm1.2}$ compound heterozygotes some embryos had nodes which failed to emerge, whilst others showed an elongated phenotype. The commonality in both datasets, showing a number of embryos with nodes which failed to emerge, suggests that FGF signalling, most likely FGF8, is needed for the correct emergence of the node. Exactly how FGF(8) signalling may be functioning in this process is not known, but we can hypothesise a number of ways in which this might occur. FGF signalling may be necessary in order for the endodermal cells which overly the node to migrate away and reveal the underlying node cells. Alternatively, FGF signalling may be needed for correct node crown cell formation or identity, indeed, the presence of “extra-nodal” cells expressing *Cerl2* were apparent in both experimental cohorts. This supports the idea that there is some mis-formation or mis-identification of the cells comprising the node structure when FGF signalling is perturbed; and that without FGF signalling crown cells, which respond to flow, cannot correctly form and provide a distinct edge of the node. The elongated node phenotype seen in a number of *Fgf8*$^{Tm1.1/Tm1.2}$ mutant embryos could be argued to fit with this, as they lack an obvious edge to the node, and therefore a loss of crown cells is suggested. Additionally, the presence of

“deep” nodes in some inhibitor-cultured embryos is suggestive of a failure of crown cell identity, with the nodes appearing to collapse inwards on themselves. This deep node phenotype hints at a separate function for crown cell identity or maintenance, as the embryos which showed this were placed into culture at later stages than those which showed nodes which failed to emerge. These embryos had already formed a node prior to introduction to culture, but were still affected by the inhibitors to give a deep node phenotype. The question of how this phenotype would be produced by a failure of function in this context remains. Perhaps it is not controlled or influenced by FGF8, and that is why we do not see a similar deep node phenotype in our *Fgf8* mutant embryos. Alternatively, it may be that the FGF8 level is not low enough to produce a more severe phenotype, and the differences in phenotype seen relate to the levels of functional FGF8 protein present.

6.3 FGFs in Regulating Cilia Length

The role of FGF signalling in cilia length control in the LROs of the fish and frog has been described, with *Fgfr1* being specifically implicated in both these organisms, and the ligands Fgf8 and Fgf24 acting through this receptor to control cilia length in the zebrafish KV (Neugebauer et al. 2009). In *Xenopus* it is thought that FGF8 also plays a function in the formation of the flow-sensing cells at the LRO edge in the GRP, separate to a role in regulating cilia length in the GRP (Schneider et al. 2019). The receptor involved with FGF8 signalling in the context of L/R patterning in the mouse appears to differ, however, with FGFR1 inhibitor-cultured embryos showing no difference in their node cilia lengths. *Fgfr1* null mice have been shown to die during gastrulation and display defective mesoderm patterning (Deng et al. 1994; Yamaguchi et al. 1994). My analysis of protein localisation shows FGFR1 to be present in the node. The presence of FGFR2 in nodal cilia is intriguing, however it remains unknown whether cilia localisation plays any role in FGFR function. Interestingly, the one significant difference seen in the comparison of cilia length in the nodes of different cultured embryos was found between embryos cultured from the 1ss to

the 3ss with FGFR1-3 inhibitor and FGFR1 inhibitor. The embryos cultured with an inhibitor of FGFR1-3 showed significantly longer node cilia than those of the same developmental stage cultured with FGFR1 inhibitor, supporting the possible interpretation that FGFRs other than FGFR1 act to affect cilia length in the mouse. Perhaps even FGFR2/FGFR3, or both, act in a compensatory manner with FGFR1, and only when all/both the influencing receptors are inhibited do we see an effect. Indeed, functional redundancies of FGFR1 and FGFR2 in particular are often present during developmental processes (Ornitz and Itoh 2015). Additionally of note is that even inhibitory action of *Fgfr* splice variants has been reported, with a secreted protein produced by an *Fgfr3* variant functioning to bind FGF ligands and inhibit their signalling capabilities (Terada et al. 2001; Tomlinson et al. 2005). The lack of any difference in cilia length seen in embryos cultured with an FGFR1-4 inhibitor further suggests a complex balanced relationship between the different FGF receptors in this context. However, as there are not sufficient appropriate controls to allow for statistical analysis for this embryo culture data, conclusions can only be very loosely drawn from this data.

My analysis of $Fgf8^{Tm1.1/Tm1.2}$ embryos does support a role for FGF8 in the regulation of cilia length. The decreased length of LRO cilia in these mice fits with the similar decreased cilia lengths seen in *fgf8/fgf24* and *fgfr1* morphant zebrafish KVs. How a lack of FGF8 leads to shortened cilia is not clear, although ICK, which is involved in ciliogenesis and the regulation of cilia length, has been implicated as an interaction partner of FGFRs in the primary cilia of 293T cells (Kunova Bosakova et al. 2019). This may be provide a mechanism through which FGF signalling is controlling cilia length in the mouse node.

6.4 Implications for understanding the mechanisms of L/R determination

My findings presented here suggest that FGF signalling may be working in more than one specific way, and through this has a complex role which fits into our understanding of the

establishment of L/R asymmetry. I have discussed how FGF signalling may have a role in the regulation of NVP release in the node, and also indicated an underlying problem with the live imaging originally used as evidence for this hypothesis. While my data does not disprove the possibility of NVPs as a mechanism for the breaking of symmetry, it does cast doubt on its validity. My findings suggest that Tanaka's live-imaged NVPs are most likely to be pieces of cellular debris, which, when combined with the large size variation of NVPs seen raises doubt over their data and the conclusions drawn from it. However, the NVP hypothesis remains a possible explanation, albeit one without substantial evidence to support it. What remains to be answered about the hypothesis is exactly what is contained in NVPs. There are currently no good candidates for the signalling molecules that NVPs might contain, leaving us looking for alternative possibilities. It remains a formal possibility that these structures still function in L/R determination, but not as vesicles, perhaps in some way docking with the crown cell cilia as part of mechanosensation.

If FGF signalling is primarily influencing the formation of the node, throughout my analysis of *Fgf8*$^{Tm1.1/Tm1.2}$ compound heterozygotes, only a small proportion have a node malformation that translates into L/R asymmetry defects. Moreover, these defects are minor. This would suggest that even with perturbation of the node structure, nodal flow is still produced and translated correctly enough to give mostly normal asymmetry patterning. There is analysis which has shown that only a small number of motile pit-cell cilia are actually needed in order to produce the flow needed to break symmetry (Shinohara et al. 2012). If perturbing FGF signalling affects cilia length, or node formation, it appears that in my *Fgf8*$^{Tm1.1/Tm1.2}$ compound heterozygote embryos and FGFR inhibitor cultured embryos, sufficient flow is produced to establish asymmetric patterning, albeit perhaps slightly delayed. Alternatively, if FGF signalling is affecting the formation of the node or crown cell identity, it appears that there are enough adequately specified crown cells able to translate the flow produced into a left-sided signal. Altogether this points towards the robustness of the system by which asymmetry is established. Indeed, it has been proposed that the

components, *Nodal* and *Leftys*, act as a self-enhancement lateral-inhibition (SELI) system, whereby LEFTY diffuses more rapidly than NODAL to function as a barrier against *Nodal* expression, as NODAL induces *Nodal* expression (Nakamura et al. 2006). This allows the conversion of small L/R differences at the node to be converted into the robust L/R asymmetry we see in the LPM. In this way, the system has safeguards, combined with feedback loops which together convert an initially small asymmetry in the node into a major asymmetry between the L- and the R-LPM. A small delay in the induction of asymmetric *Nodal* expression at the node can therefore be mostly corrected to fix asymmetric fate. Therefore, it seems that in the case of my $Fgf8^{Tm1.1/Tm1.2}$ compound heterozygote mutant analysis, enough FGF8 function remains to allow normal asymmetry to become established in the majority of embryos.

6.5 The Role of Genetic Background in Phenotypes

Inbred mouse strains were established to allow different characteristics to be studied in scientific research, for example coat and eye colour (Sage 1981). From 1900 a key breeder of mice, Abbie Lathrop, began to sell her mice to geneticists at Harvard University, with many commonly used lines today, such as C57BL/6, being derived completely from animals she provided (Morse 1978). The study of genetics in mammals was crucial following the rediscovery of Mendel's laws, to see if they applied to heritable traits in organisms other than plants (Dunn 1965). Work to analyse the systemic heritability of the mouse was carried out extensively by William Castle and his lab, and led to their realisation of a need for genetically homogenous lines in order to assess this (Castle 1903). One lab member, Clarence Little, began using inbred matings to establish lines in 1909 and this resulted in the DBA mouse strain, one of the first to be used by different researchers to allow meaningful comparison of data between studies (C. C. Little and Bagg 1924). Little went on to play an instrumental role in the founding of the Jackson Laboratory, which today maintains and supplies defined mouse lines to geneticists worldwide. Historically, different

inbred strains have been used for different purposes: with differences in radiation sensitivity; ease of use in creating embryonic stem cell lines; and even coat colour being important factors. Certain strains have higher incidence of particular disease phenotypes, such as C3H having high rates of mammary tumours, and 129 having a high testicular teratoma incidence; making them useful models for studying these diseases (Silver 1995). Additionally, certain strains have poor eyesight, such as C3H, or an increased prevalence for hearing impairment (BL/6J), and so are not good models for studying such phenotypes.

Strain variation is a factor that may, in part, explain differences in the results seen from my inhibitor culture experiments and my *Fgf8* mutant embryo analysis. The genetic background of the *Fgf8* mutant lines has previously been discussed (**5.3**), however when comparing results and drawing conclusions from these data and those of the inhibitor culture, there are additional considerations: namely, that the genetic background strain of the *Fgf8* mutants is the C57BL/6 strain, and the embryo culture experiments were carried out using wild-type C3H embryos. Fundamental differences exist between these two strains, and may have significantly different effects and interactions with components of the FGF signalling pathway; and on the process of L/R determination. Evidence for divergent genetic regulatory networks in different mouse strains has been shown in work on an *Fgf16* null mouse (Lu et al. 2010). The authors show not only different phenotypes and penetrance of phenotypes in mutants depending on the genetic background, they also show different baseline levels of *Fgf8*-RNA in the strains. Indeed a differing response in the levels of *Fgf8*-RNA is seen in *Fgf16* null embryos/mice on different genetic backgrounds. They propose that one of the background strains they use, Black Swiss Webster (Bsw), are more sensitive to a decrease in FGF8 levels than C57BL/6. If a similar increased sensitivity is present in the mixed genetic background we believe the *Fgf8* mutant lines were originally analysed on (Meyers et al. 1998; Meyers and Martin 1999), this may explain why we do not see the same severity and penetrance of associated phenotypes in our line congenic on C57BL/6. Also, this could explain why we see differing

responses to a depletion of FGF8 in our mutant (on C57BL/6), and an inhibition of FGFRs in our cultured embryos (wild-type C3H strain). It is not clear how the mechanism behind such differences would be functioning with *Fgf8,* but possibilities include suppression or enhancement of the expression of specific genes, or compensatory functions of modifier genes (Doetschman 2009). Suppression and enhancement of specific genes has been shown to play a role in producing variation in phenotypes seen, both in terms of penetrance and expressivity (Kallapur et al. 1999; Rozmahel et al. 1996; Threadgill et al. 1995). Alternatively, the difference in phenotypes could be due to differential expression of modifier genes/loci which give compensatory function, such as has been shown to be the case in *Tgfb1* mutants (Bonyadi et al. 1997; Tang et al. 2003; Tang et al. 2005). Modifier genes have also been shown to protect against specific phenotypes, such as a region on chromosome 13 which protects against sex reversal in BL/6 males in the context of a Y chromosome from *mus poschiavanus* (Livermore et al. 2020). Whether either of these mechanism types may be the case in the variation seen in phenotype between our and Meyers cohorts, however, remains to be discovered.

6.6 Future Experiments and Directions

6.6.1 Experiments to follow

Although the work described in this thesis has contributed to furthering our understanding of how FGF signalling is involved in the breaking of L/R symmetry, significant gaps in our knowledge remain. Further analysis of the *Fgf8* compound heterozygote mutant line discussed in **Chapter 5** of this thesis would likely bring more insight. Specific experiments to be carried out following on my work include directly quantifying the levels of *Fgf8* expression in individual mutant embryos. This would allow formal testing of the hypothesis that differing expression levels of *Fgf8* lie behind the differing phenotypic severity in our line. Through the use of a qPCR array, for example, this could be assessed. Additionally,

such an array could also assess the expression levels of other key genes involved in FGF signalling, including possible compensatory *Fgf*s, and the four *Fgfr*s, along with downstream transcriptional targets. Comparison between our compound heterozygote mutants, the individual heterozygote and wild-type counterparts could give us an idea as to whether FGFs functionally compensate, along with likely downstream signalling pathways affected. Either instead of, or additional to this qPCR analysis, RNA sequencing would provide a similar quantification. Indeed, RNA sequencing data sets exist online which with further bioinformatics analysis, and a combined approach of de novo RNA sequencing with our mutant would give increased insight and understanding as to what is happening on a molecular level in our compound heterozygotes, and how FGF signalling is involved in L/R patterning more broadly. Additional to this, quantification of protein levels of FGF8 specifically would also likely be informative.

Another avenue leading on from my work presented here could involve investigation into the role genetic background is playing. A relatively simple line of experiments would be to repeat the phenotypic analysis of E13.5 and E8.0 embryos of the *Fgf8* compound heterozygote genotype, but on a differing genetic background to the one presented here (B6J). Analysis of the *Fgf8* mutants on a mixed C3H background, for example, may further recapitulate similarities to the more severe L/R patterning defects seen by Meyers and Martin. With this in mind, an analysis of increased depth and comparable manner to that done on the BL/6 background could be carried out, through micro-CT and SEM to better characterise any differences. This, when combined with key L/R marker gene expression data, may help us to understand if there are multiple different roles at play in this context.

6.6.2 Directions of the field

Future work in the field is likely to lead to further understanding of the NVP and mechanosensation hypotheses and how the breaking of symmetry is translated at the

node. As our understanding of genetics increases, it may be that a signalling molecule is found, or a function for the structures termed NVPs might be elucidated and understood to have an alternate role outside to breaking symmetry. Moreover, further analysis of whole embryos through using single-cell RNA sequencing, with a focus on different differentiating cell populations, such as the node pit and crown cells, are likely to increase knowledge and understanding of the breaking of L/R symmetry, and the role FGF signalling in this process.

Furthermore, embryo culture is likely to be an important tool in assessing the different roles FGFs may play in L/R determination, and further pinpointing the timing during which FGF signalling is functional. As time-specific intervention is one of the advantages of whole embryo culture, which genetic approaches generally lack. Further analysis with embryos from different genetic backgrounds may provide insight into differences in the mechanisms between different strains and will prove far quicker and cheaper than breeding *Fgf8* alleles onto multiple genetic backgrounds. Ideally, embryos with depleted or no *Fgf8* expression could have other FGFs added to the culture to assess their compensatory functions. However, there are current limitations to this as genotyping would not be possible until post-culture and analysis, which may prove problematic in terms of numbers of embryos needed. The use of germline or Cre-mediated deletion may provide better experimental cohorts for experiments such as these, and as technology moves forward this is likely to become less of an issue. Additionally, as technology and reagent efficiency progress, it may be simpler to carry out routine genotypic analysis using small embryonic samples. The use of embryo culture as a technique in the field is becoming more prevalent, and increased culture times is becoming more feasible. A recent paper showed successful culture of mouse embryos from 5.5dpc to 11dpc (Aguilera-Castrejon et al. 2021). As techniques improve further, *ex utero* embryo culture is likely to be increasingly utilised in order to allow time-sensitive/specific pharmacological intervention and experimentation to

further elucidate our understanding of the processes, signalling pathways and genetics involved in mouse embryonic development.

6.6.3 Closing remarks

Systematic analysis of phenotypes on a single genetic background by the IMPC raises some concerns. Whilst it is important for this to be carried out on a defined background in order to give reproducible and comparable results and phenotypes, there is the potential for the important factor of genetic background to be overlooked in this analysis. There have been calls for mouse geneticists to initially characterise null mutants in particular on a defined, mixed genetic background (Doetschman 2009). If phenotypes are seen on this background, especially those with incomplete penetrance and variable expressivity, the impact of a specific background strain could be eliminated/understood by also examining the mutant on one of two congenic strains. Increasingly the field has moved away from the use of mixed genetic backgrounds with the development of more elegant and faster approaches to produce targeted specific mutations in the mouse on a genetic background of choice, such as through the use of the gene editing CRSIPR/Cas9 system (Wu et al. 2019). This has the potential to lead to problems with the conclusions drawn from mouse data, with a lack of understanding of the genetic processes of the genetic background that are at play, and the role they are having in the presentation and penetrance of a disease phenotype. However, as more of the mouse genome is characterised, and gene functions understood (Lloyd et al. 2020), perhaps it is inevitable that we will, as a field, move over investigation onto other genetic backgrounds more readily to understand the role that confounding genetic factors/interactions are having. Indeed, this will allow us to begin to better understand the genetic variability, incomplete penetrance and variable expressivity present in human genetics.

Bibliography

Abu-Issa, R., et al. (2002), 'Fgf8 is required for pharyngeal arch and cardiovascular development in the mouse', *Development,* 129 (19), 4613-25.

Adachi, H., et al. (1999), 'Determination of left/right asymmetric expression of nodal by a left side-specific enhancer with sequence similarity to a lefty-2 enhancer', *Genes Dev,* 13 (12), 1589-600.

Afzelius, B. A. (1976), 'A human syndrome caused by immotile cilia', *Science,* 193 (4250), 317-9.

--- (1995), 'Situs inversus and ciliary abnormalities. What is the connection?', *Int J Dev Biol,* 39 (5), 839-44.

Aguilera-Castrejon, A., et al. (2021), 'Ex utero mouse embryogenesis from pre-gastrulation to late organogenesis', *Nature*.

Amelar, R. D., Dubin, L., and Schoenfeld, C. (1980), 'Sperm motility', *Fertil Steril,* 34 (3), 197-215.

Antic, D, et al. (2010), 'Planar cell polarity enables posterior localization of nodal cilia and left-right axis determination during mouse and Xenopus embryogenesis', *PloS one,* 5 (2).

Anvarian, Z., et al. (2019), 'Cellular signalling by primary cilia in development, organ function and disease', *Nat Rev Nephrol,* 15 (4), 199-219.

Asante, D., Stevenson, N. L., and Stephens, D. J. (2014), 'Subunit composition of the human cytoplasmic dynein-2 complex', *J Cell Sci,* 127 (Pt 21), 4774-87.

Awan, A., et al. (2010), 'Immunoflourescence and mRNA analysis of human embryonic stem cells (hESCs) grown under feeder-free conditions', *Methods Mol Biol,* 584, 195-210.

Backwell, P. R., et al. (2007), 'What are the consequences of being left-clawed in a predominantly right-clawed fiddler crab?', *Proc Biol Sci,* 274 (1626), 2723-9.

Bae, Y. K. and Barr, M. M. (2008), 'Sensory roles of neuronal cilia: cilia development, morphogenesis, and function in C. elegans', *Front Biosci,* 13, 5959-74.

Bangs, F and Anderson, KV (2017), 'Primary Cilia and Mammalian Hedgehog Signaling', *Cold Spring Harbor perspectives in biology,* 9 (5).

Beddington, R. S. and Robertson, E. J. (1999), 'Axis development and early asymmetry in mammals', *Cell,* 96 (2), 195-209.

Beenken, A. and Mohammadi, M. (2009), 'The FGF family: biology, pathophysiology and therapy', *Nat Rev Drug Discov,* 8 (3), 235-53.

Beisson, J and Wright, M (2003), 'Basal body/centriole assembly and continuity', *Current opinion in cell biology,* 15 (1).

Blacque, O. E., Scheidel, N., and Kuhns, S. (2018), 'Rab GTPases in cilium formation and function', *Small GTPases,* 9 (1-2), 76-94.

Bloodgood, R. A. (2009), 'From central to rudimentary to primary: the history of an underappreciated organelle whose time has come. The primary cilium', *Methods in cell biology,* 94, 3-52.

Blum, M. and Ott, T. (2018), 'Animal left-right asymmetry', *Curr Biol,* 28 (7), R301-r04.

Blum, M., et al. (2007), 'Ciliation and gene expression distinguish between node and posterior notochord in the mammalian embryo', *Differentiation,* 75 (2), 133-46.

Bonyadi, M., et al. (1997), 'Mapping of a major genetic modifier of embryonic lethality in TGF beta 1 knockout mice', *Nat Genet,* 15 (2), 207-11.

Boskovski, M. T., et al. (2013), 'The heterotaxy gene GALNT11 glycosylates Notch to orchestrate cilia type and laterality', *Nature,* 504 (7480), 456-9.

Brown, C. B., et al. (2004), 'Cre-mediated excision of Fgf8 in the Tbx1 expression domain reveals a critical role for Fgf8 in cardiovascular development in the mouse', *Dev Biol,* 267 (1), 190-202.

Cartwright, J. H., Piro, O., and Tuval, I. (2004), 'Fluid-dynamical basis of the embryonic development of left-right asymmetry in vertebrates', *Proc Natl Acad Sci U S A,* 101 (19), 7234-9.

Cartwright, J. H., et al. (2007), 'Embryonic nodal flow and the dynamics of nodal vesicular parcels', *J R Soc Interface,* 4 (12), 49-55.
Cartwright, J. H. E., Piro, O., and Tuval, I. (2020), 'Chemosensing versus mechanosensing in nodal and Kupffer's vesicle cilia and in other left-right organizer organs', *Philos Trans R Soc Lond B Biol Sci,* 375 (1792), 20190566.
Caspary, T., Larkins, C. E., and Anderson, K. V. (2007), 'The graded response to Sonic Hedgehog depends on cilia architecture', *Dev Cell,* 12 (5), 767-78.
Castle, W.E. (1903), *The laws of Galton and Mendel and some laws governing race improvement by selection* (Proceedings of the American Academy of Arts and Sciences).
Cheng, L., et al. (2014), 'Transforming growth factor-β1 (TGF-β1) induces mouse precartilaginous stem cell proliferation through TGF-β receptor II (TGFRII)-Akt-β-catenin signaling', *Int J Mol Sci,* 15 (7), 12665-76.
Christensen, S. T., et al. (2012), 'Primary cilia and coordination of receptor tyrosine kinase (RTK) signalling', *J Pathol,* 226 (2), 172-84.
Cole, D. G., et al. (1993), 'Novel heterotrimeric kinesin-related protein purified from sea urchin eggs', *Nature,* 366 (6452), 268-70.
Collignon, J., Varlet, I., and Robertson, E. J. (1996), 'Relationship between asymmetric nodal expression and the direction of embryonic turning', *Nature,* 381 (6578), 155-8.
Constam, D. B., Calfon, M., and Robertson, E. J. (1996), 'SPC4, SPC6, and the novel protease SPC7 are coexpressed with bone morphogenetic proteins at distinct sites during embryogenesis', *J Cell Biol,* 134 (1), 181-91.
Danilov, A. I., et al. (2009), 'Ultrastructural and antigenic properties of neural stem cells and their progeny in adult rat subventricular zone', *Glia,* 57 (2), 136-52.
Deng, C. X., et al. (1994), 'Murine FGFR-1 is required for early postimplantation growth and axial organization', *Genes Dev,* 8 (24), 3045-57.
Deng, H, Xia, H, and Deng, S (2015), 'Genetic Basis of Human Left-Right Asymmetry Disorders', *Expert reviews in molecular medicine,* 16.
Desgrange, A., et al. (2020), 'Transient Nodal Signaling in Left Precursors Coordinates Opposed Asymmetries Shaping the Heart Loop', *Dev Cell,* 55 (4), 413-31.e6.
Diez del Corral, R., et al. (2003), 'Opposing FGF and retinoid pathways control ventral neural pattern, neuronal differentiation, and segmentation during body axis extension', *Neuron,* 40 (1), 65-79.
Doetschman, T. (2009), 'Influence of genetic background on genetically engineered mouse phenotypes', *Methods Mol Biol,* 530, 423-33.
Dunn, L.C. (1965), *A Short History of Genetics* (NY: McGraw-Hill).
Estienne, A. and Price, C. A. (2018), 'The fibroblast growth factor 8 family in the female reproductive tract', *Reproduction,* 155 (1), R53-R62.
Ezratty, E. J., et al. (2011), 'A role for the primary cilium in Notch signaling and epidermal differentiation during skin development', *Cell,* 145 (7), 1129-41.
Fanto, M. and McNeill, H. (2004), 'Planar polarity from flies to vertebrates', *J Cell Sci,* 117 (Pt 4), 527-33.
Fedorov, A., et al. (2012), '3D Slicer as an image computing platform for the Quantitative Imaging Network', *Magn Reson Imaging,* 30 (9), 1323-41.
Ferreira, R., et al. (2019), 'The cilium as a force sensor-myth versus reality', *J Cell Sci,* 132 (14).
Field, S., et al. (2011), 'Pkd1l1 establishes left-right asymmetry and physically interacts with Pkd2', *Development,* 138 (6), 1131-42.
Fu, T., et al. (2012), 'Aberrantly elevated microRNA-34a in obesity attenuates hepatic responses to FGF19 by targeting a membrane coreceptor β-Klotho', *Proc Natl Acad Sci U S A,* 109 (40), 16137-42.
--- (2016), 'FXR Primes the Liver for Intestinal FGF15 Signaling by Transient Induction of β-Klotho', *Mol Endocrinol,* 30 (1), 92-103.

Futami, T., et al. (2017), 'ASP5878, a Novel Inhibitor of FGFR1, 2, 3, and 4, Inhibits the Growth of FGF19-Expressing Hepatocellular Carcinoma', *Mol Cancer Ther,* 16 (1), 68-75.
Garcia-Gonzalo, F. R. and Reiter, J. F. (2017), 'Open Sesame: How Transition Fibers and the Transition Zone Control Ciliary Composition', *Cold Spring Harb Perspect Biol,* 9 (2).
Gavine, P. R., et al. (2012), 'AZD4547: an orally bioavailable, potent, and selective inhibitor of the fibroblast growth factor receptor tyrosine kinase family', *Cancer Res,* 72 (8), 2045-56.
Gerdes, J. M., Davis, E. E., and Katsanis, N. (2009), 'The vertebrate primary cilium in development, homeostasis, and disease', *Cell,* 137 (1), 32-45.
Glanville-Jones, H. C., Woo, N., and Arkell, R. M. (2013), 'Successful whole embryo culture with commercially available reagents', *Int J Dev Biol,* 57 (1), 61-7.
Grande, C. and Patel, N. H. (2009), 'Nodal signalling is involved in left-right asymmetry in snails', *Nature,* 457 (7232), 1007-11.
Grimes, D. T. and Burdine, R. D. (2017), 'Left-Right Patterning: Breaking Symmetry to Asymmetric Morphogenesis', *Trends Genet,* 33 (9), 616-28.
Grimes, D. T., et al. (2016), 'Genetic Analysis Reveals a Hierarchy of Interactions between Polycystin-Encoding Genes and Genes Controlling Cilia Function during Left-Right Determination', *PLoS Genet* (12).
Guagnano, V., et al. (2011), 'Discovery of 3-(2,6-dichloro-3,5-dimethoxy-phenyl)-1-{6-[4-(4-ethyl-piperazin-1-yl)-phenylamino]-pyrimidin-4-yl}-1-methyl-urea (NVP-BGJ398), a potent and selective inhibitor of the fibroblast growth factor receptor family of receptor tyrosine kinase', *J Med Chem,* 54 (20), 7066-83.
Guzzetta, A., et al. (2020), 'Hedgehog-FGF signaling axis patterns anterior mesoderm during gastrulation', *Proc Natl Acad Sci U S A,* 117 (27), 15712-23.
Hamada, H., et al. (2002), 'Establishment of vertebrate left-right asymmetry', *Nat Rev Genet,* 3 (2), 103-13.
Hao, Y., et al. (2019), 'Roles of FGF8 subfamily in embryogenesis and oral-maxillofacial diseases (Review)', *Int J Oncol,* 54 (3), 797-806.
Happe, H. and Peters, D. J. (2014), 'Translational research in ADPKD: lessons from animal models', *Nat Rev Nephrol,* 10 (10), 587-601.
Harada, H., Sato, T., and Nakamura, H. (2016), 'Fgf8 signaling for development of the midbrain and hindbrain', *Dev Growth Differ,* 58 (5), 437-45.
Harris, C. (2012), 'Rodent whole embryo culture', *Methods Mol Biol,* 889, 215-37.
Harris, P. C. and Torres, V. E. (2009), 'Polycystic kidney disease', *Annu Rev Med,* 60, 321-37.
Hashimoto, M., et al. (2010), 'Planar polarization of node cells determines the rotational axis of node cilia', *Nat Cell Biol,* 12 (2), 170-6.
Hirokawa, N., et al. (2006), 'Nodal flow and the generation of left-right asymmetry', *Cell,* 125 (1), 33-45.
Hogan, M. C., et al. (2009), 'Characterization of PKD protein-positive exosome-like vesicles', *J Am Soc Nephrol,* 20 (2), 278-88.
Holley, M., et al. (2010), 'Emx2 and early hair cell development in the mouse inner ear', *Dev Biol,* 340 (2), 547-56.
Honda, A., et al. (2018), 'FGFR1-mediated protocadherin-15 loading mediates cargo specificity during intraflagellar transport in inner ear hair-cell kinocilia', *Proc Natl Acad Sci U S A*.
Huangfu, D. and Anderson, K.V. (2005), 'Cilia and Hedgehog Responsiveness in the Mouse', *Proceedings of the National Academy of Sciences of the United States of America,* 102 (32).
Huangfu, D., et al. (2003), 'Hedgehog Signalling in the Mouse Requires Intraflagellar Transport Proteins', *Nature,* 426 (6962).
Humbert, M. C., et al. (2012), 'ARL13B, PDE6D, and CEP164 form a functional network for INPP5E ciliary targeting', *Proc Natl Acad Sci U S A,* 109 (48), 19691-6.

Hébert, J. M., et al. (2003), 'FGF signaling through FGFR1 is required for olfactory bulb morphogenesis', *Development,* 130 (6), 1101-11.
Inacio, J. M., et al. (2013), 'The dynamic right-to-left translocation of Cerl2 is involved in the regulation and termination of Nodal activity in the mouse node', *PLoS One,* 8 (3), e60406.
Insinna, C., et al. (2019), 'Investigation of F-BAR domain PACSIN proteins uncovers membrane tubulation function in cilia assembly and transport', *Nat Commun,* 10 (1), 428.
Ishikawa, H and Marshall, WF (2011), 'Ciliogenesis: building the cell's antenna', *Nature reviews. Molecular cell biology,* 12 (4).
Jin, S. C., et al. (2017), 'Contribution of rare inherited and de novo variants in 2,871 congenital heart disease probands', *Nat Genet,* 49 (11), 1593-601.
Jones, M. R., Chong, L., and Bellusci, S. (2020), 'Fgf10/Fgfr2b Signaling Orchestrates the Symphony of Molecular, Cellular, and Physical Processes Required for Harmonious Airway Branching Morphogenesis', *Front Cell Dev Biol,* 8, 620667.
Kallapur, S., Ormsby, I., and Doetschman, T. (1999), 'Strain dependency of TGFbeta1 function during embryogenesis', *Mol Reprod Dev,* 52 (4), 341-9.
Kee, H. L., et al. (2012), 'A size-exclusion permeability barrier and nucleoporins characterize a ciliary pore complex that regulates transport into cilia', *Nat Cell Biol,* 14 (4), 431-7.
Kitajima, K., et al. (2013), 'Wnt signaling regulates left-right axis formation in the node of mouse embryos', *Dev Biol,* 380 (2), 222-32.
Knobel, K. M., Peden, E. M., and Barr, M. M. (2008), 'Distinct protein domains regulate ciliary targeting and function of C. elegans PKD-2', *Exp Cell Res,* 314 (4), 825-33.
Knödler, A., et al. (2010), 'Coordination of Rab8 and Rab11 in primary ciliogenesis', *Proc Natl Acad Sci U S A,* 107 (14), 6346-51.
Kobayashi, T. and Dynlacht, B. D. (2011), 'Regulating the transition from centriole to basal body', *J Cell Biol,* 193 (3), 435-44.
Konecny, G. E., et al. (2013), 'Activity of the fibroblast growth factor receptor inhibitors dovitinib (TKI258) and NVP-BGJ398 in human endometrial cancer cells', *Mol Cancer Ther,* 12 (5), 632-42.
Kozminski, K. G., et al. (1993), 'A motility in the eukaryotic flagellum unrelated to flagellar beating', *Proc Natl Acad Sci U S A,* 90 (12), 5519-23.
Krebs, LT, et al. (2003), 'Notch Signaling Regulates Left-Right Asymmetry Determination by Inducing Nodal Expression', *Genes & development,* 17 (10).
Kunova Bosakova, M., et al. (2019), 'Fibroblast growth factor receptor influences primary cilium length through an interaction with intestinal cell kinase', *Proc Natl Acad Sci U S A,* 116 (10), 4316-25.
Lange, K. (2011), 'Fundamental role of microvilli in the main functions of differentiated cells: Outline of an universal regulating and signaling system at the cell periphery', *J Cell Physiol,* 226 (4), 896-927.
Lantinga-van Leeuwen, I. S., et al. (2007), 'Kidney-specific inactivation of the Pkd1 gene induces rapid cyst formation in developing kidneys and a slow onset of disease in adult mice', *Hum Mol Genet,* 16 (24), 3188-96.
Lee, J. D. and Anderson, K. V. (2008), 'Morphogenesis of the node and notochord: the cellular basis for the establishment and maintenance of left-right asymmetry in the mouse', *Dev Dyn,* 237 (12), 3464-76.
Linck, R. W., Chemes, H., and Albertini, D. F. (2016), 'The axoneme: the propulsive engine of spermatozoa and cilia and associated ciliopathies leading to infertility', *J Assist Reprod Genet,* 33 (2), 141-56.
Little, C.C. and Bagg, H.J. (1924), 'The occurrence of four inheritable morphological variations in mice and their possible relation to treatment with x-rays', *Journal of Experimental Zoology*.

Little, R.B. and Norris, D.P. (2020), 'Right, left and cilia: How asymmetry is established', *Seminars in Cell Development*.
Livermore, C., et al. (2020), 'Protection Against XY Gonadal Sex Reversal by a Variant Region on Mouse Chromosome 13', *Genetics,* 214 (2), 467-77.
Lloyd, K. C. K., et al. (2020), 'The Deep Genome Project', *Genome Biol,* 21 (1), 18.
Lu, Q., et al. (2015), 'Early steps in primary cilium assembly require EHD1/EHD3-dependent ciliary vesicle formation', *Nat Cell Biol,* 17 (4), 531.
Lu, S. Y., et al. (2010), 'Embryonic survival and severity of cardiac and craniofacial defects are affected by genetic background in fibroblast growth factor-16 null mice', *DNA Cell Biol,* 29 (8), 407-15.
Lu, W., et al. (1997), 'Perinatal lethality with kidney and pancreas defects in mice with a targetted Pkd1 mutation', *Nat Genet,* 17 (2), 179-81.
Ma, R., et al. (2005), 'PKD2 functions as an epidermal growth factor-activated plasma membrane channel', *Mol Cell Biol,* 25 (18), 8285-98.
Marques, S., et al. (2004), 'The activity of the Nodal antagonist Cerl-2 in the mouse node is required for correct L/R body axis', *Genes Dev,* 18 (19), 2342-7.
Marshall, W. F. and Kintner, C. (2008), 'Cilia orientation and the fluid mechanics of development', *Curr Opin Cell Biol,* 20 (1), 48-52.
Martin, L., et al. (2018), 'Constitutively-active FGFR3 disrupts primary cilium length and IFT20 trafficking in various chondrocyte models of achondroplasia', *Hum Mol Genet,* 27 (1), 1-13.
Mavrakis, K. J., et al. (2007), 'Arkadia enhances Nodal/TGF-beta signaling by coupling phospho-Smad2/3 activity and turnover', *PLoS Biology,* 5 (3), e67.
McGrath, J., et al. (2003), 'Two Populations of Node Monocilia Initiate Left-Right Asymmetry in the Mouse', *Cell,* 114 (1), 61-73.
Meier, I. D., et al. (2010), 'Short DNA sequences inserted for gene targeting can accidentally interfere with off-target gene expression', *FASEB J,* 24 (6), 1714-24.
Menini, A. (2010), 'The Neurobiology of Olfaction'.
Meyers, E. N. and Martin, G. R. (1999), 'Differences in left-right axis pathways in mouse and chick: functions of FGF8 and SHH', *Science,* 285 (5426), 403-6.
Meyers, E. N., Lewandoski, M., and Martin, G. R. (1998), 'An Fgf8 mutant allelic series generated by Cre- and Flp-mediated recombination', *Nat Genet,* 18 (2), 136-41.
Minegishi, K., et al. (2017), 'A Wnt5 Activity Asymmetry and Intercellular Signaling via PCP Proteins Polarize Node Cells for Left-Right Symmetry Breaking', *Dev Cell,* 40 (5), 439-52.e4.
Moreno, T. A. and Kintner, C. (2004), 'Regulation of segmental patterning by retinoic acid signaling during Xenopus somitogenesis', *Dev Cell,* 6 (2), 205-18.
Morse, H.C. (1978), 'Introduction', *Origins of Inbred Mice* (NY: Academic Press), 1-31.
Mukhopadhyay, S., et al. (2017), 'Trafficking to the primary cilium membrane', *Mol Biol Cell,* 28 (2), 233-39.
Nagy, A. and Rossant, J. (1993), 'Production of completely ES cell-derived fetuses', in A. L. Joyner (ed.), *Gene targeting: A practical approach* (Oxford: IRL Press), 147-79.
Nakamura, T., et al. (2006), 'Generation of robust left-right asymmetry in the mouse embryo requires a self-enhancement and lateral-inhibition system', *Dev Cell,* 11 (4), 495-504.
--- (2012), 'Fluid flow and interlinked feedback loops establish left-right asymmetric decay of Cerl2 mRNA', *Nat Commun,* 3, 1322.
Nakaya, M. A., et al. (2005), 'Wnt3a links left-right determination with segmentation and anteroposterior axis elongation', *Development,* 132 (24), 5425-36.
Nauli, S. M., et al. (2003), 'Polycystins 1 and 2 mediate mechanosensation in the primary cilium of kidney cells', *Nat Genet,* 33 (2), 129-37.

Neugebauer, J. M., et al. (2009), 'FGF signalling during embryo development regulates cilia length in diverse epithelia', *Nature,* 458 (7238), 651-4.
Niu, J., et al. (2020), 'Curtailing FGF19's mitogenicity by suppressing its receptor dimerization ability', *Proc Natl Acad Sci U S A,* 117 (46), 29025-34.
Niwa, Y., et al. (2011), 'Different types of oscillations in Notch and Fgf signaling regulate the spatiotemporal periodicity of somitogenesis', *Genes Dev,* 25 (11), 1115-20.
Nonaka, S., et al. (2002), 'Determination of left-right patterning of the mouse embryo by artificial nodal flow', *Nature,* 418 (6893), 96-9.
--- (1998), 'Randomization of left-right asymmetry due to loss of nodal cilia generating leftward flow of extraembryonic fluid in mice lacking KIF3B motor protein', *Cell,* 95 (6), 829-37.
Norris, D. P. and Robertson, E. J. (1999), 'Asymmetric and node-specific nodal expression patterns are controlled by two distinct cis-acting regulatory elements', *Genes Dev,* 13 (12), 1575-88.
Norris, D. P., et al. (2002), 'The Foxh1-dependent autoregulatory enhancer controls the level of Nodal signals in the mouse embryo', *Development,* 129 (14), 3455-68.
Nweeia, M. T., et al. (2012), 'Vestigial tooth anatomy and tusk nomenclature for monodon monoceros', *Anat Rec (Hoboken),* 295 (6), 1006-16.
Okada, Y., et al. (2005), 'Mechanism of nodal flow: a conserved symmetry breaking event in left-right axis determination', *Cell,* 121 (4), 633-44.
--- (1999), 'Abnormal nodal flow precedes situs inversus in iv and inv mice', *Mol Cell,* 4 (4), 459-68.
Oki, S., Kitajima, K., and Meno, C. (2010), 'Dissecting the Role of Fgf Signaling During Gastrulation and Left-Right Axis Formation in Mouse Embryos Using Chemical Inhibitors', *Developmental dynamics : an official publication of the American Association of Anatomists,* 239 (6).
--- (2007), 'Sulfated glycosaminoglycans are necessary for Nodal signal transmission from the node to the left lateral plate in the mouse embryo', *Development,* 134 (21), 3893-904.
Olson, E. N., et al. (1996), 'Know your neighbors: three phenotypes in null mutants of the myogenic bHLH gene MRF4', *Cell,* 85 (1), 1-4.
Ornitz, D. M. and Itoh, N. (2001), 'Fibroblast growth factors', *Genome Biol,* 2 (3), Reviews3005.
--- (2015), 'The Fibroblast Growth Factor signaling pathway', *Wiley Interdiscip Rev Dev Biol,* 4 (3), 215-66.
Ornitz, D. M. and Legeai-Mallet, L. (2017), 'Achondroplasia: Development, pathogenesis, and therapy', *Dev Dyn,* 246 (4), 291-309.
Pala, R., Alomari, N., and Nauli, S. M. (2017), 'Primary Cilium-Dependent Signaling Mechanisms', *Int J Mol Sci,* 18 (11).
Pennekamp, P., et al. (2002), 'The ion channel polycystin-2 is required for left-right axis determination in mice', *Curr Biol,* 12 (11), 938-43.
Peters, K. G., et al. (1992), 'Two FGF receptor genes are differentially expressed in epithelial and mesenchymal tissues during limb formation and organogenesis in the mouse', *Development,* 114 (1), 233-43.
Pham, C. T., et al. (1996), 'Long-range disruption of gene expression by a selectable marker cassette', *Proc Natl Acad Sci U S A,* 93 (23), 13090-5.
Piliszek, A., Kwon, G. S., and Hadjantonakis, A. K. (2011), 'Ex utero culture and live imaging of mouse embryos', *Methods Mol Biol,* 770, 243-57.
Poladia, D. P., et al. (2006), 'Role of fibroblast growth factor receptors 1 and 2 in the metanephric mesenchyme', *Dev Biol,* 291 (2), 325-39.
Ramsdell, A. F. (2005), 'Left-right asymmetry and congenital cardiac defects: Getting to the heart of the matter in vertebrate left-right axis determination', *Dev Biol,* 288, 1-20.
Raya, A., et al. (2003), 'Notch activity induces Nodal expression and mediates the establishment of left-right asymmetry in vertebrate embryos', *Genes Dev,* 17 (10), 1213-8.

Roberson, E. C., et al. (2020), 'A comparative study of the turnover of multiciliated cells in the mouse trachea, oviduct, and brain', *Dev Dyn,* 249 (7), 898-905.
Rosenbaum, J. L. and Witman, G. B. (2002), 'Intraflagellar transport', *Nat Rev Mol Cell Biol,* 3 (11), 813-25.
Rousseau, F., et al. (1994), 'Mutations in the gene encoding fibroblast growth factor receptor-3 in achondroplasia', *Nature,* 371 (6494), 252-4.
Rozmahel, R., et al. (1996), 'Modulation of disease severity in cystic fibrosis transmembrane conductance regulator deficient mice by a secondary genetic factor', *Nat Genet,* 12 (3), 280-7.
Sage, R.D. (1981), 'Wild mice', in H.L. Foster, J.D. Small, and J.G. Fox (eds.), *The Mouse in Biomedical Research* (I; NY: Academic Press), 40-90.
Salomé, P. A. and Merchant, S. S. (2019), 'A Series of Fortunate Events: Introducing Chlamydomonas as a Reference Organism', *Plant Cell,* 31 (8), 1682-707.
Satir, P. and Christensen, S. T. (2007), 'Overview of structure and function of mammalian cilia', *Annu Rev Physiol,* 69, 377-400.
Sato, T., et al. (2017), 'Organizing activity of Fgf8 on the anterior telencephalon', *Dev Growth Differ,* 59 (9), 701-12.
Schindelin, J., et al. (2012), 'Fiji: an open-source platform for biological-image analysis', *Nat Methods,* 9 (7), 676-82.
Schneider, I., et al. (2019), 'A dual function of FGF signaling in Xenopus left-right axis formation', *Development*.
Schneider, L., et al. (2005), 'PDGFRalphaalpha signaling is regulated through the primary cilium in fibroblasts', *Curr Biol,* 15 (20), 1861-6.
--- (2010), 'Directional cell migration and chemotaxis in wound healing response to PDGF-AA are coordinated by the primary cilium in fibroblasts', *Cell Physiol Biochem,* 25 (2-3), 279-92.
Schweisguth, F (2004), 'Regulation of Notch Signaling Activity', *Current biology : CB,* 14 (3).
Sempou, E, et al. (2018), 'Candidate Heterotaxy Gene FGFR4 Is Essential for Patterning of the Left-Right Organizer in Xenopus', *Frontiers in physiology,* 9.
Shi, X., et al. (2017), 'Super-resolution microscopy reveals that disruption of ciliary transition-zone architecture causes Joubert syndrome', *Nat Cell Biol,* 19 (10), 1178-88.
Shiang, R., et al. (1994), 'Mutations in the transmembrane domain of FGFR3 cause the most common genetic form of dwarfism, achondroplasia', *Cell,* 78 (2), 335-42.
Shinohara, K., et al. (2012), 'Two rotating cilia in the node cavity are sufficient to break left-right symmetry in the mouse embryo', *Nat Commun,* 3, 622.
Shiratori, H., et al. (2006), 'Conserved regulation and role of Pitx2 in situs-specific morphogenesis of visceral organs', *Development,* 133 (15), 3015-25.
Silver, L.M. (1995), *Mouse Genetics: Concepts and Applications* (Oxford: Oxford University Press).
Singla, V. and Reiter, J. F. (2006), 'The primary cilium as the cell's antenna: signaling at a sensory organelle', *Science,* 313 (5787), 629-33.
Sirbu, IO and Duester, G (2006), 'Retinoic-acid Signalling in Node Ectoderm and Posterior Neural Plate Directs Left-Right Patterning of Somitic Mesoderm', *Nature cell biology,* 8 (3).
Song, H., et al. (2010), 'Planar cell polarity breaks bilateral symmetry by controlling ciliary positioning', *Nature,* 466 (7304), 378-82.
Splitt, M. P., Burn, J., and Goodship, J. (1996), 'Defects in the determination of left-right asymmetry', *J Med Genet,* 33 (6), 498-503.
Sreekumar, V. and Norris, D. P. (2019), 'Cilia and development', *Curr Opin Genet Dev,* 56, 15-21.
Stewart, M. (2007), 'Molecular mechanism of the nuclear protein import cycle', *Nat Rev Mol Cell Biol,* 8 (3), 195-208.
Stolen, C. M. and Griep, A. E. (2000), 'Disruption of lens fiber cell differentiation and survival at multiple stages by region-specific expression of truncated FGF receptors', *Dev Biol,* 217 (2), 205-20.

Sulik, K., et al. (1994), 'Morphogenesis of the murine node and notochordal plate', *Dev Dyn,* 201 (3), 260-78.
Sun, Jingjing and Stathopoulos, Angelike (2018), 'FGF controls epithelial-mesenchymal transitions during gastrulation by regulating cell division and apicobasal polarity'.
Sun, L., et al. (1999a), 'Design, synthesis, and evaluations of substituted 3-[(3- or 4-carboxyethylpyrrol-2-yl)methylidenyl]indolin-2-ones as inhibitors of VEGF, FGF, and PDGF receptor tyrosine kinases', *J Med Chem,* 42 (25), 5120-30.
Sun, X., et al. (1999b), 'Targeted disruption of Fgf8 causes failure of cell migration in the gastrulating mouse embryo', *Genes Dev,* 13 (14), 1834-46.
Sánchez, I and Dynlacht, BD (2016), 'Cilium assembly and disassembly', *Nature cell biology,* 18 (7).
Takao, D., et al. (2014), 'An assay for clogging the ciliary pore complex distinguishes mechanisms of cytosolic and membrane protein entry', *Curr Biol,* 24 (19), 2288-94.
--- (2013), 'Asymmetric distribution of dynamic calcium signals in the node of mouse embryo during left-right axis formation', *Dev Biol,* 376 (1), 23-30.
Takeda, S., et al. (1999), 'Left-right asymmetry and kinesin superfamily protein KIF3A: new insights in determination of laterality and mesoderm induction by kif3A-/- mice analysis', *J Cell Biol,* 145 (4), 825-36.
Tanaka, C, et al. (2007), 'Long-range action of Nodal requires interaction with GDF1', *Genes Dev,* 21 (24), 3272-82.
Tanaka, Y., Okada, Y., and Hirokawa, N. (2005), 'FGF-induced vesicular release of Sonic hedgehog and retinoic acid in leftward nodal flow is critical for left-right determination', *Nature,* 435 (7039), 172-7.
Tang, Y., et al. (2003), 'Genetic modifiers interact with maternal determinants in vascular development of Tgfb1(-/-) mice', *Hum Mol Genet,* 12 (13), 1579-89.
--- (2005), 'Epistatic interactions between modifier genes confer strain-specific redundancy for Tgfb1 in developmental angiogenesis', *Genomics,* 85 (1), 60-70.
Tanos, B. E., et al. (2013), 'Centriole distal appendages promote membrane docking, leading to cilia initiation', *Genes Dev,* 27 (2), 163-8.
Tavares, B., et al. (2017), 'Notch/Her12 signalling modulates, motile/immotile cilia ratio downstream of Foxj1a in zebrafish left-right organizer', *Elife,* 6.
Terada, M., et al. (2001), 'Fibroblast growth factor receptor 3 lacking the Ig IIIb and transmembrane domains secreted from human squamous cell carcinoma DJM-1 binds to FGFs', *Mol Cell Biol Res Commun,* 4 (6), 365-73.
Threadgill, D. W., et al. (1995), 'Targeted disruption of mouse EGF receptor: effect of genetic background on mutant phenotype', *Science,* 269 (5221), 230-4.
Tohyama, O., et al. (2014), 'Antitumor activity of lenvatinib (e7080): an angiogenesis inhibitor that targets multiple receptor tyrosine kinases in preclinical human thyroid cancer models', *J Thyroid Res,* 2014, 638747.
Tomlinson, D. C., et al. (2005), 'Alternative splicing of fibroblast growth factor receptor 3 produces a secreted isoform that inhibits fibroblast growth factor-induced proliferation and is repressed in urothelial carcinoma cell lines', *Cancer Res,* 65 (22), 10441-9.
Tsang, W. Y. and Dynlacht, B. D. (2013), 'CP110 and its network of partners coordinately regulate cilia assembly', *Cilia,* 2 (1), 9.
Tsiairis, C. D. and McMahon, A. P. (2009), 'An Hh-dependent pathway in lateral plate mesoderm enables the generation of left/right asymmetry', *Curr Biol,* 19 (22), 1912-7.
Tsiokas, L., et al. (1997), 'Homo- and heterodimeric interactions between the gene products of PKD1 and PKD2', *Proc Natl Acad Sci U S A,* 94 (13), 6965-70.
Verkhratsky, A. (2007), 'Calcium and cell death', *Subcell Biochem,* 45, 465-80.
Viotti, M., et al. (2012), 'Role of the gut endoderm in relaying left-right patterning in mice', *PLoS Biol,* 10 (3), e1001276.

Visel, A., Thaller, C., and Eichele, G. (2004), 'GenePaint.org: an atlas of gene expression patterns in the mouse embryo', *Nucleic Acids Res,* 32 (Database issue), D552-6.
Vogel, P., et al. (2010), 'Situs inversus in Dpcd/Poll-/-, Nme7-/- , and Pkd1l1-/- mice', *Vet Pathol,* 47 (1), 120-31.
Vogel, T. W., et al. (2012), 'The role of primary cilia in the pathophysiology of neural tube defects', *Neurosurg Focus,* 33 (4), E2.
Warburton, D., et al. (2005), 'Molecular mechanisms of early lung specification and branching morphogenesis', *Pediatr Res,* 57 (5 Pt 2), 26R-37R.
Watanabe, Y., et al. (2010), 'Role of mesodermal FGF8 and FGF10 overlaps in the development of the arterial pole of the heart and pharyngeal arch arteries', *Circ Res,* 106 (3), 495-503.
Wheway, G., et al. (2013), 'Aberrant Wnt signalling and cellular over-proliferation in a novel mouse model of Meckel-Gruber syndrome', *Dev Biol,* 377 (1), 55-66.
Williams, C. M., et al. (2021), 'Monomeric/dimeric forms of Fgf15/FGF19 show differential activity in hepatocyte proliferation and metabolic function', *FASEB J,* 35 (2), e21286.
Winter, S. F., et al. (2007), 'Conditional activation of FGFR1 in the prostate epithelium induces angiogenesis with concomitant differential regulation of Ang-1 and Ang-2', *Oncogene,* 26 (34), 4897-907.
Wood, C. R., et al. (2013), 'The cilium secretes bioactive ectosomes', *Curr Biol,* 23 (10), 906-11.
Wu, C. T., Chen, H. Y., and Tang, T. K. (2018), 'Myosin-Va is required for preciliary vesicle transportation to the mother centriole during ciliogenesis', *Nat Cell Biol,* 20 (2), 175-85.
Wu, G., et al. (2002), 'Trans-heterozygous Pkd1 and Pkd2 mutations modify expression of polycystic kidney disease', *Hum Mol Genet,* 11 (16), 1845-54.
Wu, N., et al. (2019), 'The Progress of CRISPR/Cas9-Mediated Gene Editing in Generating Mouse/Zebrafish Models of Human Skeletal Diseases', *Comput Struct Biotechnol J,* 17, 954-62.
Yadav, S. P., et al. (2016), 'Centrosomal protein CP110 controls maturation of the mother centriole during cilia biogenesis', *Development,* 143 (9), 1491-501.
Yamaguchi, T. P., et al. (1994), 'fgfr-1 is required for embryonic growth and mesodermal patterning during mouse gastrulation', *Genes Dev,* 8 (24), 3032-44.
Ye, X., et al. (2014), 'C2cd3 is critical for centriolar distal appendage assembly and ciliary vesicle docking in mammals', *Proc Natl Acad Sci U S A,* 111 (6), 2164-9.
Yoshiba, S., et al. (2012), 'Cilia at the node of mouse embryos sense fluid flow for left-right determination via Pkd2', *Science,* 338 (6104), 226-31.
Yu, F. X. and Guan, K. L. (2013), 'The Hippo pathway: regulators and regulations', *Genes Dev,* 27 (4), 355-71.
Yu, S., et al. (2004), 'Distinct transcriptional control and action of fibroblast growth factor receptor 4 in differentiating skeletal muscle cells', *Lab Invest,* 84 (12), 1571-80.
Yushkevich, P. A., et al. (2006), 'User-guided 3D active contour segmentation of anatomical structures: significantly improved efficiency and reliability', *Neuroimage,* 31 (3), 1116-28.
Zaidi, S., et al. (2013), 'De novo mutations in histone-modifying genes in congenital heart disease', *Nature,* 498 (7453), 220-3.
Zhang, D., et al. (2021), 'Targeting local lymphatics to ameliorate heterotopic ossification via FGFR3-BMPR1a pathway', *Nat Commun,* 12 (1), 4391.
Zhao, H., et al. (2004), 'Role of fibroblast growth factor receptors 1 and 2 in the ureteric bud', *Dev Biol,* 276 (2), 403-15.
Zheng, C., et al. (2019), 'Suppressing UPR-dependent overactivation of FGFR3 signaling ameliorates SLC26A2-deficient chondrodysplasias', *EBioMedicine,* 40, 695-709.
Zhu, D., et al. (2009), 'Growth arrest induces primary-cilium formation and sensitizes IGF-1-receptor signaling during differentiation induction of 3T3-L1 preadipocytes', *J Cell Sci,* 122 (Pt 15), 2760-8.

Zhu, R., et al. (2017), 'Pectin Penta-Oligogalacturonide Suppresses Intestinal Bile Acids Absorption and Downregulates the FXR-FGF15 Axis in High-Cholesterol Fed Mice', *Lipids,* 52 (6), 489-98.

Zhuang, L., Falquet, L., and Trueb, B. (2010), 'Genome-wide comparison of FGFRL1 with structurally related surface receptors', *Exp Ther Med,* 1 (1), 161-68.

Appendix

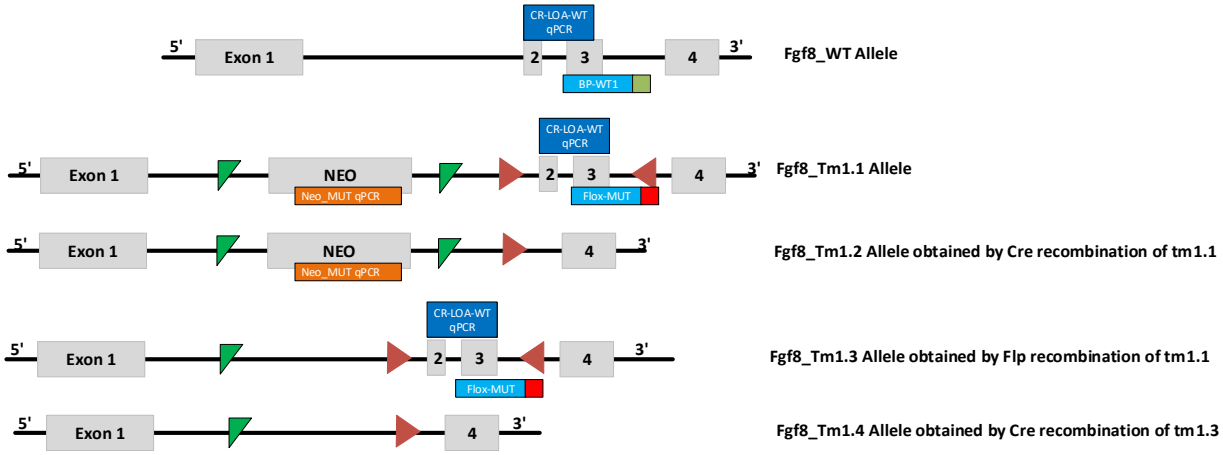


Figure1: Showing WT and different Mutant alleles of Fgf8. The qPCR assays are designed at 3' end near loxp insertion using Universal forward and a Universal Probe (light blue boxes) with WT specific reverse primer (olive green box) for the WT allele (BP-WT assay) and MUT specific reverse primer (Red box) for the Mutant allele (Flox-MUT assay for Tm1.1 and Tm1.3). There is CR-LOA-WT assay (Dark blue box) designed near Exons 2 and 3 to detect cre recombination i.e. Tm1.2 and Tm1.4 and Neo Mutant assay to detect the presence of Neo in Tm1.1 and Tm1.2 alleles. Please refer to Table 1 for expected copy numbers and genotypes.

Fgf8-BP-WT1	Fgf8-CR-LOA-WT1	Fgf8-Flox-MUT1	Fgf8-CRE-DEL-Mut1	Neo	Genotype
2	2	0	0	0	WT
1	2	1	0	1	Fgf8_Tm1.1:Het
1	1	0	1	1	Fgf8_Tm1.2:Het
1	2	1	0	0	Fgf8_Tm1.3:Het
1	1	0	1	0	Fgf8_Tm1.4:Het
0	1	1	1	2	Fgf8_Tm1.1:Het; Fgf8_Tm1.2:Het
0	2	2	0	1	Fgf8_Tm1.1:Het; Fgf8_Tm1.3:Het
0	1	1	1	0	Fgf8_Tm1.3:Het; Fgf8_Tm1.4:Het

Table A1: Copy number chart for various assays as shown in Figure 1 (above) and expected genotypes.

Inhibitor	Concentration
SU5402	20µM
BGJ398	60µM
AZD4547	10µM

Table A2: Concentrations for each inhibitor when used in embryo culture.

Gene primer	Sequence
*Fgfr3*_F	AGCGACAGGTGTCCTTGGAA
*Fgfr3*_R	GGATGCCAGGATACGGTGAG
*Fgfr4*_F	AACGACTGAGACTGGGCGAT
*Fgfr4*_R	GCTGCCCTCTTTGTACCAGT

Table A3: Sequences of primers used in production of WISH probes for *Fgfr3* and *Fgfr4*.

Company/ cat. no.	Against	Dilution	Species raised in
Abcam ab136648	ARL13B	1:200	Mouse
Protein tech 17711-1-AP	ARL13B	1:200	Rabbit
Sigma-Aldrich F5421	FGFR1	1:100	Rabbit
Abnova H00002263-A01	FGFR2	1:200	Mouse
SantaCruz sc-390423	FGFR3	1:100	Mouse
SantaCruz sc-136988	FGFR4	1:50	Mouse
Abcam ab96879	Mouse IgG (DyLight® 488)	1:500	Goat
Abcam ab96882	Mouse IgG (DyLight® 650)	1:500	Goat
Abcam ab96883	Rabbit IgG (DyLight® 488)	1:500	Goat
Abcam ab96894	Rabbit IgG (DyLight® 650)	1:500	Donkey

Table A3: Antibodies used in immunofluorescence experiments.

Antibody against	References
FGFR1	(Holley et al. 2010; Peters et al. 1992; Stolen and Griep 2000; Winter et al. 2007)
FGFR2	*
FGFR3	(Cheng et al. 2014; Zhang et al. 2021; Zheng et al. 2019)
FGFR4	(Fu et al. 2012; Fu et al. 2016; Futami et al. 2017; Niu et al. 2020; Tohyama et al. 2014; Williams et al. 2021; R. Zhu et al. 2017)

Table A4: Validation of FGFR antibodies used in immunofluorescence experiments. * no information currently available due to discontinuation.

medium	start stage	end stage	use
SU5402	HFs	2ss	SEM
SU5402	HFs	2ss	SEM
SU5402	HFs	2ss	SEM
SU5402	4-6ss	5ss	WISH
SU5402	4-6ss	8/9ss	WISH
SU5402	s/b	0ss	SEM
SU5402	HFs	2ss	SEM
SU5402	HFs	2ss	SEM
SU5402	HFs	2ss	WISH
SU5402	HFs	2ss	WISH
SU5402	1-3ss	3ss	WISH
SU5402	s/b	0ss	SEM
SU5402	s/b	2ss	WISH
SU5402	s/b	2ss	SEM
SU5402	s/b	1ss	SEM
SU5402	s/b	2/3ss	SEM
SU5402	s/b	2ss	SEM
SU5402	s	2ss	WISH
SU5402	b	2ss	WISH
SU5402	1-3ss	3ss	SEM
SU5402	1-3ss	3ss	SEM
SU5402	1-3ss	3ss	SEM
SU5402	1-3ss	3ss	SEM
SU5402	1-3ss	3ss	SEM
SU5402	1-3ss	3ss	WISH
SU5402	HFs	3ss	WISH
SU5402	HFs	3ss	WISH
SU5402	2/3ss	4ss	SEM
SU5402	2/3ss	4ss	WISH
SU5402	2/3ss	4ss	SEM
SU5402	2/3ss	4ss	SEM
SU5402	2/3ss	4ss	WISH
SU5402	2/3ss	5ss	SEM
SU5402	4-6ss	8ss	SEM
SU5402	4-6ss	9ss	SEM
SU5402	4-6ss	6ss	SEM
SU5402	2/3ss	5ss	SEM
SU5402	2/3ss	5ss	SEM
SU5402	s/b	2ss	WISH
SU5402	s/b	2ss	WISH
SU5402	s/b	3ss	WISH
SU5402	s/b	3ss	WISH
SU5402	s/b	3ss	WISH

SU5402	s	b	WISH
SU5402	s	b	WISH
SU5402	2/3ss	5ss	SEM
SU5402	2/3ss	5ss	SEM
SU5402	4-6ss	12ss	WISH
SU5402	4-6ss	7ss	WISH
SU5402	b	b	WISH
SU5402	b	b	WISH
SU5402	b	b	WISH
SU5402	s	b	WISH
SU5402	b	b	SEM
SU5402	b	b	SEM
SU5402	b	b	SEM
SU5402	s/b	HFs	SEM
SU5402	s/b	HFs	SEM
SU5402	s	b	SEM
SU5402	2/3ss	6ss	SEM
SU5402	2/3ss	6ss	WISH
SU5402	s	b	SEM
SU5402	s	b	SEM
SU5402	s	b	SEM
SU5402	s	HFs	WISH
SU5402	s/b	HFs	SEM
SU5402	s	HFs	SEM
SU5402	s	HFs	SEM
SU5402	s	HFs	SEM
SU5402	s	HFs	WISH
SU5402	b	HFs	WISH
SU5402	b	HFS	WISH
SU5402	s	HFS	WISH
SU5402	s	s	WISH
SU5402	s	s	SEM
SU5402	s	s	SEM
SU5402	s	s	SEM
SU5402	b	s/b	WISH
SU5402	s	s/b	WISH
SU5402	HFs	0ss	WISH
SU5402	6ss	8ss	WISH
SU5402	1ss	3ss	WISH
control	HFs	2ss	WISH
control	s/b	HFS	WISH
control	s/b	HFS	WISH
control	s/b	s/b	WISH
control	s/b	3SS	WISH
control	s/b	2SS	WISH

control	s/b	HFS	WISH
control	s/b	3SS	WISH
control	s/b	s/b	SEM
control	s/b	s/b	SEM
control	s/b	s/b	SEM
control	s/b	3SS	WISH
control	s/b	1SS	WISH
control	s/b	1SS	WISH
control	s/b	b	WISH
control	s/b	b	WISH
control	s/b	b	WISH
control	s/b	HFS	WISH
control	s/b	HFS	WISH
control	s/b	4SS	WISH
control	s/b	3SS	WISH
control	s/b	3SS	WISH
control	s	HFs	WISH
control	s	HFs	WISH
control	s	HFs	WISH
control	s	HFs	WISH
control	s	s/b	SEM
control	s	s/b	SEM
control	s	s/b	SEM
control	s	s/b	SEM
control	s	s/b	SEM
control	s	HFs	WISH
control	s	b	WISH
control	s	2ss	WISH
control	s	2ss	WISH
control	s	1ss	WISH
control	s	b	WISH
control	s	4SS	WISH
control	s	4SS	WISH
control	s	s	WISH
control	s	b	WISH
control	s	b	WISH
control	s	b	WISH
control	s	b	WISH
control	s	s	SEM
control	s	b	SEM
control	s	s	SEM
control	s	s	SEM
control	s	s	SEM
control	s	b	SEM
control	s	b	SEM

control	HFs	4SS	WISH
control	HFs	2ss	WISH
control	HFs	2/3ss	WISH
control	HFs	1/2ss	WISH
control	HFs	2/3ss	SEM
control	HFs	3ss	SEM
control	HFs	2ss	SEM
control	HFs	2/3ss	SEM
control	HFs	2ss	WISH
control	HFs	3ss	WISH
control	HFs	1ss	WISH
control	HFs	2ss	WISH
control	HFs	5ss	WISH
control	HFs	5ss	WISH
control	HFs	4ss	SEM
control	HFs	2ss	SEM
control	HFs	2ss	WISH
control	HFs	2ss	WISH
control	b	0ss	WISH
control	b	0ss	WISH
control	b	0ss	WISH
control	b	HFs	WISH
control	b	HFs	WISH
control	b	2ss	WISH
control	b	3ss	WISH
control	b	4SS	WISH
control	b	3SS	WISH
control	b	s/b	WISH
control	b	2ss	WISH
control	b	2ss	WISH
control	b	1ss	WISH
control	b	3ss	WISH
control	b	HFs	WISH
control	b	HFs	WISH
control	b	s/b	SEM
control	b	s/b	SEM
control	b	0ss	SEM
control	5ss	7ss	WISH
control	4-6ss	7/8ss	WISH
control	4-6ss	6/7ss	WISH
control	4-6ss	8ss	WISH
control	4-6ss	5ss	WISH
control	4-6ss	6ss	SEM
control	4-6ss	7ss	SEM
control	4-6ss	6/7ss	SEM

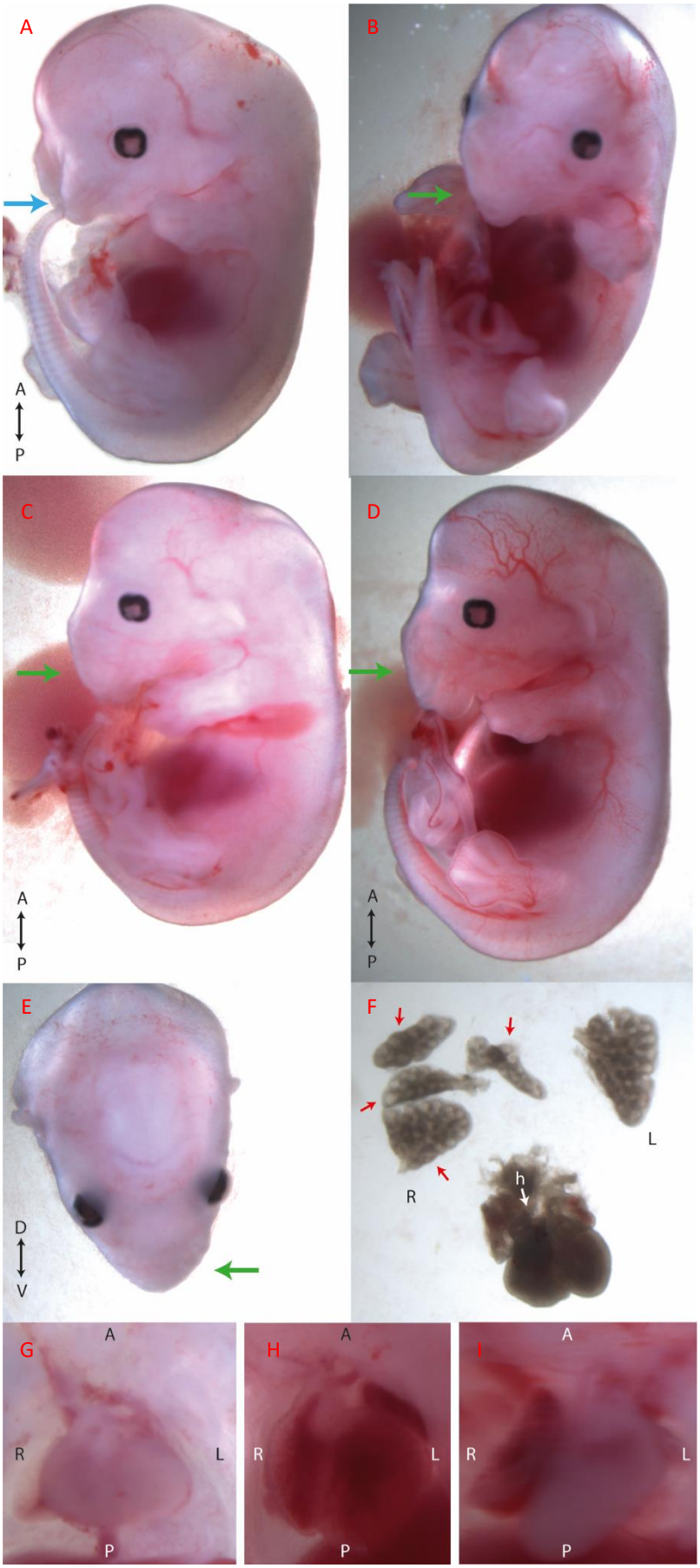
control	4-6s	8ss	SEM
control	4-6s	6ss	SEM
control	4-6s	7ss	SEM
control	4-6s	7ss	SEM
control	1-3ss	3ss	SEM
control	1-3ss	4ss	SEM
control	1-3ss	7ss	SEM
control	1-3ss	2ss	WISH
control	1-3ss	4ss	WISH
control	1-3ss	6ss	WISH
control	1-3ss	4ss	WISH
control	1-3ss	2ss	WISH
control	1-3ss	4ss	WISH
control	1-3ss	4ss	SEM
control	1-3ss	4ss	SEM
control	1-3ss	4ss	WISH
control	1-3ss	5ss	WISH
control	1-3ss	6ss	WISH
control	1-3ss	4ss	SEM
control	1-3ss	4ss	SEM
control	1-3ss	3/4ss	SEM
control	1-3ss	6ss	SEM
control	1-3ss	7ss	SEM
control	1-3ss	4ss	SEM
control	1-3ss	4ss	SEM
control	1-3ss	3ss	SEM
control	1-3ss	3/4ss	SEM
control	1-3ss	3/4ss	SEM
control	1-3ss	4ss	SEM
control	1-3ss	4ss	SEM
control	1-3ss	4ss	SEM
control	1-3ss	3/4ss	SEM
control	1-3ss	4ss	SEM
control	1-3ss	5ss	SEM
control	1-3ss	5/6ss	SEM
control	1-3ss	4ss	SEM
control	HFs	5ss	WISH
BGJ	1ss	3ss	WISH
BGJ	5ss	6ss	WISH
BGJ	s/b	0ss	SEM
BGJ	HFs	2ss	SEM
BGJ	HFs	2ss	SEM
BGJ	1-3ss	3ss	WISH
BGJ	1-3ss	3ss	WISH
BGJ	1-3ss	3ss	SEM

BGJ	HFs	2ss	WISH
BGJ	HFs	2ss	WISH
BGJ	HFs	2ss	WISH
BGJ	HFs	2ss	WISH
BGJ	1-3ss	3ss	WISH
BGJ	1-3ss	3ss	WISH
BGJ	1-3ss	3ss	WISH
BGJ	1-3ss	3ss	WISH
BGJ	1-3ss	3ss	SEM
BGJ	2-3ss	4ss	SEM
BGJ	2-3ss	4ss	WISH
BGJ	2-3ss	5ss	SEM
BGJ	HFs	2ss	SEM
BGJ	2-3ss	5ss	WISH
BGJ	2-3ss	6ss	SEM
BGJ	2-3ss	6ss	WISH
BGJ	s/b	0ss	WISH
BGJ	s/b	0ss	WISH
BGJ	s/b	0ss	WISH
BGJ	s/b	0ss	WISH
BGJ	HFs	2ss	WISH
BGJ	HFs	3ss	WISH
BGJ	HFs	5ss	WISH
BGJ	s/b	1ss	WISH
BGJ	s/b	1ss	WISH
BGJ	s/b	1SS	WISH
BGJ	b	1ss	WISH
BGJ	b	2ss	WISH
BGJ	s	2ss	WISH
BGJ	s	2ss	WISH
BGJ	s/b	3ss	WISH
BGJ	s/b	3ss	WISH
BGJ	b	3ss	WISH
BGJ	s	3ss	WISH
BGJ	b	3ss	WISH
BGJ	b	3ss	WISH
BGJ	s	b	SEM
BGJ	s	b	SEM
BGJ	s	b	SEM
BGJ	s	b	SEM
BGJ	b	b	WISH
BGJ	b	b	WISH
BGJ	b	b	WISH
BGJ	s	b	SEM
BGJ	s	b	SEM
BGJ	s	b	SEM

BGJ	s/b	HFS	WISH
BGJ	HFs	2ss	WISH
BGJ	s/b	HFs	WISH
BGJ	b	HFs	SEM
BGJ	s/b	s/b	WISH
BGJ	s	s	SEM
BGJ	s	s	SEM
BGJ	s	s	SEM
BGJ	s	s	SEM
BGJ	s	s	SEM
BGJ	s	s	SEM
BGJ	b	s/b	WISH
BGJ	b	s/b	SEM
AZD	5ss	7ss	WISH
AZD	HFs	1ss	WISH
AZD	7ss	8ss	WISH
AZD	HFs	3ss	WISH
AZD	HFs	2ss	WISH
AZD	HFs	2ss	WISH
AZD	1-3ss	3ss	SEM
AZD	1-3ss	3ss	WISH
AZD	1-3ss	3ss	WISH
AZD	s/b	HFs	SEM
AZD	s/b	HFs	SEM
AZD	s/b	s/b	SEM
AZD	HFs	2ss	WISH
AZD	HFs	3ss	WISH
AZD	1-3ss	3ss	WISH
AZD	1-3ss	3ss	SEM
AZD	1-3ss	3ss	SEM
AZD	1-3ss	3ss	SEM
AZD	HFs	2ss	SEM
AZD	HFs	2ss	SEM
AZD	1-3ss	4ss	SEM
AZD	1-3ss	4/5ss	SEM
AZD	1-3ss	5ss	WISH
AZD	1-3ss	5ss	WISH
AZD	s/b	s/b	SEM
AZD	s/b	s/b	SEM
AZD	s/b	s/b	SEM
AZD	s/b	s/b	SEM
AZD	s	s	SEM
AZD	s	s	SEM
AZD	s	s	SEM
AZD	s	HFs	SEM

AZD	b	HFs	SEM
AZD	b	HFs	SEM
AZD	b	1ss	SEM
AZD	s/b	1ss	SEM
AZD	1-3ss	6/7ss	SEM
AZD	1-3ss	6ss	WISH
AZD	HFs	3ss	WISH
AZD	HFs	4ss	WISH
AZD	s/b	HFs	WISH
AZD	s/b	HFs	WISH
AZD	s/b	HFs	WISH
AZD	s/b	HFs	WISH
AZD	s/b	HFs	WISH
AZD	s/b	HFs	WISH
AZD	s/b	HFs	WISH
AZD	s/b	HFs	WISH
AZD	b	HFs	WISH
AZD	b	HFs	WISH
AZD	s	HFs	WISH
AZD	s/b	2ss	WISH
AZD	s/b	2ss	WISH
AZD	s	HFs	WISH
AZD	s/b	3ss	WISH
AZD	s/b	3ss	WISH
AZD	s/b	3ss	WISH
AZD	s/b	2ss	WISH
AZD	HFs	5ss	WISH
AZD	b	2ss	WISH
AZD	s/b	1ss	WISH
AZD	s/b	1ss	WISH
AZD	s/b	1ss	WISH
AZD	s/b	1ss	WISH
AZD	s/b	1ss	WISH
AZD	b	1ss	WISH
AZD	b	1ss	WISH
AZD	b	1ss	WISH
AZD	s/b	0ss	WISH
AZD	s/b	0ss	WISH
AZD	s/b	0ss	WISH
AZD	s	0ss	WISH

Table A5: Full data set from **Figure 4.2.5**, showing each embryos culture medium, stage pre- and post-culture, and the method by which the embryo was further analysed and imaged.



Appendix Figure 2: Phenotypes in E13.5 Fgf8 mutant embryos (corresponds with **Figure 5.2.4**). **A** shows an *Fgf8* tm1.2 heterozygous embryo with a malformed snout, blue arrow (as indicated in **Figure 5.2.4 B** in grey). **B-E** show embryos with a malformed, elongated and pointed snout/head shape, pointed out with green arrows (indicated in orange in **Figure 5.2.4 B**). Anterior (A), posterior (P), dorso (D) and ventral(V) axes are as indicated. **F** shows the normal lung lobe patterning of the mouse embryo, with 4 right (R) lung lobes, indicated by red arrows, and a singular left lung lobe (corresponding to **Figure 5.2.4 D**). The accompanying heart (h) is also pictured. **G-I** show various heart defects, corresponding to **Figure 5.2.4 E** and **F**, with anterior (A), posterior (P), left (L) and right (R) orientations indicated. **G** shows an embryos with double-outlet right ventricle (DORV). **H** shows an embryonic heart with DORV and interrupted aortic arch (IAA). **I** shows an embryo with a central directed heart, with IAA also.